The Mass Growth of Galaxies over the Last 8 Gyr

Richard Anthony Beare

PhD

School of Physics

April 2014

Abstract

We measured the stellar mass growth of galaxies over the last 8 Gyr ($z <\sim 1.2$) by deriving B and K-band luminosity functions and inferring mass evolution from these. Accuracy was achieved using improved methods for determining both total apparent magnitudes and K-corrections. The very large sample size of 335 000 galaxies in Boötes is ∼10 times larger than samples in previous studies covering a similar redshift range, and this reduced cosmic variance errors to a minimum.

Our accurate method of accounting for all the light coming from an individual galaxy was based on analysis of growth curves of magnitude with aperture diameter for isolated galaxies. Our measurements of galaxy luminosity used an improved method of determining K-corrections which is both simpler and more accurate than many previous methods, being based on a quadratic function of just one suitably chosen observed colour. The method relies on the extensive and accurate new set of 125 empirical galaxy template SEDs from Brown et al. (2013).

Our sample was divided into red and blue subsamples using an evolving cut in restframe colour-magnitude space and we studied these separately as well as together. To quantify luminosity evolution we fitted Schechter functions to our B and K-band luminosity functions and compared the evolution of these with previous studies in the literature.

Assuming published K-band stellar mass to light ratios based on optical colour, we derived stellar mass functions. We found that the stellar mass density of red galaxies increased by a factor of ∼1.9 from $z = 1.1$ to $z = 0.3$, while that of blue galaxies increased only by $\times \sim 1.4$. These measurements are consistent with migration of blue galaxies to the red sequence as they cease to form stars. We also found that the most massive red galaxies hardly changed in mass from $z = 1.1$ to $z = 0.3$, whilst the most massive blue galaxies decreased in mass by a factor of $\times \sim 0.6$. This further confirmed the phenomenon of "downsizing" reported by many authors whereby the most massive star-forming galaxies ceased star formation first and moved to the red sequence. For red galaxies we compared these results with inferences from our measurements of B-band luminosity function evolution.

In addition to using the new K-correction method for our B and K-band luminosity functions, we also derived K-corrections for the five Sloan Digital Sky Survey filters and make tables of the parameters for these publicly available to the astronomical community. Using a sample of SDSS galaxies we demonstrated that our method provides superior accuracy in several respects to the commonly used *kcorrect* method, with clearer restframe colour separation of red and blue galaxies, a much tighter red sequence, and no spurious cloud of extremely red galaxies at $z \sim 0.2$ which is not present in the low redshift Universe.

Contents

List of Figures

List of Tables

Declaration

This thesis contains no material that has been accepted for the award of any other degree or diploma in any university or other institution. To the best of my knowledge, this thesis contains no material previously published or written by another person, except where due reference is made in the text of the thesis

.

Acknowledgements

I would like to thank my supervisor Michael Brown for his helpful and meticulous comments on various drafts of this thesis and the research which went into it. His ready availability to discuss issues at any time despite his busy schedule has been much appreciated. The scientific value of the work here described is due in large part to the scientifically highly significant atlas of galaxy SED templates that Michael Brown and collaborators have produced and I consider myself fortunate to have been able to make use of this far-reaching resource. I also wish to thank my co-supervisor Kevin Pimbblet for his valuable advice at various points. I am also extremely grateful to Monash University for providing me with financial support including international scholarships to enable me to carry out the work here described.

I would also like to acknowledge the friendly and supportive role of my fellow astrophysics PhD students, especially David Palamara, Tim Dolley and Nic Bonne, and that of Gary Ruben who introduced me to the Python programming language. Without Python and its associated components my research would have been a lot harder and much less enjoyable and I am very grateful to the numerous people who have contributed to the development of this Open Source software.

Finally I would like to thank my wife Louise for her encouragement and patience during the writing of this thesis.

1. INTRODUCTION

1.1. What is a galaxy?

Galaxies are large gravitationally bound assemblies of stars, gas and dust embedded in dark matter halos. Prior to 1925 it was not known whether galaxies were separate "island Universes" outside of our Milky Way Galaxy or were contained within it. Astronomers were divided on the issue and in 1922 a debate was organised between Heber Curtis who argued that the so-called "Andromeda Nebula" lay outside the Milky Way and Harold Shapley who argued that it was a much smaller object inside it. The debate was inconclusive but Opik (1922) measured the distance to the Andromeda Nebula to be 450 kpc, too far away to be within the Milky Way. Using Cepheid variable stars whose periods were a known function of their luminosity, Edwin Hubble proved in 1925 that galaxies did indeed lie outside the Milky Way and were comparable in composition to it (Hubble 1926). This was the start of extragalactic astronomy.

Later observations by Hubble led him to classify galaxies into disc galaxies, ellipticals and irregulars according to their morphology (Hubble 1926, 1936) and he proposed that the various morphologies formed a sequence as shown in Figure 1. Refinements of the Hubble sequence are still used today to classify galaxies (e.g. de Vaucouleurs 1974). Examples of Hubble's different morphologies are shown in Figure 2 which contains images of nearby galaxies from the Sloan Digital Sky Survey (SDSS York et al. 2000; Stoughton et al. 2002). Hubble called disc types "late type" and ellipticals and lenticulars "early type", but these names merely refer to position in the Hubble sequence and do not imply evolution from "early" to "late" type. Although these names do not have any physical meaning they are still very much in use today.

Elliptical galaxies are ellipsoid in shape and the stars within them move in orbits with a variety of orientiations. They contain mainly old stars and little gas, dust or star formation. Ellipticals vary in the degree that they appear flattened and this is quantified by the *ellipticity* $e = (1 - b/a)$ where a is the semi-major axis and b is the semi-minor axis. Ellipticals that appear circular (E0) have $e = 0$ while the most flattened (E7) have $b = 0.3a$ and $e = 0.7$.

Disc type galaxies are highly flattened systems, with central bulges that vary greatly in prominence and are similar to small elliptical galaxies. Within the disc region, stars, dust and gas move in highly ordered, nearly circular orbits. Most disc galaxies have a spiral structure within their discs, but some do not (lenticulars). The spiral arms of spiral galaxies contain star-forming regions that are bright and blue because they contain recently formed highly luminous hot blue stars. The blue stars account for most of the luminosity but not the

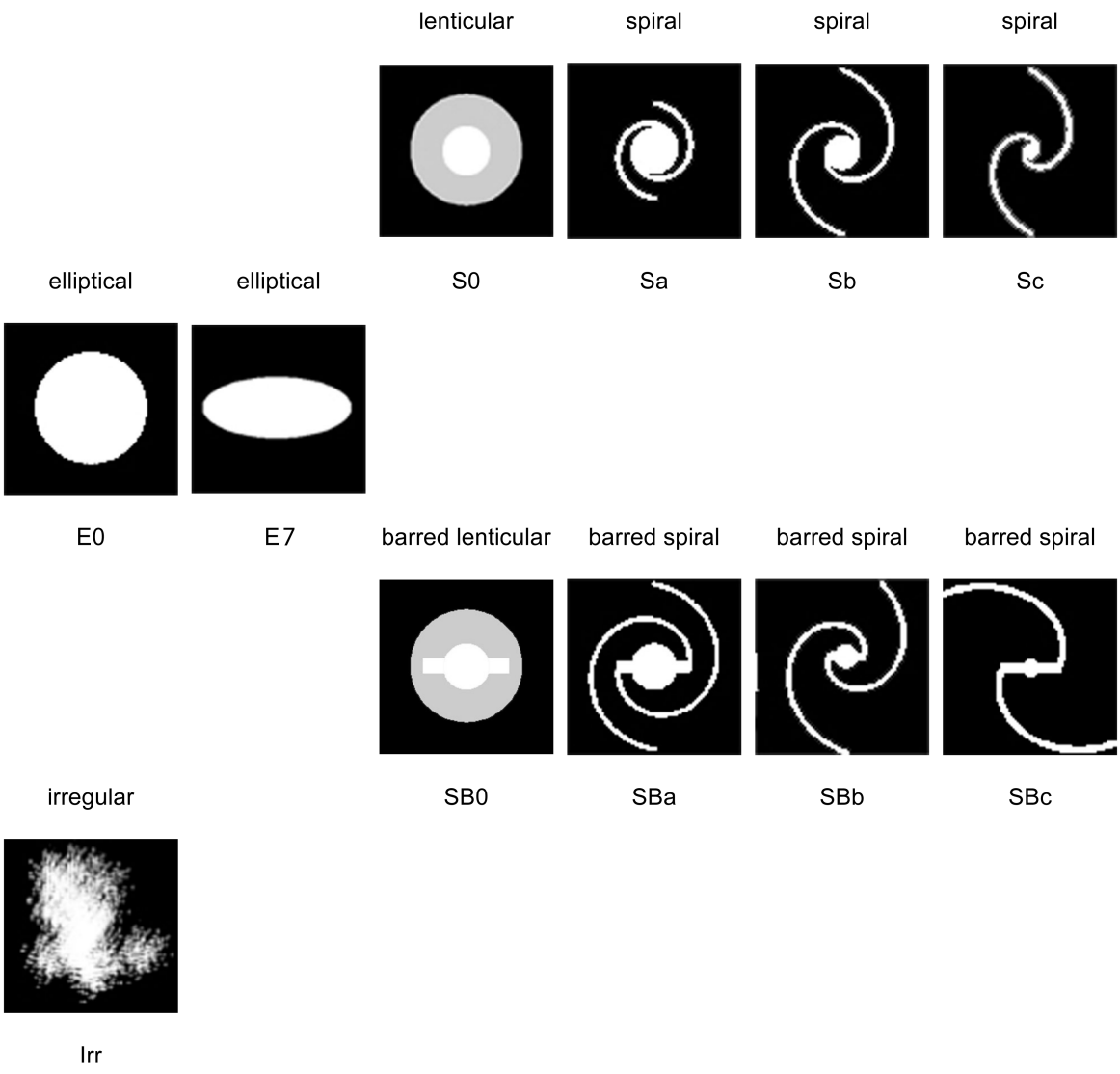

Fig. 1.—: **A schematic based on Hubble's original tuning fork diagram of galaxy types (Hubble 1936).** Sa to Sc are spiral galaxies, SBa to SBc are barred spirals, S0 is a lenticular galaxy, E0 to E7 are elliptical galaxies whose ellipticity (see text) varies from 0 to 0.7. Irr is an irregular galaxy. The pitch angles of the logarithmic spiral arms have been doubled for clarity.

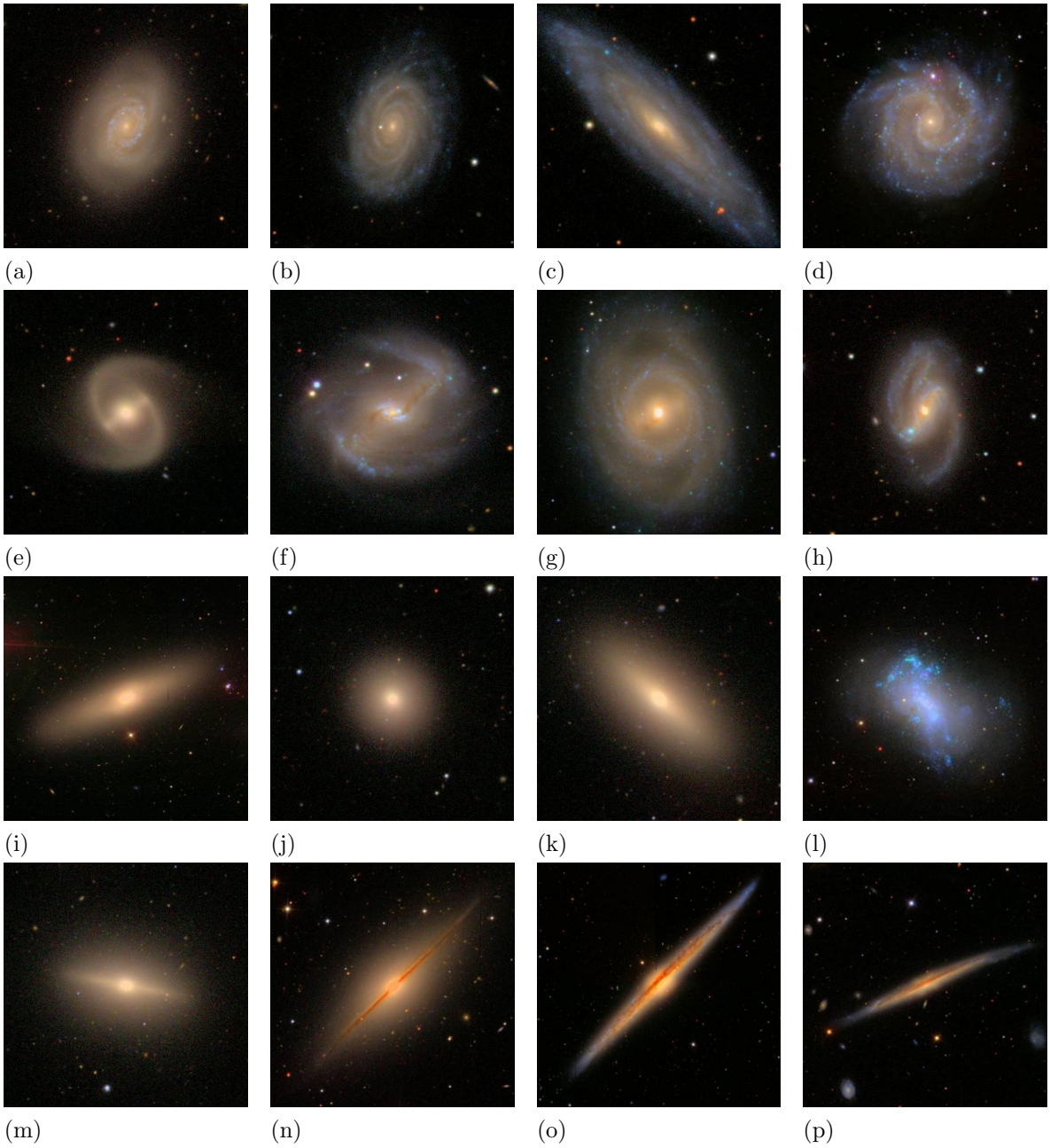

Fig. 2.—: **A selection of nearby galaxies with their Hubble classifications.** *Top row:* Four spiral galaxies (Sa, Sb, Sb, Sc). *Second row:* Four barred spiral galaxies (SBa, SBb, SBb, SBb). *Third row:* A lenticular galaxiy (S0), two elliptical galaxies (E0, E6), an irregular galaxy (irr). *Bottom row:* Four edge-on disc galaxies (S0, Sab, Sb, Sc). (Images are colour composites of Sloan Digital Sky Survey g, r and i images. The vivid colours are due to the wide separation of the g, r and i filters.)

mass, most of which resides in the much more numerous, less massive cooler stars. Spiral arms also contain "HII" regions that glow pink due to ionisation of hydrogen atoms by radiation from nearby bright stars. Dust is visible as dark regions, especially on the inside edges of spiral arms. The spiral sequence from Sa to Sc is characterised by increasingly open spiral arms, decreasing bulge to disc ratio, increasingly 'clumpy' and 'ragged' spiral arms, and a generally increasing proportion of gas and dust. About 50% of spirals have central bars (Binney & Merrifield 1998) and these are shown in the barred sequence SBa to SBc in Figure 2. Lenticular (S0) galaxies are disc galaxies without spiral arms that generally exhibit a large bulge to disc ratio, no star formation and little dust. As the bottom row of images in Figure 2 shows, edge-on disc galaxies can appear appreciably reddened due to absorption and scattering by dust.

Irregular galaxies have no obvious symmetry, central bulge or barred structure. Most are small, have high gas content and contain a relatively small number of bright blue star-forming regions.

1.2. Cosmology

One of the central problems in astronomy over the last half century has been to understand how galaxies form. The background to solving this problem is provided by cosmology - our understanding of the Universe as a whole. At the end of the 1920s Hubble and Humason showed that galaxies were receding at velocities proportional to their distances from us (Hubble 1929; Hubble & Humason 1931) and this implied that the Universe was expanding. Interestingly, Einstein added an additional "cosmological" constant Λ to the field equations of his General Theory of Relavity of 1915, specifically in order to *avoid* it predicting that the Universe must be expanding (or contracting). Once he learned of Hubble and Humason's discovery he removed the cosmological constant, stating that its inclusion had been the greatest blunder of his life.

Originally suggested by Gamow (1946), the model now known as the Hot Big Bang Model suggested that the Universe originated in a "Big Bang" from an initial point like state of infinite temperature and density from which it expanded with nuclear reactions creating the chemical elements ("nucleosynthesis"). Alpher et al. (1948) proposed that atomic nuclei were formed by successive capture of neutrons, and although their theory succesfully accounted for the proportions of hydrogen and helium in the Universe, their model of nuclear reactions was flawed and there were difficulties in accounting for the nucleosynthesis of heavier elements. Partly motivated by antipathy to the idea of a "Big Bang", Hoyle and others (e.g. Hoyle 1954) attempted to account for formation of all the elements through nucleosynthesis inside

stars. They were successful in accounting for the formation of elements heavier than lithium, but could not account for the formation of hydrogen, helium and lithium, which we now know were formed by big bang nucleosynthesis as proposed by Gamow and others.

Gamow realised that a remnant of the Big Bang would remain in the form of background radiation which would have increased in wavelength as the Universe expanded until it now formed a cosmic microwave background (CMB) with a temperature of a few degrees kelvin. Penzias & Wilson (1965) serendipitously discovered the CMB and it did prove to be almost isotropic with a temperature of 2.7 K, exactly as predicted by the Hot Big Bang model (Dicke et al. 1965). This discovery finally established the Hot Big Bang model as the dominant cosmological theory, rather than the rival steady state theory espoused by Hoyle, Bondi and Gold (Bondi & Gold 1948).

Study of the CMB gives valuable insights into the state of the Universe at the "era of recombination", the time about 380 000 years after the Big Bang (redshift ~ 1100) when it had cooled to about 3000 K, the temperature at which almost all free electrons would have combined with atomic nuclei to form neutral atoms (mainly hydrogen and helium). At this point the Universe became transparent to electromagnetic radiation and the radiation which had been in equilibrium with the plasma at ~ 3000 K no longer interacted with it. It has been travelling across space ever since gradually becoming longer in wavelength as space has expanded, until nowadays it has the wavelengths of ~ 0.1 mm to ~ 0.1 m that we see in the CMB today. Today's CMB spectrum is that of a black body at 2.725 K instead of the ~ 3000 K that it would have had at the time of recombination, when it was last scattered.

The fact that the Universe is almost isotropic on large scales originally caused a problem because it implied that regions that are too far apart today for light to have been able to travel between them during the lifetime of the Universe must nevertheless have been in causal contact in the past. Another difficulty was explaining why the Universe is flat to a high degree of accuracy (i.e. why it has zero spatial curvature) when the smallest initial deviation from flatness would have been expected to have been amplified enormously. Guth (1981) and others proposed a radical explanation for these two anomalies: that very shortly after the Big Bang the Universe underwent a period of extraordinarily rapid expansion know as "inflation". The idea of inflation is now part of standard cosmology.

1.3. Dark matter

The first evidence for "dark matter", detectable only by its gravitational effects, was provided by Zwicky (1933) who found that the visible mass of the galaxies in the Coma Cluster was insufficient in relation to individual galaxy velocities for the cluster to hold together. Rubin

& Ford (1970) showed from the redshifts of HII regions in the Andromeda Galaxy that its rotation curve remained flat with increasing radius. They subsequently showed that other spiral galaxies (Rubin et al. 1978, 1980) had flat rotation curves, implying the presence of unseen dark matter inside spiral galaxies. Other studies showed that the Milky Way and other galaxies must be embedded in massive dark matter halos in order to account for the motions of their satellite galaxies (e.g. Einasto et al. 1974; Ostriker et al. 1974).

Many suggestions have been made as to the nature of dark matter. One early suggestion was massive neutrinos (an example of "hot dark matter" or HDM, e.g. Gershtein & Zel'dovich 1966; Cowsik & McClelland 1972) but these were shown to have velocities too high for galaxies to form. Particles of larger mass and therefore lower velocities were needed. The term warm dark matter (WDM) is used for such particles less massive than (m_0 = 1keV) and "cold dark matter" (CDM) for particles more massive than 1keV (Smith & Markovic 2011). Simulations using the more slowly moving CDM particles were found to be much more successful in explaining the distributions of galaxies that we observe today in clusters, filaments and voids. Such CDM models are now standard in theories of structure formation. While there are many plausible dark matter candidates, for the purposes of galaxy evolution the differences are not relevant, provided their only significant interactions are via gravity (i.e. the cross-section for other interactions is low).

Because dark matter is largely coupled to normal baryonic matter only via gravitation and has a much higher density, dark matter density perturbations in the early Universe grew relatively independently of matter and radiation prior to the era of recombination and were already well developed by this time. The radiation and baryonic matter interacted strongly with each other at this time and were also coupled to the gravitational field of the dark matter distribution. Once electrons and atomic nuclei had "recombined" (actually combined for the first time to form neutral atoms), the baryonic matter so formed was able to fall rapidly into the already formed dark matter gravitational potential wells, so eventually forming the cluster, group, filament and void structures that we see today.

The tiny (one part in 10^5) fluctuations that we see today in the CMB are the result of tiny fluctuations in the baryonic density $\sim 380\,000$ years after the Big Bang as radiation finally decoupled from it and it began to fall into dark matter potential wells. Measuring temperature fluctuations in the CMB therefore provides a powerful insight into the baryonic density of the Universe at the time of recombination and a large scientific effort has accordingly been made over the last 40 years to measure the CMB power spectrum with ever increasing accuracy. This provides the spectrum of baryonic acoustic oscillations at the time of recombination which can be compared with predictions from theoretical models of the growth of structure in the Universe.

1.4. Modelling the growth of dark matter halos

Press & Schechter (1974) developed a theoretical model that predicted the resulting mass function (i.e. mass distribution) of the collapsed objects produced by hierarchical clustering. This initially assumed spherical collapse but was later extended to model ellipsoidal collapse in which form it matches well mass functions from simulations (Jenkins et al. 2001).

White & Rees (1978) used an N-body simulation assuming 80% dark matter and $\Omega_{\rm m} \simeq 0.2$ where the cosmological parameter $\Omega_{\rm m} = \rho_{\rm m}/\rho_{\rm c}$ is the ratio of the total matter density of the Universe (baryonic plus dark) to the critical density (the density corresponding to a flat non-accelerating Universe). They showed that the result of gravitational collapse of gas into dark matter halo potential wells would be the formation of giant galaxies surrounded by satellite galaxies within halos, provided that the gas had time to cool and fragment to form individual stars. The required time for cooling would set an upper limit on galaxy luminosities. They were able to derive a luminosity function which agreed reasonably well with observations.

Analytical models (e.g. Press & Schechter 1974) are very powerful while density fluctuations are growing linearly, but to model the growth of dark matter structure over the majority of the history of the Universe N-body simulations are needed (e.g. Davis et al. 1985; Springel et al. 2005). Cosmological simulations assuming a flat CDM cosmology and values for the Hubble constant of ~ 50km s^{-1}Mpc^{-1} and no cosmological constant were soon found to give a good match to the observed clustering of galaxies (e.g. Davis et al. 1985), except that they predicted less clustering on large scales than observations indicated (e.g. Maddox et al. 1990).

It was realised that this failing could be remedied by reintroducing the cosmological constant Λ into standard CDM cosmology, and other evidence also pointed in this direction (e.g. Turner & White 1997). Furthermore Big Bang Nucleosynthesis also pointed to low matter densities (Copi et al. 1995). Reintroducing Λ became observationally necessary when in 1998 and 1999 two groups independently showed that the expansion of the Universe is accelerating (Riess et al. 1998; Perlmutter et al. 1999). Both groups used Type 1a supernovae as standard candles in order to reach this conclusion. ΛCDM cosmology (e.g. Spergel et al. 2003) has now been the "de facto" standard for a decade or more and its parameters are now well determined (e.g. Spergel et al. 2007). In order for the Universe to be flat the cosmological constant Λ must produce an effective density ρ_Λ such that the total mass density of the Universe is equal to the critical density, i.e. $\rho_\Lambda + \rho_{\rm m} = \rho_{\rm c}$ (or $\Omega_\Lambda + \Omega_{\rm m} = 1$ where $\Omega_\Lambda = \rho_\Lambda/\rho_{\rm c}$).

Initially the growth of over-dense regions in N-body simulations is slowed by the expansion of space and is approximately linear. However, when the dark matter overdensity in a region

becomes comparable to the mean density, the gravitational collapse "breaks away" from the overall expansion of the Universe and becomes much more rapid, resulting in the formation of a dark matter halo. Over cosmic time, dark matter halos continue to grow in mass and size by gravitationally induced mergers and by the accretion of smaller halos by larger ones, so forming substructure in the form of subhalos inside massive halos. As with luminosity functions, halos mass functions can be represented approximately by a Schechter function. From N-body simulations one can generate "merger trees", which trace the merger history of the dark matter halos observed in the Universe today, showing the masses of all progenitor halos at any time in the past. These can be a useful tool for understanding galaxy growth, particularly in the context of semi-analytical models (§1.5).

1.5. Modelling the hierarchical growth of galaxies

Stars form when clouds of molecular gas within over-dense regions become cool enough and dense enough to collapse gravitationally. This requires that the gas is able to lose sufficient energy and become cool enough and dense enough for star formation to occur.

White & Rees (1978) were the first to suggest that galaxies would grow by hierarchical mergers, i.e. bottom up with smaller galaxies forming first and then merging to form larger galaxies. A competing scenario is the monolithic collapse (top down) model whereby large galaxies form early on from the collapse of large over-dense regions of baryonic matter (Eggen et al. 1962). One of the main motivators for modelling galaxy formation and evolution has been to decide between these two opposing pictures, and a consensus has now emerged favouring hierarchical mergers.

Toomre & Toomre (1972) showed using elegant simulations of N gravitationally interacting particles, each representing a number of stars, that mergers between similarly sized spiral galaxies could result in the formation of elliptical galaxies with random stellar orbits. They also showed that encounters which were not quite so close would result in the wide variety of tidal tail and other features that can be seen in images of interacting galaxies today. The outcome of any particular interaction depended on the distance of closest approach between the two galactic centres, the orientation of the two discs, the directions and velocities of stellar rotation relative to the directions of travel of the galaxies, and the relative mass of the two galaxies. By adjusting their model parameters they were able to reproduce the observed stellar distributions in two pairs of interacting galaxies: The Antennae (NGC4038/9) and The Mice (NGC 4676). This work showed in detail for the first time how interactions between galaxies could change their morphology and how mergers between two spiral galaxies could result in an elliptical galaxy.

To model the formation and evolution of individual galaxies it is necessary to add into dark matter simulations the physical processes describing the collapse of baryonic matter into dark matter potential wells and the physics of star formation from cool gas. However, cosmological N-body simulations are immensely demanding of computer processing time and power, the widely quoted Millennium Simulation for example following $N = 2160^3$ particles, each representing a mass of $8.6 \times 10^8 h^{-1} M_\odot$ within a comoving box of side $500 h^{-1}$Mpc (Springel et al. 2005). It is therefore impractical to build the physics of star and galaxy formation into large dark matter simulations. Instead two types of additional model are used: semi-analytic models and cosmological hydrodynamic simulations. Such simulations reproduce the formation of disc galaxies from gas that is cool enough and dense enough. They also model how galaxies grow by the accretion of smaller galaxies by larger ones (minor mergers), and how elliptical galaxies result from the merging of two galaxies of comparable size (Toomre & Toomre 1972).

Semi-analytic models (SAMs, e.g. White & Frenk 1991; Kauffmann et al. 1999; Cole et al. 2000; Baugh et al. 2005; Croton et al. 2006; De Lucia et al. 2006; Bower et al. 2006; De Lucia & Blaizot 2007; Guo & White 2008) "paint on" the physics of star and galaxy formation to the merger trees resulting from N-body simulations, the Millennium Simulation being the most frequently used of these. Within each dark matter halo or subhalo present at each redshift SAMs model the evolution of the three baryonic components: hot gas, cold gas and stars. Simple models are used to quantify the conversion of hot gas into cool gas by cooling, the formation of stars from cold gas, and the effect of massive stars and AGN in heating both hot gas and cool gas, the heating of cool gas preventing it from condensing sufficiently to form stars. Chemical evolution models keep track of the chemical composition of each baryonic component. Models are included to account for dust extinction. In addition, the physical processes occurring when two halos merge are also modelled, e.g. the way that hot gas is shocked to a new virial temperature. Figure 3 summarises one particular semi-analytic model in the literature.

A semi-analytic model simulation is applied to each of the merger trees corresponding to the halos in a given halo catalogue as produced by an N-body simulation. In this way it generates a population of galaxies that corresponds to the present day halo mass function distribution. The parameters governing the physics of the SAM are then adjusted to fit observed present day observations of such things as luminosity functions and spatial correlation functions.

The predicted star formation history, initial mass function and and metallicity are then fed into stellar population synthesis (SPS) models such as the PEGASE (Fioc & Rocca-Volmerange 1997) and the Bruzual & Charlot (2003) models to predict the evolution of

Table 1. Selected references to semi-analytic models and cosmological hydrodynamic simulations.

type of model	ref	applies to	selected comments and results	z min	z max	min mass $10^{11}M_\odot$	max mass $10^{11}M_\odot$	zf 50%	za 50%
	White & Frenk (1991)	all galaxies	developed first semi-analytic model; successful in many respects but predicted too many faint galaxies						
SAM	Kauffmann et al. (1999)	all galaxies	examine LCDM and tauCDM and conclude can 't yet use SAMs to constrain cosmological parameters						
Durham SAM	Cole et al. (2000)	all galaxies	describes GALFORM model - B and K band LFs compared with obs - too many faint galaxies					<= 1.5	
MPA SAM	Croton et al. (2006)	all galaxies	includes radio AGN feedback; early and late type B band LFs compared with 2dFGRS, also K band; predicts too many faint red galaxies (based on B-V=0.8 cut)						
MPA SAM	De Lucia et al. (2006)	ellipticals	includes radio AGN feedback as in Croton et al. (2006)			1 0.04 0.025 0.125 0.625 3.12	 0.125 0.625 3.12 15.6	2.6 1.9 1.9 2.1 2.2 3.1	0.8 1.5 1.8 1.8 1.1 0.51
Durham SAM	Bower et al. (2006)	all galaxies	includes radio AGN feedback as in Croton et al. (2006); modelled $0 \leq z < 5$ evolution	0	5			1.6	
MPA SAM	De Lucia & Blaizot (2007)	BCGs						5	0.5
SAM	Guo & White (2008)	> MW size ∼MW size < MW size all halos	massive mergers dominate SM growth at all z SF dominates at $z > 1$, mergers at $z < 1$, minor mergers dominate over major for all z SF dominates at all z, minor mergers dominate over major at all z SF increases rapidly with z, major mergers depend strongly on SM but little on z halo growth depends strongly on z but little on mass						
SAM	Almeida et al. (2008)	LRGs	compares Bower et al. (2006) and Baugh et al. (2005) models; LFs of LRGs matched well at $z \sim 0.24$ but not $z \sim 0.5$			1	inf	2.2	1.5
hydro	Gabor & Davé (2012)		galaxies with mass $\sim 10^{10.5}M_\odot$ quenched first and move to red sequence at $z > 2$						
SAM (MPA and Durham)	Zehavi et al. (2012)	central galaxies in smaller DM halos central galaxies in larger DM halos number of stars in place at $z \sim 1$ twice that from clustering measurements	SF grows mostly by SF since $z \sim 1$ SF grows mostly by mergers since $z \sim 1$			0 $20h^{-1}$ (halo)	$20h^{-1}$ (halo) inf		1 >∼ 1
SAM, hydro	Hirschmann et al. (2012)		compares SAM and hydrodynamical models						

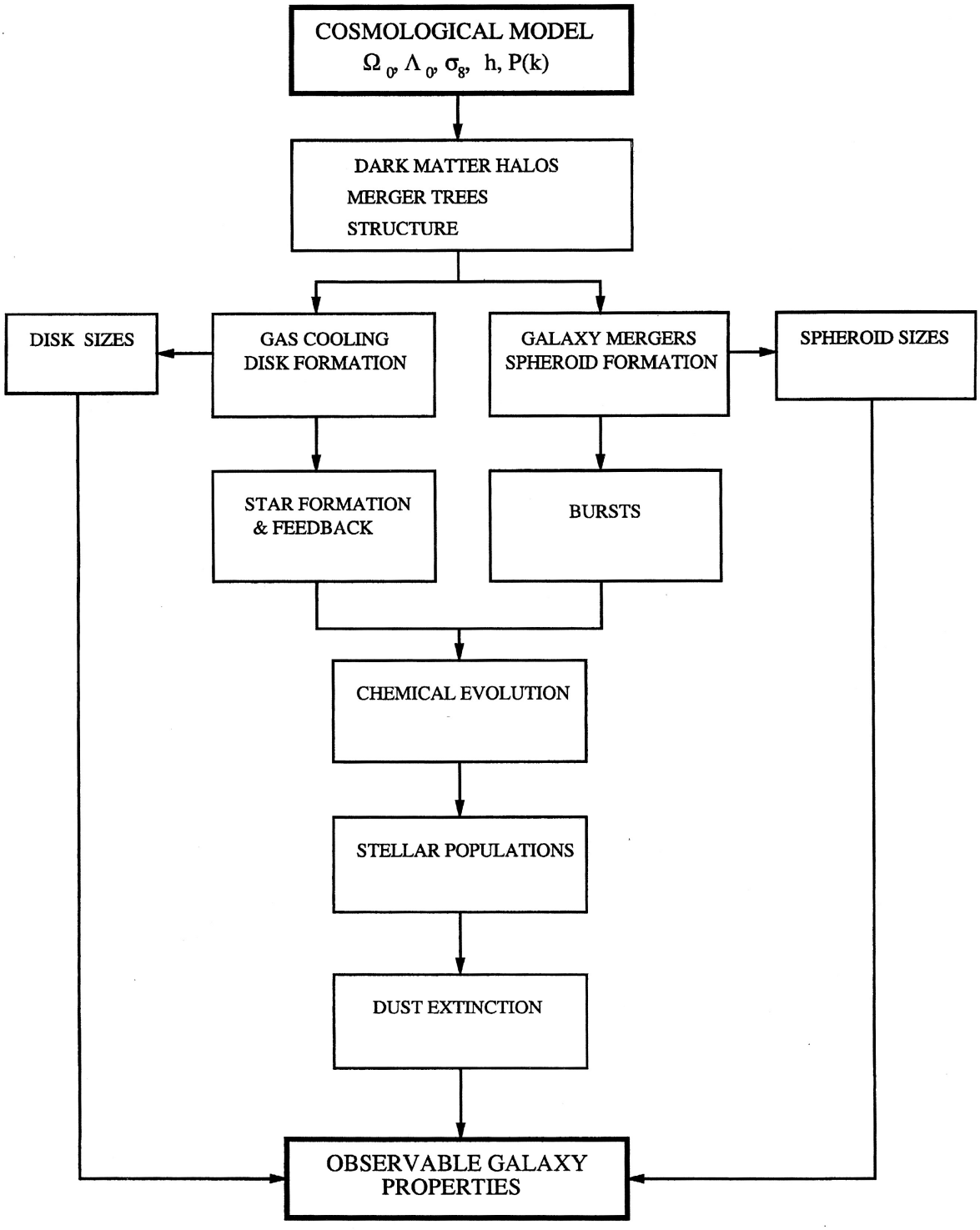

Fig. 3.—: **An example semi-analytic model.** This flow chart of the Durham model (from Cole et al. 2000) illustrates the various components included in semi-analytical models showing how they are linked together.

galaxy properties such as stellar mass, luminosity, colour and spectral energy density. First developed by Tinsley (1968), SPS models trace the evolution of an assembly of individual component stellar populations formed at specific times in the past, according to a given star formation history, for example a burst of star formation at redshift $z_{\rm form} = 4$ followed by exponential decay of star formation with time constant $\tau = 0.6$ Gyr.

By contrast with SAMs, cosmological hydrodynamical models (e.g. Gabor & Davé 2012) take a representative small volume simulated by an N-body method and include both the physics of galaxy and star formation alongside the physics of dark matter halo formation. SAMs and hydrodynamical simulations are explicitly compared in Hirschmann et al. (2012).

SAMs and hydrodynamical models have been used to predict the B and K-band luminosity functions, both at the present (e.g. Croton et al. 2006) and at various epochs in the past (e.g. Bower et al. 2006). Other predictions of these models include the colour-magnitude distribution of galaxies, their morphologies and stellar velocities, galaxy clustering, the increase in mean stellar age with galaxy mass, and for Sb and Sc spiral galaxies, the Tully-Fisher relation, the cold gas fraction/stellar mass relation and the cold gas metallicity/stellar mass relation.

To a large extent predictions of models based on the concordance ΛCDM cosmology agree well with observations. Nevertheless, there are differences between them dependent on the exact assumptions built into the model regarding the physics of star and galaxy formation. For example, Croton et al. (2006) investigated "radio mode" AGN feedback that heats gaseous halos, so preventing them from cooling and forming stars. They showed that this feedback mechanism corrects the overprediction of the luminosities of massive galaxies by about two magnitudes. It also correctly reproduces the sharp bright end cut-off in observed luminosity functions. Bower et al. (2006) use a different AGN feedback model to suppress cooling flows, but obtained similar results for the luminosity function and colour distribution of galaxies in the low redshift Universe, although there are differences in detail as would be expected. Measurements of luminosity function evolution also show that too few faint galaxies are currently predicted by theoretical simulations in comparison with observations (e.g. Cole et al. 2000), but the cause of this discrepancy could be in observational inaccuracies as much as model assumptions .

Table 1 lists key predictions of a number of significant SAMs and hydrodynamical model papers. A key conclusion of many recent studies is (e.g. De Lucia et al. 2006) that the stars in massive galaxies are formed early on but assembled later than in less massive galaxies. This accounts for the "downsizing" seen in observational studies whereby star formation ceases earlier in more massive galaxies (Cowie et al. 1996). It also explains why the stellar populations of massive galaxies are made up of old stars. De Lucia et al. (e.g. 2006) found

that 50% of the stars in massive elliptical galaxies $M > 10^{11} M_{\odot}$ were formed at $z_f \sim 2.6$ ($\sim$11 Gyr ago) but not assembled until $z_a \sim 0.8$ ($\sim$7 Gyr ago). The stars in smaller galaxies $M \sim 10^{10} M_{\odot}$ were 50% formed at $z_f \sim 2.0$ ($\sim$10.3 Gyr ago) and already 50% assembled by $z_a \sim 1.8$ ($\sim$10.0 Gyr ago).

1.6. Luminosity functions and the growth of galaxies

The stellar mass in a galaxy grows by the formation of new stars from cool dense gas and by the acquisition of new stars through mergers with other galaxies. Stellar mass cannot be measured directly but depends on the use of stellar population synthesis models to infer stellar mass from stellar luminosity and this is complicated by the assumption of differing star formation histories and different stellar initial mass functins. Measurements of stellar luminosity are complicated by the problem of dust obscuration.

A key tool for measuring the evolution of stellar luminosity is the *galaxy luminosity function* - the space density of galaxies with different luminosities at any particular epoch, i.e. any given redshift. Luminosity functions are generally parameterised using the Schechter function (Schechter 1976) which gives the comoving number space density ϕ at any given redshift as a function of luminosity:

$$\phi_L\left(L\right) dL = \left(\frac{\phi^*}{L^*}\right) \left(\frac{L}{L^*}\right)^{\alpha} \exp\left(\frac{-L}{L^*}\right) dL. \tag{1}$$

Here ϕ^* is a normalising factor, L^* is the characteristic luminosity corresponding roughly to the transition from a power law luminosity function to an exponential one, and α determines the slope of the power law variation at the faint end. The form of this function was originally motivated by a hierarchical model of dark matter halo clustering (Schechter 1976), but in practice it can be considered to be an empirical function describing observed galaxy luminosity distributions. An example Schechter function is shown in Figure 4.

Observationally it is more useful to write the Schechter function in terms of absolute magnitude $M = M_{\odot} - 2.5 \log_{10}(L/L_{\odot})$ rather than luminosity ($L_{\odot}$ and $M_{\odot}$ are the solar luminosity and absolute magnitude):

$$\phi_M\left(M\right) dM = -0.4 \ln 10 \phi^* 10^{-0.4(\alpha+1)(M-M^*)} \exp(-10^{-0.4(M-M^*)}) dM. \tag{2}$$

The space density at $L = L^*$ (or $M = M^*$) is $-0.4 \ln(10)\phi^*$ or $0.92\phi^*$, so ϕ^* effectively measures the space density of galaxies at the characteristic luminosity or magnitude.

The total stellar luminosity density j can be calculated by integrating the Schechter function over all luminosities L to give:

$$j = \phi^* L^* \Gamma(\alpha + 2). \tag{3}$$

where Γ is the gamma function

As shown in Figure 5a, red galaxies typically have $\alpha \sim -0.5$ and this results in a sharp drop in galaxy numbers at the faint end of the luminosity function. Blue galaxies typically have $\alpha \sim -1.3$ and this results in the opposite behaviour at the faint end, i.e. rapidly increasing numbers. As Figures 5b and 5c make clear, 80% of the total red galaxy stellar luminosity arises from galaxies less than $\sim$1.3 mag brighter or fainter than M^*, so that evolution of total red galaxy luminosity density effectively reflects the evolution of the typical luminosity L^* of red galaxies (but not necessarily the evolution of individual $\sim L^*$ red galaxy luminosities because the transfer of galaxies from the blue cloud to the red sequence must be taken into account). For blue galaxies a much larger proportion of the stellar light in the central 80% of luminosity is due to galaxies fainter than L^* (up to $\sim$3 mag fainter) and total luminosity is not such a clear indicator of L^* galaxy evolution.

Inferring stellar mass functions from luminosity functions depends on assumptions about stellar mass to light ratios (e.g. Bell & de Jong 2001; Bell et al. 2003; Mostek et al. 2012; Wilkins et al. 2013), and is therefore model dependent. Near infrared wavebands such as the K-band are particularly useful because stellar mass to light ratios vary much less than in the optical, by a factor of only $\sim$2 in the K-band, as compared with a factor of 7 in the B-band and 3 in the I-band (Bell & de Jong 2001). This is because the restframe K-band samples the black body Rayleigh-Jeans tail of stellar spectra which is dependent mainly on stellar surface temperatures and these in turn are tightly correlated with stellar mass.

Nevertheless, it is still possible to draw some conclusions about changes in red galaxy stellar mass densities from the evolution of optical (e.g. B-band) luminosity functions (e.g. Bell et al. 2004; Brown et al. 2007). Because red galaxies do not contain significant star formation, evolution in total luminosity density is due to two processes only: passive evolution of the old stellar population and growth by mergers (accretion). As passive evolution can be modelled by SPS models (e.g. Bruzual & Charlot 2003), the growth in stellar mass can be inferred.

Measurements of how highly luminous ($M > 10^{11} M_\odot$) galaxies evolve provide tests for the predictions of models of galaxy formation, and such galaxies can be observed at relatively high redshifts, but because the luminosity function drops so steeply at the bright end it is difficult to measure evolution of the space density of very bright galaxies. To get around this

problem one can instead measure the evolution in the absolute magnitude corresponding to a fixed space density. For massive red galaxies we can then infer the rate of change of mass and compare this with the predictions of theoretical models (e.g. Brown et al. 2007)

.

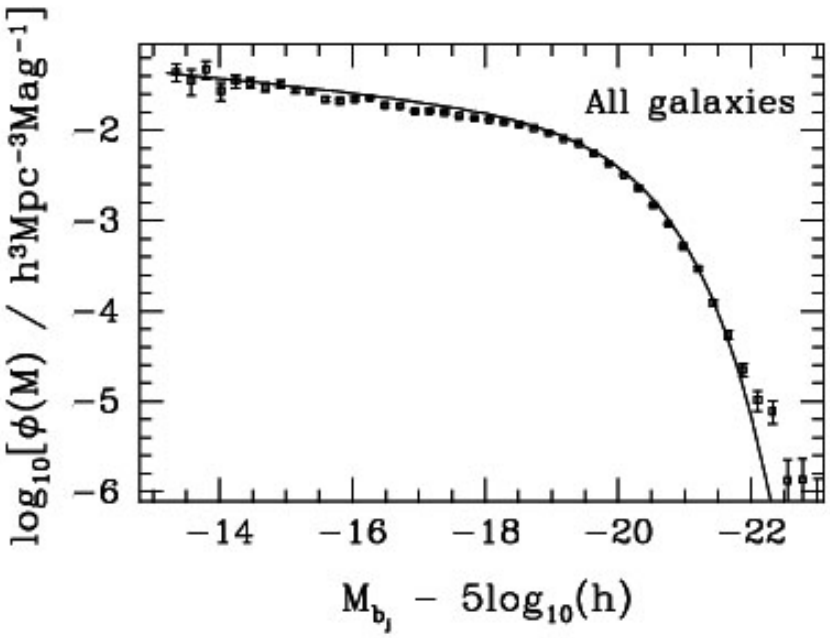

Fig. 4.—: **An example luminosity function from Madgwick et al. (2002).** The points show binned space densities for all galaxies from the 2dFGRS survey and the solid line shows a Schechter function fit to the data points.

1.7. Measuring galaxy luminosities

To determine the luminosity of a galaxy, or equivalently its absolute magnitude, two things need to be measured: how bright it appears in the sky (apparent magnitude) and how far away it is. Neither the measurement of galactic distances nor the determination of apparent magnitudes is straightforward, and nor is the determination of absolute magnitudes from apparent magnitudes. Great care is therefore needed if accurate and reliable results are to be obtained.

1.7.1. Measuring apparent magnitudes

There are three difficulties when measuring the apparent magnitude of a galaxy by placing a circular measurement aperture over the galaxy in a digital image and these are illustrated in Figure 6. Firstly, one needs to account for the light from the galaxy which falls outside the measurement aperture and for extended sources such as galaxies this can be significant. Secondly, inspection of digital images shows that many galaxies have one or more objects very close to them which will contribute extraneous light inside the measurement aperture. Thirdly, background noise in an image can be significant, particularly in relation to faint galaxies and particularly if large apertures are used. To obtain an accurate measurement of the total flux from a galaxy, an aperture diameter must be chosen that is not so large that undue background and extraneous light are included, but not so small that light from the galaxy itself is not properly sampled. Having done this, corrections should be made for the galaxy light falling outside the aperture and for extraneous light falling inside it.

Published studies differ in whether and to what extent they have addressed these three issues, and this affects comparisons of their results. Many studies, for example, have used the MAGAUTO facility built into the SExtractor (Bertin & Arnouts 1996) source detection code, and this has been shown to systematically underestimate the total flux for faint objects by up to $\sim$0.2 mag (Labbé et al. 2003; Graham et al. 2005; Brown et al. 2007).

1.7.2. Finding galaxy distances by measuring their redshifts

As photons travel through the expanding Universe their wavelengths λ are stretched along with space itself. Their frequencies ν and photon energies E are reduced correspondingly according to the equations $\nu = c/\lambda$ and $E = h\nu$. By imaging the spectrum of a galaxy one can therefore accurately determine its redshift by measuring the wavelength shift of its emission or absorption lines, provided a few of these can be identified as in Figure 7. Galaxy

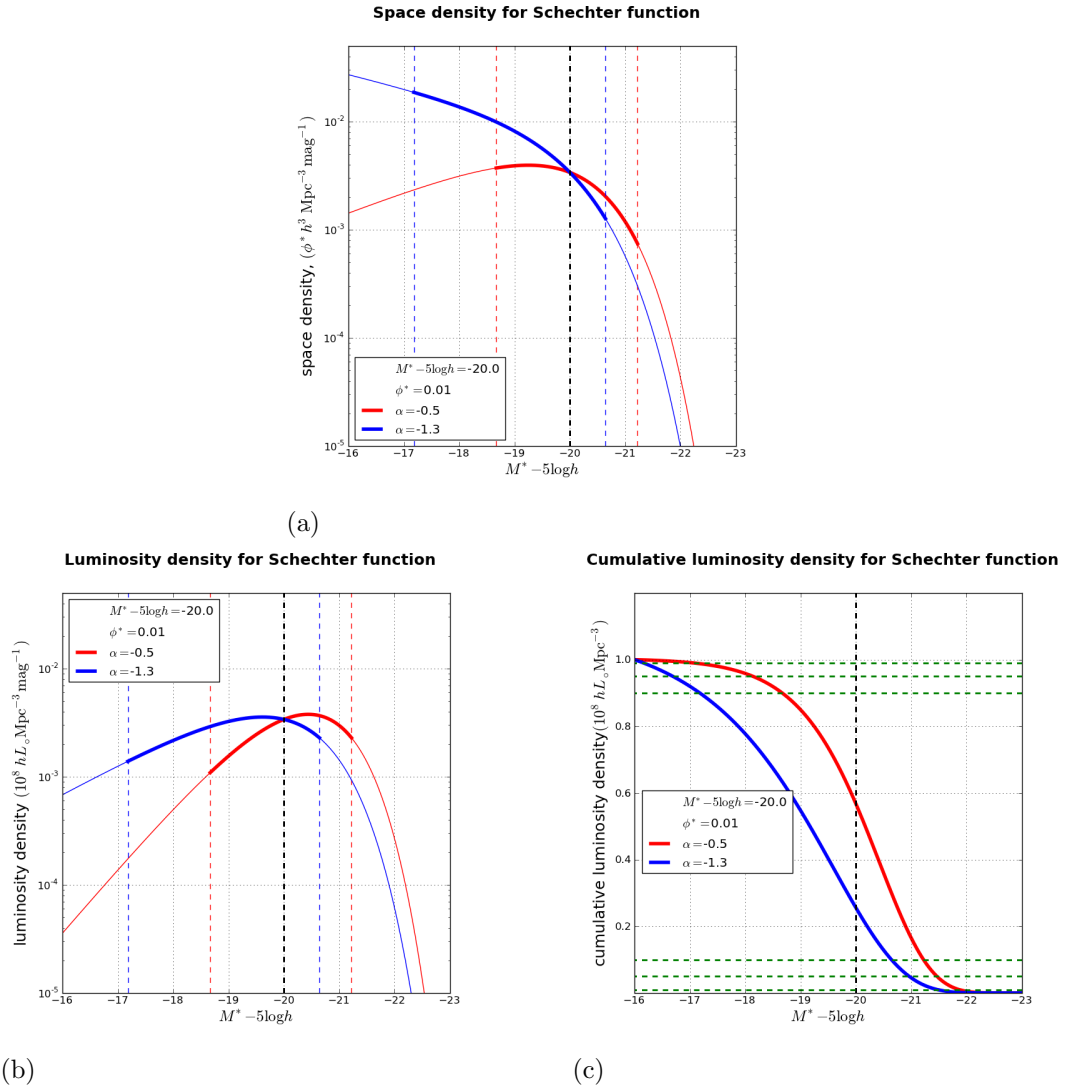

Fig. 5.—: **Typical Schechter functions for red and blue galaxies.** (a) Schechter functions for α values typical of red and blue galaxies: $\alpha_{\rm red} = -0.5$ and $\alpha_{\rm blue} = -1.3$; (b) the corresponding luminosity densities; (c) the cumulative luminosity density distribution with horizontal dashed lines indicating the 1%, 5%, 10%, 90%, 95%, and 99% percentiles. The thick lines indicate the central 80% of luminosity density. For red galaxies this lies between ∼1.3 mag fainter and ∼1.2 mag brighter with ∼57% being due to galaxies fainter than L^*, while for blue galaxies 80% lies between ∼2.8 mag fainter and ∼0.6 mag brighter with ∼75% being due to galaxies fainter than L^*. This shows that most of the stellar light from red galaxies is due to galaxies with luminosities close to L^*, but for blue galaxies most of it is due to fainter galaxies. It is worth noting, however, that in practice the faint-end slope for red galaxies steepens at fainter luminosities (e.g. Loveday et al. 2012). (The value $M^* - 2.5\log h = -20$ used to generate these figures is a ball park figure and ϕ^* is an arbitrary value that does not affect these results.)

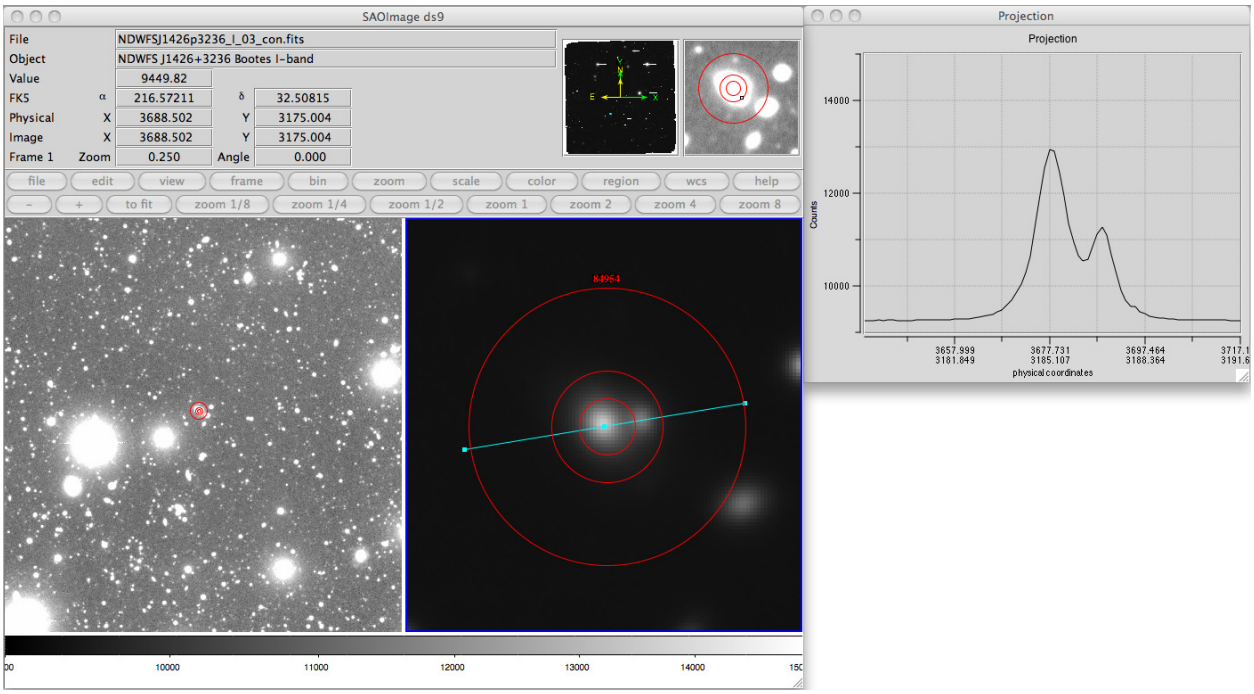

Fig. 6.—: **Problems encountered when measuring the apparent magnitude of a galaxy.** The three red circles in the central image represent measurement apertures of diameters 2, 4 and 10 arcsecond. On the right is a surface brightness profile cut along the pale blue dashed line showing how a nearby object contributes extraneous light that would be significant even with the 2 arcsecond diameter aperture. Only the 10 arcsecond diameter aperture includes most of the light from the galaxy. The left hand image shows the same galaxy but at much reduced magnification so that surrounding objects can be seen. The display settings are chosen to make the presence of background noise more apparent. This figure is a screenshot made using the SAOImage ds9 visualisation software (http://hea-www.harvard.edu/RD/ds9).

distances are determined from their redshifts by a relation deriving from General Relativity which depends on the cosmological parameters H_0, Ω_m and Ω_k. For low redshifts $z < 0.1$ the relationship is almost a linear one, $d = cz/H_0$, but at higher redshifts distance increases increasingly less rapidly with redshift and must be determined by integration.

Spectroscopic redshifts are accurate, but only a small proportion of galaxies has been spectrally imaged, except for those that are very close, and this proportion becomes smaller the higher the redshift, until beyond $z \sim 0.8$ it becomes very small indeed. An alternative is to use *photometric redshifts*. These have greater uncertainties, but can be derived for most galaxies which have been photometrically imaged in several wavebands. This is particularly valuable at higher redshifts where few spectroscopic redshifts are available. Photometric redshifts allows much larger sample sizes and correspondingly smaller uncertainties due to random error and to cosmic variance.

Photometric redshifts are determined by comparing a range of observed galaxy colours with those to be expected at different redshifts for a range of standard galaxies with specified spectral energy distributions (SEDs). One method of determining photometric redshifts uses template galaxies as the standards, matching the observed colours to redshifted template colours. Another method uses an artificial neural network code that is first "taught" the correspondence between a set of colours and redshift using a large "training set". These two methods are described in more detail in Chapter 3.

1.7.3. Determining absolute magnitudes

The total luminous flux at all wavelengths from a galaxy of luminosity L is:

$$F = \frac{L}{4\pi {d_L}^2}. \tag{4}$$

where d_L is the *luminosity distance* of the galaxy, which at low redshift is almost identical to the ordinary Euclidean distance so that (4) becomes just the inverse square law.

Distance modulus D_M compares the total apparent magnitude m of an object at its true distance to the (hypothetical) total magnitude that it would have at a standard distance of $d_{10} = 10$ parsec, this magnitude being known as the object's *total absolute magnitude* M, i.e.:

$$D_M = m - M = +5 \log_{10} \frac{d_L}{d_{10}}. \tag{5}$$

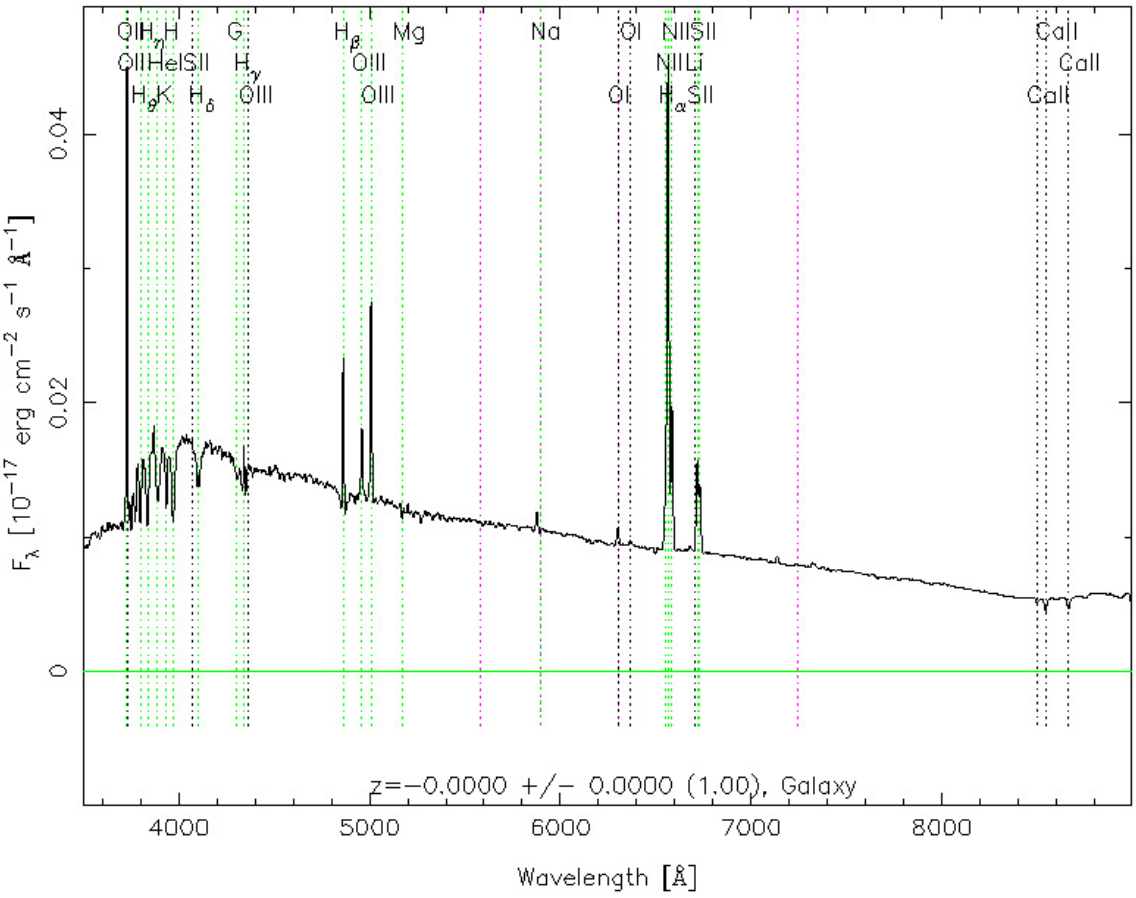

Fig. 7.—: **Spectrum of a star-forming galaxy showing clearly identifiable spectral lines.** This spectrum at $z = 0$ is one of the standard spectral templates used by the Sloan Digital Sky Survey to determine galaxy types. The restframe wavelengths of the absorption and emission lines in a galaxy spectrum are known from laboratory experiments. This enables the galaxy redshift to be determined from the wavelengths that the same lines are observed at.

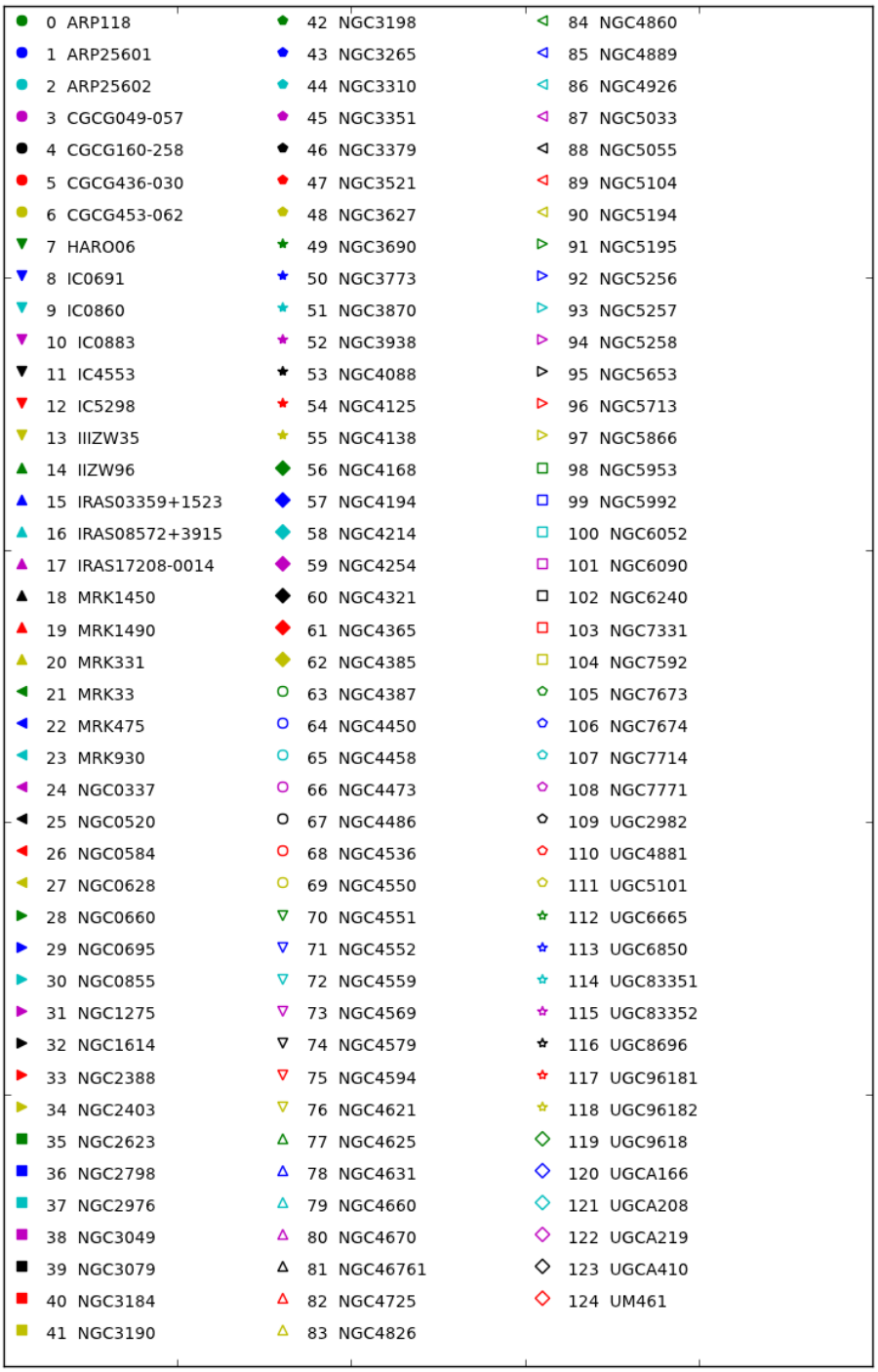

Fig. 8.—: **The 125 templates from Brown et al. (2013).** The symbols are the same as those used in Figures 11 to 17.

In practice one always measures apparent magnitude in a particular filter waveband X and one normally quotes absolute magnitude in a specific *restframe* waveband W which may or may not be the same as X. (A restframe waveband is that of an imaginary filter placed directly in front of the galaxy at its own distance, i.e. in its own restframe, and then redshifted to the telescope). Depending on the redshift, the redshifted restframe W waveband will overlap the X waveband to a larger or a smaller degree. In other words the light that would be transmitted through an imaginary X filter directly in front of the galaxy will be transmitted to a larger or smaller degree through the telescope filter W. To allow for this an extra term k_{WX} is added to (5) called a *K-correction*:

$$M_W = m_X - D_M + k_{WX}. \tag{6}$$

.

The K-correction term can be thought of as "correcting" for the fact that the X filter at the telescope samples a different part of the galaxy SED to a hypothetical W-band filter in the galaxy's restframe. K-corrections are therefore different for different SEDs and representative "template SEDs" are used to represent the (unkown) SEDs of real galaxies. Different methods of calculating K-corrections use different ways of approximating real galaxy SEDs with template SEDs but all depend on comparing relative apparent magnitudes in different wavebands (i.e. colours). Significant differences between methods of calculating K-corrections and the use of different template sets can result in significant differences between the results of different studies. Chapter 2 discusses K-corrections in further detail and describes our improved method for calculating them more simply and accurately than previously.

1.8. Motivation

Measurements of optical and infrared luminosity function evolution are of key importance in validating and constraining theoretical models of galaxy evolution (§1.5). Such models make theoretical predictions regarding luminosity function evolution which can be compared with observational measurements. It is found that models over-predict the number of faint galaxies and the number of very luminous galaxies unless mechanisms are incorporated to truncate star formation in low mass and high mass galaxies (e.g. Benson et al. 2003; De Lucia et al. 2006; Croton et al. 2006). Theoretical models also make predictions of stellar mass evolution which can be compared with the stellar mass evolution inferred from luminosity function evolution.

There is at present significant disagreement between various measurements of stellar mass

Table 2. Recent key measurements of the optical luminosity function and its evolution.

reference $z_{\rm min}$	evolution of LF measured?	restframe waveband measured	approx. redshift range	redshift type spectroscopic (s) or photometric (p)	approx. sample size	approx. sample area deg^2	approx. depth	sub-samples	principal surveys used
Norberg et al. (2002)	no	B	< 0.2	s	110 500	1000	$B = 19.45$	-	2dFGRS
Madgwick et al. (2002)	no	B	< 0.2	s	110 500	1000	$B = 19.45$	4 abs/em line 'types'	2dFGRS
Blanton et al. (2003b)	no	r	< 0.2	s	150 000	1000	$r = 17.8$	-	SDSS DR2 (NYU-VAGC)
Wolf et al. (2003)	yes	0.28μm, B, r	$0.2 - 1.2$	p	28 000	0.75	$R = 24$	4 abs/em line 'types'	COMBO-17
Bell et al. (2004)	yes	B	$0.2 - 1.1$	p	25 000	0.75	$R = 24$	red only	COMBO-17
Loveday (2004)	yes	r	$0.001 - 0.5$	s	93 000	2100	$r = 17.8$	-	SDSS DR1
Blanton et al. (2005a)	no	r	< 0.2	s	28 000	1100	$r = 17.8$	-	SDSS DR2
Ilbert et al. (2005)	yes	U, B, V, R, I	< 2.0	s	11 000		$I_{AB} = 24.0$	-	VVDS
Ilbert et al. (2006a)	yes	B	< 1.2	605 s + 3555 p	4 000	0.044	$I_{AB} = 24.0$	bulge/disc dominated	VVDS + COMBO-17 + HST/ACS
Willmer et al. (2006)	yes	B	$0.2 - 1.4$	p	11 300	1.13	$B = 19.45$	red, blue	DEEP2
Faber et al. (2007)	yes	B	$0.2 - 1.1$	p, s	39 000	1.9	$R = 24$, $R_{AB} = 24.0$	red, blue	COMBO-17 + DEEP2
Brown et al. (2007)	yes	B	$0.2 - 1.0$	p	60 000	7.0	$I = 23.5$	red only	NDWFS + SDWFS
Cool et al. (2012)	yes	B, r	$0.05 - 0.75$	s	12 500	7.6	$I_{AB} = 20.0$	red, blue	AGES
Loveday et al. (2012)	no	u, g, r, i, z	< 0.1	s	52 000	144	$r = 19.6$	red, blue	GAMA DR1
Loveday et al. (2012)	yes	u, g, r, i, z	$0.002 < 0.5$	s	121 000	144	$r = 19.6$	red, blue	GAMA DR1
this work	yes	B, K	$0.2 - 1.2$	p	335 000	7.0	$I = 23.5$	red, blue	NDWFS + SDWFS

evolution in the literature and this is a motivation for striving to obtain more reliable measurements. For example, Brown et al. (2007) found that 80% of the stellar mass in $\sim 4L^*$ massive red galaxies was already in place at $z \sim 0.7$, luminosity evolution since then being largely the result of passive evolution, with little contribution from mergers and little contribution from massive star-forming blue galaxies ceasing star formation and becoming red. Similarly, Ilbert et al. (2013) did not find any significant evolution of the high-mass end of the mass function of massive quiescent galaxies at $z < 1$. On the other hand van Dokkum (2005) found that most of today's most luminous elliptical field galaxies were assembled at low redshift through dry mergers.

Brown et al. (2013) measured a doubling of the stellar mass density of red galaxies since $z = 0.9$, and Arnouts et al. (2007) and Ilbert et al. (2010) obtained similar increases for quiescent galaxies since $z = 1.2$ and $z = 0.9$ respectively. Ilbert et al. (2013) obtained a smaller increase of less than 1.6 times for quiescent galaxies since $z = 1$. On the other hand, Bell et al. (2004) found little change in the luminosity density of galaxies on the red sequence and argued that this implies an increase in stellar mass density of at least 2 when the passive fading of ancient stellar populations is taken into account. Similarly, Faber et al. (2007) found that the luminosity density of red galaxies has remained nearly constant since $z = 1$, concluding that this implies a larger red galaxy stellar mass increase of $\sim$3 to 6 times when a plausible increase in stellar mass to light ratio of 1 - 2 mag is taken into account.

Given the diversity of measured rates of evolution in stellar mass density, it is of the greatest importance to our understanding of the physical processes by which galaxies are formed that we endeavour to obtain more accurate measurements of luminosity function evolution, and by inference stellar mass evolution. However, measurement of luminosity functions is a multi-stage process and significant technical difficulties present themselves at every stage. In essence the stages can be summarised:

(i) identification of suitable photometric surveys, ideally covering as large an area as possible to the greatest depth possible, with spectroscopic data available for at least some of the sample,

(ii) photometric measurement of total apparent magnitudes in a number of optical and/or infrared wavebands,

(iii) measurement of photometric redshifts (if spectroscopic redshifts are not available),

(iv) selection of the sample by exclusion from the data set of unwanted objects such as stars, image artefacts and extremely faint objects,

(v) calculation of absolute magnitudes using K-corrections,

(vi) determination of binned luminosity functions, possibly differentiating galaxy types by restframe colour or some other criterion,

(vii) the fitting of a parametric functional representation (e.g. a Schechter function) to the luminosity data using a method such as maximum likelihood or $1/V_{\rm max}$, and determination of the associated functional parameters, and,

(viii) measurement of luminosity function evolution based on evolution of these parameters.

A limitation of most previous studies is that they *either* involve large areas and sample sizes but are restricted to the local Universe, typically $z < 0.2$, (e.g. for optical luminosity functions Norberg et al. 2002; Madgwick et al. 2002; Blanton et al. 2003b), *or* they are sufficiently deep to be able to image more distant objects and hence measure luminosity evolution, but only cover a small area in the sky and contain smaller numbers of objects (e.g. Wolf et al. (2003); Bell et al. (2004); Willmer et al. (2006); Faber et al. (2007). Large area surveys are important for reducing the effects of cosmic variance. For example, Bell et al. (2004) concluded that even with three independent fields of $\sim$0.25 deg^2 each, cosmic variance is a considerable source of uncertainty (their Figure 4 and text). Large sample sizes are important in reducing the $\sim 1/\sqrt{(N)}$ Poisson errors in a count of size N, but even with these uncertainties are always dominated by cosmic variance, except for the very brightest galaxies.

Developments in telescope technology (including space telescopes) have meant that successive generations of surveys have been wider and/or deeper and have covered more wavebands, including the infrared ones which become important at higher redshifts where restframe optical wavebands are observed in the near infrared. This has meant that measurements of luminosity function evolution have been able to cover wider areas and/or greater redshift ranges as time has gone on and this progress can be seen in Table 2 which lists key measurements of optical luminosity function since 2002. Similar progress can be seen in measurements of K-band infrared luminosity function evolution (presented later in Table 21 in Chapter 4).

Larger deeper surveys have generally employed photometric redshifts (e.g. Wolf et al. (2003); Bell et al. (2004); Faber et al. (2007); Brown et al. (2007) as considerable telescope time is required to obtain spectra of faint distant objects, and few spectroscopic redshifts are therefore available at higher redshift. When spectroscopic redshifts are used in studies of evolution from $z > 1$ (e.g. Willmer et al. 2006) the spectroscopic redshift selection function (i.e. the proportion of objects with spectroscopic redshifts at any given magnitude) has to be known (introducing an additional source of uncertainty).

An important new survey for understanding galaxy evolution is GAMA (Driver et al. 2009, 2011) which will eventually provide ∼300 000 spectroscopic redshifts over a large area (290 deg^2) for objects down to $r = 19.8$. The first data release enabled Loveday et al. (2012) to measure luminosity function evolution in all five Sloan wavebands from $z = 0.5$ to the present using large sample sizes (∼121 000) covering a total area of 144 deg^2.

However, for optical luminosity function evolution from $z \sim 1$ or more to the present the only large-scale surveys are those based on COMBO-17 (Wolf et al. 2003; Bell et al. 2004) and DEEP2 (Willmer et al. 2006), and that of Brown et al. (2007) (which we discuss below). Faber et al. (2007) combines data from both of these COMBO-17 and DEEP2 (Table 2). COMBO-17 uses photometric redshifts derived from apparent magnitudes in 17 optical wavebands and DEEP2 uses spectroscopic redshifts. Faber et al. (2007) combined and compared data and results from both of these surveys. They noted that COMBO-17 had a high photometric redshift failure rate for the faintest blue galaxies at high redshift, necessitating such objects being dropped from their analysis. These redshift failures are to be expected given that blue restframe wavelengths get redshifted beyond optical wavelengths at $z > 1$ so that none of the restframe emission in optical wavebands is observed in any of the COMBO-17 filters. For this reason it is desirable for photometric redshifts to be based on both optical and infrared photometry, particularly at higher redshift.

The accuracy of K-corrections is an important issue and becomes of greater concern the higher the redshifts being studied. For example, Willmer et al. (2006) note that their use of the Kinney et al. (1996) template SEDs results in calculated $(U - B)$ colours for the reddest templates that are too red by ∼0.08 mag when compared with values from the *Third Reference Catalogue of Bright Galaxies* (de Vaucouleurs et al. 1991). They state that this is to be expected given that the Kinney templates are based on images of the centres of galaxies only and the anomaly is in the direction of the internal colour gradient of the galaxies. Furthermore, Willmer et al. (2006) state that they do not detect any significant evolution in the $(M_U - M_B)$ colour of the red sequence from $z = 1.3$ to $z = 0.3$ (their Figure 4) in contradiction to what we know must occur due to the passive evolution of red galaxies.

Willmer et al. (2006) only used 34 of the 43 Kinney templates because the others produced "outliers" (with unspecified offsets) when synthesised and observed $(B - R)$ colours were compared by plotting both against observed $(R - I)$ colour. This highlights the issue of appropriate choice of template SEDs for the determination of K-corrections and the fact that not all templates may be suitable. We discuss this more fully later in §2.3 but note here that apart from studies which use the Kinney templates (which have the problems just highlighted), only very small sets of templates have been generally been used to determine

K-corrections, chiefly the five templates of Coleman et al. (1980), the five EAZY templates (Brammer et al. 2008), and the five "basis" templates used by the *kcorrect* code (Blanton & Roweis 2007). Apart from issues of wavelength coverage and how representative these SEDs are of real whole galaxy SEDs, there is the concern that five or six templates can never hope to produce the full range of galaxy colours observed in real galaxy populations, so that less "typical" galaxies will inevitably be poorly matched resulting in inaccurate K-corrections or even outliers (as observed by Willmer et al. 2006).

Taylor et al. (2009) investigated the accuracy of their K-corrections in the redshift range $0 < z < 1.2$, finding random scatter of $\sim$0.05 mag and systematic offsets of a similar size when they compared plots of computed and observed plots of $(R-I)$ against $(V-I)$, noting that for the reddest galaxies the systematic error could rise to $\sim$0.1 mag. The accuracy of their K-corrections was comparable whether they used their usual EAZY templates, Kinney templates, or Coleman et al. (1980) templates supplemented by a Kinney starburst SED. They found, however, that use of templates based on Bruzual & Charlot (2003) models could result in systematics as large as $\sim$0.2 mag, while *kcorrect* resulted in random and systematic errors at the 0.1 mag level (peak to peak).

It is clear from this discussion that the accuracy of K-corrections is an issue of major concern and that there are problems with the methods that have been used in the prior literature. Additionally, there are problems with some of the photometric redshifts used in previous large-scale studies (e.g. Faber et al. 2007). The work described in this thesis improves on previous work in both these respects, while at the same time using a very large sample size covering a large area and to sufficient depth to allow evolution of luminosity functions from $z = 1.2$ to be measured. It is motivated by two recent key developments, the first of which was also exploited by Brown et al. (2007) in their study of red galaxy evolution since $z = 1$:

(i) the availability in the Boötes field of deep ($I < 23.5$) optical and infrared photometric surveys covering a large area ($\sim$8 deg^2) in several wavebands, and,

(ii) the newly available, extensive and accurate atlas of 129 template galaxy SEDs from Brown et al. (2013).

These two developments permit more accurate luminosity functions to be determined than previously for the following reasons:

(i) *Large depth and area minimise Poisson and cosmic variance errors.* The depth of the Boötes data enables luminosity functions to be measured out to $z = 1.2$ and its large area provides a sample size ($\sim$335 000 galaxies) that is $\sim$10 times larger than those previously used to measure luminosity function evolution in the range $0.2 \leq z < 1.2$ (Table 2). The

large sample size significantly reduces random Poisson errors and the large area minimises errors due to cosmic variance [in stages (vi), (vii) and (viii) referred to above].

(ii) *Extensive template SED coverage and wide multi-waveband photometry provide accurate photometric redshifts.* The extensive wavelength and SED coverage of the new templates, coupled with the availability of Boötes photometry in a wide range of optical and infrared wavebands ($u, B_w, R, I, y, J, H, K_s$ and 3.6, 4.5, 5.8, 8.0 and 24 μm), enables accurate and reliable photometric redshifts to be determined out to $z \sim 1.2$ by the template fitting method [in stage(iii)].

(iii) *Extensive template SED coverage permits an accurate new method for K-corrections.* The extensive wavelength and SED coverage of the new templates provides the basis for a new method of calculating K-corrections that uses empirical models fitted to a large and much more representative set of templates [stage (v)], rather than just a few templates, as in methods used by previous authors. Because the 125 new templates effectively span the complete range of real galaxy SEDs, accurate K-corrections can be calculated for galaxies which do not correspond closely to one of a small number of template types. Furthermore, a reliable estimate of the variance in computed K-corrections due to inherent galaxy variability can be obtained. It also turns out that the resulting new method is both simpler than existing methods and in certain cases more accurate. Because the template SEDs extend into the infrared accurate K-corrections can also be determined for infrared wavebands.

(iv) *Multi-waveband photometry allows accurate measurements of K-band luminosity evolution using the same sample as for the B-band.* Because our photometry spans wavebands from the optical to the infrared, and we have an accurate method of calculating K-corrections that works well in the infrared, we can accurately measure K-band luminosity evolution from $z = 1.2$ to the present using a sample which is over 10 times larger than the previous largest study (Arnouts et al. 2007). We are also able to use the same sample with the same photometric redshifts and red-blue restframe colour cut as for the optical B-band, enabling us to directly compare optical and infrared luminosity evolution and their implications for stellar mass evolution.

In combination, the preceding factors combine to permit the most accurate determinations of optical and near infrared luminosity function evolution to date, and, by extension, accurate inferences regarding the evolution of stellar mass, including the evolution of the stellar mass function. We expect our measurements to be particularly useful for validating theoretical models of galaxy evolution.

Our methods and software codes will also allow us to investigate the dependence of luminosity and mass evolution on environment which we see as an important extension to the present work which hope to carry out in the near future.

The accuracy and simplicity of our new method of calculating K-corrections will be of value to the wider astronomical community and we are therefore making publicly available our tables of parameters for calculating K-corrections as simple second order polynomial functions of a single observed colour at any given redshift $0 \leq z \leq 0.5$.

1.9. Structure of this thesis

Chapter 2 describes our improved method for calculating K-corrections based on a new set of ~ 125 empirical galaxy templates (Brown et al. 2013), and then applies this method to calculation of K-corrections for the Sloan Digital Sky Survey u, g, r, i, z filter set.

Chapter 3 first describes our data, the method we used to obtain accurate total observed B-band magnitudes, and the method of calculating template based photometric redshifts and how these compare with spectroscopic redshifts and redshifts calculated by an artificial neural network method. It then describes our sample selection including our method for separating red and blue galaxies based on an evolving cut in absolute colour-magnitude space. Next our binned $1/V_{\rm max}$ luminosity function results are presented for red, blue and all galaxies and compared with prior results in the literature. Then the maximum likelihood method for fitting Schechter functions is described and results are presented for evolution of the Schechter parameters ϕ^*, M^* and α, as well for evolution of the total luminosity density j_B, the magnitude of highly luminous $\sim 4L^*$ galaxies, and that of highly luminous red galaxies. Finally conclusions are drawn regarding the evolution of the mass in red galaxies since $z \sim 1.2$ and compared with the literature.

Chapter 4 describes how we calculated luminosity functions for the K-band using a similar method to that for the B-band in Chapter 3. Stellar mass to light ratios are then used to determine evolution of the stellar mass function of red, blue and all galaxies since $z \sim 1.2$. Our K-band luminosity function and stellar mass function results are compared with the prior literature.

Chapter 5 summarises our work and outlines directions for future research.

We use AB magnitudes in Chapter 2 for Sloan waveband K-corrections, and Vega based magnitudes in Chapters 3 and 4 for our determination of the B and K-band luminosity functions, and the stellar mass function. In Chapters 3 and 4 we adopt the following cosmology: $\Omega_{\rm m} = 0.25$, $\Omega_{\rm k} = 0$, $H_0 = 72$km s^{-1}Mpc^{-1}.

2. IMPROVED K-CORRECTIONS APPLIED TO THE SLOAN WAVEBANDS

2.1. Introduction

Measuring the absolute magnitudes of distant galaxies is essential for any observational study relevant to how galaxies form and evolve. Ideally one would like to know the total or *bolometric* absolute magnitude of a galaxy, i.e. the magnitude compared to a standard source of magnitude zero (either Vega or AB) also emitting in all wavelengths. In practice we have to measure the absolute magnitude in a particular waveband W, the absolute magnitude that would be measured if a W waveband filter could be placed directly in front of the galaxy, i.e. in its own *restframe*. It is important to remember that when we refer to a waveband W, we are really referring to a filter (real or theoretical) with a particular transmission function $T(\lambda)$ or $T(\nu)$.

To determine the absolute magnitude of a galaxy in a given restframe waveband W we need to measure its apparent magnitude in one or more observed wavebands, and we need to know its redshift z, and hence its distance modulus $D_{\rm M}$. In addition we need to know the K-correction $K_{\rm WX}$ which accounts for the difference between the part of the SED sampled by the restframe waveband W and that sampled by one of the observed wavebands X. For convenience we repeat here the relation between these quantities from §1.7.3:

$$M_W = m_X - D_{\rm M} + K_{WX}.$$

The K-correction K_{WX} for a galaxy at a given redshift can be computed from its SED (if known), together with the transmission functions $T_W(\lambda)$ and $T_X(\lambda)$. The derivation is given below in Section §2.2.

K-corrections for a galaxy whose SED is unknown are determined by comparing it with one or more *template* galaxies with similar properties. Template galaxy SEDs can either be drawn from a representative range of real galaxies (e.g. Coleman et al. 1980; Kinney et al. 1996; Brown et al. 2013) or based on a range of artificial galaxies derived from stellar population synthesis models (e.g. Bruzual & Charlot 2003; Fioc & Rocca-Volmerange 1997), or both, with models being used to extend real ultraviolet and optical template spectra such as those of Coleman et al. (1980); Kinney et al. (1996) into the infrared. Both types of templates can suffer from the deficiency that they do not fully span the entire range of galaxy spectral types.

A major benefit of using templates based on stellar population synthesis models is that additional physical quantities such as stellar mass and star formation rate can be derived from

the models. However, the star formation histories needed to match particular broadband spectra are not always unique and this can result in uncertainty in the values of derived quantities such as stellar mass.

In principle observationally based templates should have the advantage that they are based on real galaxy spectra. However, the ones that have been most widely used historically (Coleman et al. 1980; Kinney et al. 1996) are largely the spectra of galaxy nuclei rather than entire galaxies, and not necessarily truly representative of the spectra of entire galaxies. More recent observationally based templates (e.g. Chary & Elbaz 2001; Polletta et al. 2007; Rieke et al. 2009) have been able to make use of photometric measurements extending into the mid-infrared from space-based telescopes such as the Infrared Space Observatory, *Spitzer* Space Telescope, *Akari* (Astro-F) and Wide-field Infrared Space Explorer (WISE).

The simplest way of calculating the K-correction of red or blue galaxies is to assume that they are a simple function of redshift, these functions being determined from template SEDs. This approach can be used satisfactorily at low redshifts ($z \sim 0.2$ or less).

A commonly used method for determining K-corrections is to do a maximum likelihood fit of stellar population synthesis (SPS) models to observed photometry (e.g. Bell et al. 2004; Brown et al. 2007). Brown et al. (2007) used this method for red galaxies fitting Bruzual & Charlot (2003) SPS models to $B_W RI$ photometry. In their models they assumed a Salpeter (1955) initial stellar mass function, a formation redshift of $z = 4$ and an exponentially declining star formation rate. Such models provide a reasonable approximation to the observed SEDs of red galaxies. When blue galaxies are included as well as red, the situation is more difficult, because blue galaxies have complex star formation histories, dust obscuration and nebular emission lines. As a result they do not have tightly constrained colour-colour relationships in the same way that red sequence galaxies do.

Blanton et al. (2003a) introduced a method for calculating K-corrections based on matching broadband photometric observations of galaxies to template SEDs generated from Bruzual & Charlot (2003) models. Their key innovation was to use multiple components to reproduce galaxy SEDs and their method works reasonably well when plenty of high quality photometry is available. They claim that *kcorrect*, the associated software tool, is suitable for ultraviolet, optical and near infrared observations in the redshift range $0 < z < 1.5$. The K-corrections produced by *kcorrect* relate absolute magnitudes with apparent magnitudes in the same waveband, i.e. *kcorrect* calculates K_{WW} which from (6) is given by:

$$M_W = m_W - D_{\rm M} + K_{WW}. \tag{7}$$

In its most recent form, the resulting *kcorrect* v4_2 software (Blanton & Roweis 2007) uses

a basis set of five template SEDs, each consisting of a linear combination of 450 individual Bruzual & Charlot (2003) models with instantaneous bursts of star formation and varying metallicities, together with 35 models of emission from ionized gas (Kewley et al. 2001). The five templates were optimised to span the space of observed galaxy spectra and broadband optical and near infrared photometry using a method similar to principal component analysis (PCA, Connolly et al. 1995) called nonnegative matrix factorisation (NMF, Lee & Seung 1999; Blanton & Roweis 2007, Appendix). This method minimises χ^2 for the offsets between non-negative linear combinations of the models and the spectrocopic and photometric data. Spectra are obtained from SDSS (York et al. 2000) and photometry from SDSS, 2MASS (Skrutskie et al. 2006), GALEX (Martin et al. 2005), DEEP2 (Davis et al. 2003; Willmer et al. 2006) and GOODS (Giavalisco et al. 2004). Once a training set of galaxies had been used to determine the five templates, *kcorrect* performed χ^2 minimisation using NMF in order to determine an approximate model spectrum for any galaxy with measured broadband photometry, and hence compute K-corrections.

Blanton & Roweis (2007) point out that principal component analysis of galaxy spectra has shown that most of the variance in the distribution of galaxies in spectral space can be explained using a few templates. They find that five is an adequate number for reproducing the observed variance in their spectral and photometric data. They caution that their five templates do not have any hope of reproducing the many individual variations in equivalent widths of galaxy emission lines.

Given the wide variety of galaxy morphologies and sizes, star formation histories and merger histories, we expect that there will be many real galaxies whose spectra cannot be adequately reproduced using linear combinations of the five *kcorrect* NMF templates, for example compact blue galaxies. We also suspect (§2.7) that *kcorrect* may in some cases produce linear combinations of the template spectra which do not correspond to any observed galaxy spectra, causing it to fit unphysical model spectra to noise.

Rudnick et al. (2003, Appendix C) developed a different method of calculating K-corrections by interpolating between two templates. In order to determine the absolute magnitude of a galaxy at redshift z in waveband W, they first determine which two observed wavebands Y and Z straddle (or are close to) the redshifted W waveband. They then compare the observed $(m_Y - m_Z)$ colour of the galaxy with the computed $(m_Y - m_Z)$ colours that all their template galaxies would be observed to have if at the same redshift z. The two templates with the nearest colours are then picked and $K_{WZ} = M_W - m_Z - D_{\rm M}$ for the galaxy is determined by linear interpolation between the theoretically determined $M_W - m_Z - D_{\rm M}$ values for these two templates. In this way the absolute magnitude M_W can then be determined from the $(m_Y - m_Z)$ colour of the galaxy.

Taylor et al. (2009) implemented the method of Rudnick et al. (2003) in producing their publicly available *InterRest* IDL code to calculate K-corrections. *InterRest* makes use of the six EAZY templates developed for use with the EAZY photometric redshift code of Brammer et al. (2008). The EAZY templates comprise five basis templates derived from PEGASE (Fioc & Rocca-Volmerange 1997) stellar population synthesis models using nonnegative matrix factorisation, together with a dusty starburst model. The inputs to *InterRest* are observed colours and the output is the difference between the redshifted absolute magnitude and an observed apparent magnitude, and this is the K-correction $K_{WZ} = (M_W - D_{\rm M}) - m_Z$. The method has the benefit of being simple to use.

Chilingarian et al. (2010) showed that K-corrections computed using both *kcorrect* (Blanton & Roweis 2007) and the fitting of PEGASE models (Fioc & Rocca-Volmerange 1997) could be approximated using polynomials involving the redshift z and just one observed colour, e.g.:

$$K_{gg} = \sum_{j=0}^{5} \sum_{k=0}^{3} a_{jk} z^j (g-r)^k. \tag{8}$$

They provided tables giving the relevant polynomial coefficients and an on-line K-correction calculator. Instead of using galaxy colour in addition to redshift, Westra et al. (2010) showed that similar analytical approximations to K-corrections could also be based on redshift and the D_n4000 index that measures the depth of the 4000Å break and they applied this technique to the Smithsonian Hectospec Lensing Survey (Geller et al. 2005).

kcorrect and Chilingarian et al. (2010) both calculate K for the same restframe waveband and observed wavebands W, i.e. they provide values for K_{WW}. At greater redshifts when the redshifted restframe W band is far from the observed W band this will introduce errors due to the variability of galaxy SEDs in between the restframe and observed wavebands. Furthermore, in some cases, measurements in the observed W band may be subject to greater observational error than those in other wavebands. The advantage of the method of Rudnick et al. (2003) is that it enables observed wavebands Y and Z to be used which are close to the redshifted restframe W band. Also, it often allows observed wavebands with small observational errors to be chosen.

kcorrect and *InterRest* use only a few template galaxies (5 and 6 respectively), and although these are optimised to span as representative a range of real galaxy properties as possible, their small number means that some real galaxies will inevitably be poorly matched.

Our method is a modification of that of Rudnick et al. (2003). It uses a model that simultaneously fits the colours of (~ 125) observationally based templates to the observed colours

of galaxies. Our templates are the most extensive and accurate set of observationally based templates yet produced (Brown et al. 2013), and have accurate spectra extending from the ultraviolet to the mid-infrared. We discuss these in §2.3. The templates have been chosen to span the full range of observed galaxy properties and morphologies and we therefore expect that they will provide accurate K-corrections for a wider range of sample galaxies than a small number of templates. Willmer et al. (2006) used a similar method based on 34 of the Kinney et al. (1996) templates, but they did not determine the best observed colours to use and they did not check the validity of their models as we have done.

Importantly, our K-corrections are based on a model that simultaneously fits *all* the templates rather than using the one or two nearest fitting templates, as many other methods do (e.g. *InterRest,* Taylor et al. 2009; Brown et al. 2007; Rudnick et al. 2003). In this way we expect to avoid the unphysical preferential choice of certain K-correction values (i.e. aliasing).

As with Rudnick et al. (2003) and *InterRest* we calculate K-corrections K_{WX} compared to a different waveband X from the restframe waveband W where this will result in greater accuracy. We discuss this in detail in §2.4.

2.2. Theory of K-corrections

Following is the theoretical justification for our method of determining absolute magnitudes of galaxies from colour indices based on the measured apparent magnitudes in two carefully chosen wavebands. The derivation is similar to that in Hogg et al. (2002), which is based on the original papers of Humason et al. (1956) and Oke & Sandage (1968).

Let ($L(\lambda_{em})$ be the luminosity density per unit wavelength increment $\delta\lambda_{em}$ as emitted by an object at redshift z and luminosity distance d_L.

For a template galaxy, the luminosity density will be proportional to the spectral energy density (or SED) of $S(\lambda)$:

$$L(\lambda) = AS(\lambda). \tag{9}$$

where A is a normalising constant.

By the definition of luminosity distance d_L, the observed flux in wavelength interval $\delta\lambda_{obs} = (1+z)\delta\lambda_{em}$ from a galaxy at redshift z with luminosity density $L(\lambda)$ is:

$$F_{obs}(\lambda_{obs})\delta\lambda_{obs} = \frac{L(\lambda_{em})}{4\pi d_L^2}\delta\lambda_{em}. \tag{10}$$

where $\lambda_{obs} = (1+z)\lambda_{em}$.

Here, $F_{obs}(\lambda_{obs})$ is the observed flux density at luminosity distance d_L and wavelength $\lambda_{obs} = (1+z)\lambda_{em}$. The signal from a CCD is proportional to the number of photons counted, and this is proportional to the flux density $F_{obs}(\lambda_{obs})$ divided by the individual photon energies, which, for photons of wavelength λ_{obs} are hc/λ_{obs}.

Let $T^X(\lambda)$ be the probability that a photon of wavelength λ and energy hc/λ will get transmitted through a filter X and be counted by the CCD (taking account of its quantum efficiency and any other factors). From a total (energy) flux of $F_{obs}(\lambda_{obs})\delta\lambda_{obs}$ in a particular wavelength interval $\delta\lambda_{obs}$, the rate at which photons arrive is:

$$\delta n_{arriving} = \frac{F_{obs}(\lambda_{obs})\delta\lambda_{obs}}{(hc/\lambda_{obs})} = \frac{\lambda_{obs}F_{obs}(\lambda_{obs})\delta\lambda_{obs}}{hc}. \tag{11}$$

and the rate at which they get counted is therefore:

$$\delta n_{counted} = \frac{\lambda_{obs}F_{obs}(\lambda_{obs})T^X(\lambda_{obs})\delta\lambda_{obs}}{hc}. \tag{12}$$

As the pixel values in an image produced by a CCD are proportional to the numbers of photons counted at that point in the image, we can integrate $n_{counted}$ over all wavelengths and compare with a standard flux density $G(\lambda)$, (usually either Vega or AB), to obtain the observed (apparent) magnitude in waveband X:

$$m_X = -2.5\log_{10}\left\{\frac{\int \lambda_{obs}F_{obs}(\lambda_{obs})T^X(\lambda_{obs})d\lambda_{obs}}{\int \lambda G(\lambda)T^X(\lambda)d\lambda}\right\}. \tag{13}$$

which, in terms of emitted wavelengths only, becomes, using (10):

$$m_X = -2.5\log_{10}\left\{\frac{[1+z]}{4\pi d_L^2}\frac{\int \lambda_{em}L(\lambda_{em})T^X([1+z]\lambda_{em})d\lambda_{em}}{\int \lambda G(\lambda)T^X(\lambda)d\lambda}\right\}. \tag{14}$$

For a template galaxy at redshift z we can write (14) in terms of its SED $S(\lambda)$ by using Equation (9):

$$m_X = -2.5 \log_{10} \left\{ \frac{A[1+z]}{4\pi d_L^2} \frac{\int \lambda_{em} S(\lambda_{em}) T^X([1+z]\lambda_{em}) d\lambda_{em}}{\int \lambda G(\lambda) T^X(\lambda) d\lambda} \right\}. \quad (15)$$

To derive a formula for the absolute magnitude in waveband W, we replace d_L with $d_{10} = 10\,\mathrm{pc}$, substitute $z \simeq 0$, and replace X with W in (14), since the absolute magnitude in any waveband is the observed magnitude that a point source of equal luminosity would have at a distance of 10 pc:

$$M_W = -2.5 \log_{10} \left\{ \frac{1}{4\pi d_{10}^2} \frac{\int \lambda_{em} L(\lambda_{em}) T^W(\lambda_{em}) d\lambda_{em}}{\int \lambda H(\lambda) T^W(\lambda) d\lambda} \right\}. \quad (16)$$

Here, the flux density and transmission function are evaluated at emission wavelengths since $z \simeq 0$ at a distance of $d_{10} = 10pc$. We have also allowed for the possibility of a different reference flux density $H(\lambda)$ for the magnitudes in waveband W.

For a template galaxy (16) can be written in terms of its SED as follows:

$$M_W = -2.5 \log_{10} \left\{ \frac{A}{4\pi d_{10}^2} \frac{\int \lambda_{em} S(\lambda_{em}) T^W(\lambda_{em}) d\lambda_{em}}{\int \lambda H(\lambda) T^W(\lambda) d\lambda} \right\}. \quad (17)$$

Subtracting (16) from (14), we obtain a formula that relates the apparent magnitude of a galaxy in the X waveband to its absolute magnitude in the W waveband:

$$m_X = M_W + D_M - 2.5 \log_{10} \left\{ \frac{[1+z] \int \lambda_{em} L(\lambda_{em}) T^X([1+z]\lambda_{em}) d\lambda_{em}}{\int \lambda G(\lambda) T^X(\lambda) d\lambda} \frac{\int \lambda H(\lambda) T^W(\lambda) d\lambda}{\int \lambda_{em} L(\lambda_{em}) T^W(\lambda_{em}) d\lambda_{em}} \right\}. \quad (18)$$

where $D_M = 5 \log[d_L/d_{10}]$ is the distance modulus. The quantity $(M_W + D_M)$ is called the *restframe magnitude* by some authors (e.g. Taylor et al. 2009). It is effectively the absolute magnitude dimmed to account for distance, or, alternatively, the apparent magnitude that one would observe if the filter W were moved from the telescope and somehow placed directly in front of the galaxy.

Equation (18) is normally written more succinctly as:

$$m_X = M_W + D_M + k_{WX}. \quad (19)$$

.

where k_{WX} is the *k-correction*, so called because it "corrects" the restframe magnitude $(M_W + D_M)$ in one waveband W to give the observed or apparent m_X magnitude in another waveband, X.

(18) will be seen to be equivalent to Equation (13) of Hogg et al. (2002), if it is rewritten in the form (19) with:

$$k_{WX} = -2.5 \log_{10} \left\{ \frac{1}{[1+z]} \frac{\int \lambda_{obs} L(\frac{\lambda_{obs}}{[1+z]}) T^X(\lambda_{obs}) d\lambda_{obs}}{\int \lambda G(\lambda) T^X(\lambda) d\lambda} \frac{\int \lambda H(\lambda) T^W(\lambda) d\lambda}{\int \lambda_{em} L(\lambda_{em}) T^W(\lambda_{em}) d\lambda_{em}} \right\}. \quad (20)$$

Here, T^W, T^X, G, H correspond to Q, R, g^Q_λ, g^R_λ respectively in Hogg et al. (2002), and the suffices "*obs*" and "*em*" to Hogg's "*o*" and "*e*".

2.3. The templates

We used the ∼125 SED templates from Brown et al. (2013) which are based on 125 nearby ($z < 0.05$) galaxies (Figure 8. This is an atlas of spectral energy distributions (SEDs) with wavelength coverage spanning from ∼0.15 μm in the far ultraviolet to the ∼24 μm in the mid-infrared. The SEDs combined ground-based optical spectrophotometry with infrared spectroscopy from Spitzer and Akari (Murakami et al. 2007), with gaps in spectral coverage being filled using MAGPHYS models (da Cunha et al. 2008). The spectroscopy and models were normalised, constrained and verified using matched aperture photometry measured using imagery from Swift (Roming et al. 2005), GALEX (Morrissey et al. 2007), SDSS, 2MASS, Spitzer and WISE (Wright et al. 2010). Typically 70% or more of the galaxy light was collected in each waveband. The availability of 26 photometric bands allowed Brown et al. to identify and mitigate systematic errors present in the data.

(Note: the most up to date version of the atlas comprises 129 templates but we have continued to use the 125 templates in the "beta" version of the atlas - this does not affect any of our results more than marginally.)

We reproduce here from Figure 1 of Brown et al. (2013) an example SED (for NGC 6240) together with UV, optical, near infrared and mid-infrared images of the NGC 6240 (Figure 9).

Their atlas spans a broad range of absolute magnitudes ($-14.4 < M_g < -22.3$), colours ($0.1 < u - g < 1.9$) and types, including ellipticals, spirals, merging galaxies, blue compact dwarfs and luminous infrared galaxies (LIRGs). Within each type there is considerable

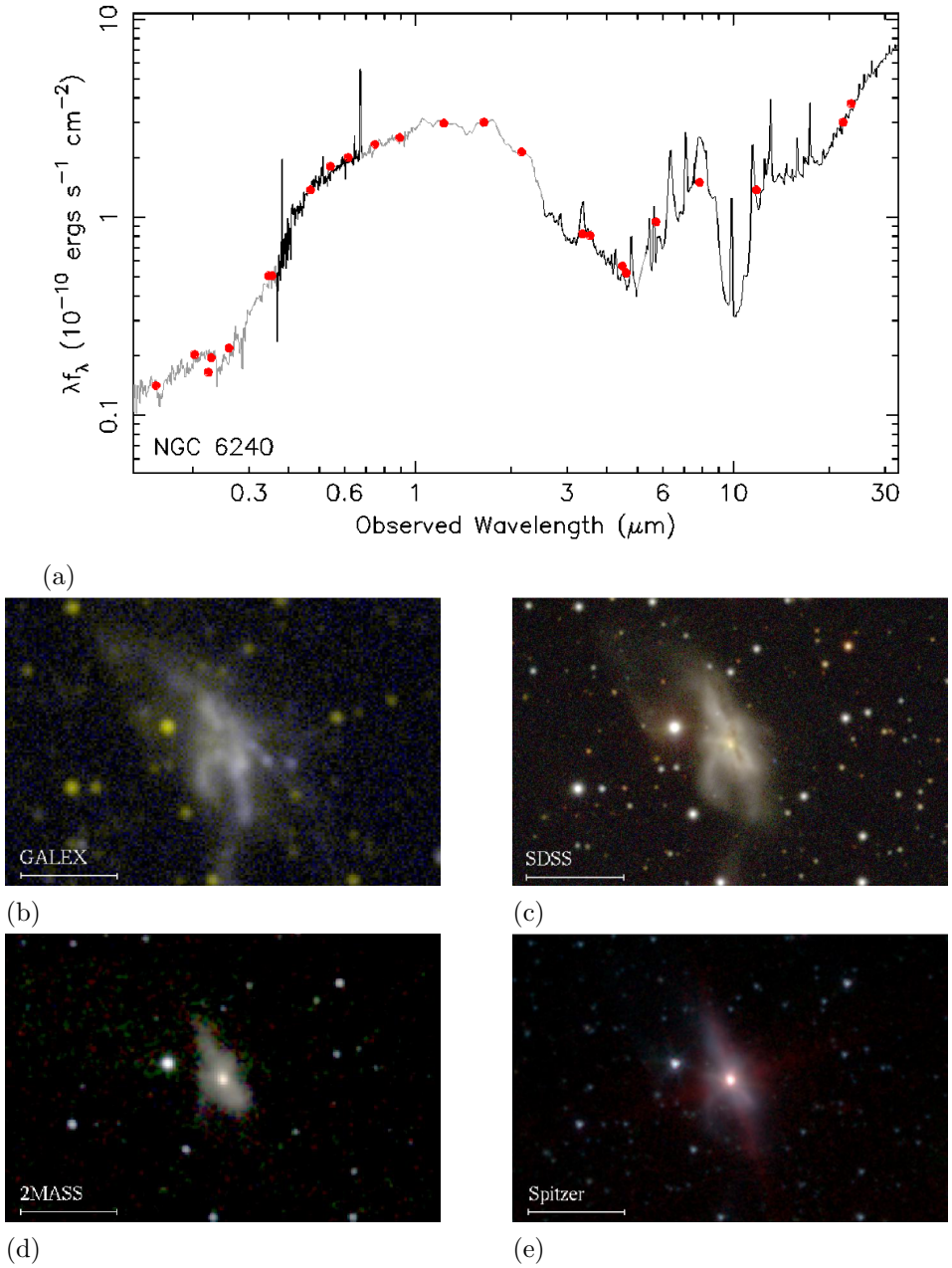

Fig. 9.—: **An example template galaxy SED and UV to mid-infrared images.** *Top:* the UV to mid-infrared SED of NGC 6240 from the Brown et al. (2013) atlas of galaxy SEDs. *Lower panels:* Some of the GALEX, SDSS, 2MASS and Spitzer images that were used to constrain and verify the SED. The horizontal bar indicates an angular scale of 1 arcmin. In the top panel, the observed and model spectra are shown in black and grey respectively, while the photometry used to constrain and verify the spectra is shown with red dots.

diversity. For example, the atlas includes the observed diversity of elliptical ultraviolet SEDs, as well as ellipticals with significant star formation and dust emission in the mid-infrared. Brown et al. (2013) point out that multi-wavelength photometry reveals the true diversity of galaxy properties and shows that this diversity cannot be adequately modelled with a small number of galaxy templates. Nevertheless, some galaxy types (such as ultra-compact dwarfs, low surface brightness galaxies, and quasars) are not included while some others (such as LIRGs) are over-represented.

For each template the residuals were calculated between the actual observed magnitudes in each of the 26 wavebands and the observed magnitudes predicted by convolving the SED with the filter transmission curve. The median and standard deviation σ of these offsets (across the 125 templates) between observed and predicted magnitudes are less than 0.1 mag (i.e. a flux difference of $\sim$10%) for almost of all of the wavebands, the most significant error ($\sigma = 1.3$ mag) being in the 5.8 μm waveband (for reasons which are not entirely clear).

Comparison of their SEDs with other template libraries and the observed colours of galaxies indicated that the systematic errors in their templates are smaller than those in other atlases. In addition their atlas spans a broader range of galaxy types.

2.4. Calculation of K-corrections for the Sloan filter set

The SEDs of representative template galaxies are shown in Figure 10 in relation to the Sloan filter set. We measure K-corrections for our sample galaxies by first measuring their colours $(m_Y - m_Z)$ using two carefully selected wavebands Y and Z. We then use models based on plots of $K_{WZ} = (M_W + D_M) - m_Z$ against $(m_Y - m_Z)$ for $\sim$ 125 template SEDs at the same redshifts to determine values for $(M_W + D_M) - m_Z$ and hence M_W for the sample galaxies.

As we show below, the wavebands Y and Z can be chosen so that plots of $y = (M_W + D_M) - m_Z$ against $x = m_Y - m_Z$ for the templates at any redshift lie close to a smooth curve to which a simple quadratic function can be fitted, i.e.:

$$y = ax^2 + bx + c. \tag{21}$$

To maximise the accuracy of our K-correction determinations we choose the comparison wavebands Y and Z so that there is a large spread of $m_Y - m_Z$ values on the x-axis and a relatively small spread of $(M_W + D_M) - m_Z$ values on the y-axis. We also look for comparison wavebands which have as little scatter as possible in the y-direction and very few obvious

outliers or none at all. Section §2.5 below shows that this does not always result in the use of observed colours which straddle or are as close as possible to the redshifted restframe waveband W, and in this respect our method differs from that of Rudnick et al. (2003) and the *InterRest* software (Taylor et al. 2009). Table 3 lists the input colours that we have found the best to use and Figures 11 to 17 show the resulting plots.

We calculate the model parameters a, b and c in Equation 21 for a one-dimensional grid of 51 redshifts between $z = 0.0$ and $z = 0.5$ minimising the sum of the squared y-offsets, performing three iterations in order to eliminate from the fit any templates with a y-offset of more than 0.2 mag. Tables 4 to 8 list our results for the five Sloan filters u, g, r, i and z and indicate which are the best input colours to use at different redshifts. Also tabulated are the RMS y-offsets between the models and the template points (excluding any templates with offsets greater than 0.2 mag). The RMS offsets are also shown on Figures 11 to 17.

To accurately determine the absolute magnitude of any galaxy in one of the Sloan wavebands, we use Table 3 to select the appropriate input colour for the given redshift. We then interpolate (in colour) to find the parameters a, b and c. When the redshift does not coincide precisely with one of those tabulated we interpolate between the sets of parameter values for the two nearest redshifts on either side of the desired redshift. Using (21) we see that the required absolute magnitude is:

$$M_W = a(m_Y - m_Z)^2 + b(m_Y - m_Z) + c - D_M + m_Z. \tag{22}$$

Our method provides a quick and simple way of accurately determining the absolute magnitudes of galaxies using just one observed colour and it requires no lengthy calculations or specially written software such as *kcorrect* or *InterRest*. Because the templates span almost the whole spectral range of real galaxies one can be confident in the model used and in the possible offsets from the model due to the scatter in the templates and due to possible error in the observed input colour.

For M_g we prefer $(g-r)$ as input colour from $z = 0$ to $z = 0.34$ and $(r-i)$ from $z = 0.34$ to $z = 0.5$. This strategy avoids (a) the relatively large scatter about the model fit with input colour $(g-r)$ beyond $z \sim 0.3$ (Figure 12), and (b) the small range of $(r-i)$ input colour and corresponding highly curved model fit at $z \sim 0.1$ (Figure 13). Using redshift and apparent magnitude data from the New York Value-Added Galaxy Catalogue (VAGC, Blanton et al. 2005b), we show in Figure 19 that this does not result in a discontinuity in M_g values at $z = 0.34$.

Similarly in Figure 20 the discontinuity in calculated absolute r-band magnitudes is no more than 0.01 mag at redshift $z = 0.12$ where we recommend switching from $(g - r)$ to $(r - z)$

input colour. We prefer $(g-r)$ at low redshifts because observational errors in r are typically much less than those in z, but at higher redshifts we prefer $(r-z)$ because there are no outliers and because the RMS template scatter about the fitted model is significantly smaller than for $(g-r)$ ($\sim$0.03 as opposed to $\sim$0.08).

Figures 20, 14 and 15 indicate that we could in fact use $(r-z)$ input colour at all redshifts if we wished and this makes the point that one can generally find an alternative input colour to that recommended if measurements are not available in a particular waveband (e.g. g in this case).

Similarly in Figure 21 we show that $(g-i)$ could be used as input colour for determining absolute i-band magnitudes instead of our preferred colour $(r-z)$ if no z-band magnitudes were available. For redshifts less than $\sim$0.25 the systematic offset between the two sets of measurements is mostly less than $\sim$0.01 mag, and for $0.25 < z < 0.5$ it is less than $\sim$0.03 mag. It is worth noting that the more obvious choice of $(i-z)$ as input colour would be less satisfactory because as Figure 21b shows the model fit to the templates is highly curved and has a very small input colour range at $z \sim 0.3$.

Willmer et al. (2006, Appendix A) also used second order polynomials to determine restframe $(M_U - M_B)$ colour and K_{BR} (our notation, theirs is K_{RB}) as a function of observed $(B-R)$ and $(R-I)$ colours in the range $0 \leq z < 1.4$. They used the polynomials for K_{BR} to determine absolute B-band magnitudes from their BRI photometry. Although the method of Willmer et al. (2006) is similar to ours there are important differences which we now explain.

To avoid galaxies with extreme observed colours being assigned unreasonable restframe colours and K-corrections, Willmer et al. (2006) restricted the range of input colours ($(B-R)$ or $(R-I)$) to the range covered by the Kinney templates. We have avoided the problem by the alternative strategy of discarding galaxies whose input colours lie outside a range 20% greater than that for our templates. Unlike the Kinney et al. (1996) templates, our templates span the full range occupied by real galaxies in colour-colour space (Figure 22. We illustrate this in Figure 23 for the sample of galaxies in the Boötes field that we use in Chapter 3 to measure evolution of the B-band luminosity function. This is because they are based on whole galaxy spectra, rather than just the central regions of galaxies, because there are many more of them, and because they are derived from more accurate modern photometry than was available to Kinney et al. (1996). We can therefore be confident in rejecting galaxies whose observed colours lie well outside the range for our templates on the grounds that their photometry is likely to be in error.

Where the restframe $(M_U - M_B)$ colour lay between the observed $(B-R)$ and $(R-I)$ colours, Willmer et al. (2006) interpolated between the $(B-R)$ and $(R-I)$ derived quantities.

Otherwise they used the closest pair of filters. We note that this procedure works relatively well over much of the redshift range, but not all of it, for the following reasons. Willmer et al. (2006) do not show their fitted polynomials on their plots and they do not give the root mean square error between restframe template colours and restframe model colours in their paper. This is an important omission because as we show later in §2.5, it is possible for the second order polynomial fits to be very sharply convex for certain choice of input colours at certain redshifts, particularly if the input range is small and there is large scatter near the end of the range of input colours. For example, we found this to be the case using $(R-I)$ to determine K_{BR} at $z = 0.2$ (Figure 55) and it is clear from Figure 13(b) of Willmer et al. (2006) that the situation will be even worse using the Kinney templates which exhibit much more scatter than ours. It is not therefore sufficient to choose the nearest input colours without carefully examining the shape of the second order polynomial, the range of input colours relative to output colours, and the root mean square error in output colour. It is possible that these problems may have been partially concealed in Willmer et al. (2006) by (a) the restriction on input colours which prevented unreasonable absolute magnitudes being produced, and (b) the fact that different plots in Willmer et al. (2006) cover different redshift ranges: e.g. $0.1 \leq z < 0.9$ for K_{BR} plotted agains $(R-I)$ but $0.3 \leq z < 1.4$ for $(M_U - M_B)$ plotted agains $(R-I)$.

Table 3. The observed colours used to determine K-corrections.

restframe waveband M_W	central wavelength μm	redshift range	colour $(m_Y - m_Z)$
u	0.3551	0.0 to 0.5	$(u-g)$
g	0.4686	0.0 to 0.34	$(g-r)$
g	0.4686	0.34 to 0.5	$(r-i)$
r	0.6166	0.0 to 0.12	$(g-r)$
r	0.6166	0.12 to 0.5	$(r-z)$
i	0.7480	0.0 to 0.5	$(r-z)$
z	0.8932	0.0 to 0.5	$(r-z)$

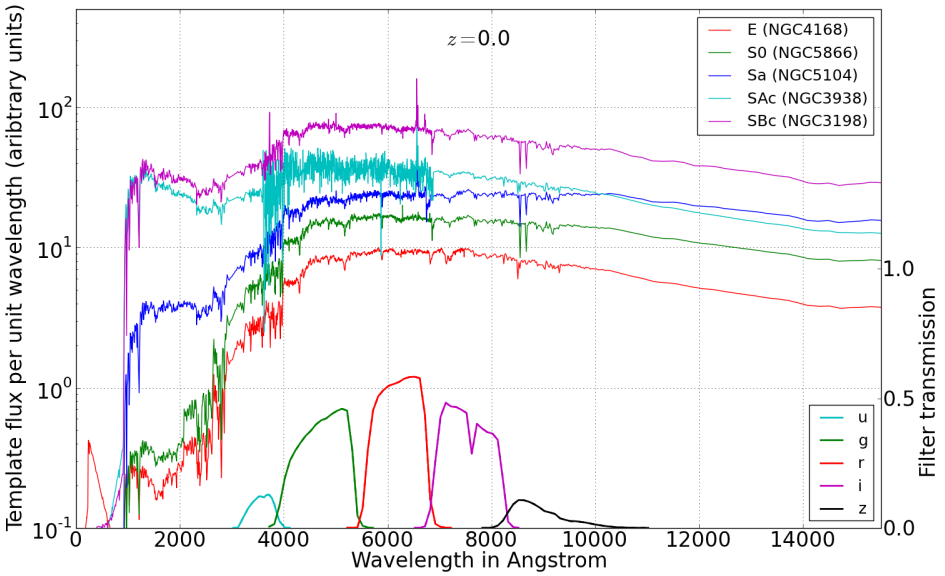

(a)

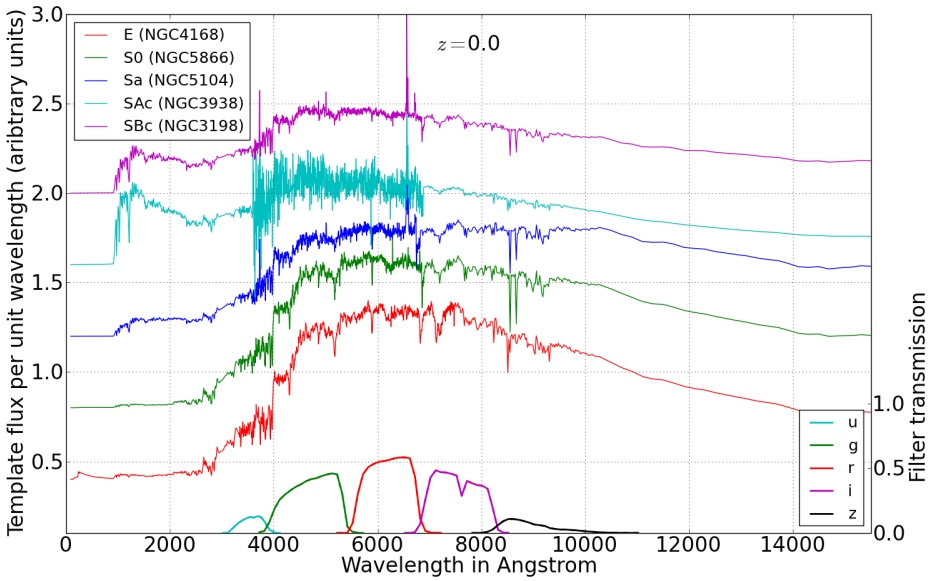

(b)

Fig. 10.—: **The SEDs of representative template galaxies in relation to the Sloan filter set.** *Top:* using a logarithmic scale to show the full range of flux variation; *bottom:* using a linear scale to show spectral features in the optical and near infrared more clearly. (The SEDs are offset artificially for clarity.)

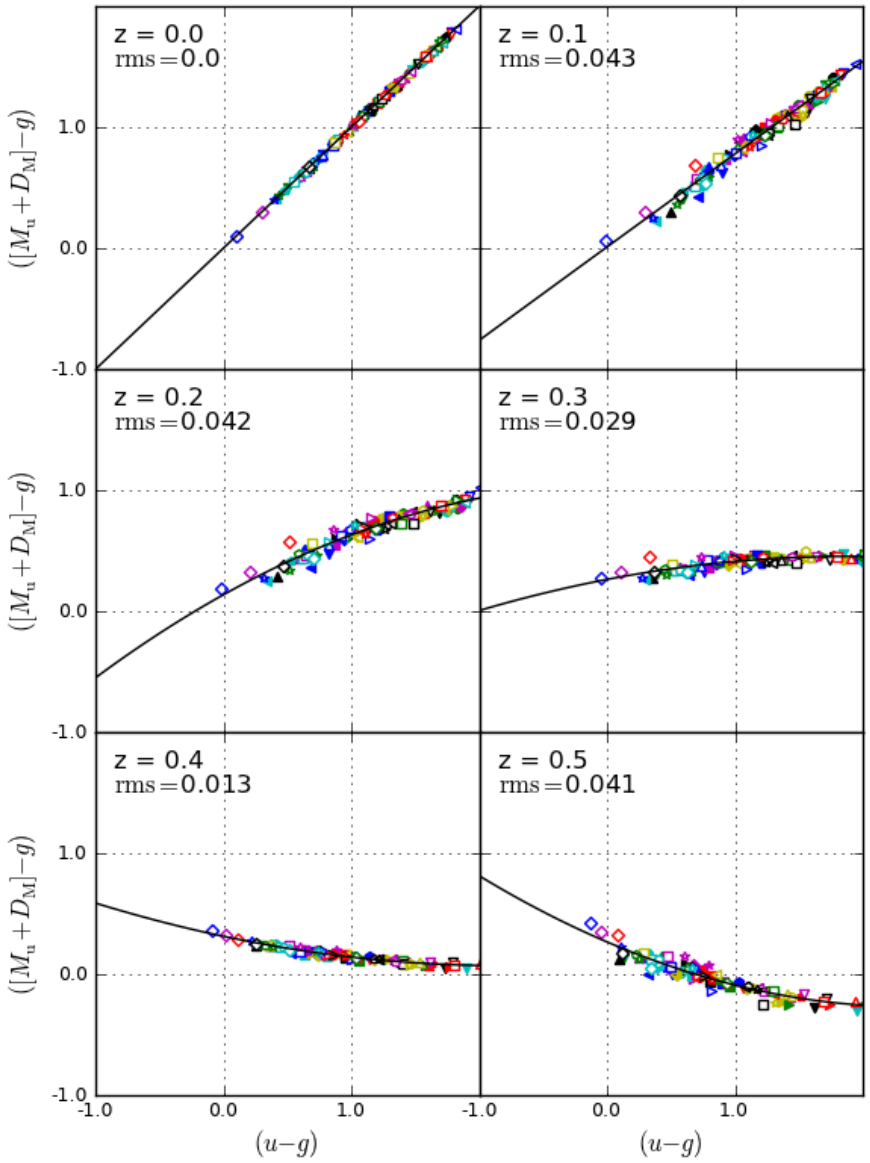

Fig. 11.—: **Determination of absolute u magnitudes.** Evolution of the second order polynomial used to determine M_u from observed $(u - g)$ colour.

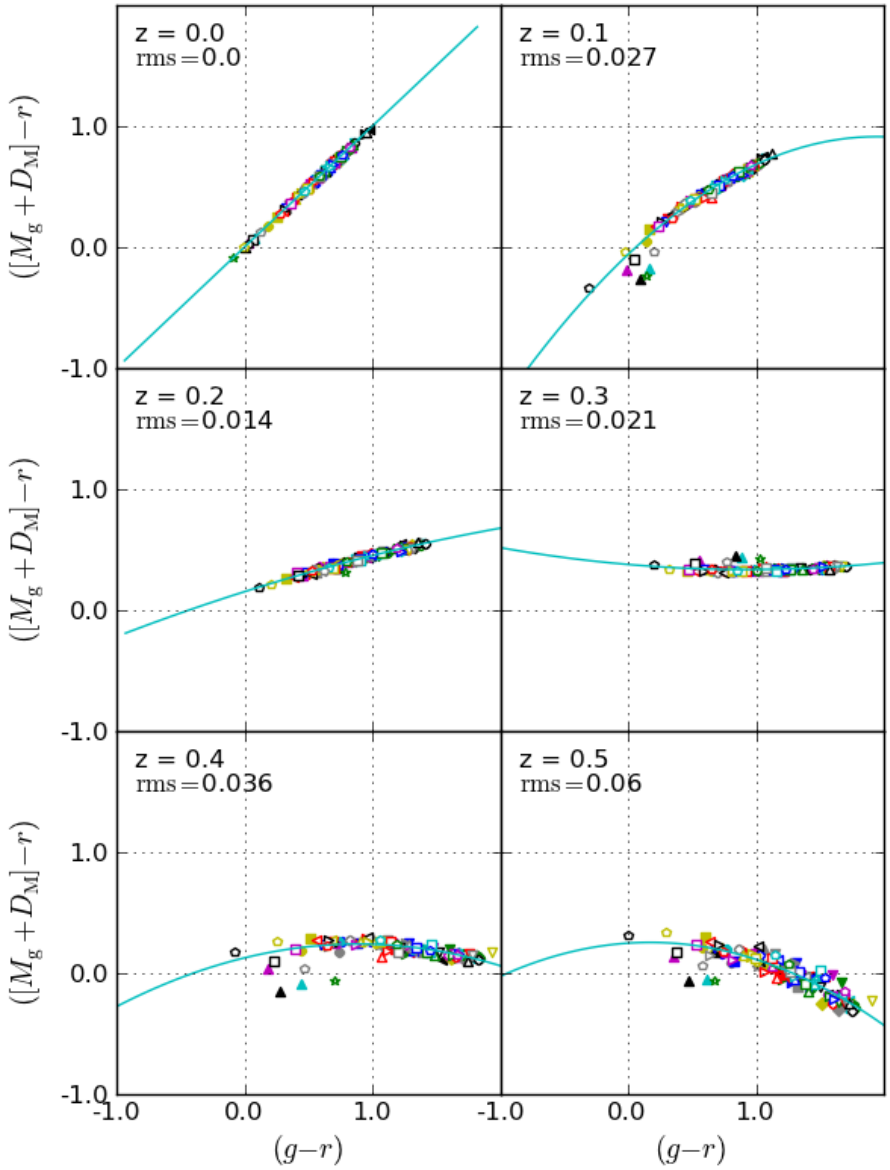

Fig. 12.—: **Determination of absolute g magnitudes between $z = 0$ and $z = 0.34$.** Evolution of the second order polynomial used to determine M_g from observed $(g-r)$ colour from $z = 0$ to $z = 0.34$. At $z = 0.1$ there are two galaxies ~ 0.3 mag bluer than the model: UM461 (Figure 18), which is a compact blue galaxy with a very prominent Balmer jump at 3650Å and MRK1450 (behind it) which is a compact starburst galaxy. The other blue galaxies with smaller blue offsets of ~ 0.1 are the compact blue galaxies UGCA410 and UGCA6850 and the starburst galaxy MRK930.

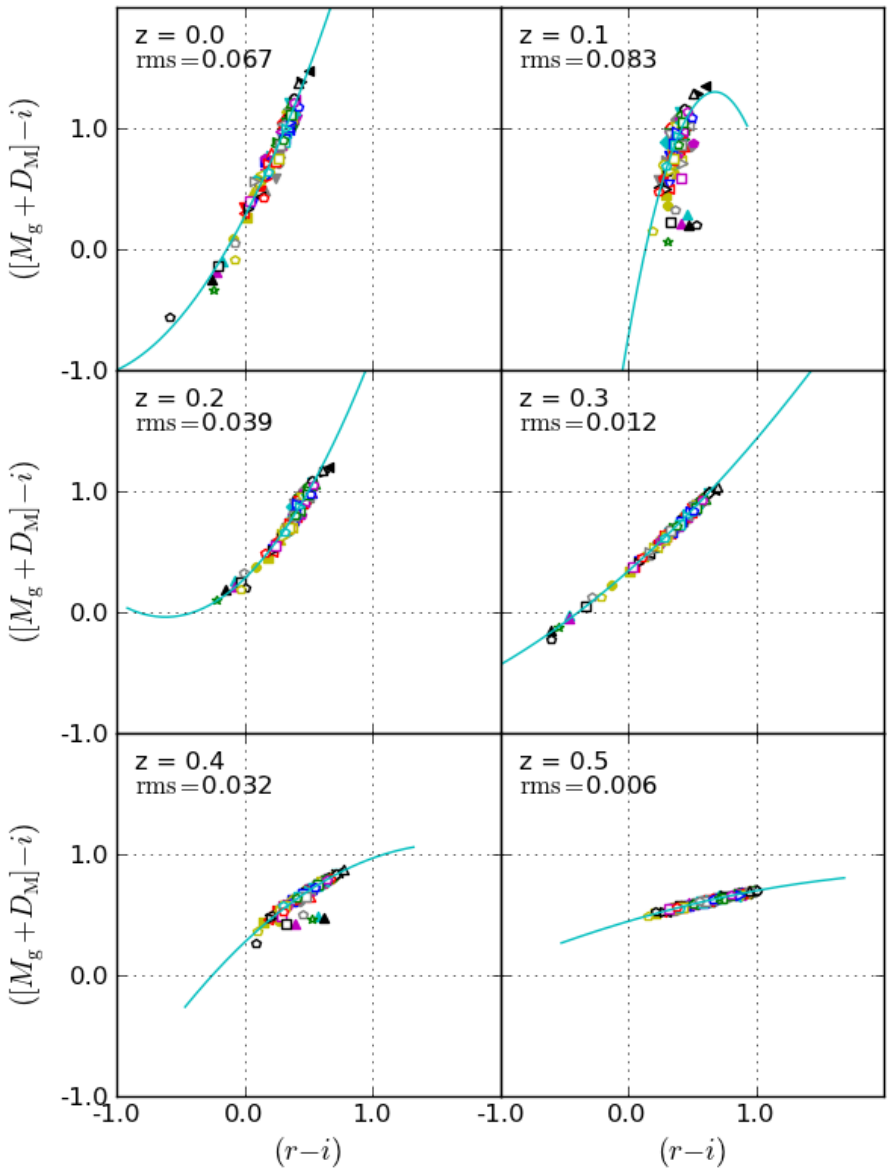

Fig. 13.—: **Determination of absolute g magnitudes between $z = 0.34$ and $z = 0.5$.** Evolution of the second order polynomial used to determine M_g from observed $(r - i)$ colour from $z = 0.34$ to $z = 0.5$. At $z = 0.4$ there are two galaxies ~ 0.3 mag bluer than the model: UM461, which is a compact blue galaxy with a very prominent Balmer jump at 3650Å and MRK1450 which is a compact starburst galaxy. The galaxies with smaller blue offsets of $\sim 0.1 - 0.2$ mag are the compact blue galaxies UGCA410, UGCA166 and UGCA6850 and the starburst galaxy MRK930.

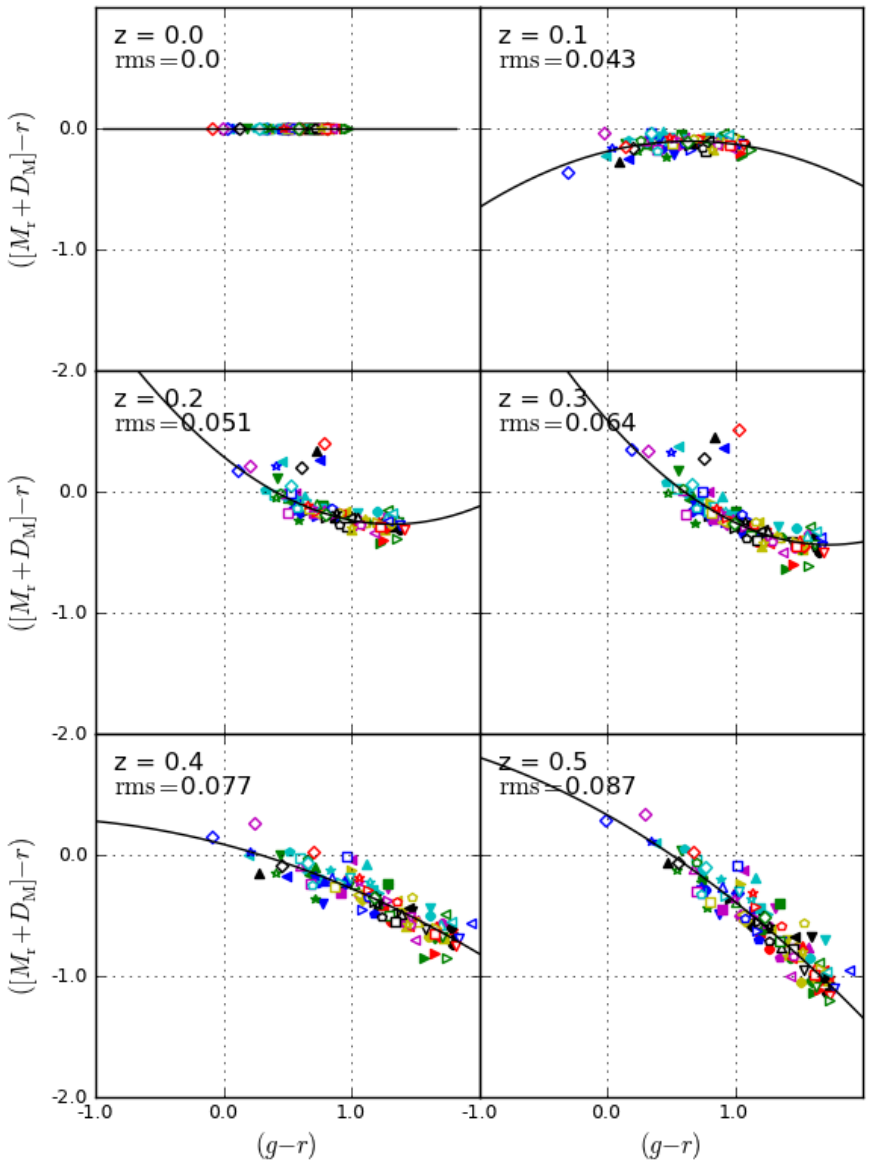

Fig. 14.—: **Determination of absolute r magnitudes between $z = 0$ and $z = 0.12$.** Evolution of the second order polynomial used to determine M_r from observed $(g-r)$ colour from $z = 0.0$ to $z = 0.12$. The RMS deviation for the model is relatively large beyond $z \sim 0.12$ because the restframe r-band lies outside the range spanned by the observed g and r-bands, so that the model depends on extrapolation.

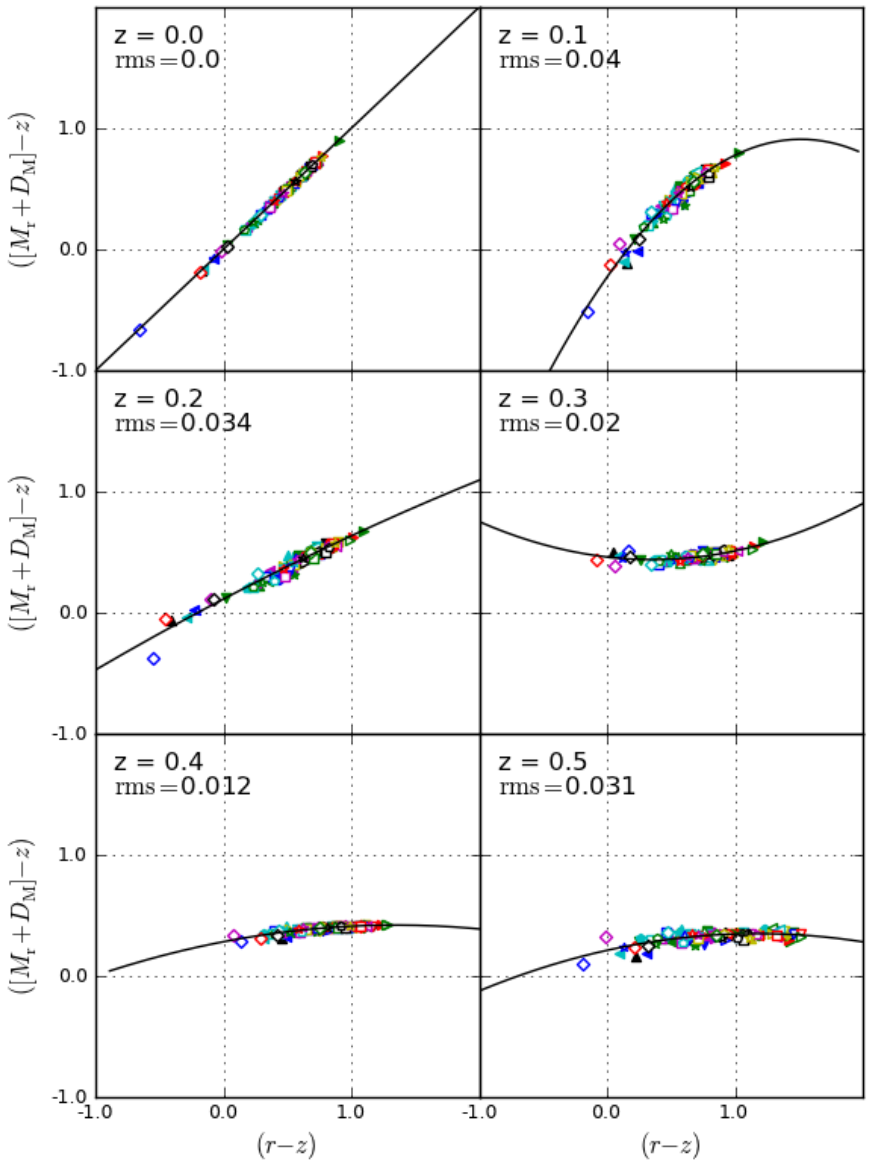

Fig. 15.—: **Determination of absolute r magnitudes between $z = 0.12$ and $z = 0.5$.** Evolution of the second order polynomial used to determine M_r from observed $(r-z)$ colour from $z = 0.12$ to $z = 0.5$. At $z = 0.2$ the compact blue galaxy UGCA166 is ~ 0.3 mag bluer than the model.

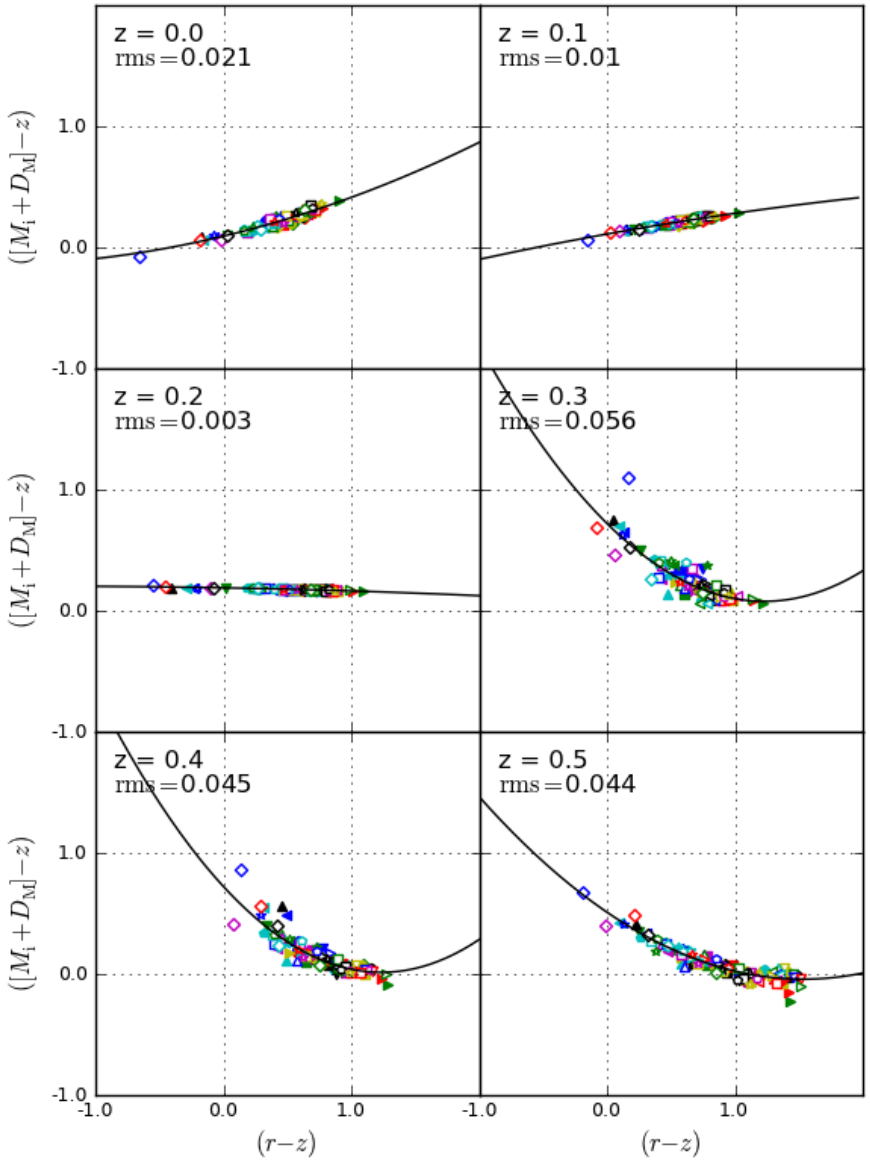

Fig. 16.—: **Determination of absolute i magnitudes.** Evolution of the second order polynomial used to determine M_i from observed $(r-z)$ colour. In the range $z \sim 0.3$ to $z \sim 0.4$ the compact blue galaxy UGCA166 is $\sim 0.3-0.5$ mag redder than the polynomial while the compact blue galaxy UGCA219 is ~ 0.3 bluer. Even by the standards of compact blue galaxies both have an extraordinarily rapid increase in optical and ultraviolet flux per unit wavelength at shorter wavelengths and very substantial optical emission.

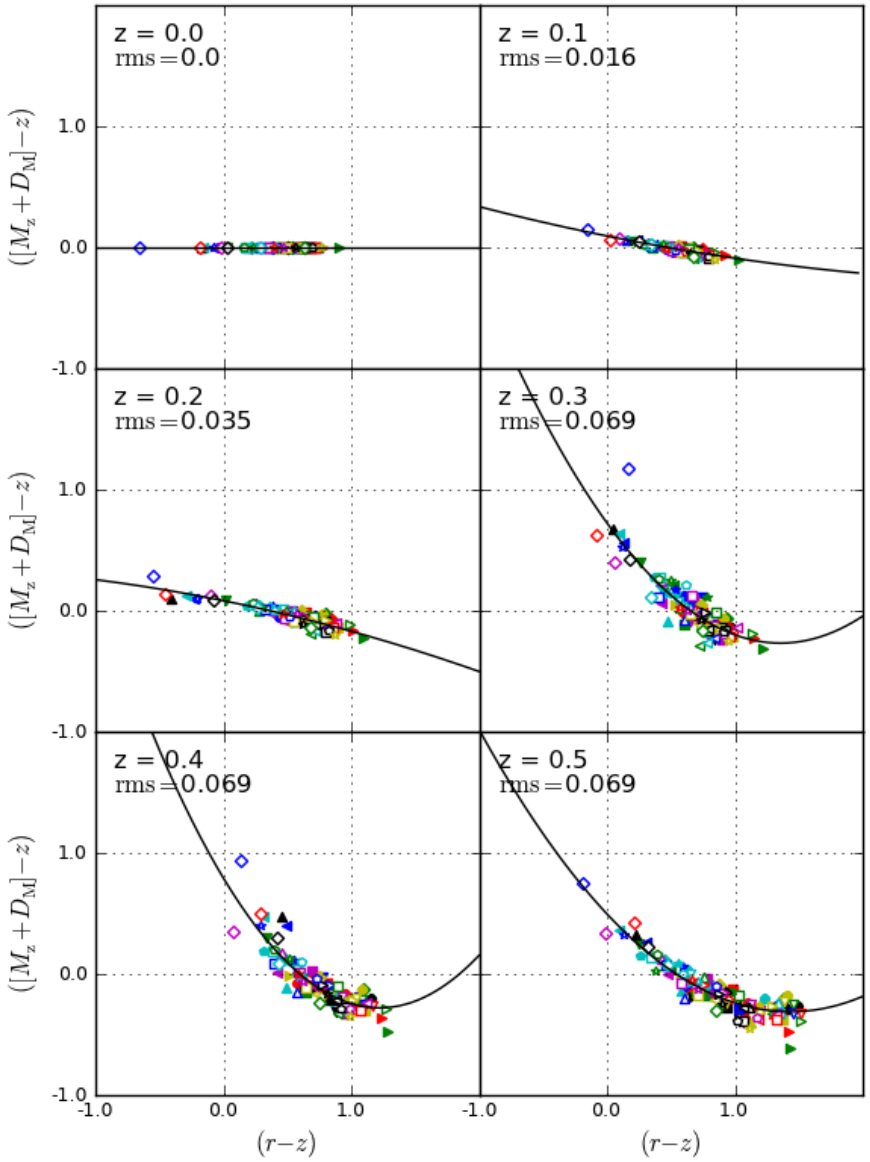

Fig. 17.—: **Determination of absolute z magnitudes.** Evolution of the second order polynomial used to determine M_z from observed $(r - z)$ colour. The RMS deviation for the model is relatively large beyond $z \sim 0.25$ because the redshifted restframe z-band lies outside the range spanned by the observed r and z-bands, so that the model depends on extrapolation. As in Figure 16 the compact blue galaxies UGCA166 and UGCA219 show large offsets in the range $z \sim 0.3$ to $z \sim 0.4$.

Fig. 18.—: **The extremely compact blue galaxy UM461.** This galaxy is significantly offset from the models (the open red diamond shape) at a number of redshifts in Figures 11 to 17. Figure 30 gives an explanation.

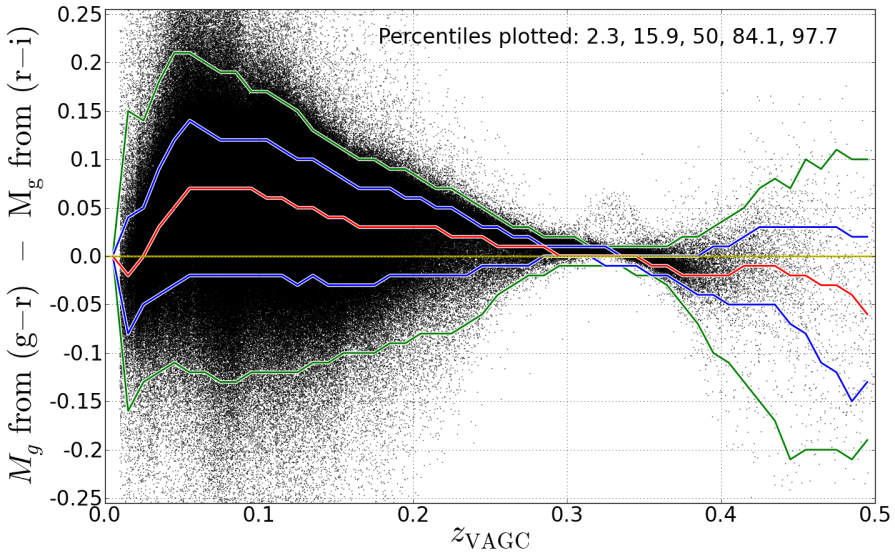

Fig. 19.—: **Showing that there is no discontinuity in calculated M_g values on switching from $(g-r)$ to $(r-i)$ input colour at $z = 0.34$.** The absolute g-magnitudes compared are for the New York Value-Added Galaxy Catalogue (VAGC, Blanton et al. 2005b).

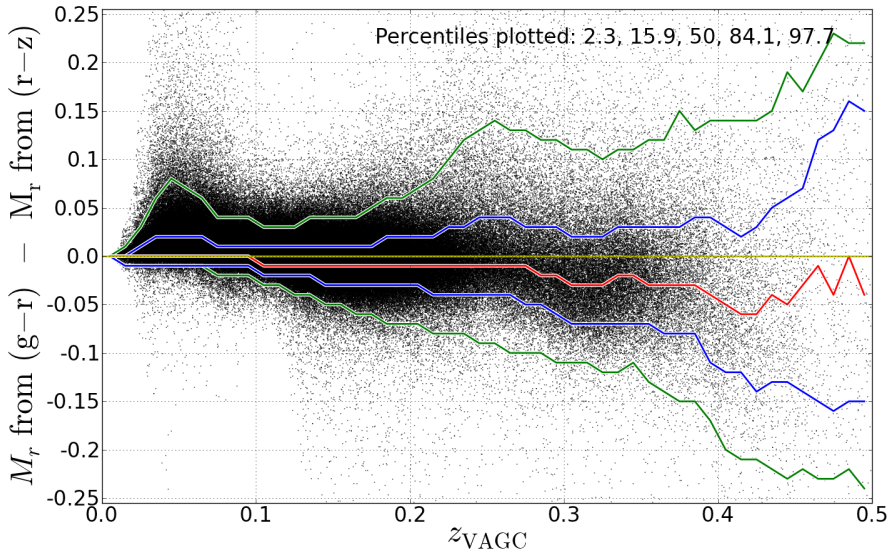

Fig. 20.—: **Showing that alternative input colours can be used when measurements in particular wavebands are not available.** The plot compares M_r values calculated using $(g-r)$ and $(r-z)$ input colours. $(r-z)$ is preferred as input colour beyond redshift 0.12 there is less template scatter about the best fit model (compare Figures 14 and 15). However, if z-band apparent magnitudes are unavailable or have large random error, $(g-r)$ can be used as input colour instead. The absolute r-magnitudes compared are for the New York Value-Added Galaxy Catalogue (VAGC, Blanton et al. 2005b).

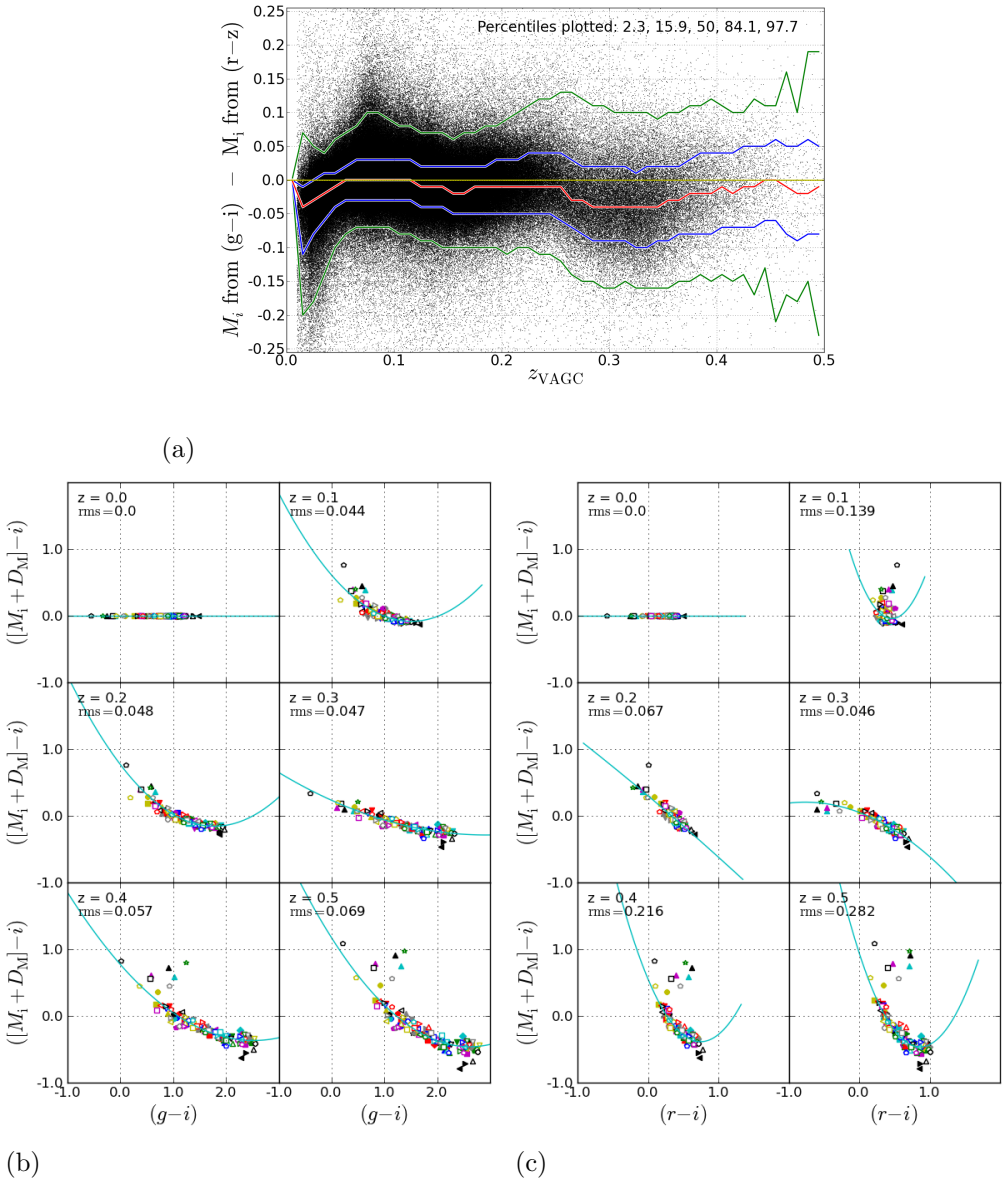

Fig. 21.—: **Another example where an alternative input colour has been used.** The top panel compares M_i values calculated using $(g-i)$ and $(r-z)$ input colours. $(r-z)$ is preferred as input colour for calculating M_i. However, should z band apparent magnitudes not be available $(g-i)$ can be used instead, albeit with increased template RMS scatter about the best fit model (compare the lower left panel with Figure 16). The lower right plot shows that $(r-i)$ is less suitable as input colour because of the smaller range of input colours and the higher degree of curvature in various redshift ranges. The absolute i-magnitudes compared are for the New York Value-Added Galaxy Catalogue (VAGC, Blanton et al. 2005b).

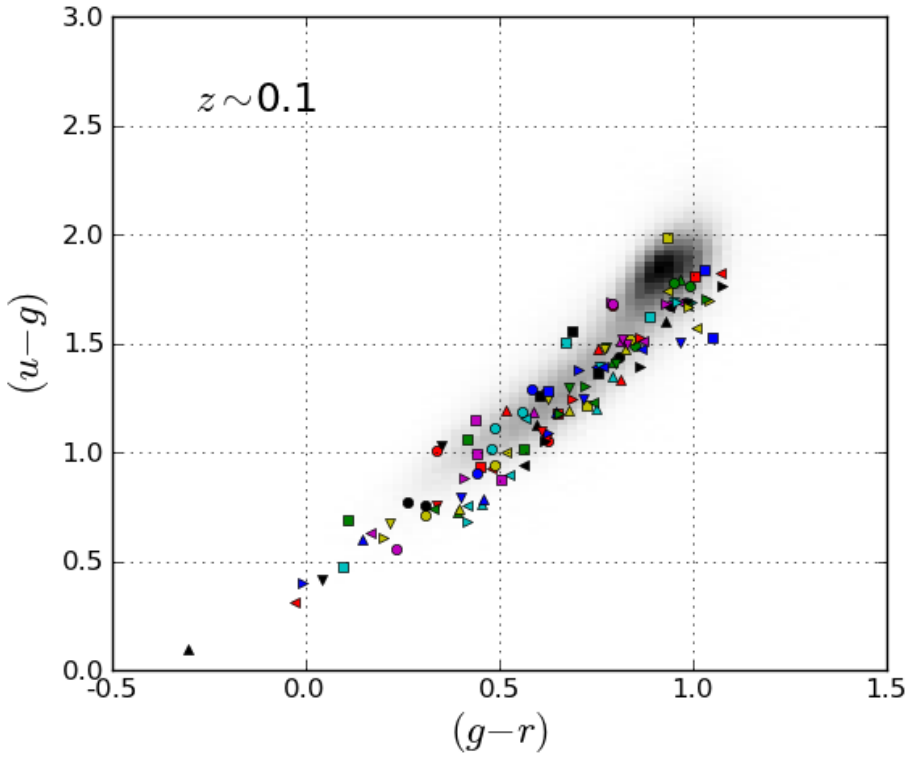

Fig. 22.—: **Showing that the templates span the observed** $(u-g)$ **versus** $(g-r)$ **colour-colour space at** $z \sim 0.1$**.** The binned densities are based on galaxies in the VAGC catalogue (which is not fully representative of all galaxies in this redshift range).

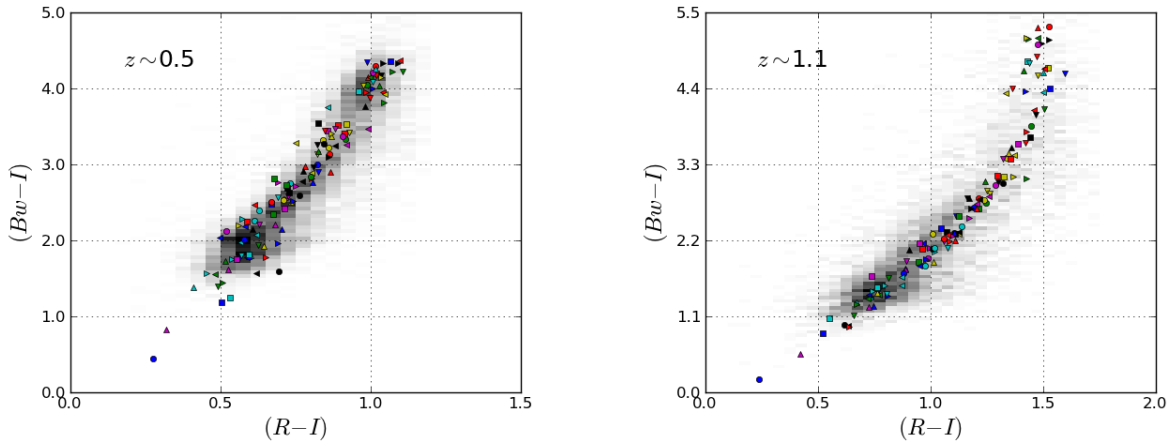

(a) (b)

Fig. 23.—: **Showing that our template galaxies provide good coverage in colour-colour space of the range of real galaxies.** $(Bw - I)$ versus $(R - I)$ for (a) $0.48 \leq z_{\rm phot} < 0.52$ and (b) $1.08 \leq z_{\rm phot} < 1.1$.

Table 4. Parameters for calculating absolute magnitudes $M_u = a(u-g)^2 + b(u-g) + c - D_M + g$.

red-shift	input colour	parameters a	b	c	rms error
0.00	$(u-g)$	0.0000	1.0000	0.0000	0.0000
0.01	$(u-g)$	0.0286	0.9238	0.0127	0.0082
0.02	$(u-g)$	0.0524	0.8549	0.0235	0.0128
0.03	$(u-g)$	0.0695	0.8001	0.0287	0.0192
0.04	$(u-g)$	0.0799	0.7574	0.0316	0.0253
0.05	$(u-g)$	0.0789	0.7373	0.0286	0.0306
0.06	$(u-g)$	0.0660	0.7362	0.0268	0.0341
0.07	$(u-g)$	0.0522	0.7393	0.0229	0.0374
0.08	$(u-g)$	0.0319	0.7602	0.0081	0.0406
0.09	$(u-g)$	0.0134	0.7704	0.0059	0.0420
0.10	$(u-g)$	-0.0016	0.7704	0.0102	0.0431
0.11	$(u-g)$	-0.0148	0.7663	0.0163	0.0440
0.12	$(u-g)$	-0.0265	0.7565	0.0260	0.0445
0.13	$(u-g)$	-0.0366	0.7407	0.0391	0.0447
0.14	$(u-g)$	-0.0472	0.7246	0.0518	0.0446
0.15	$(u-g)$	-0.0570	0.7059	0.0656	0.0442
0.16	$(u-g)$	-0.0672	0.6874	0.0788	0.0441
0.17	$(u-g)$	-0.0760	0.6655	0.0931	0.0435
0.18	$(u-g)$	-0.0844	0.6432	0.1071	0.0430
0.19	$(u-g)$	-0.0908	0.6177	0.1216	0.0424
0.20	$(u-g)$	-0.0956	0.5904	0.1359	0.0418
0.21	$(u-g)$	-0.0994	0.5627	0.1490	0.0414
0.22	$(u-g)$	-0.1013	0.5331	0.1615	0.0407
0.23	$(u-g)$	-0.1010	0.5012	0.1741	0.0399
0.24	$(u-g)$	-0.1000	0.4695	0.1848	0.0392
0.25	$(u-g)$	-0.0964	0.4339	0.1961	0.0381
0.26	$(u-g)$	-0.0890	0.3898	0.2108	0.0367
0.27	$(u-g)$	-0.0809	0.3435	0.2253	0.0348
0.28	$(u-g)$	-0.0723	0.2973	0.2384	0.0330
0.29	$(u-g)$	-0.0635	0.2510	0.2506	0.0310
0.30	$(u-g)$	-0.0543	0.2033	0.2625	0.0286
0.31	$(u-g)$	-0.0456	0.1578	0.2720	0.0265
0.32	$(u-g)$	-0.0362	0.1113	0.2813	0.0238
0.33	$(u-g)$	-0.0252	0.0626	0.2898	0.0207
0.34	$(u-g)$	-0.0135	0.0134	0.2988	0.0178
0.35	$(u-g)$	-0.0025	-0.0310	0.3050	0.0147
0.36	$(u-g)$	0.0089	-0.0727	0.3089	0.0120
0.37	$(u-g)$	0.0193	-0.1106	0.3113	0.0099
0.38	$(u-g)$	0.0308	-0.1505	0.3135	0.0097
0.39	$(u-g)$	0.0411	-0.1869	0.3129	0.0111
0.40	$(u-g)$	0.0513	-0.2231	0.3134	0.0134
0.41	$(u-g)$	0.0592	-0.2512	0.3061	0.0166
0.42	$(u-g)$	0.0657	-0.2769	0.2981	0.0200
0.43	$(u-g)$	0.0705	-0.2986	0.2881	0.0233
0.44	$(u-g)$	0.0722	-0.3098	0.2706	0.0280
0.45	$(u-g)$	0.0724	-0.3180	0.2526	0.0332
0.46	$(u-g)$	0.0747	-0.3369	0.2477	0.0362
0.47	$(u-g)$	0.0789	-0.3635	0.2511	0.0378
0.48	$(u-g)$	0.0832	-0.3898	0.2540	0.0393
0.49	$(u-g)$	0.0888	-0.4199	0.2602	0.0405
0.50	$(u-g)$	0.0951	-0.4516	0.2668	0.0415

Table 5. Parameters for calculating absolute magnitudes $M_g = a(g-r)^2 + b(g-r) + c - D_M + r$ or $M_g = a(r-i)^2 + b(r-i) + c - D_M + i$. Asterisks denote recommended colours giving the greatest accuracy.

red-shift	input colour	parameters a	b	c	rms error	red-shift	input colour	parameters a	b	c	rms error
0.00	$(g-r)$*	0.0000	1.0000	0.0000	0.0000	0.00	$(r-i)$	0.7820	2.0331	0.2562	0.0673
0.01	$(g-r)$*	-0.0148	0.9593	0.0154	0.0033	0.01	$(r-i)$	0.8241	2.0471	0.2372	0.0652
0.02	$(g-r)$*	-0.0306	0.9278	0.0264	0.0056	0.02	$(r-i)$	0.8734	2.1459	0.1767	0.0631
0.03	$(g-r)$*	-0.0476	0.9069	0.0310	0.0065	0.03	$(r-i)$	-0.6713	3.2182	-0.0419	0.0606
0.04	$(g-r)$*	-0.0611	0.8887	0.0319	0.0072	0.04	$(r-i)$	-2.8399	5.0201	-0.4540	0.0765
0.05	$(g-r)$*	-0.0922	0.8975	0.0236	0.0092	0.05	$(r-i)$	-4.1760	6.1836	-0.7468	0.0811
0.06	$(g-r)$*	-0.1348	0.9243	0.0082	0.0137	0.06	$(r-i)$	-3.9422	6.0209	-0.7671	0.0862
0.07	$(g-r)$*	-0.1936	0.9818	-0.0207	0.0220	0.07	$(r-i)$	-7.0703	8.0814	-1.1178	0.0902
0.08	$(g-r)$*	-0.2726	1.0790	-0.0676	0.0349	0.08	$(r-i)$	-10.8549	10.6142	-1.5366	0.0922
0.09	$(g-r)$*	-0.2364	0.9984	-0.0496	0.0250	0.09	$(r-i)$	-9.3657	9.5449	-1.3610	0.0932
0.10	$(g-r)$*	-0.2589	1.0043	-0.0606	0.0269	0.10	$(r-i)$	-5.0359	6.4367	-0.8252	0.0860
0.11	$(g-r)$*	-0.2679	0.9912	-0.0650	0.0272	0.11	$(r-i)$	-2.9544	4.9337	-0.5659	0.0833
0.12	$(g-r)$*	-0.2539	0.9404	-0.0546	0.0261	0.12	$(r-i)$	-1.9182	4.0458	-0.3914	0.0785
0.13	$(g-r)$*	-0.2204	0.8586	-0.0314	0.0236	0.13	$(r-i)$	-0.5309	2.7396	-0.1054	0.0795
0.14	$(g-r)$*	-0.1704	0.7535	-0.0016	0.0267	0.14	$(r-i)$	0.4311	1.8270	0.0916	0.0737
0.15	$(g-r)$*	-0.1073	0.6277	0.0354	0.0324	0.15	$(r-i)$	0.8457	1.4066	0.1818	0.0647
0.16	$(g-r)$*	-0.0857	0.5545	0.0635	0.0272	0.16	$(r-i)$	0.9664	1.2561	0.2162	0.0544
0.17	$(g-r)$*	-0.0687	0.4902	0.0883	0.0229	0.17	$(r-i)$	0.9524	1.1697	0.2343	0.0526
0.18	$(g-r)$*	-0.0559	0.4331	0.1118	0.0192	0.18	$(r-i)$	0.9187	1.1038	0.2511	0.0494
0.19	$(g-r)$*	-0.0453	0.3825	0.1326	0.0161	0.19	$(r-i)$	0.8789	1.0582	0.2644	0.0442
0.20	$(g-r)$*	-0.0344	0.3329	0.1540	0.0136	0.20	$(r-i)$	0.8287	1.0208	0.2768	0.0396
0.21	$(g-r)$*	-0.0254	0.2883	0.1739	0.0115	0.21	$(r-i)$	0.7631	0.9980	0.2870	0.0355
0.22	$(g-r)$*	-0.0163	0.2452	0.1935	0.0100	0.22	$(r-i)$	0.6982	0.9784	0.2961	0.0320
0.23	$(g-r)$*	-0.0067	0.2019	0.2139	0.0092	0.23	$(r-i)$	0.6341	0.9652	0.3039	0.0285
0.24	$(g-r)$*	0.0007	0.1629	0.2332	0.0087	0.24	$(r-i)$	0.5545	0.9660	0.3100	0.0248
0.25	$(g-r)$*	0.0095	0.1205	0.2549	0.0094	0.25	$(r-i)$	0.4452	0.9877	0.3137	0.0211
0.26	$(g-r)$*	0.0189	0.0757	0.2789	0.0110	0.26	$(r-i)$	0.3403	1.0027	0.3179	0.0184
0.27	$(g-r)$*	0.0256	0.0354	0.3014	0.0130	0.27	$(r-i)$	0.2543	1.0041	0.3224	0.0167
0.28	$(g-r)$*	0.0340	-0.0088	0.3273	0.0156	0.28	$(r-i)$	0.2154	0.9790	0.3281	0.0150
0.29	$(g-r)$*	0.0425	-0.0526	0.3536	0.0184	0.29	$(r-i)$	0.1841	0.9538	0.3331	0.0136
0.30	$(g-r)$*	0.0493	-0.0924	0.3790	0.0208	0.30	$(r-i)$	0.1570	0.9296	0.3378	0.0121
0.31	$(g-r)$*	0.0546	-0.1266	0.4017	0.0227	0.31	$(r-i)$	0.1330	0.9080	0.3419	0.0109
0.32	$(g-r)$*	0.0597	-0.1607	0.4252	0.0247	0.32	$(r-i)$	0.1102	0.8862	0.3457	0.0097
0.33	$(g-r)$*	0.0549	-0.1651	0.4261	0.0210	0.33	$(r-i)$	0.0680	0.8859	0.3430	0.0073
0.34	$(g-r)$*	0.0424	-0.1468	0.4105	0.0150	0.34	$(r-i)$*	0.0094	0.9013	0.3363	0.0052
0.35	$(g-r)$	0.0095	-0.0659	0.3476	0.0097	0.35	$(r-i)$*	-0.1090	0.9784	0.3135	0.0079
0.36	$(g-r)$	-0.0426	0.0678	0.2499	0.0260	0.36	$(r-i)$*	-0.3020	1.1384	0.2685	0.0216
0.37	$(g-r)$	-0.0772	0.1451	0.1958	0.0345	0.37	$(r-i)$*	-0.4070	1.2247	0.2360	0.0327
0.38	$(g-r)$	-0.1075	0.1974	0.1693	0.0295	0.38	$(r-i)$*	-0.4374	1.2073	0.2365	0.0294
0.39	$(g-r)$	-0.1298	0.2366	0.1436	0.0328	0.39	$(r-i)$*	-0.4163	1.1532	0.2417	0.0325
0.40	$(g-r)$	-0.1489	0.2659	0.1236	0.0354	0.40	$(r-i)$*	-0.3243	1.0207	0.2672	0.0323
0.41	$(g-r)$	-0.1628	0.2765	0.1174	0.0374	0.41	$(r-i)$*	-0.2404	0.8840	0.2981	0.0289
0.42	$(g-r)$	-0.1743	0.2795	0.1159	0.0398	0.42	$(r-i)$*	-0.3885	0.9314	0.2969	0.0364
0.43	$(g-r)$	-0.1819	0.2708	0.1218	0.0421	0.43	$(r-i)$*	-0.3154	0.8216	0.3206	0.0293
0.44	$(g-r)$	-0.1893	0.2591	0.1301	0.0445	0.44	$(r-i)$*	-0.2337	0.7034	0.3467	0.0229
0.45	$(g-r)$	-0.1963	0.2453	0.1394	0.0472	0.45	$(r-i)$*	-0.1743	0.6074	0.3682	0.0176
0.46	$(g-r)$	-0.2010	0.2232	0.1539	0.0498	0.46	$(r-i)$*	-0.1284	0.5246	0.3878	0.0123
0.47	$(g-r)$	-0.2056	0.1983	0.1703	0.0525	0.47	$(r-i)$*	-0.1029	0.4637	0.4028	0.0080
0.48	$(g-r)$	-0.2108	0.1731	0.1864	0.0554	0.48	$(r-i)$*	-0.0898	0.4162	0.4146	0.0052
0.49	$(g-r)$	-0.2129	0.1357	0.2128	0.0582	0.49	$(r-i)$*	-0.0723	0.3611	0.4302	0.0046
0.50	$(g-r)$	-0.2141	0.0952	0.2406	0.0614	0.50	$(r-i)$*	-0.0554	0.3081	0.4458	0.0064

Table 6. Parameters for calculating absolute magnitudes $M_r = a(g-r)^2 + b(g-r) + c - D_M + r$ or $M_r = a(r-z)^2 + b(r-z) + c - D_M + z$. Asterisks denote recommended colours giving the greatest accuracy.

red-shift	input colour	parameters a	b	c	rms error	red-shift	input colour	parameters a	b	c	rms error
0.00	$(g-r)$*	0.0000	0.0000	0.0000	0.0000	0.00	$(r-z)$	0.0000	1.0000	0.0000	0.0000
0.01	$(g-r)$*	-0.0182	0.0125	-0.0087	0.0036	0.01	$(r-z)$	-0.0056	1.0000	-0.0070	0.0039
0.02	$(g-r)$*	-0.0588	0.0736	-0.0439	0.0093	0.02	$(r-z)$	-0.0354	1.0470	-0.0374	0.0095
0.03	$(g-r)$*	-0.1156	0.1705	-0.0993	0.0194	0.03	$(r-z)$	-0.1505	1.2057	-0.1079	0.0195
0.04	$(g-r)$*	-0.1699	0.2644	-0.1539	0.0293	0.04	$(r-z)$	-0.4450	1.5876	-0.2479	0.0333
0.05	$(g-r)$*	-0.1900	0.2882	-0.1717	0.0336	0.05	$(r-z)$	-0.5936	1.7599	-0.3084	0.0396
0.06	$(g-r)$*	-0.2089	0.3059	-0.1841	0.0363	0.06	$(r-z)$	-0.6579	1.8248	-0.3334	0.0432
0.07	$(g-r)$*	-0.2292	0.3250	-0.1959	0.0383	0.07	$(r-z)$	-0.6589	1.8052	-0.3299	0.0444
0.08	$(g-r)$*	-0.2507	0.3501	-0.2110	0.0413	0.08	$(r-z)$	-0.6470	1.7673	-0.3195	0.0450
0.09	$(g-r)$*	-0.2371	0.3243	-0.2085	0.0428	0.09	$(r-z)$	-0.5832	1.6524	-0.2807	0.0427
0.10	$(g-r)$*	-0.2018	0.2614	-0.1910	0.0431	0.10	$(r-z)$	-0.4953	1.5019	-0.2289	0.0399
0.11	$(g-r)$*	-0.1234	0.1225	-0.1414	0.0419	0.11	$(r-z)$	-0.3403	1.2534	-0.1420	0.0363
0.12	$(g-r)$*	-0.0309	-0.0565	-0.0680	0.0443	0.12	$(r-z)$*	-0.1825	1.0028	-0.0551	0.0357
0.13	$(g-r)$	0.0532	-0.2178	-0.0020	0.0474	0.13	$(r-z)$*	-0.0918	0.8462	0.0002	0.0362
0.14	$(g-r)$	0.1521	-0.3983	0.0680	0.0478	0.14	$(r-z)$*	-0.0397	0.7415	0.0386	0.0365
0.15	$(g-r)$	0.2302	-0.5514	0.1316	0.0482	0.15	$(r-z)$*	-0.0192	0.6812	0.0619	0.0363
0.16	$(g-r)$	0.2626	-0.6304	0.1674	0.0472	0.16	$(r-z)$*	-0.0122	0.6412	0.0772	0.0359
0.17	$(g-r)$	0.2959	-0.7185	0.2114	0.0489	0.17	$(r-z)$*	-0.0138	0.6135	0.0881	0.0353
0.18	$(g-r)$	0.3208	-0.7947	0.2527	0.0507	0.18	$(r-z)$*	-0.0191	0.5909	0.0974	0.0347
0.19	$(g-r)$	0.3096	-0.7976	0.2593	0.0492	0.19	$(r-z)$*	-0.0259	0.5725	0.1049	0.0341
0.20	$(g-r)$	0.3196	-0.8451	0.2896	0.0510	0.20	$(r-z)$*	-0.0314	0.5535	0.1129	0.0336
0.21	$(g-r)$	0.3266	-0.8863	0.3183	0.0529	0.21	$(r-z)$*	-0.0388	0.5369	0.1207	0.0330
0.22	$(g-r)$	0.3314	-0.9234	0.3457	0.0549	0.22	$(r-z)$*	-0.0453	0.5185	0.1297	0.0322
0.23	$(g-r)$	0.3367	-0.9613	0.3738	0.0568	0.23	$(r-z)$*	-0.0468	0.4908	0.1436	0.0306
0.24	$(g-r)$	0.3393	-0.9945	0.4009	0.0588	0.24	$(r-z)$*	-0.0431	0.4526	0.1635	0.0285
0.25	$(g-r)$	0.3454	-1.0360	0.4360	0.0565	0.25	$(r-z)$*	-0.0253	0.3901	0.1955	0.0248
0.26	$(g-r)$	0.3454	-1.0664	0.4638	0.0582	0.26	$(r-z)$*	0.0130	0.2894	0.2462	0.0196
0.27	$(g-r)$	0.3386	-1.0835	0.4865	0.0601	0.27	$(r-z)$*	0.0644	0.1647	0.3092	0.0153
0.28	$(g-r)$	0.3449	-1.1336	0.5311	0.0604	0.28	$(r-z)$*	0.1185	0.0336	0.3764	0.0151
0.29	$(g-r)$	0.3456	-1.1655	0.5630	0.0620	0.29	$(r-z)$*	0.1524	-0.0590	0.4258	0.0177
0.30	$(g-r)$	0.3427	-1.1890	0.5922	0.0637	0.30	$(r-z)$*	0.1708	-0.1213	0.4603	0.0204
0.31	$(g-r)$	0.3377	-1.2045	0.6174	0.0656	0.31	$(r-z)$*	0.1590	-0.1222	0.4629	0.0206
0.32	$(g-r)$	0.3321	-1.2180	0.6414	0.0675	0.32	$(r-z)$*	0.1429	-0.1115	0.4575	0.0194
0.33	$(g-r)$	0.3266	-1.2267	0.6606	0.0693	0.33	$(r-z)$*	0.1259	-0.0971	0.4486	0.0177
0.34	$(g-r)$	0.3041	-1.1758	0.6294	0.0653	0.34	$(r-z)$*	0.1016	-0.0675	0.4319	0.0154
0.35	$(g-r)$	0.2452	-1.0342	0.5409	0.0686	0.35	$(r-z)$*	0.0704	-0.0252	0.4095	0.0125
0.36	$(g-r)$	0.1695	-0.8550	0.4335	0.0716	0.36	$(r-z)$*	0.0288	0.0386	0.3769	0.0096
0.37	$(g-r)$	0.1105	-0.6988	0.3196	0.0672	0.37	$(r-z)$*	-0.0197	0.1197	0.3347	0.0080
0.38	$(g-r)$	0.0453	-0.5501	0.2322	0.0694	0.38	$(r-z)$*	-0.0513	0.1714	0.3065	0.0092
0.39	$(g-r)$	-0.0170	-0.4069	0.1463	0.0715	0.39	$(r-z)$*	-0.0649	0.1898	0.2940	0.0106
0.40	$(g-r)$	-0.0871	-0.2775	0.0878	0.0768	0.40	$(r-z)$*	-0.0756	0.2040	0.2831	0.0123
0.41	$(g-r)$	-0.1174	-0.2372	0.0732	0.0808	0.41	$(r-z)$*	-0.0939	0.2380	0.2591	0.0159
0.42	$(g-r)$	-0.1345	-0.2248	0.0719	0.0829	0.42	$(r-z)$*	-0.1296	0.3062	0.2190	0.0214
0.43	$(g-r)$	-0.1443	-0.2426	0.0897	0.0788	0.43	$(r-z)$*	-0.1343	0.3119	0.2114	0.0232
0.44	$(g-r)$	-0.1531	-0.2573	0.1081	0.0784	0.44	$(r-z)$*	-0.1341	0.3100	0.2071	0.0247
0.45	$(g-r)$	-0.1597	-0.2797	0.1293	0.0799	0.45	$(r-z)$*	-0.1332	0.3077	0.2026	0.0264
0.46	$(g-r)$	-0.1597	-0.3177	0.1553	0.0816	0.46	$(r-z)$*	-0.1222	0.2838	0.2100	0.0266
0.47	$(g-r)$	-0.1597	-0.3567	0.1800	0.0838	0.47	$(r-z)$*	-0.1142	0.2662	0.2137	0.0274
0.48	$(g-r)$	-0.1576	-0.4081	0.2104	0.0822	0.48	$(r-z)$*	-0.1088	0.2548	0.2135	0.0288
0.49	$(g-r)$	-0.1524	-0.4652	0.2482	0.0826	0.49	$(r-z)$*	-0.1041	0.2441	0.2135	0.0299
0.50	$(g-r)$	-0.1208	-0.5955	0.3308	0.0872	0.50	$(r-z)$*	-0.1002	0.2353	0.2123	0.0314

Table 7. Parameters for calculating absolute magnitudes $M_i = a(r-z)^2 + b(r-z) + c - D_M + z$.

red-shift	input colour	parameters a	b	c	rms error
0.00	$(r-z)$	0.0670	0.2530	0.0929	0.0215
0.01	$(r-z)$	0.0616	0.2430	0.0956	0.0202
0.02	$(r-z)$	0.0565	0.2406	0.0927	0.0183
0.03	$(r-z)$	0.0433	0.2541	0.0821	0.0158
0.04	$(r-z)$	-0.0004	0.3046	0.0603	0.0137
0.05	$(r-z)$	-0.0264	0.3180	0.0561	0.0130
0.06	$(r-z)$	-0.0397	0.3123	0.0591	0.0125
0.07	$(r-z)$	-0.0426	0.2917	0.0679	0.0119
0.08	$(r-z)$	-0.0427	0.2678	0.0781	0.0112
0.09	$(r-z)$	-0.0325	0.2304	0.0937	0.0105
0.10	$(r-z)$	-0.0191	0.1901	0.1106	0.0096
0.11	$(r-z)$	0.0013	0.1405	0.1309	0.0090
0.12	$(r-z)$	0.0172	0.0983	0.1482	0.0084
0.13	$(r-z)$	0.0217	0.0722	0.1595	0.0076
0.14	$(r-z)$	0.0206	0.0538	0.1672	0.0065
0.15	$(r-z)$	0.0162	0.0400	0.1722	0.0053
0.16	$(r-z)$	0.0108	0.0280	0.1758	0.0039
0.17	$(r-z)$	0.0055	0.0166	0.1789	0.0025
0.18	$(r-z)$	0.0005	0.0055	0.1817	0.0012
0.19	$(r-z)$	-0.0039	-0.0056	0.1847	0.0011
0.20	$(r-z)$	-0.0068	-0.0190	0.1893	0.0026
0.21	$(r-z)$	-0.0089	-0.0340	0.1953	0.0044
0.22	$(r-z)$	-0.0088	-0.0547	0.2048	0.0067
0.23	$(r-z)$	0.0011	-0.0956	0.2252	0.0100
0.24	$(r-z)$	0.0221	-0.1579	0.2575	0.0146
0.25	$(r-z)$	0.0680	-0.2654	0.3124	0.0217
0.26	$(r-z)$	0.1489	-0.4390	0.4009	0.0331
0.27	$(r-z)$	0.1872	-0.5585	0.4770	0.0381
0.28	$(r-z)$	0.2774	-0.7483	0.5759	0.0489
0.29	$(r-z)$	0.3329	-0.8733	0.6436	0.0562
0.30	$(r-z)$	0.4251	-1.0456	0.7203	0.0563
0.31	$(r-z)$	0.4105	-1.0335	0.7167	0.0563
0.32	$(r-z)$	0.3870	-1.0020	0.7012	0.0548
0.33	$(r-z)$	0.3856	-1.0069	0.7009	0.0556
0.34	$(r-z)$	0.3994	-1.0304	0.7025	0.0529
0.35	$(r-z)$	0.4764	-1.1588	0.7468	0.0515
0.36	$(r-z)$	0.5679	-1.3167	0.8057	0.0524
0.37	$(r-z)$	0.5207	-1.2354	0.7654	0.0484
0.38	$(r-z)$	0.4895	-1.1791	0.7361	0.0447
0.39	$(r-z)$	0.4760	-1.1624	0.7291	0.0448
0.40	$(r-z)$	0.4644	-1.1481	0.7231	0.0449
0.41	$(r-z)$	0.4433	-1.1061	0.6978	0.0450
0.42	$(r-z)$	0.3713	-0.9670	0.6276	0.0477
0.43	$(r-z)$	0.3443	-0.9169	0.6031	0.0452
0.44	$(r-z)$	0.3214	-0.8742	0.5825	0.0436
0.45	$(r-z)$	0.2995	-0.8332	0.5628	0.0425
0.46	$(r-z)$	0.2955	-0.8313	0.5645	0.0429
0.47	$(r-z)$	0.2862	-0.8171	0.5590	0.0430
0.48	$(r-z)$	0.2721	-0.7921	0.5470	0.0430
0.49	$(r-z)$	0.2529	-0.7558	0.5289	0.0434
0.50	$(r-z)$	0.2344	-0.7199	0.5100	0.0440

Table 8. Parameters for calculating absolute magnitudes $M_z = a(r-z)^2 + b(r-z) + c - D_M + z$.

red-shift	input colour	parameters a	b	c	rms error
0.00	$(r-z)$	0.0000	0.0000	0.0000	0.0000
0.01	$(r-z)$	-0.0032	-0.0127	0.0055	0.0021
0.02	$(r-z)$	-0.0056	-0.0265	0.0117	0.0041
0.03	$(r-z)$	-0.0065	-0.0446	0.0206	0.0058
0.04	$(r-z)$	0.0007	-0.0755	0.0346	0.0073
0.05	$(r-z)$	0.0094	-0.1066	0.0475	0.0087
0.06	$(r-z)$	0.0184	-0.1377	0.0599	0.0101
0.07	$(r-z)$	0.0245	-0.1645	0.0709	0.0115
0.08	$(r-z)$	0.0308	-0.1903	0.0817	0.0129
0.09	$(r-z)$	0.0318	-0.2053	0.0891	0.0145
0.10	$(r-z)$	0.0294	-0.2130	0.0941	0.0161
0.11	$(r-z)$	0.0137	-0.1998	0.0915	0.0178
0.12	$(r-z)$	-0.0073	-0.1785	0.0858	0.0199
0.13	$(r-z)$	-0.0208	-0.1683	0.0829	0.0219
0.14	$(r-z)$	-0.0304	-0.1640	0.0808	0.0237
0.15	$(r-z)$	-0.0357	-0.1669	0.0796	0.0254
0.16	$(r-z)$	-0.0393	-0.1728	0.0791	0.0272
0.17	$(r-z)$	-0.0410	-0.1811	0.0790	0.0290
0.18	$(r-z)$	-0.0411	-0.1905	0.0791	0.0309
0.19	$(r-z)$	-0.0410	-0.2005	0.0800	0.0328
0.20	$(r-z)$	-0.0397	-0.2131	0.0830	0.0347
0.21	$(r-z)$	-0.0371	-0.2286	0.0878	0.0368
0.22	$(r-z)$	-0.0324	-0.2506	0.0970	0.0390
0.23	$(r-z)$	-0.0175	-0.2957	0.1192	0.0415
0.24	$(r-z)$	0.0096	-0.3654	0.1553	0.0447
0.25	$(r-z)$	0.0015	-0.4096	0.1972	0.0451
0.26	$(r-z)$	0.0781	-0.5762	0.2865	0.0501
0.27	$(r-z)$	0.1733	-0.7774	0.3958	0.0548
0.28	$(r-z)$	0.2639	-0.9813	0.5102	0.0615
0.29	$(r-z)$	0.4800	-1.3406	0.6616	0.0650
0.30	$(r-z)$	0.5389	-1.4621	0.7242	0.0692
0.31	$(r-z)$	0.4096	-1.2788	0.6616	0.0710
0.32	$(r-z)$	0.3891	-1.2451	0.6433	0.0697
0.33	$(r-z)$	0.4119	-1.2792	0.6492	0.0680
0.34	$(r-z)$	0.4465	-1.3278	0.6576	0.0661
0.35	$(r-z)$	0.5858	-1.5468	0.7320	0.0677
0.36	$(r-z)$	0.7493	-1.8180	0.8346	0.0699
0.37	$(r-z)$	0.7066	-1.7301	0.7859	0.0654
0.38	$(r-z)$	0.7230	-1.7555	0.7920	0.0661
0.39	$(r-z)$	0.7226	-1.7586	0.7934	0.0673
0.40	$(r-z)$	0.7178	-1.7545	0.7926	0.0685
0.41	$(r-z)$	0.7794	-1.8077	0.7865	0.0642
0.42	$(r-z)$	0.7739	-1.7614	0.7412	0.0644
0.43	$(r-z)$	0.7036	-1.6523	0.7017	0.0659
0.44	$(r-z)$	0.6416	-1.5483	0.6601	0.0653
0.45	$(r-z)$	0.5984	-1.4808	0.6364	0.0663
0.46	$(r-z)$	0.5771	-1.4541	0.6318	0.0663
0.47	$(r-z)$	0.5473	-1.4083	0.6164	0.0663
0.48	$(r-z)$	0.5101	-1.3454	0.5916	0.0663
0.49	$(r-z)$	0.4257	-1.1880	0.5235	0.0689
0.50	$(r-z)$	0.3938	-1.1277	0.4954	0.0691

2.5. Choice of the best observed colours to use

As already mentioned in §2.4 the use of observed colours which straddle or are close to the redshifted restframe waveband W, as in Rudnick et al. (2003) and the *InterRest* software (Taylor et al. 2009), does not always result in the greatest accuracy. In fact the distribution of points in plots of $(M_W + D_M) - m_Z$ against $(m_Y - m_Z)$ (Figures 11 to 17) depends on a complex interplay between several factors at any given redshift.

We illustrate this for the specific case of determining the r band absolute magnitude M_r at $z \sim 0.28$ and refer to the SED plots for representative galaxies shown in Figure 24. The top panel shows that at $z = 0.28$ the restframe r-band (shown dashed), lies between the observed i and z-bands. We might therefore expect $(i - z)$ to be a good observed colour for determing the absolute r magnitude. However, as the bottom left panel shows there is very little spread in $(i - z)$ values on the x-axis for the different templates at this redshift. This can be attributed to the fact that the different SED templates are close to being parallel to each other at this redshift with the H_α emission line lying precisely between the i and z filters so that variations in H_α line strength between templates have almost no effect. This emission line does nevertheless lie within the redshifted restframe r-band and variations in its strength between templates contributes to a reasonably large variation in $(M_r + D_M) - m_z$ values on the y-axis. As a result the RMS deviation of the y-values from the model is relatively large, (0.036) and a small random uncertainty in observed colour results in a much larger uncertainty in $(M_r + D_M) - m_z$, and hence M_r. Furthermore the model is highly convex, potentially resulting in large errors outside the $(i - z)$ range for the templates (the range of observed colours we allow is 20% wider). The bottom right panel shows that $(r - z)$ is a better observed colour to use: the range of input colours is much greater, the RMS deviation is less (0.015), and the model has much smaller curvature.

We find that the least squares fitting procedure can produce some very unexpected results when the range of observed colours on the x-axis is small, e.g. at $z = 0.1$ in Figure 13 where the plot of $(M_g + D_M) - m_i$ against $(r - i)$ turns over very rapidly at $(r - i) \sim 0.5$. This can be understood as follows. The majority of the points constrain the model fit to a curved shape, but because the range of x-values is so much less than the range of y-values a very large (negative) value of a is required to produce even the relatively small amount of curvature in the data points. This large negative value of a is responsible for the sharp turnover seen at $z = 0.1$. To make this clear we show in Figure 25 the unique quadratic function $y = ax^2 + bx + c$ that passes through the three points (0.3 , 0.25), (0.35 , 0.6875) and (0.4 , 1.0). This exhibits a sharp maximum at $x = 0.5$.

2.6. Systematic errors arising from highly curved model fits

A large coefficient a in the model function $y = ax^2 + bx + c$ corresponding to high curvature could result in a significant systematic error $a\sigma^2$ when the input x values for individual galaxies have gaussian random errors with standard deviation σ and this provides an additional reason for avoiding choosing models that are not too "curved", or more precisely have small a values. This systematic error and the random errors in computed absolute magnitudes arising from random errors in the input colour x can be analysed as follows.

To simplify the notation let $x_1 = m_Y$ and $x_2 = m_Z$ denote the true values of the Y and Z apparent magnitudes for a particular galaxy. Let the measured values be $X_1 = x_1 + e_1$ and $X_2 = x_2 + e_2$ where e_1 and e_2 are random measurement errors with variances σ_1^2 and σ_2^2. Let M be the true value of the absolute magnitude in waveband W and the values deduced from the measured X_1 and X_2 values be $M + E$. Our aim is to find the mean and variance of the resulting random absolute magnitude error E.

Substituting in the model equation:

$$(M + E) + D_M - (x_2 + e_2) = a[(x_1 + e_1) - (x_2 + e_2)]^2 + b[(x_1 + e_1) - (x_2 + e_2)] + c. \quad (23)$$

Subtracting $M + D_M - x_2 = a(x_1 - x_2)^2 + b(x_1 - x_2) + c$ and rearranging:

$$E = a(e_1 - e_2)^2 + 2a(x_1 - x_2)(e_1 - e_2) + b(e_1 - e_2) + e_2. \quad (24)$$

Over a large number repeated measurements all terms except the first would cancel leaving a mean (i.e. systematic) error of:

$$\bar{E} = a(\sigma_1^2 + \sigma_2^2). \quad (25)$$

The variance of E is:

$$\sigma_E^2 = \bar{E^2} - \overline{E}^2. \quad (26)$$

Ignoring powers higher than the second in e_1 and/or e_2 and terms which average to zero, substituting (24) in (26) gives:

$$\sigma_E^2 = [2a(x_1 - x_2) + b]^2(\sigma_1^2 + \sigma_2^2) + \sigma_2^2. \quad (27)$$

In addition to this random error σ_E arising from apparent magnitude errors there is also an error due to the scatter of real galaxy colours about the model in plots of $(M_W + D_M) - m_Z$ against $(m_Y - m_Z)$. We can take the variances $\sigma_{\rm model}$ of this error to be that of the variance in $(M_W + D_M) - m_Z$ for the ~ 125 galaxy templates. This is the mean square deviation in $(M_W + D_M) - m_Z$ which we tabulate for different redshifts and also show by the rms values in the top left hand corner of the plots in Figures 11 to 17. Combining σ_E and $\sigma_{\rm model}$ in quadrature we arrive at a value for the variance in absolute magnitude for each galaxy in our sample:

$$\sigma^2_{\rm total} = \sigma^2_E + \sigma^2_{\rm model}. \tag{28}$$

It is a significant benefit of our method that it enables the random errors in computed absolute magnitude values to be calculated.

For the model shown in the top panel of Figure 24 at $z = 0.28$ the parameters in Equation 22 are $a = -2.518, b = 2.045, c = -0.04175$. A random error of $\sigma = 0.1$ in the input colour produces a systematic shift in the model of $a\sigma^2 = -0.025$. This is verified by the simulation shown in Figure 26.

In most cases this systematic error in absolute magnitude will be insignificant relative to the random errors arising directly from random apparent magnitudes errors. The maximum (absolute) values of a in our tables are 0.55 at $z = 0.36$ for M_i and 0.77 for M_z. Assuming realistic random errors of $\sigma = 0.02$ in each of the two observed magnitudes r and z, we have $\sigma \sim 0.03$ for the input colour $(r - z)$ and maximum systematic offsets of less than $\sim$0.001 mag.

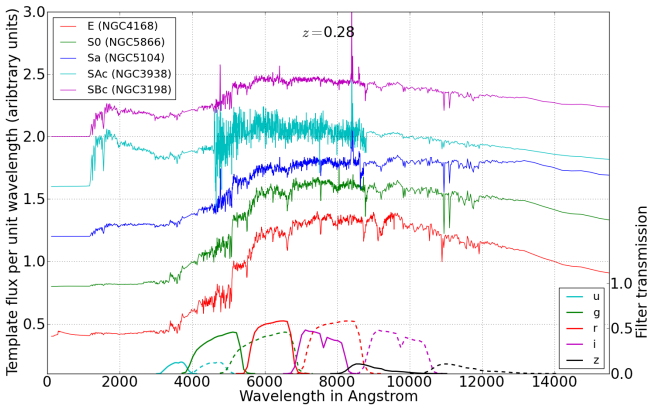

(a)

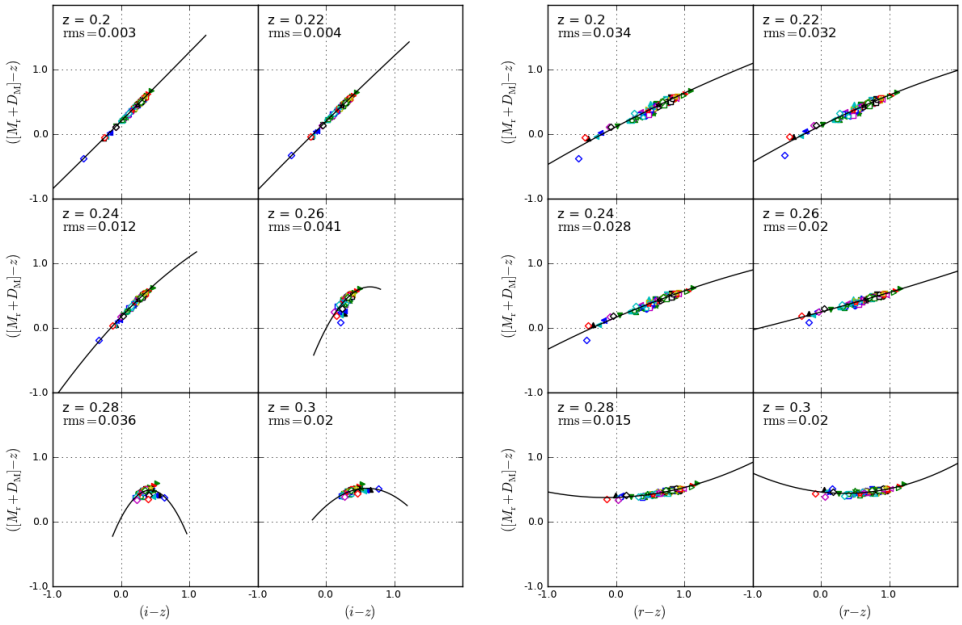

(b) (c)

Fig. 24.—: **The nearest filters to the redshifted restframe waveband do not necessarily provide the best comparison colour.** *Top:* SEDs (offset for clarity and using a linear scale) for a selection of representative galaxies at $z = 0.28$ in relation to the Sloan filter set (solid lines) and the Sloan filter set in the restframe of the galaxies (dashed lines). There is very little spread in the $(i - z)$ colour at $z = 0.28$ because typical template SEDs are essentially parallel in the relevant region and the H_α line lies between the observed i and z filters. *Bottom left:* as a result $(i - z)$ is not a good comparison colour for determining absolute r magnitudes at $z = 0.28$ giving RMS error 0.036 and a very convex curve. *Bottom right:* $(r - z)$ is a much better comparison colour at $z = 0.28$ giving a greater range of input colour, RMS error 0.015, and much smaller curvature.

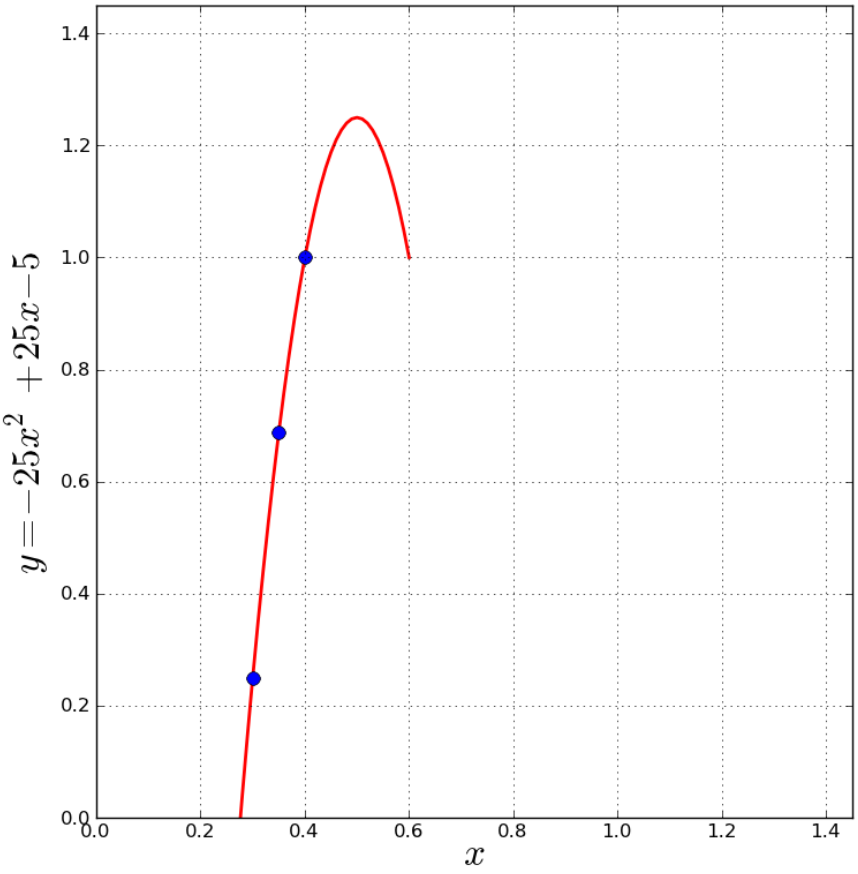

Fig. 25.—: **Showing how a small range of observed colours can result in a highly convex second order polynomial fit.** The unique quadratic function passing through (0.3 , 0.25), (0.35 , 0.6875) and (0.4 , 1.0) is $y = -25x^2 + 25x - 5$. Because a is large (and negative) a highly convex curve results, similar to that for $z = 0.1$ in Figure 13.

2.6.1. Outliers

2.6.2. Starburst and compact blue galaxies

Starburst and compact blue galaxies (Figure 27) show very rapidly increasing flux per unit wavelength as the wavelength decreases from ∼10 000 Å through the optical and ultraviolet and up to ∼1000 Å. They also display very prominent emission lines, including especially H_α (6548 Å), O[III] (5007 Å), H_β (4861 Å) and O[II] (3727 Å).

Figure 28a shows how at redshifts ∼ 0.3 and above the large ultraviolet flux from starburst and blue compact galaxies gets redshifted into the observed g-band. Additionally, prominent emission lines move into and out of different observed filters as the redshift increases. These two effect jointly produce significant offsets from the models shown in Figures 11 to 17 at various redshifts. The process is complex and for any given model can only be properly understood by detailed analysis of the relative strengths of the emission lines and the continuum spectrum in relation to the filters.

2.6.3. IC2810

It is likely that this galaxy suffers from a sky background subtraction problem in the optical spectrum, and (as of November 2013) it has been dropped from the final (Brown et al. 2013) sample.

IC2810 (Figures 29, 30) was originally one of the template galaxy SEDs used in Brown et al. (2013). However, it is likely that this galaxy suffers from a sky background subtraction problem in the optical spectrum, and (as of November 2013) it has been dropped from the final Brown et al. (2013) samples. We found that IC2810 had a substantial offset of ∼+0.2 from the very tight sequence in a plot of at $([M_u + D_{\rm M}] - g)$ against $(u - g)$ at $z = 0.2$ (as in Figure 11). Examination of the SED (Figure 30) showed that it had a very prominent Balmer jump at 3650 Å with an unusually flat SED on either side. (The two very prominent dips near the Balmer break are due to noise.) As z increases from $z \sim 0.1$ to $z \sim 0.35$ the Balmer break moves through the observed g-band, and the step-like shape of the SED means that the observed g magnitude increases less than for representative galaxies. This causes the observed $(u - g)$ value to decrease relative to typical galaxies. At the same time the value of $([M_u + D_{\rm M}] - g)$ on the y-axis also decreases, but less rapidly than $(u - g)$. The net result is to cause the point representing IC2810 to move to the left and up somewhat relative to the majority of templates.

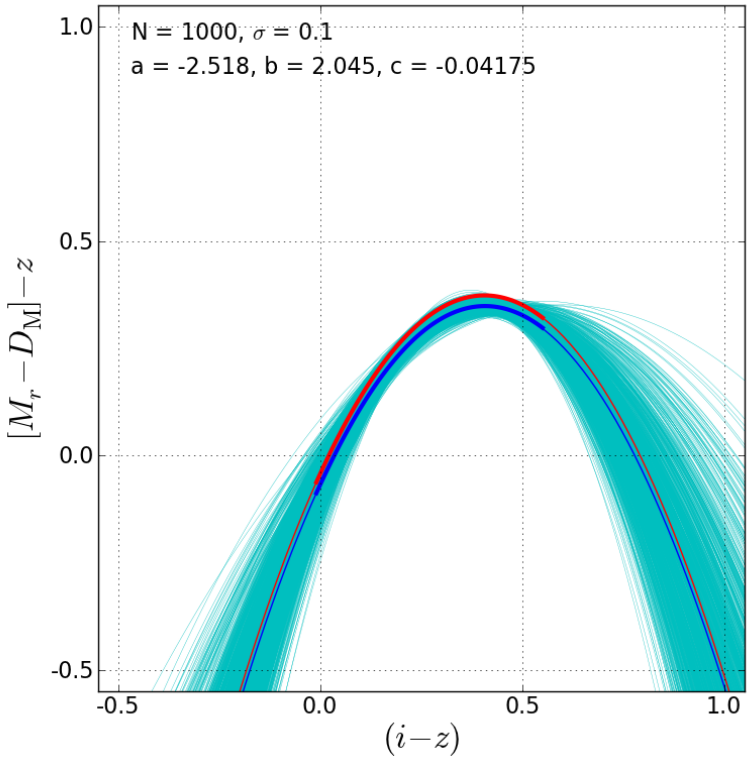

Fig. 26.—: **Showing how random observational errors can produce systematic errors in non-linear models.** The red curve shows the function $y = ax^2 + bx + c$ plotted using 101 equally spaced x-values covering the range shown in bold. a, b and c have the values in the model in Figure 13 at $z = 0.1$. 1000 random simulations have been carried out in which each of the 101 x-values has had a gaussian ($\sigma = 0.1$) perturbation added to it before calculating y. The pale blue (cyan) curves are the best fits to these 1000 perturbed sets of data points. The thick blue line shows the mean of these 1000 best fits. The thin blue line is the original function shifted in the y-direction by $\Delta y = a\sigma^2 = 0.025$. The thick blue line is exactly coincident with the thin blue line, confirming that the systematic error resulting from a random error of $\sigma = 0.1$ is $a\sigma^2$ as derived theoretically in the text (§2.5).

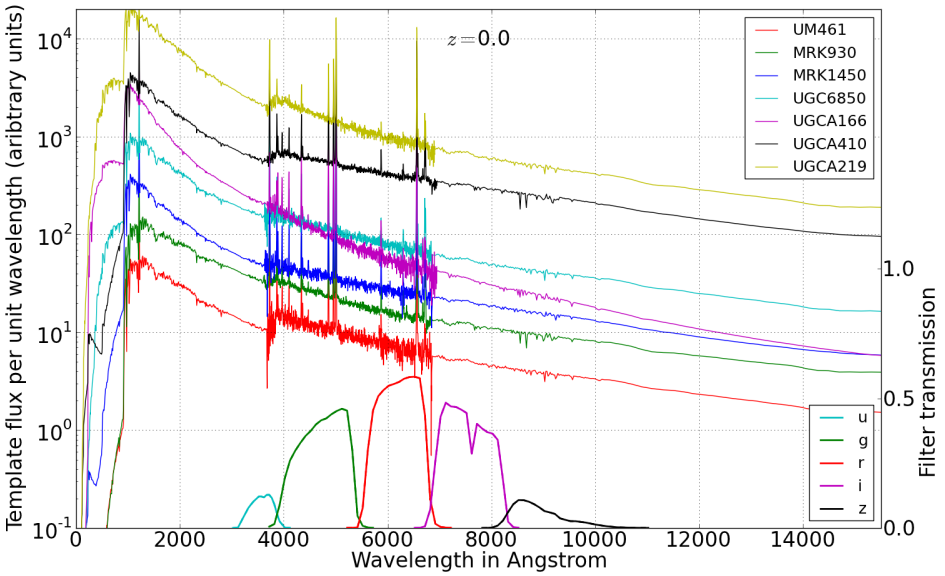

(a)

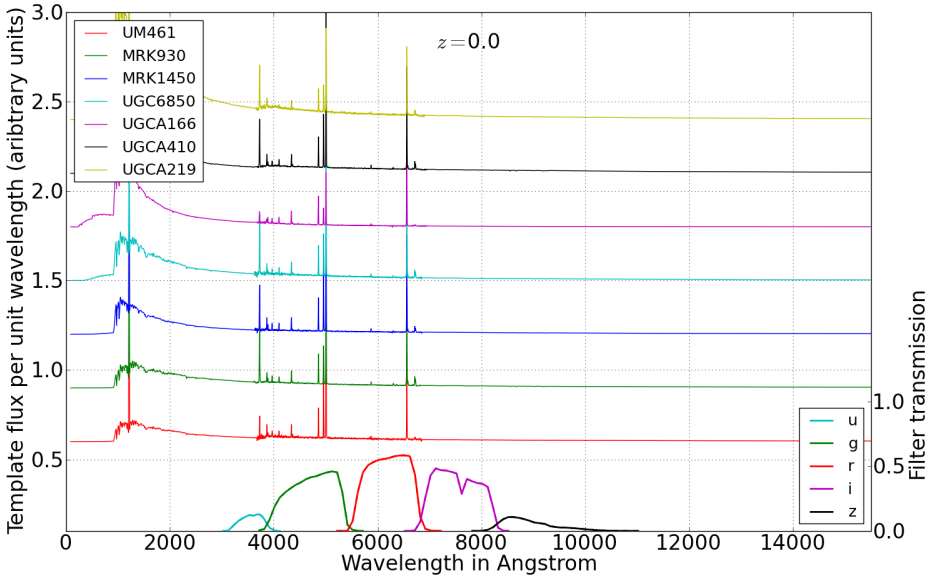

(b)

Fig. 27.—: **The SEDs of starburst and compact blue galaxies in relation to the Sloan filter set.** *Top:* using a logarithmic scale to show spectral features in the optical and near infrared more clearly; *bottom:* using a linear scale to give a better idea of the large relative contributions of the emission lines and the ultraviolet emission. (The SEDs are offset artificially for clarity.)

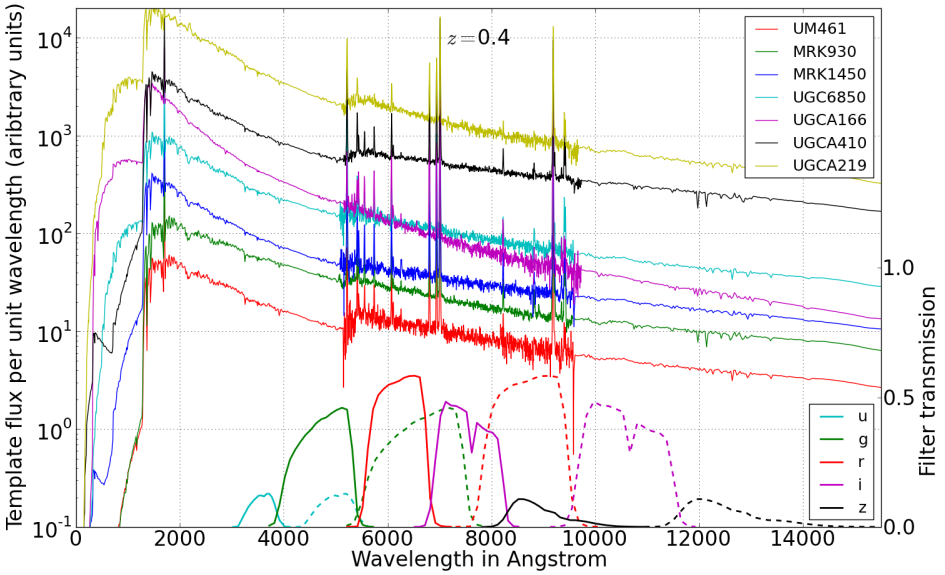

(a)

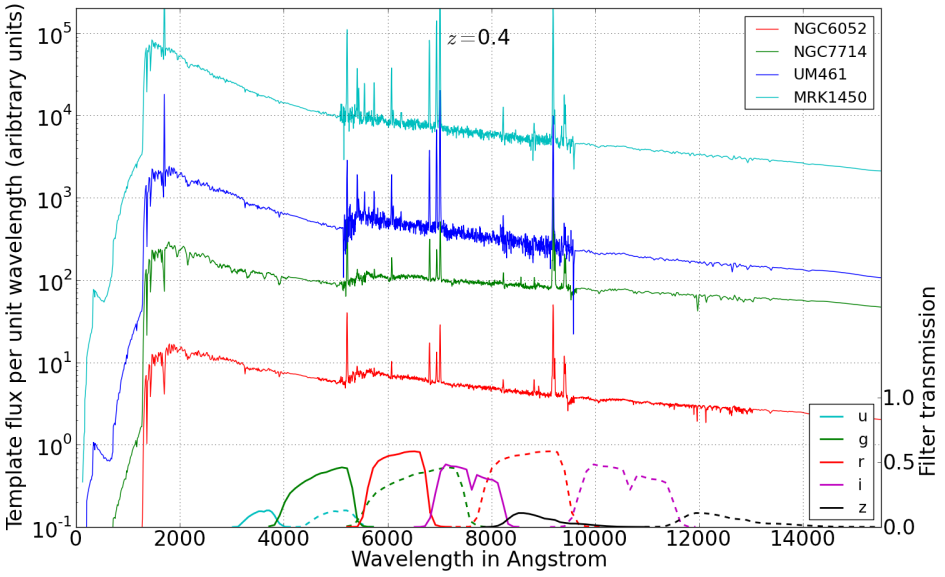

(b)

Fig. 28.—: **Showing why compact blue galaxies show offsets of up to ~ 0.3 mag from the models at certain redshifts.** *Top:* SEDs for starburst and compact blue galaxy templates at $z \sim 0.4$ in relation to the Sloan filter set (solid lines) and the Sloan filter set in the restframes of the galaxies (dashed lines). *Bottom:* comparing the SEDs for starburst galaxy MRK1450 and compact blue galaxy UM461 with two star-forming galaxies without noticeable offsets, NGC6052 and NGC7714. (SEDs are offset artificially for clarity in both figures.)

2.6.4. The significance of outliers

For any given input colour outliers only become significant at certain redshifts. The majority of them result from faint compact blue galaxies. To assess whether our method results in significant errors for the galaxy types producing outliers we need determine whether such galaxies would in fact be visible at the redshifts in question, i.e. whether their apparent magnitudes are brighter than the limiting magnitude in any particular galaxy survey. Table 9 lists the galaxies producing outliers offset by more than ∼0.2 from the model fit in Figures 11 to 17 as well as the input colours and redshifts at which the outliers might be significant. In the case of model fits used to determine M_g and M_r redshift ranges for which a given input colour is not used are omitted. The apparent magnitudes in the table were derived from measured absolute magnitudes using the formula $g = M_g - D_{\rm M} - K_{gg}$ where the K-corrections were computed from the relevant template SEDs.

It can be seen that no outliers would be visible in a survey with limiting magnitude $g = 21.5$ or fainter. In a survey with limiting magnitude $g = 23.0$ only the following outlier galaxies would be visible: compact blue galaxies similar to UGCA410 at $z \sim 0.1$ ($g \sim 22.2$) and similar to UGCA219 at $z \sim 0.3$ ($g \sim 22.6$) and starburst galaxies similar to MRK1450 at $z \sim 0.1$ ($g \sim 21.7$) and similar to MRK930 at $z \sim 0.4$ ($g \sim 21.7$), and spiral galaxies with SEDs similar to NGC0660 at $z \sim 0.4 - 0.5$ ($g \sim 21.7 - 21.9$). NGC0660 is a very untypical galaxy which must have recently undergone a violent collision as indicated by its prominent tidal tails and two intersecting dust lanes (Figure 31. Galaxies with similar SEDs (and therefore inaccurate K_{zz} corrections) at $z \sim 0.4 - 0.5$ are expected to comprise a negligible fraction of any galaxy sample.

No outliers lying more than 0.2 mag from the best fit template model are included in the fitting process. Therefore outliers do not influence the calculation of K-corrections for the remaining template galaxies. We conclude therefore that outliers do not significantly affect our calculation of K-corrections except in the case of deep surveys (limiting magnitude $g > 21.5$) where some compact blue, starburst galaxies will be assigned absolute magnitudes that are 0.2 to 0.3 mag too bright.

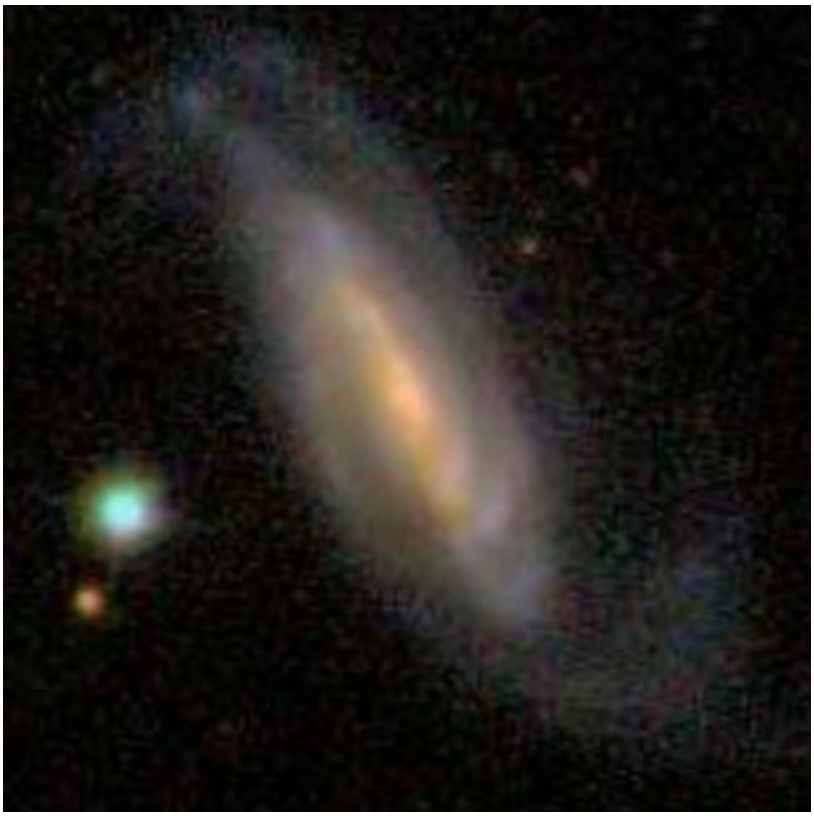

Fig. 29.—: **The luminous red template galaxy IC2810.** This was found to be offset from the model in Figure 11 by ∼0.2 mag and was dropped from the list of template SEDs in Brown et al. (2013). Figure 30 gives an explanation.

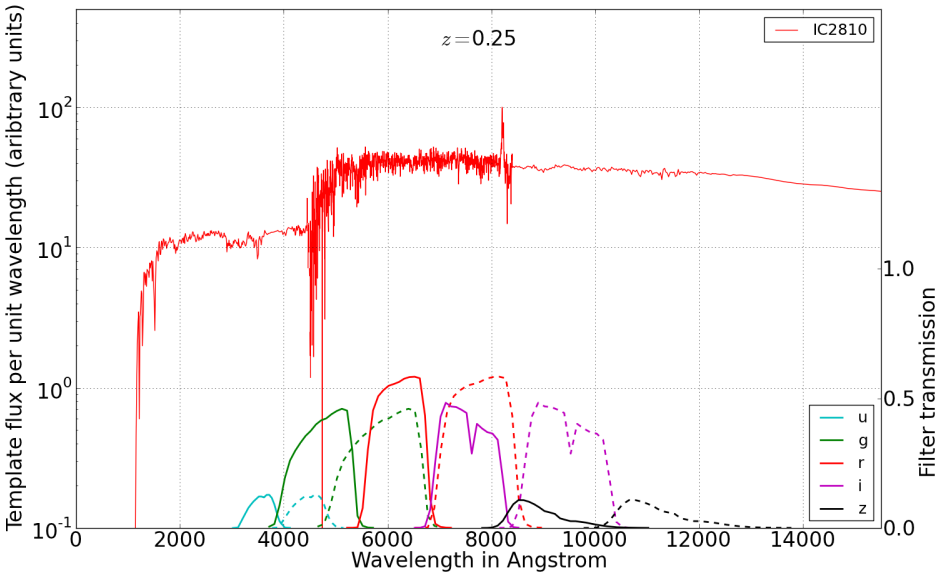

(a)

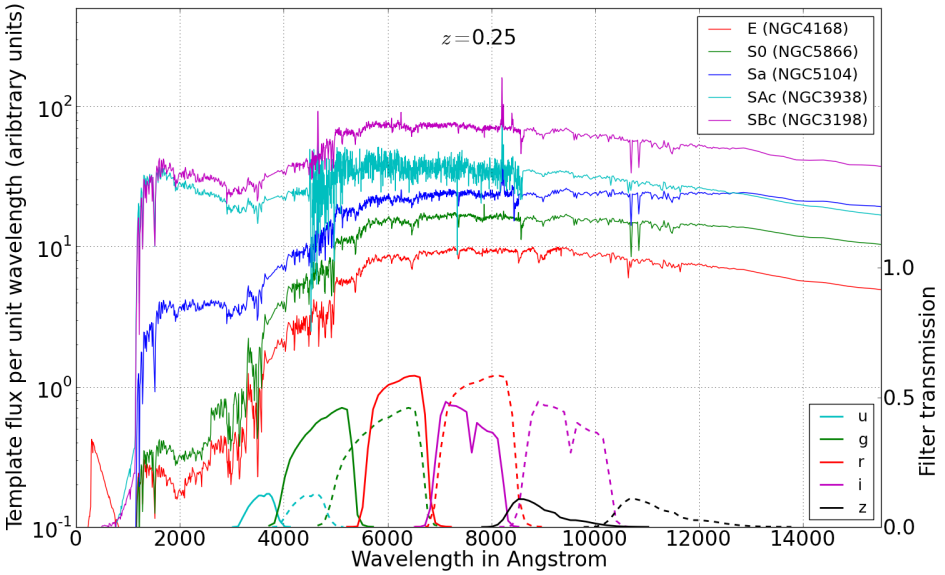

(b)

Fig. 30.—: **Showing why the template IC2810 is displaced from the model at $z \sim 0.25$ as shown in Figure 11.** *Top:* the SED of IC2810 at $z \sim 0.25$ in relation to the Sloan filter set (solid lines) and the Sloan filter set in the restframe of the galaxy (dashed lines); *bottom:* similar but showing a selection of representative galaxies (offset artificially for clarity).

Table 9. Significant outliers

Name	type	approx redshift	abs mag required	input colour	approx offset	reference abs mag M_g	distance modulus	K_{gg}	reference app mag g
UGCA410	compact blue dwarf	0.1	M_g	$(g-r)$	-0.2	-15.82	38.26	0.24	22.2
		0.4	M_g	$(r-i)$	-0.2	-15.82	41.65	0.42	25.41
MRK475	compact blue dwarf	0.1	M_g	$(g-r)$	-0.3	-14.43	38.26	0.34	23.49
		0.4	M_g	$(r-i)$	-0.3	-14.43	41.65	0.35	26.87
UM461	compact blue dwarf	0.1	M_g	$(g-r)$	-0.3	-14.93	38.26	0.37	22.96
		0.4	M_g	$(r-i)$	-0.2	-14.93	41.65	0.77	25.95
		0.4	M_i	$(r-z)$	-0.25	-14.93	41.65	0.77	25.95
MRK1450	compact starburst	0.1	M_g	$(g-r)$	-0.3	-16.17	38.26	0.36	21.73
		0.4	M_g	$(r-i)$	-0.3	-16.17	41.65	0.43	25.05
MRK930	starburst	0.4	M_g	$(r-i)$	-0.2	-19.8	41.65	0.16	21.69
UGC6850	pec - compact blue?	0.4	M_g	$(r-i)$	-0.2	-16.46	41.65	0.12	25.07
UGCA166	compact blue	0.3	M_i	$(r-z)$	0.5	-15.13	40.92	-0.18	25.97
		0.4	M_i	$(r-z)$	0.3	-15.13	41.65	-0.26	26.78
		0.3	M_z	$(r-z)$	0.7	-15.13	40.92	-0.18	25.97
		0.4	M_z	$(r-z)$	0.3	-15.13	41.65	-0.26	26.78
UGCA219	Scp - compact blue?	0.3	M_i	$(r-z)$	-0.25	-18.32	40.92	-0.02	22.62
		0.3	M_z	$(r-z)$	-0.25	-18.32	40.92	-0.02	22.62
		0.4	M_z	$(r-z)$	-0.3	-18.32	41.65	-0.01	23.34
		0.5	M_z	$(r-z)$	-0.2	-18.32	42.24	-0.04	23.96
NGC0660	SB(s)a with AGN	0.4	M_z	$(r-z)$	-0.25	-18.59	41.65	1.45	21.61
		0.5	M_z	$(r-z)$	-0.25	-18.59	42.24	1.77	21.88

2.7. Comparison with *kcorrect*

We compared our absolute magnitudes with those in the New York Value-Added Galaxy Catalogue (VAGC, Blanton et al. 2005b) which were calculated using *kcorrect* version 4_2 (Blanton & Roweis 2007). The VAGC uses AB magnitudes and the observed apparent u, g, r, i and z magnitudes listed are based on SDSS magnitudes corrected to account for the small offsets between the "SDSS natural system" and the AB system. As the exact corrections applied are unpublished (Daniel Eisenstein, private communication), we calculated these corrections using the prescription $M - (m - A) + K + D_{\rm M}$, where $D_{\rm M}$ is the distance modulus, and the absolute magnitudes M, the apparent magnitudes m, the extinctions A and the K-corrections are all as given in the VAGC. In this way we ensured that our extinction corrected, SDSS to AB corrected, apparent magnitudes were identical to those used in the VAGC. The SDSS to AB corrections that resulted were -0.036, 0.012, 0.010, 0.028, 0.040 respectively for the u, g, r, i and z-wavebands. We note that these values differ from those given on the SDSS website for data releases 7 and 8 which are -0.04, ∼0.00, ∼0.00, ∼0.00, 0.02.

We show our comparisons in Figures 32 to 36. In all wavebands except u the systematic offset is no more than ∼0.02 out to $z = 0.4$ but the spread in the differences between the two sets of values increases with redshift. In the u-band the *kcorrect* magnitudes are systematically ~ 0.08 fainter than ours out to $z \sim 0.2$.

Banding of spacing ∼0.007 and magnitude ∼0.3 mag can be seen in all these plots. This is an artefact of *kcorrect* as the spacing does not correspond to the redshift intervals used in our code. This banding will produce scatter in the magnitudes and colours produced by *kcorrect*.

As a further comparison we show colour magnitude plots of $(M_u - M_g)$ against M_g for our absolute magnitudes and those from *kcorrect* at redshifts of 0.05, 0.1 and 0.2 in Figure 37. The red sequence, blue cloud and green valley are significantly better defined using our results, particularly at higher redshift as can be seen from the histograms in the right hand panels.

In addition the *kcorrect* results for $z = 0.2$ show a substantial population of galaxies redder than $(M_u - M_g) = 2$. We do not see any such galaxies in the low redshift Universe and they are not present in our results. There are 1402 objects in the VAGC with redshifts between 0.18 and 0.22 that have extremely red *kcorrect* colours $(M_u - M_g) > 2.0$, but normal red sequence colours $(M_u - M_g) < 1.7$ as determined by our method. We eyeballed images and spectra for these objects using the SDSS ImageList tool and found that they are predominantly faint objects whose apparent u-band magnitudes within ∼1 mag of the Sloan 95%

u-band limit of 22.0. Their u-band uncertainties are typically $\sim$20 times larger than those for the other four filters. We found that the spectra of these objects were typical of normal elliptical galaxies (and not star-forming dust-obscured galaxies), exhibiting prominent absorption lines, especially Ca, K, Mg, and (usually) H_α, with relatively insignificant emission lines, and a steady decrease in spectral energy density down to $\sim$0.4 μm. The difference between our $(M_u - M_g)$ colours and those from textitkcorrect is largely due to the difference between the computed M_u values; the $M - g$ values differ very little.

We illustrate these points with the example galaxies shown in Figure 38. The galaxy in the top panels has redshift 0.208, and its *ugriz* (modelmag) magnitudes are 21.13, 18.96, 17.61, 17.10 and 16.76 with uncertainties 0.15, 0.01, 0.01, 0.01 and 0.0. Its spectrum is typical of a normal elliptical galaxy. Our values for M_u and M_g are -19.561 and -21.257 mag while those from *kcorrect* are -19.271 and -21.282 mag. The *kcorrect* M_u values are fainter by 0.290 mag while the M_g values are brighter by the much smaller difference of 0.025 mag.

The galaxy in the lower panels has redshift 0.215 and *ugriz* (modelmag) magnitudes of 21.18, 18.84, 17.69, 17.22 and16.83 with uncertainties 0.20, 0.01, 0.01, 0.01 and 0.02. Again the spectrum is typical of a normal elliptical galaxy. Our values for M_u and M_g are -19.684 and -21.228 mag while those from *kcorrect* are -19.215 and -21.259 mag. The *kcorrect* M_u values are fainter than ours by 0.469 mag while their M_g values are brighter by the much smaller difference of 0.031 mag.

We conclude that *kcorrect* does not produce accurate absolute u-band magnitudes for objects with faint (> 21.0) apparent u-band magnitudes. This is to be expected given that it uses a basis set of five templates and one therefore needs good photometry in at least five wavebands to constrain the components of these templates. When the u-band photometry is poor this will not be the case and it is likely that errors will occur due to fitting to what is effectively noise.

We take both of these points as evidence that our method is producing K-corrections and absolute magnitudes which are at least as good as *kcorrect* and sometimes better, especially at redshifts of $\sim$0.2 and above.

Fig. 31.—: **The outlier galaxy NGC0660** This galaxy is an outlier when determining z-band absolute magnitudes using $(r - z)$ input colour (Figure 17). The prominent tidal tails and two intersecting dust lanes show that it must have recently undergone a violent collision.

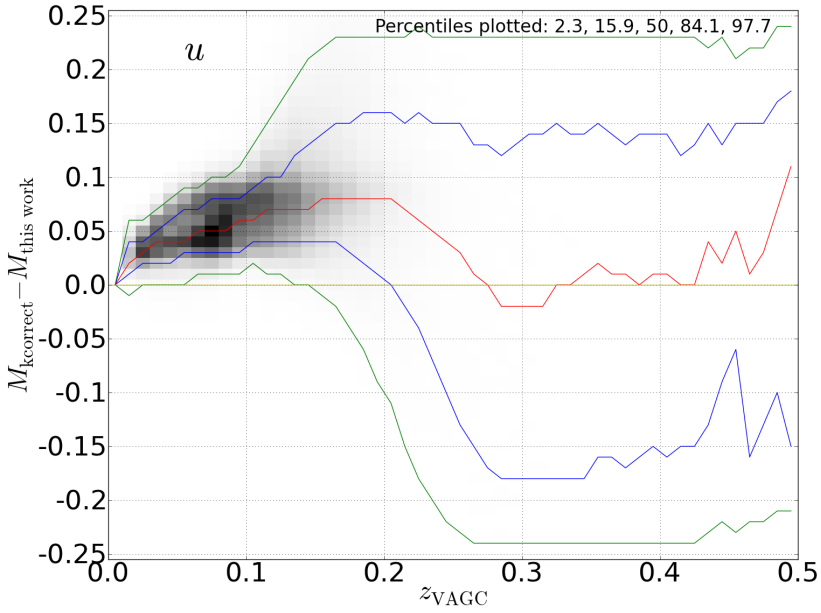

(a)

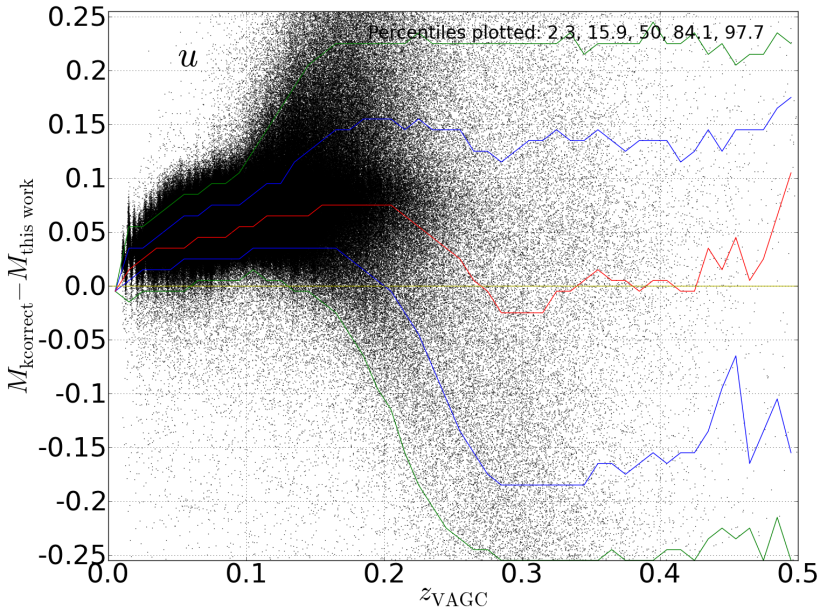

(b)

Fig. 32.—: **Comparing our u-band absolute magnitudes with those from *kcorrect*.** *Top:* binned plot; *bottom:* scatter plot to show outliers. In the u-band the *kcorrect* magnitudes are systematically ~ 0.08 brighter than ours out to $z \sim 0.2$.

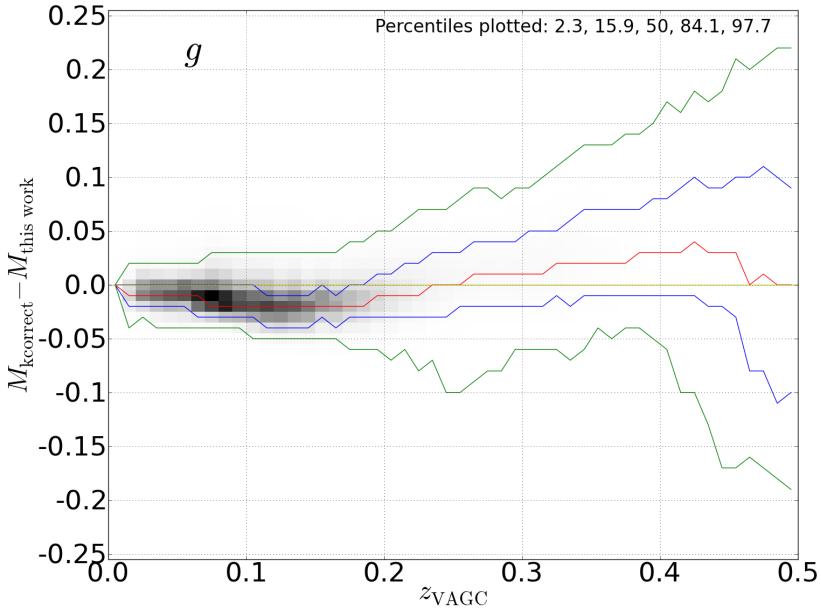

(a)

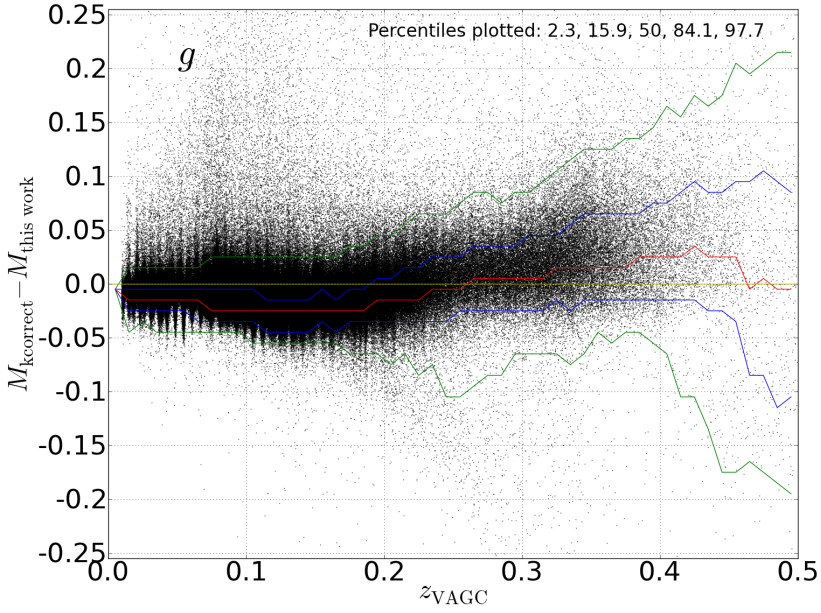

(b)

Fig. 33.—: **Comparing our g-band absolute magnitudes with those from *kcorrect*.** *Top:* binned plot; *bottom:* scatter plot to show outliers.

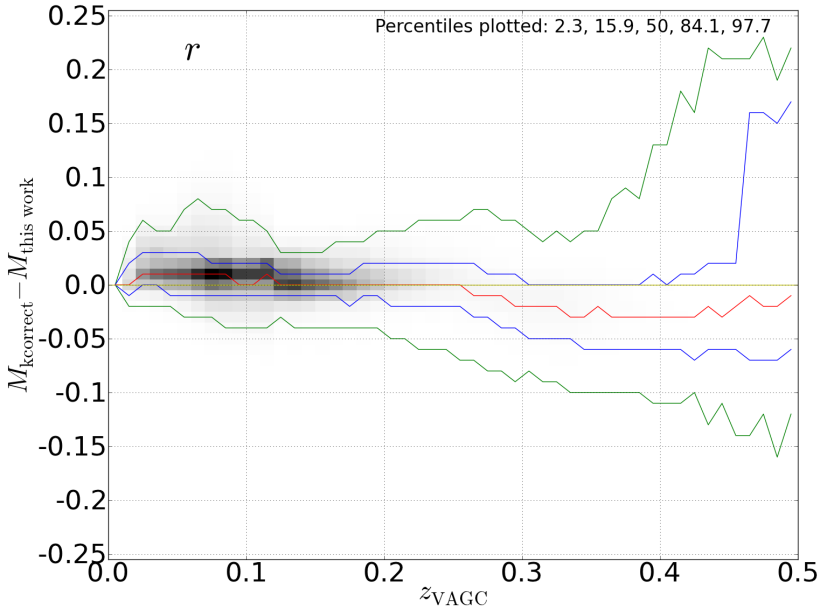

(a)

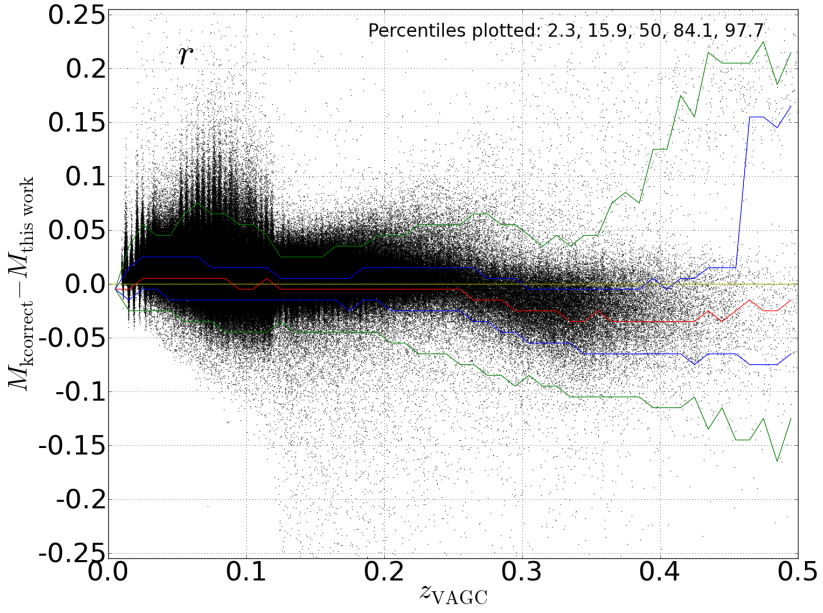

(b)

Fig. 34.—: **Comparing our r-band absolute magnitudes with those from *kcorrect*.** *Top:* binned plot; *bottom:* scatter plot to show outliers.

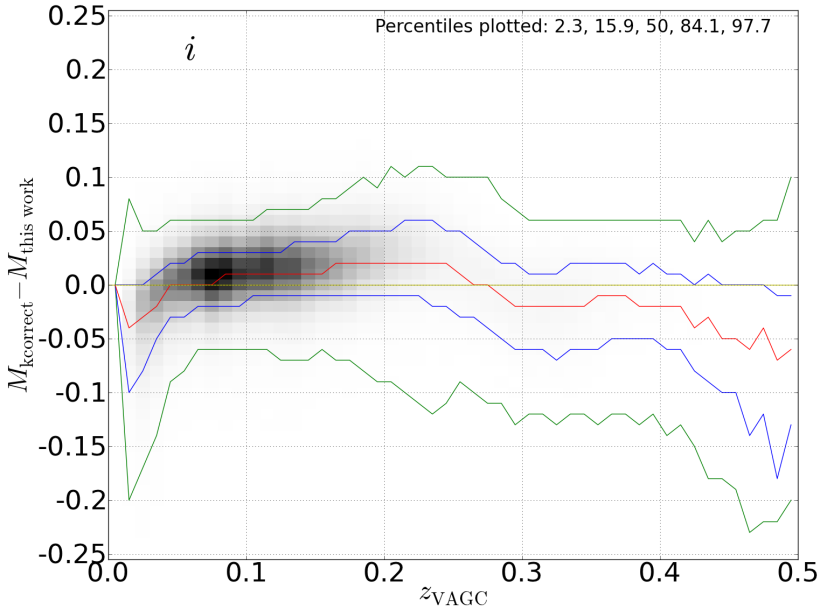

(a)

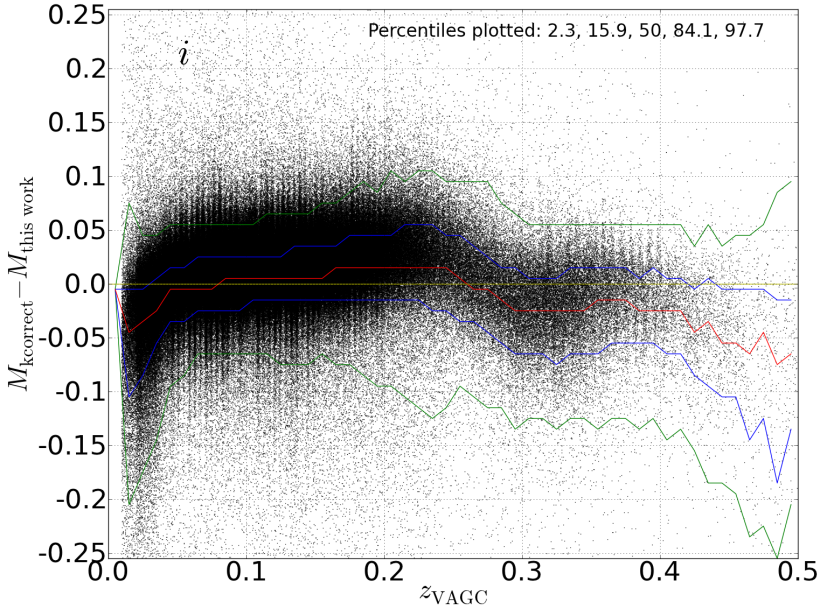

(b)

Fig. 35.—: **Comparing our i-band absolute magnitudes with those from *kcorrect*.** *Top:* binned plot; *bottom:* scatter plot to show outliers.

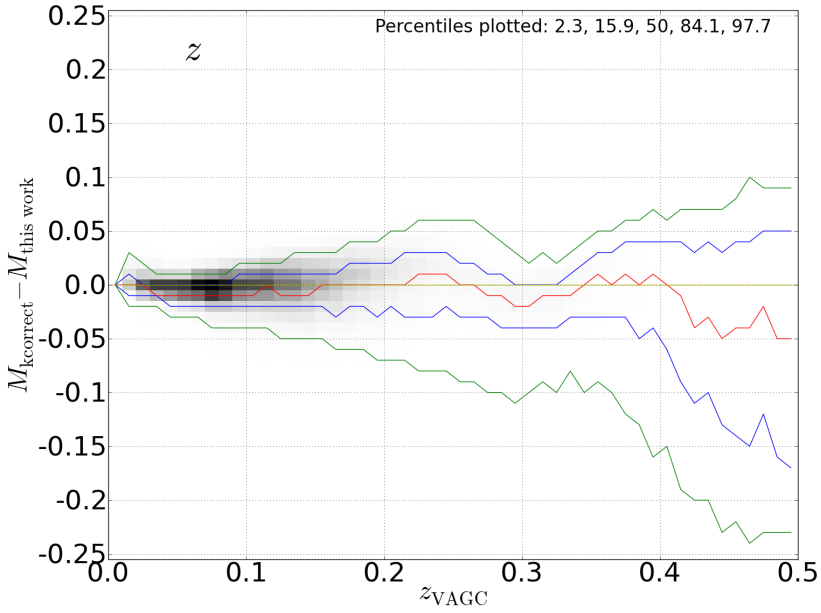

(a)

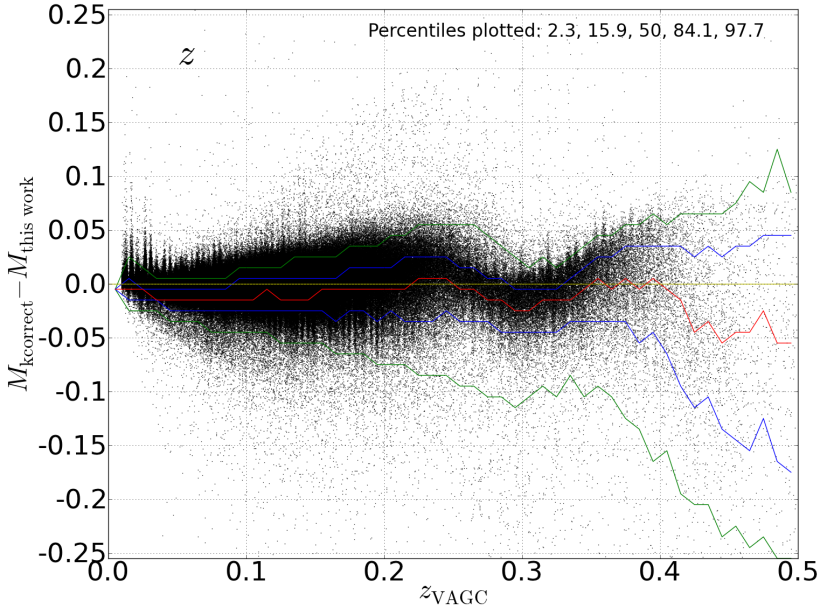

(b)

Fig. 36.—: **Comparing our z-band absolute magnitudes with those from *kcorrect*.** *Top:* binned plot; *bottom:* scatter plot to show outliers.

We illustrate these points with the example galaxies shown in Figure 38. The galaxy in the top panels has redshift 0.215 and *ugriz* (modelmag) magnitudes of 21.18, 18.84, 17.69, 17.22 and16.83 with uncertainties 0.20, 0.01, 0.01, 0.01 and 0.02. The spectrum is typical of a normal elliptical galaxy. Our values for M_u and M_g are -19.684 and -21.228 mag while those from *kcorrect* are -19.215 and -21.259 mag. The *kcorrect* M_u values are fainter by 0.469 mag while the M_g values are brighter by the much smaller difference of 0.032 mag.

The galaxy in the lower panels has redshift 0.208 and *ugriz* (modelmag) magnitudes of 21.13, 18.96, 17.81, 17.10 and16.76 with uncertainties 0.15, 0.01, 0.01, 0.01 and 0.01. Again the spectrum is typical of a normal elliptical galaxy. Our values for M_u and M_g are -19.561 and -21.228 mag while those from *kcorrect* are -19.271 and -21.282 mag. The *kcorrect* M_u values are fainter by 0.290 mag while the M_g values are brighter by the much smaller difference of 0.025 mag.

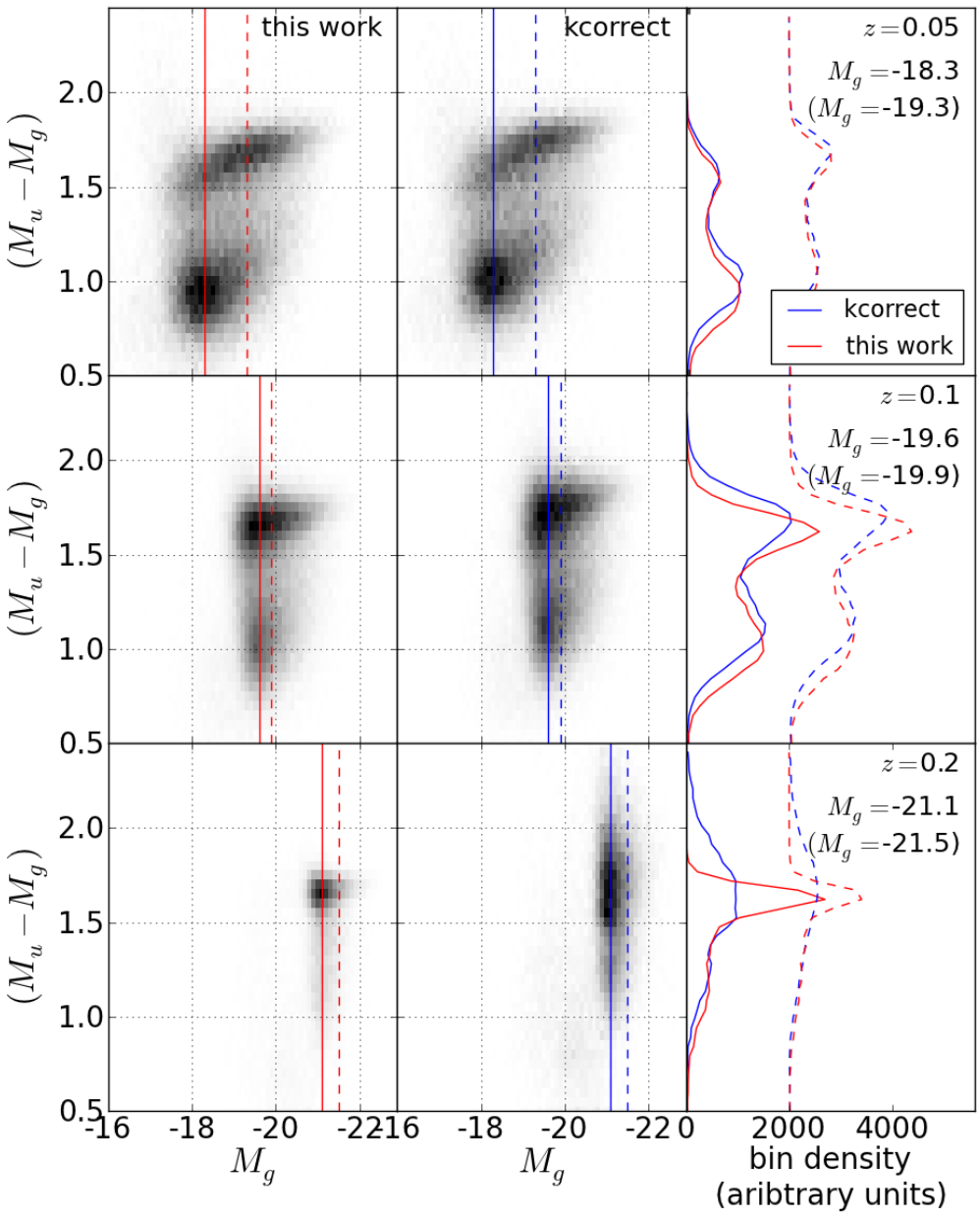

Fig. 37.—: **Comparing our $(M_u - M_g)$ versus M_g colour magnitude plots with those from *kcorrect*.** The histograms on the right show bin densities along the slices indicated in the plots on the left. Our results show a significantly more well defined red sequence, blue cloud and green valley. Unlike the *kcorrect* results we do not see a substantial population of galaxies redder than $(M_u - M_g) = 2$ at $z = 0.2$ which is not present in the low redshift Universe. We take both of these points to indicate that our K-corrections are at least as good as those from *kcorrect*, and probably better, particularly at redshifts ∼0.2 and above.

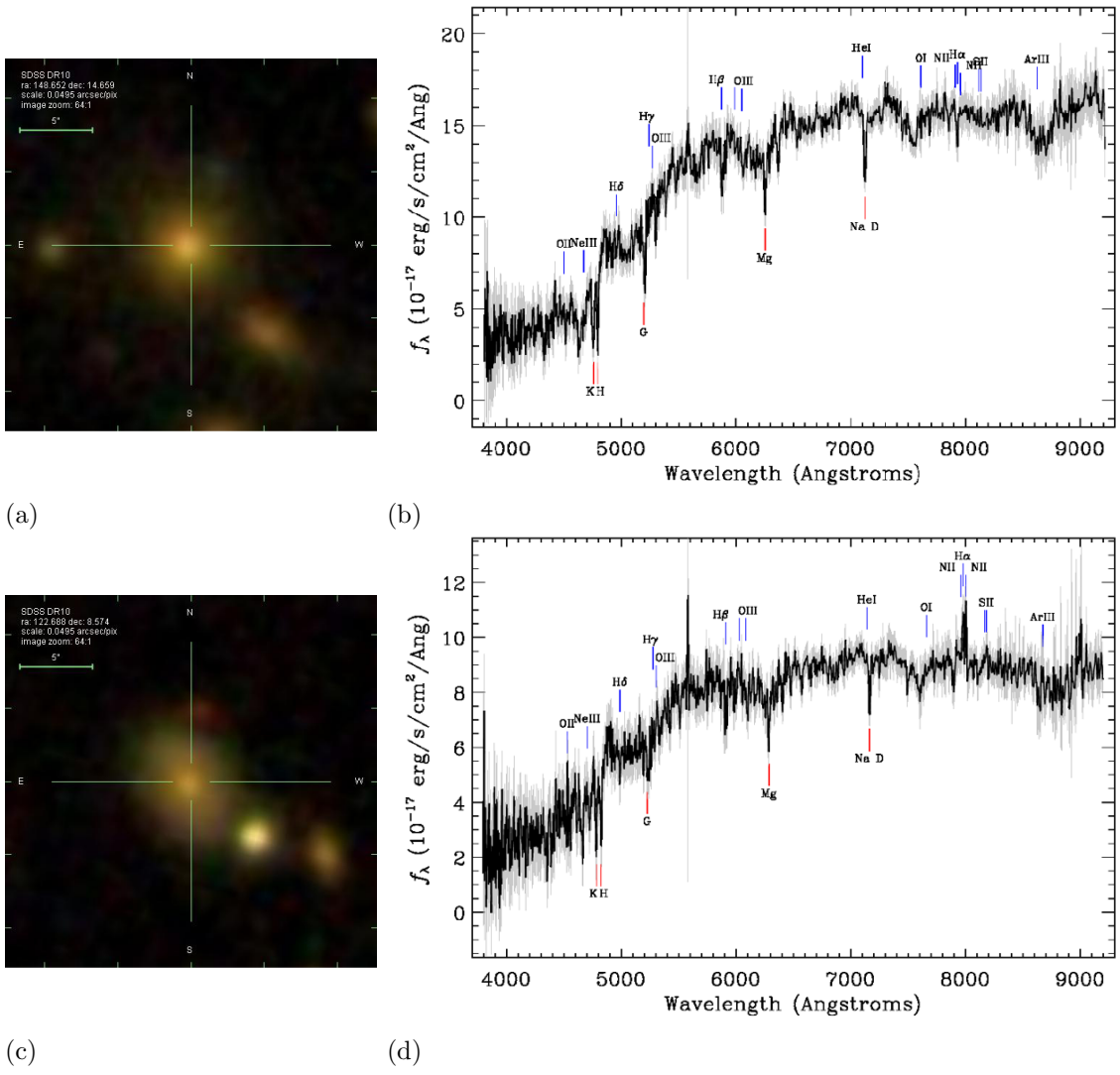

Fig. 38.—: **Two galaxies with anomalously red** $(M_u - M_g)$ **colour as computed by *kcorrect*.** *Left panels: gri* colour images from SDSS; *right panels:* spectra from SDSS. At $z \sim 0.2$ *kcorrect* produces anomalously red $(M_u - M_g)$ colours for faint galaxies with u-band apparent magnitudes within ∼1 mag of the Sloan 95% u-band limit of 22.0 whereas our K-correction method does not. The spectra of these objects with anomalously red *kcorrect* colours are typical of normal elliptical galaxies. The galaxy shown in the upper panels is at (RA = 148.6517508 deg, Dec = 14.65899089 deg) and redshift 0.208, and its *ugriz* (modelmag) magnitudes are 21.13, 18.96, 17.61, 17.10 and 16.76 with uncertainties 0.15, 0.01, 0.01, 0.01 and 0.01. The galaxy shown in the lower panels is at (RA = 122.68805, Dec = 8.574092106 deg) and redshift 0.215, and its *ugriz* (modelmag) magnitudes are 21.18, 18.84, 17.69, 17.22 and16.83 with uncertainties 0.20, 0.01, 0.01, 0.01 and 0.02.

2.8. Summary

We have developed an improved method for calculating the K-corrections that enable absolute magnitudes M_W in a waveband W to be determined from observed magnitudes m_Z in another waveband Z. K-corrections are defined by $K_{WZ} = (M_W + D_M) - m_Z$ (where D_M is the distance modulus). Our method is both simpler than most other methods and in many cases more accurate. We demonstrated that it is possible to calculate K-corrections using a simple quadratic function $K_{WZ} = ax^2 + bx + c$ of a suitably chosen observed colour $x = (m_Y - m_Z)$, provided the two wavebands Y and Z employed to measure the colour have been correctly chosen. The coefficients a, b, c are determined at any redshift by fitting quadratic functions to plots of $K_{WZ} = (M_W + D_M) - m_Z$ against $(m_Y - m_Z)$ for the $\sim$125 template galaxy SEDs from Brown et al. (2013). These SEDs form the most extensive and accurate set of galaxy templates yet available and enable us to measure K-corrections with high accuracy, because for suitable chosen colours the plots form a remarkably tight sequence.

We list the appropriate observed colours to use in determining absolute magntiudes in different redshift ranges between $z = 0$ and $z = 0.5$ for all five SDSS filters ($ugriz$), and we make publicly available the corresponding tables of the polynomial coefficients a, b and c. We also tabulate the root mean square deviations for our model fits and investigate outliers, notably starburst and compact blue galaxies and dusty edge-on spirals.

We demonstrate that choosing the closest pair of filters to the redshifted restframe waveband W does not always produce the most accurate results, as has been suggested by several previous authors. We give examples to demonstrate this and provide criteria for appropriate choices of observed SDSS colour for determining any SDSS absolute magnitude at any given redshift $0 < z < 0.5$. The key requirements are a large range in observed colour $x = (m_Y - m_Z)$, s small range in $y = (M_W + D_M) - m_Z$, a quadratic fit without large (positive or negative) parameter a (i.e. small radius of curvature), and a small scatter in template values about the fitted model.

We compare our K-corrections with those from *kcorrect* using the sample of SDSS galaxies in the New York Value-Added Galaxy Catalogue and find that our method provides clearer separation between red and blue galaxies and a much tighter red sequence. Furthermore it does not generate the spurious cloud of extremely red galaxies at $z \sim 0.2$ which is produced by *kcorrect* but not seen in the low redshift Universe.

3. EVOLUTION OF THE OPTICAL LUMINOSITY FUNCTION

3.1. Introduction

As discussed in §1.6, a key tool for analysing galaxy growth and evolution is the luminosity function: the number per unit comoving volume of galaxies per unit absolute magnitude (or luminosity) in a given waveband. Measurements of luminosity function evolution provide a key constraint on theoretical models of galaxy growth and evolution, particularly if the evolution of star-forming and quiescent galaxies can be studied separately. To differentiate star-forming from quiescent galaxies authors have used a variety of techniques including separation by colour ("red" or "blue"), morphology (e.g. concentration index, Bell et al. 2003), and measurement of star-formation rate by fitting SPS models (e.g. Moustakas et al. 2013).

Measurements of luminosity functions have become increasingly accurate as survey data has become available covering larger areas and/or greater optical depths. Recent studies of optical luminosity function evolution include Madgwick et al. (2002), Bell et al. (2004), Blanton et al. (2005a), Ilbert et al. (2006b), Willmer et al. (2006), Faber et al. (2007), Brown et al. (2007), Cool et al. (2012) and Loveday et al. (2012). For an overview of studies published prior to 2007 we refer the reader to Faber et al. (2007).

Most of these studies use spectroscopic redshifts, but a few use photometric redshifts (as we do) (e.g. COMBO-17, Bell et al. 2004; Faber et al. 2007; Wolf et al. 2003). Photometric redshifts are based on empirically determined relations between galaxy colours in several pairs of wavebands and galaxy redshift. These relations can be determined by redshifting the SEDs of real galaxies used as templates and calculating their colours. Alternatively they can be determined from stellar population synthesis (SPS) models. Spectroscopic redshifts have the advantage that they are accurate because they depend on measuring how much certain easily identified spectral lines are redshifted. However, the throughput of spectrgraphs is low compared to that of imaging cameras and the number of pixels devoted to a single spectrum is far greater than that for a typical galaxy image. For this reason spectra have only been obtained for a fraction of galaxies and this fraction becomes smaller and smaller the higher the redshift, until beyond $z \sim 0.8$ it becomes very small indeed. Although photometric redshifts have greater uncertainties, their great advantage is that they can be derived for any galaxy which has photometry in several wavebands. This means much larger sample sizes and correspondingly smaller uncertainties due to random Poisson error and cosmic variance. This is particularly valuable at higher redshifts, i.e. $z \sim 1$ and beyond.

Surveys deep enough to enable spectroscopic redshifts to be determined at high redshift (i.e. $z > 1$), (e.g. DEEP2 Willmer et al. 2006) require a very large ($\sim$10 metre class)

telescope in order to obtain a spectrum from a very faint object. Among these surveys is the Deep Evolutionary Exploratory Probe 2 (DEEP2, Davis et al. 2003; Willmer et al. 2006) which gathered high quality spectra of 60 000 galaxies with $z > 0.75$ in order to study the properties and large-scale clustering of galaxies at $z \sim 1$. It used the DEep Imaging Multi-Object Spectrograph (DEIMOS, Faber et al. 2003) on the 10-m Keck II Telescope on Mauna Kea, with spectroscopic targets being selected using B, R and I-band images from the 3.6 metre Canada Hawaii France Telescope (CFHT) also on Mauna Kea. The multiplexing power and high efficiency of DEIMOS enabled it to target 1000 faint galaxies per clear night.

Another deep spectroscopic survey is the VIMOS VLT Deep Survey (VVDS Le Fèvre et al. 2005) which spectrally imaged 11 564 objects at redshifts $0 < z < 5$ selected by apparent magnitudes $17.5 \leq I_{\rm AB} \leq 24$ from an area of 0.61 deg^2. The aim of VVDS was to trace back the evolution of galaxies, active galactic nuclei and clusters to epochs where the Universe was about 20 per cent of its current age. It used the Visible Imaging Multiobject Spectrograph (VIMOS Le Fèvre et al. 2003) which is able to carry out $UBVRIz$ imaging and ∼600 target multiobject spectroscopy, as well as having a 6400 fibre integral field spectroscopy mode.

Another deep spectroscopic survey that made use of VIMOS is the zCOSMOS survey, which was designed to characterise the environments of galaxies in the COSMOS field from the 100 kpc scales of galaxy groups up to the 100 Mpc scale of the cosmic web and to produce diagnostic information on galaxies and active galactic nuclei (Lilly et al. 2007). zCOSMOS comprised two separate surveys. zCOSMOS-bright obtained spectra for a $I_{\rm AB} < 22.5$ magnitude limited sample of ∼22 000 galaxies at $0.1 \leq z < 1.2$ in the full ∼1.7 deg^2 of the COSMOS field. zCOSMOS-deep acquired spectra of ∼10 000 galaxies at $1.4 \leq z < 3.0$ in the central ∼1.7 deg^2 of the COSMOS field.

3.1.1. Luminosity functions in the low redshift Universe

Measurements of luminosity functions in the low redshift Universe (i.e. $z < 0.2$) are important for studies of luminosity function evolution because they enable measurements made at higher redshift to be "anchored" to measurements made at low redshift using larger data sets. Two of the most widely quoted low redshift optical surveys have been the Sloan Digital Sky Survey (SDSS York et al. 2000; Stoughton et al. 2002) and the Two Degree Field Galaxy Redshift Survey (2dFGRS Norberg et al. 2002; Madgwick et al. 2002).

2dFGRS used the 3.9 metre Anglo-Australian Telescope to image ∼400 spectra simultaneously, finally obtaining ∼250 000 spectra of galaxies in two strips of total area 2151.6 deg^2,

one in the Northern Galactic Hemisphere and one centred on the South Galactic Pole. Using 2dFGRS data, Norberg et al. (2002) analysed more than 110 500 galaxies with accurate spectroscopic redshifts and obtained a luminosity function for the Johnson B-band. Following on from this Madgwick et al. (2002) divided a sample of 75 589 $z \leq 0.15$ 2dFGRS galaxies into four "types" using principal component analysis (PCA) and defined an index η dependent on the strength of emission and absorption lines. This index was used to divide galaxies into different types, ranging from quiescent ("Type 1") to highly star-forming ("Type 4"). Separate luminosity functions were derived for each type as well as for all galaxies. We take the Madgwick et al. (2002) "Type 1" to correspond to "red" galaxies in our study.

Blanton et al. (2005a) used the Second Data Release of the Sloan Digital Sky Survey (SDSS 2DR) to obtain a luminosity function for the Sloan r-band. The Sloan survey eventually imaged a full one quarter of the Northern sky ($\sim 10\,000\mathrm{deg}^2$) in five wavebands (u, g, r, i, z) ranging from the near ultra-violet to the near infrared. The g-band limiting (AB) magnitude was $\sim$23. It used a dedicated 2.5 metre drift scan telescope at Apache Point Observatory in New Mexico for photometric imaging, and also obtained the spectra of 930 000 galaxies, 120 000 quasars, and 460 000 stars, acquiring $\sim$600 spectra at each pointing.

Blanton et al. (2005a) used a sample of 28 089 SDSS galaxies at distances of $10h^{-1}\mathrm{Mpc} < d < 150h^{-1}\mathrm{Mpc}$ and redshifts $0 < z < 0.2$ from the New York University - Value Added Galaxy Catalogue (NYU-VAGC) which is based on a subset of SDSS galaxies (Blanton et al. 2005b). They reported that their g-band luminosity functions were "roughly consistent" (sic) with those from the 2dFGRS (Norberg et al. 2002).

Both Madgwick et al. (2002) and Blanton et al. (2005a) observed that fitting a single Schechter function to observations will underestimate the number of very faint galaxies ($M \geq -18$). To account for this Madgwick et al. (2002) added a residual term $10^{4.7+0.5M}$ to the Schechter function, while Blanton et al. (2005a) added a second Schechter term similar to the original, but with different values of the Schechter parameters ϕ^* and α.

3.1.2. Luminosity function evolution since redshift $z = 1$

Three of the key early papers in the study of galaxy luminosity functions at higher redshifts made use of photometric redshifts: Wolf et al. (2003), Bell et al. (2004) and Faber et al. (2007). All of these were based on the COMBO-17 survey (Classifying Objects by Medium-Band Observations in 17 Filters) (Wolf et al. 2003). This imaged $\sim$25 000 $R < 24$ galaxies in an area of 0.78 deg^2 using the Wide Field Imager (Baade et al. 1999) at the MPG/ESO 2.2-m telescope on La Silla, Chile and employed 17 narrow band optical filters ranging in wavelength from $\sim$0.36 to $\sim$0.91 μm. These 17 filters produced what was effectively a coarse

spectrum that could be used to estimate photometric redshifts. This was originally done by comparison with modified versions of the Kinney et al. (1996) galaxy templates, but Bell et al. (2004) and subsequent authors used improved galaxy templates based on the PEGASE (Fioc & Rocca-Volmerange 1997) stellar population synthesis (SPS) code, and were able to quote redshift accuracies of within $\delta z/(1+z) < 0.01$ at $R < 21$ and within $\delta z/(1+z) < 0.05$ down to $R = 24$.

Although COMBO-17 used 17 filters, these all lay in the optical region so that the effective range of the restframe spectral energy distribution (SED) sampled at $z \sim 1$ was only $\sim$0.18 μm to $\sim$0.46 μm, resulting in a high photometric redshift failure rate for the faintest blue galaxies, that necessitated data for the faintest bins being dropped from the analysis (Faber et al. 2007). For this reason the 17 filters used in COMBO-17 do not always produce more accurate photometric redshifts for fainter and $z > 1$ galaxies than smaller numbers of filters covering a wider waveband range, (as in our study which also uses filter in the near infrared). Taylor et al. (2009) discuss the errors in the COMBO-17 photometric redshifts arising from the lack of near infrared data (their Figure 14).

Bell et al. (2004) measured the rest-frame colours and B-band luminosities of $\sim$25 000 galaxies in the redshift range $0.2 < z \leq 1.1$ using redshift bins of width 0.1 and showed clearly that the bimodality in restframe $(U-V)$ colour between "red" and "blue" galaxies persists at least out to $z = 1$. When $(U-V)$ colour was plotted against absolute V-band magnitude, red galaxies lay on a tight sequence with brighter galaxies being redder, while blue galaxies formed a "blue cloud" below the red sequence. As galaxies have evolved towards the present day, both the red sequence and the blue cloud have become redder, enabling a model independent separation to be made by means of an evolving red/blue cut drawn through the centre of the "green valley" between the red sequence and blue cloud. They found that the numbers of galaxies within the blue cloud has dropped significantly since $z \sim 1$.

The mean colour of the red sequence was found to evolve in a way that is consistent with passive stellar evolution, i.e. the fading of an ancient stellar population in a galaxy without any star formation. On the other hand the luminosity density of the red sequence was found to have changed very little since $z \sim 1$. By comparing the observed fading with that predicted by a stellar population synthesis model, Bell et al. (2004) were able to conclude that the stellar mass on the red sequence must have increased by a factor of $\sim$2 since $z = 1$. They attributed this to a combination of galaxy mergers and the cessation of star formation in star-forming galaxies, both of which move stellar mass from the blue cloud to the red sequence.

A key result of Bell et al. (2004) for our work is that there are insufficient massive blue galaxies at redshifts $\sim$1 to account for any growth in massive red galaxy numbers since then

due to the cessation of star formation. They reached this conclusion by examining possible evolutionary scenarios for massive blue galaxies in PEGASE (Fioc & Rocca-Volmerange 1997) stellar population synthesis models as shown in their Figure 1 which we reproduce here as our Figure 39. The relevant features of these plots for the present discussion are as follows. The sloping solid line is an evolving best fit to the red sequence which was found by Bell et al. (2004) to be described by $M_U - M_V = 1.40 - 0.31z - 0.08(M_V - 5\log h + 20)$. The parallel sloping dashed line is 0.25 mag bluer than the solid line and shows the red/blue cut that was used. In each redshift bin the two solid lines joining crosses show different endpoints of PEGASE simulations, one for bright galaxies and one for faint. Along the bright line the crosses represent galaxies with a formation redshift of $z_f = 2$, solar metallicity and identical star formation histories except for the manner in which the star formation turned off. The reddest model in each case shows the endpoint of a simulation with exponential decay of star formation proportional to $e^{-t/\tau}$ with $\tau = 4\,\mathrm{Gyr}$, and the others represent, in order of increasing blueness, sudden cessation of star formation after elapsed times of 90%, 80%, 50% and 10% of the age of the galaxy at the epoch in question. By following a given cross from redshift to redshift down from $z \sim 1.05$ it can be seen that at no redshift can the most massive red galaxies be the result of the cessation of star formation in massive blue galaxies. Bell et al. (2004) explain that their evolutionary models are illustrative only and only intended to show that at all redshifts there are very few blue galaxies luminous enough to fade into the brightest red sequence galaxies. Further details of their argument are given in §6.4 of their paper.

Bell et al. (2004) state that cosmic variance is their main source of error, even with three independent fields of $\sim 0.25\mathrm{deg}^2$ each, as in the COMBO-17 survey. They observed that it was necessary to cover substantially larger areas to similar depths to significantly improve on these results.

Faber et al. (2007) compared the results of the spectroscopic DEEP2 survey (Willmer et al. 2006) and the photometric redshift COMBO-17 survey (Wolf et al. 2003) using redshift bins of width 0.2 in the redshift range $0.2 < z \leq 1.2$. Their combined sample contained 39 000 galaxies to $R \sim 24$. Willmer et al. (2006) and Faber et al. (2007) measured evolution separately for red and blue galaxies divided on the basis of colour bimodality. The red/blue cut for the DEEP2 data was a line of slope -0.032 in $(M_U - M_B)$ versus M_B colour-magnitude space chosen to pass through the middle of the colour valley in each redshift bin. The red/blue cut for the COMBO-17 data was an evolving one in $M_U - M_V$ versus M_V colour-magnitude space as in Bell et al. (2003). By combining the two surveys Faber et al. (2007) were able to reduce cosmic variance to 7% to 15% per redshift bin.

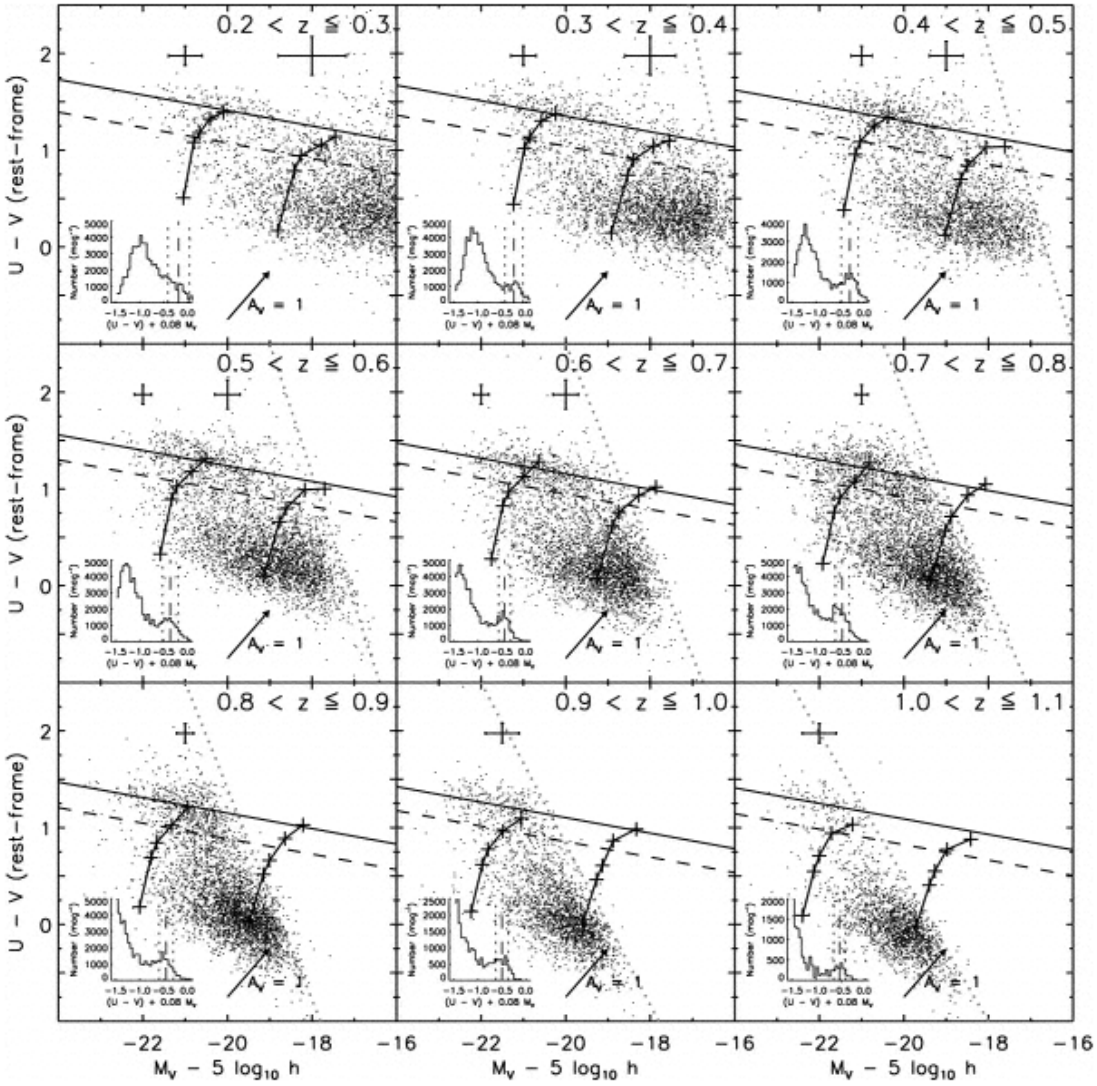

Fig. 39.—: **Colour-magnitude evolution from Bell et al. (2004) showing that massive red galaxies cannot have been produced by the cessation of star formation in massive blue galaxies.** Crosses joined by lines represent endpoints of stellar population synthesis models with different star formation histories. The left hand set of crosses is for highly luminous galaxies. Following these from panel to panel from higher redshift to lower, it can be seen that none of the SPS models represents a highly luminous blue galaxy evolving to a highly luminous red galaxy. See the text for further details.

To quantify B-band luminosity function evolution, Faber et al. (2007) fitted a Schechter function (2) in each of five redshift bins from $z = 0.2$ to $z = 1.2$ for red and blue galaxies separately and for all galaxies. Because the faint end of the luminosity function is very poorly constrained at higher redshifts, they used the same fixed value of alpha in all redshift bins, determined by the best fitting value at low redshifts. Good agreement was found between the results from the two surveys, and good agreement with the results for all galaxies from previous surveys. They found that the characteristic magnitude M^* for both red and blue galaxies has increased by almost the same amount in both surveys, $\sim$1.3 mag from $z \sim 1$ to the present, implying a reduction in characteristic luminosity L^* by a factor of $\sim$0.33. They found that the space density of blue galaxies near M^* (i.e. $0.92\phi^*$) has hardly changed but that of red galaxies has at least doubled since $z \sim 1$.

In agreement with Bell et al. (2004), the red galaxy B-band luminosity density was found by Faber et al. (2007) to have changed relatively little since $z \sim 1$. That of blue galaxies fell by a factor of ~ 4. Taking account of the passive fading of quiescent red galaxies, they concluded that the mass density of red galaxies has *at least* doubled from $z \sim 1$ to the present day.

To account for the increase in red galaxy numbers, i.e. the numbers near to $L = L^*$, Faber et al. (2007) suggested that $\sim L^*$ red galaxies formed from star-forming blue galaxies by a mixture of different processes lying between two extremes. In one extreme scenario blue star-forming galaxies have their star formation quenched while still small; they then migrate to the red sequence and undergo a series of "dry" mergers while there (i.e. mergers between galaxies without gas to form new stars as a result of the merger). In the other extreme scenario, star formation in blue galaxies is quenched late on, once they have grown to a mass comparable with that of $\sim L^*$ red galaxies; they then migrate to the red sequence and become $\sim L^*$ red galaxies. They propose what they call a "mixed scenario", that in reality a mixture of different processes occurs lying between the two extreme scenarios just described.

As well as being classified as "red" or "blue" according to colour bimodality, galaxies can also be classified according to their morphology, for example disc-dominated or bulge-dominated as measured by a concentration index (Bell et al. 2003). We expect morphology to be more closely related to whether a galaxy has grown primarily via star formation or via merging, as hierarchical models indicate that star-forming disc galaxies form first, and that these then become spheroidal or bulge dominated as a result of mergers. Furthermore, galaxies that appear red can in fact be dust reddened disc galaxies. However, it is difficult to obtain large samples with known morphology at high redshift because of the large telescope time required for the necessary imaging.

A study of the dependence of luminosity functions on morphology was carried out by Ilbert et al. (2006b) who measured the evolution of the rest-frame B-band luminosity function for bulge and disk-dominated galaxies separately from z = 1.2 to the present. They used a sample of 605 galaxies with spectroscopic redshifts from the VIMOS-VLT Deep Survey (VVDS, Le Fèvre et al. 2004), and 3555 galaxies with photometric redshifts from COMBO-17, coupled with multi-colour Hubble Space Telescope Advanced Camera for Surveys (HST/ACS) images from the Great Observatories Origin Deep Survey (GOODS, Giavalisco et al. 2004). Splitting the sample into bulge and disc-dominated populations on the basis of asymmetry and concentration parameters, they concluded that some red bulge-dominated galaxies were already well in place at $z \sim 1$, and their space density increased by a factor 2.7 from $z \sim 1$ to $z \sim 0.6$. They found that two thirds of bulge-dominated galaxies at $0.4 \leq z < 0.8$ are bright and red, with the other third being faint and compact blue galaxies.

At $0.4 \leq z < 0.8$ they found a faint end slope for disc-dominated galaxies which was similar to that obtained for blue galaxies in other studies. They also found that two thirds of bulge-dominated galaxies in this redshift range are bright and red $(B-I)_{AB} > 0.9$ with a faint end slope similar to that of "red" galaxies in other studies, with the other third being faint and compact blue $(B-I)_{AB} \leq 0.9$ galaxies.

Cool et al. (2012) pointed out that existing surveys of luminosity functions at $z \sim 1$ and $z \sim 0$ can indicate overall trends in galaxy properties but do not provide a detailed view of evolution between these redshifts as deep surveys have limited volumes at $z \sim 0.5$. To address this issue they studied optical luminosity function evolution from $z = 0.75$ to $z = 0.05$ using data on 12 473 galaxies in the spectroscopic AGN and Galaxy Evolution Survey (AGES, Kochanek et al. 2012) which was then the largest spectroscopic survey of intermediate redshift galaxies. AGES obtained spectra in 7.6 deg^2 of the Boötes field for about 16,000 galaxies with I-band AB magnitudes brighter than 20 out to $z = 1$, (and quasars with $I < 21.5$ out to redshift 6.5). It used the Hectospec Multiobject Optical Spectrograph on the 6.5 metre MMT telescope at Mount Hopkins. Cool et al. (2012) found strong evidence for differences in evolution between red and blue galaxies, the luminosity density evolving as $j_B \propto (1+z)^{1.64\pm0.39}$ for red galaxies and $j_B \propto (1+z)^{0.54\pm0.64}$ for blue galaxies.

A study of optical luminosity function evolution by Loveday et al. (2012) used data from the Galaxy and Mass Assembly project (GAMA, Driver et al. 2009, 2011). The primary goal of GAMA is to test the CDM paradigm of structure formation by studying structure on scales of 1 kpc to 1 Mpc. It includes a spectrosocopic survey of ∼300 000 galaxies down to $r = 19.8$ mag in ∼280 deg^2 of sky, carried out using the AAOmega multi-object spectrograph on the Anglo-Australian Telescope, as well as imaging in several wavebands from X-rays to radio, this imaging coming from several surveys, both legacy and ongoing.

Loveday et al. (2012) used data from the first phase of GAMA to determine luminosity functions over the redshift range $0.002 < z < 0.5$ in each of the Sloan wavebands u, g, r, i, z. As well as calculating luminosity functions for separate redshift bins in the range $0 < z < 0.5$ they also parameterised evolution of the luminosity function by assuming that the Schechter parameters evolve in the following way (Lin et al. 1999), relative to the reference redshift $z_0 = 0.1$:

$$\begin{aligned} \alpha(z) &= \alpha(z_0), \\ M^*(z) &= M^*(z_0) - Q(z - z_0), \\ \phi^*(z) &= \phi(0)10^{0.4Pz}. \end{aligned} \tag{29}$$

The Schechter parameters $\alpha(z_0), M^*(z_0), \phi(0)$ and the evolutionary parameters P and Q were determined using a maximum likelihood method based on (Lin et al. 1999). This model was tested against $1/V_{\rm max}$ and stepwise maximum likelihood Efstathiou et al. (SWML, 1988) estimates and found to fit well qualitatively in the r, i and z-bands (although not as well as SWML), while predicting excessively high space densities in the u and g-bands.

Loveday et al. (2012) found that in all wavebands the characteristic luminosity M^* of red galaxies faded more rapidly with time for red galaxies than for blue (2 - 2.5 mag per unit redshift as opposed to 1 - 1.5). They also found that the comoving number density of blue galaxies has been falling since $z = 0.5$ while that of red galaxies has been increasing, and concluded that the migration of galaxies from the blue cloud to the red sequence has been an important and ongoing phenomenon since $z = 0.5$, mergers playing a very minor role given the low merger fraction of $\sim$5% or less at the low redshifts involved (e.g. Conselice et al. 2009; Lotz et al. 2011). The luminosity density of red galaxies was found to be roughly constant from $z = 0.5$ to $z = 0.15$ while that of blue galaxies decreased. Since $z = 0.15$ the luminosity density of both red and blue galaxies has been decreasing.

Loveday et al. (2012) separately analysed a low redshift subsample ($z < 0.1$) and found that a Schechter function provided a good fit to the luminosity function for blue galaxies, but could not describe the increased number of red galaxies at the faint end. For red galaxies they used instead the parameterisation of Loveday (1997) which provides a multiplying factor that increases with decreasing luminosity:

$$\phi_L\left(L\right) = \phi^* \left(\frac{L}{L^*}\right)^{\alpha} \exp\left(\frac{-L}{L^*}\right) \left[1 + \left(\frac{L}{L_t}\right)^{\beta}\right]. \tag{30}$$

Here β is a constant and $L_t < L^*$ is a transition luminosity between two power laws of slope α and $(\alpha + \beta)$. This formula is equivalent to the double Schechter function fit used by

Blanton et al. (2005a). Loveday et al. (2012) point out that caution is needed in explaining the faint end upturn using halo occupation distribution models (e.g. Brown et al. 2008) as a significant fraction of faint end red galaxies are edge-on disc systems.

Brown et al. (2007) measured evolution of the luminosity function for 59 599 red galaxies in 6.96 deg^2 in Boötes . They made use of images obtained in several optical and near infrared wavebands in Boötes by two legacy surveys: $B_{\rm W}$, R and I-band images from the third data release of the NOAO Deep Wide Field Survey (NDWFS, Jannuzi & Dey 1999), and 3.6, 4.5, 5.8 and 8.0 μm near infrared images from the Spitzer Deep Wide Field Survey (SDWFS; Ashby et al. 2009; Eisenhardt et al. 2008). The large survey area meant that errors due to cosmic variance were minimised, and the image depth of $I \leq 23.5$ meant that luminosity evolution could be followed from $z = 1.0$ to $z = 0.2$.

Brown et al. (2007) used photometric redshifts determined from galaxy colour indices using the artificial neural network code ANNz (Firth et al. 2003; Collister & Lahav 2004). Provided sufficient spectroscopic redshifts are available to train the ANNz code, it works well for red galaxies because they lie on tight sequences in colour-colour spaces. Spectroscopic redshifts from several sources (see §3.2.4 below) were used to calibrate the ANNz photometric redshift code.

A significant feature of the study of Brown et al. (2007) is that the faint yet significant flux from outside their photometric aperture was accounted for and this explained in part the fact that they measured a higher space density at $z \sim 0.9$ than some of the previous literature. They found that the B-band luminosity density of red galaxies decreased by a factor of only 1.36 from $z = 1$ to $z = 0$. Taking account of the passive fading of 1.24 magnitudes per redshift for stellar populations in quiescent galaxies (a factor of 3.1 less in luminosity) they concluded that the stellar mass in $\sim L^*$ galaxies must have roughly doubled in this time (~ 8 Gyr).

3.1.3. Motivation for this work on B-band luminosity function evolution

Our work builds on that of Brown et al. (2007). The sample consists of $\sim 335\,000$ galaxies measured to a good depth (e.g. $I \leq 23.5$) in several optical and near infrared wavebands in the Boötes field. The large size of the sample minimises random Poisson variations in our measurements, and the large survey area of 8.26 square degrees ensures that cosmic variance is reduced to $\sim 5\%$, (because the survey area is large enough to include a representative sample of different environments: clusters, groups, filaments and voids, so averaging out the variation between environments).

The newly available set of $\sim$ 125 empirical galaxy templates from Brown et al. (2013) has enabled us to make more accurate K-correction calculations than has previously been possible. As described in Chapter 2, we did this by fitting a model to *all* the templates at each redshift rather than interpolating between pairs of templates as many methods have done. We expect this to provide greater accuracy in determining absolute magnitudes as it averages out variations in individual template properties.

The new templates also allowed Michael Brown to calculate photometric redshifts by fitting template SEDs to the observed apparent magnitudes in several wavebands. Comparison with spectroscopic redshifts shows our photometric redshifts to have systematic offsets which are generally less than 0.02. Initially we used photometric redshifts calculated by the same ANNz artificial neural network code as in Brown et al. (2007), but we found that when blue galaxies were included as well as red this led to an implausible distribution of redshifts with a marked drop in numbers around $z = 0.55$. This was too large to be explained by cosmic variance, not least because cosmic variance for blue galaxies is less than that for red. We therefore used template fit photometric redshifts instead for our final results. This is discussed further in §3.4.

We distinguished "red" and "blue" galaxies on the basis of an evolving colour cut running through the minimum of the green valley in restframe colour-magnitude space, rather than using a fixed offset from the evolving red sequence or a fixed non-evolving cut, as this is observationally clearer and more closely reflects the true bimodality of galaxy properties.

In order to make our measurements of total apparent magnitude as accurate as possible, we used a varying measurement aperture (Figure 6) carefully chosen to avoid extraneous light from nearby objects while at the same time capturing as much of the galaxy light as possible. We then applied a correction based on examining growth curves of measured magnitude with aperture diameter for isolated galaxies. We expect this to provide more accurate total magnitudes than other methods.

We measured evolution of the luminosity function in the B-band so that we could make direct comparisons between our results and those in the literature, including results from semi-analytic models, many of which give results for the B-band, and because at redshifts $\sim$ 1.2 the restframe B-band lies near the observed near-infrared I and J-bands and can therefore be accurately measured.

3.2. The surveys

We used data from several legacy surveys covering 8.26 square degrees in Boötes to determine photometric redshifts, to calculate absolute (restframe) magnitudes, to apply various colour cuts, and to separate red and blue galaxies on the basis of restframe colour bimodality. Our photometry is based on $B_{\rm W}$, R and I-band images from the third data release of the NOAO Deep Wide Field Survey (NDWFS, Jannuzi & Dey 1999), J-band images from the NEWFIRM Boötes Imaging Survey (Gonzalez et al. 2011, in prep.), and 3.6, 4.5, 5.8 and 8.0 μm near infrared images from the Spitzer Deep Wide Field Survey (SDWFS; Ashby et al. 2009; Eisenhardt et al. 2008).

Spectroscopic redshifts from several sources (see §3.2.4 below) were used to calibrate the ANNz photometric redshift code. In addition, where spectroscopic redshifts for galaxies were available, we used them in preference to photometric redshifts.

3.2.1. NOAO Deep Wide Field Survey (NDWFS)

The NOAO Deep Wide Field Survey imaged two fields of approximately 9.3 square degrees each, one in Boötes using the MOSAIC-I camera on the KPNO 4 metre telescope, and one in Cetus using multiple instruments and telescopes. An additional field of $\sim$ one square degree, the Extended Groth Strip (EGS), was imaged in 2008, this field being used to provide thousands of spectra of fainter objects for enhancing the training of the ANNz photometric redshift code (although we eventually chose to use template based photometric redshifts - see §3.4). The NDWFS 5σ Vega magnitude detection limits are $B_{\rm W} = 26.6$, $R = 25.8$ and $I = 25.5$. Copies of the released images were smoothed to a common Moffat point spread function (PSF) by Michael Brown. This PSF had a full width at half-maximum of $1.35''$ and an atmospheric scattering coefficient of $\beta = 2.5$, these values corresponding to the image with the worst seeing. This ensured that the fraction of the light captured by small apertures did not vary from filter to filter and from subfield to subfield across the Boötes field.

3.2.2. NEWFIRM Boötes Imaging Survey

J, H and $K_{\rm S}$-band data from Data Release 2 of the NEWFIRM Boötes Imaging Survey were used for the photometric redshifts and J-band data for photometry. The NEWFIRM survey (Gonzalez et al. in prep.) covers the whole of the Boötes region covered by the NDWFS and SDWFS infrared surveys and made use of the NOAO Extremely Wide-Field Infrared Imager (NEWFIRM camera) on the Mayall 4 metre telescope on Kitt Peak (Autry et al. 2003; van

Dokkum et al. 2009; Whitaker et al. 2011). The survey reached 5σ (Vega) depths of at least $J = 22.0$, $H = 20.8$ and $K_{\rm S} = 19.5$ within a 3 arcsecond diameter aperture.

3.2.3. Spitzer Deep Wide Field Survey

The Spitzer Deep Wide Field Survey (SDWFS; Ashby et al. 2009; Eisenhardt et al. 2008) used Spitzer's Infrared Array Camera (IRAC; Fazio et al. 2004) to image the entire Boötes field at 3.6, 4.5, 5.8 and 8.0 micron to average 5σ (Vega) depths of 19.77, 18.81, 16.50 and 15.82 respectively.

3.2.4. Spectroscopic redshifts

The vast majority of spectroscopic redshifts in the Boötes field are from the AGN and Galaxy Evolution Survey (AGES, Kochanek et al. 2012), which obtained spectra of about 16,000 galaxies with I-band magnitudes brighter than 20 out to $z = 1$, (and quasars with $I < 21.5$ out to redshift 6.5). AGES used the Hectospec Multiobject Optical Spectrograph on the 6.5 metre MMT telescope at Mount Hopkins.

Spectroscopic redshifts in the EGS are from the Deep Evolutionary Exploratory Probe 2 (DEEP2, Davis et al. 2003; Willmer et al. 2006) galaxy redshift survey and this provided thousands of redshifts of fainter galaxies for ANNz photometric redshift calibration. DEEP2 used the DEep Imaging Multi-Object Spectrograph (DEIMOS, Faber et al. 2003) on the 10-m Keck II Telescope on Mauna Kea, with spectroscopic targets being selected using B, R and I-band images from the 3.6 metre Canada Hawaii France Telescope (CFHT) also on Mauna Kea.

Several hundred additional redshifts for both fields were obtained from SDSS and from a variety of programmes with the Gemini, Keck and Kitt Peak National Observatory telescopes.

3.3. Object detection and photometry

Brown et al. (2008) detected sources using SExtractor 2.3.2 (Bertin & Arnouts 1996) run on I-band images from the NWDFS third data release. Duplicate object detections were removed from the small regions of overlap between subfields. To minimize contamination of the catalogue, regions surrounding very extended galaxies and saturated stars were removed (Figure 40). Visual inspection confirmed that the majority of these regions do in fact surround saturated stars or bright galaxies. 55 bright galaxies with $0.2 \leq z_{\rm spec} < 1.2$ which have SDSS spectroscopic redshifts were removed by the drilling process and we added these back in so that the bright end of the luminosity function was not biased. Of these 36 lay in the first redshift bin $0.2 \leq z < 0.4$. The final sample covers an area of 8.262 deg^2 over a $2.9^\circ \times 3.6^\circ$ field of view.

Brown et al. (2008) used their own code to measure the apparent magnitude of each source in each waveband using apertures with diameters ranging from 1 to 20 arcsecond. SExtractor segmentation maps were used to exclude flux associated with neighbouring objects. Corrections were also made for missing pixels, (e.g. bad pixels) using the mean flux per pixel measured in a series of annuli surrounding each object. Random uncertainties were estimated by measuring the flux at $\simeq 100$ or so positions near to each detected object. These uncertainty estimates were verified using artificial galaxies added to copies of the data which were based on typical surface brightness profiles of elliptical galaxies, i.e. de Vaucouleurs (1948) profiles, (Brown et al. 2007).

We made use of the catalogue from Brown et al. (2008) and employed a variable aperture size, as shown in Figure 41, dependent on the I-band magnitude measured using a 4 arcsecond diameter aperture. We used ds9 region files for different apparent magnitude ranges to find galaxies which are seen from visual inspection to have no near neighbours. Using just these galaxies, we then plotted Moffat point spread function corrected magnitudes as a function of aperture diameter (Figure 42) and selected an aperture where the magnitude as a function of aperture diameter changed (on average) by less than 0.03 mag arcsecond^{-1}. In the case of galaxies with $I > 20.5$, we used an area approximately 50% smaller than this, so that we avoided including any small amounts of extraneous light which would be proportionately more significant for these fainter objects. We then normalised the growth curves to the chosen aperture diameter and calculated the total correction as the sum of a Moffat PSF correction and the mean offset at larger apertures between the normalised growth curves (e.g. Figure 42b). Table 11 lists the apertures we used and the corrections applied and Figure 43 shows the varying aperture sizes used for a small part of the Boötes field.

To a large extent the flux contributed by neighbouring objects is excluded by using segmentation maps and the average flux within annuli to compensate for masked flux. However, this

process is less accurate for galaxies whose images are not perfectly axisymmetric. Figure 42 shows that the growth curves do not all level off perfectly at larger diameters due to random variations in the faint background. Our method largely corrects for this by applying a mean correction to the magnitude measured using a slightly smaller aperture than that required to include absolutely all the flux. It also has the additional advantage that it does not assume any particular surface brightness profile, (e.g. a de Vaucouleurs profile for red galaxies as in Brown et al. 2007).

As a check on our procedure, we compared our corrected apparent magnitudes with those obtained using apertures $\sim 50\%$ larger in area than our preferred values and found that the systematic offset between the two was in general less than ~ 0.05 mag for $I > 21.5$ and ~ 0.02 mag for $I < 21.5$.

As a second check we also compared our measured I-band magnitudes with those produced by SExtractor‘s MAGAUTO and found that our values were systematically brighter by 0.08 mag or more (Figure 44). We attribute this to our improved estimates of the aperture required to capture the majority of the light together with improved corrections for any remaining missing light. The difference is particularly marked for galaxies fainter than $I \sim 20$. Brown et al. (2007) obtained a similar upturn at faint magnitudes in the difference between MAGAUTO magnitudes and 4 arcsecond aperture magnitudes for red galaxies (their Figure 1), but their offsets are $\sim$0.05 mag smaller than ours for objects. We attribute this difference to our varying aperture size.

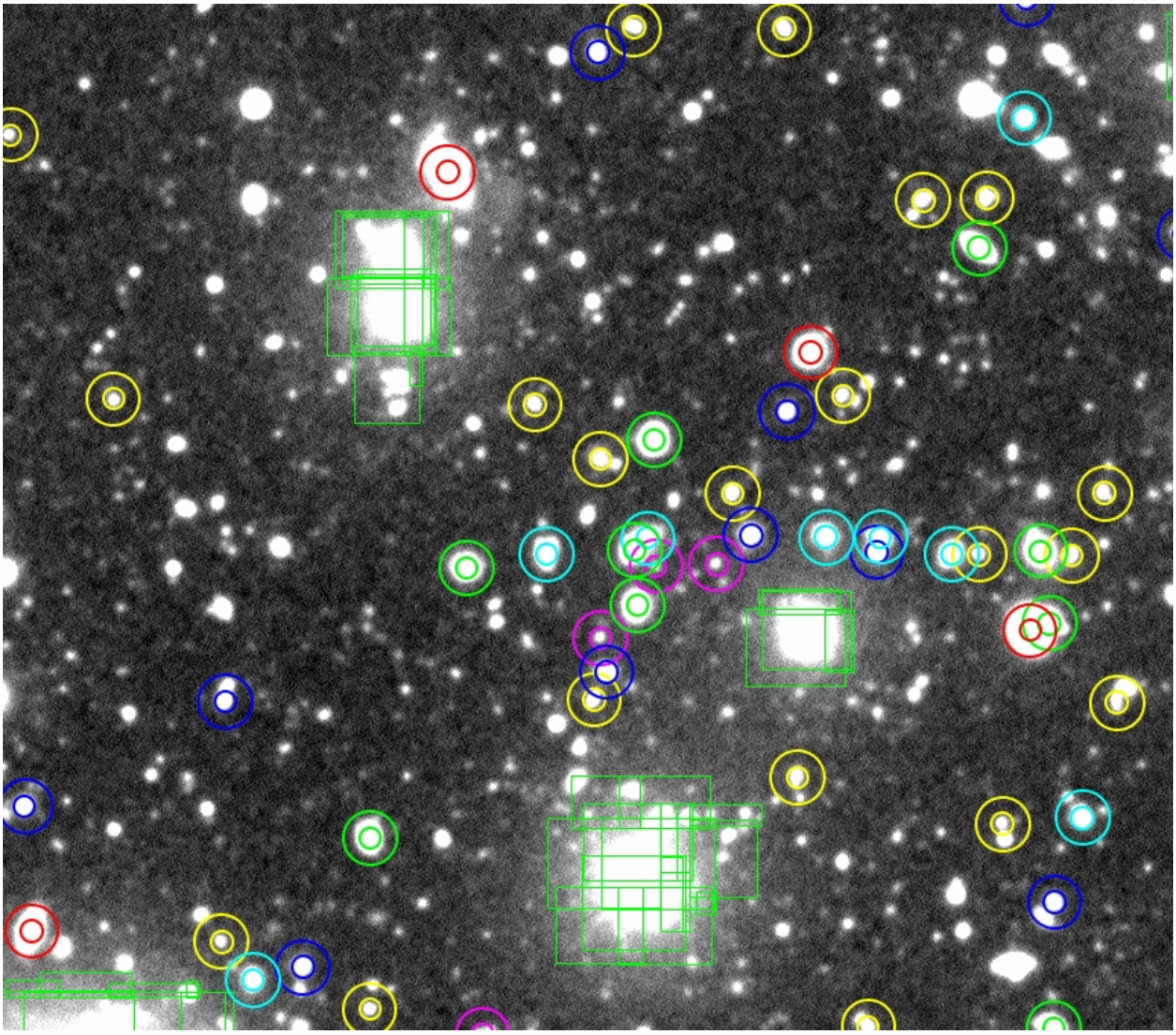

Fig. 40.—: **Showing how the majority of galaxies in a typical area of the Boötes field have significantly bright near neighbours.** Aperture diameters of 4 and 10 arcsecond are shown by means of ds9 region files. Marked galaxies have redshifts $0.2 \leq z < 0.6$. Red, green, cyan, blue, yellow and magenta denote the following I magnitude ranges (measured using a 4 arcsecond aperture): [16.5, 18.5], [18.5, 19.5], [19.5, 20.5], [20.5, 21.5], [21.5, 22.5] and [22.5, 23.5]. The green rectangles are drilled regions that are excluded from the field because they are associated with very bright stars or extended sources.

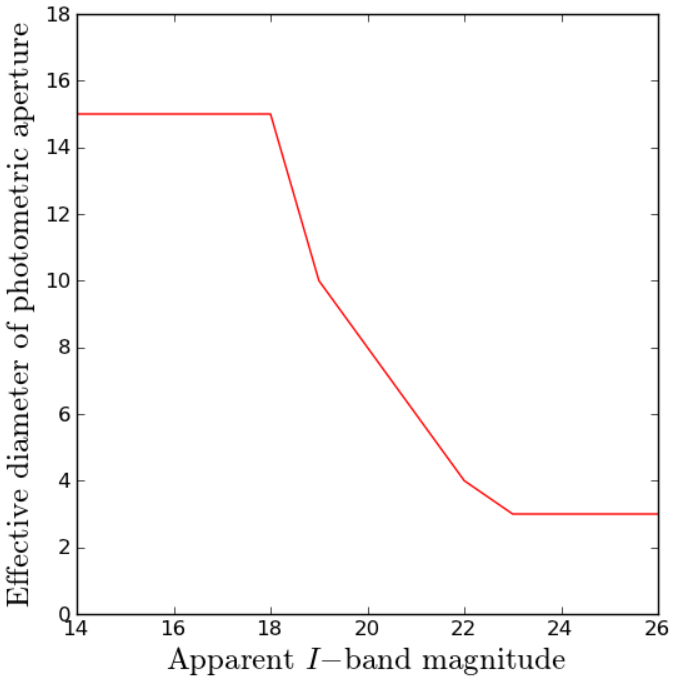

Fig. 41.—: **How the effective photometric aperture depends on apparent I-band magnitude.** Magnitudes measured using a 4 arcsecond aperture are used as the reference.

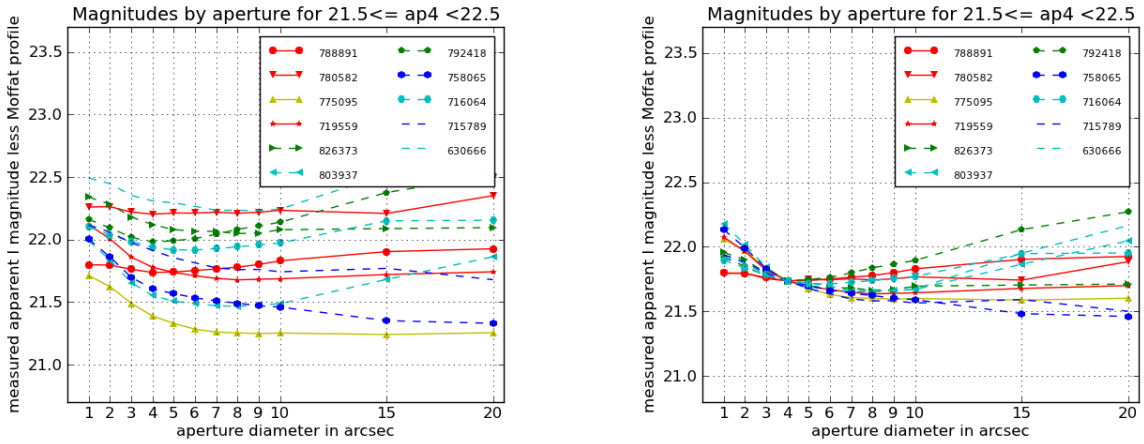

(a) (b)

Fig. 42.—: **Example growth curves of measured apparent magnitude I less Moffat point spread function correction with aperture diameter for galaxies which have no significant near neighbours on the sky.** *Left:* plots for $20.5 \leq I < 21.5$ galaxies, as measured using a 4 arcsecond diameter aperture. Continuous lines indicate galaxies with no visible near neighbours within a 10 arcsecond diameter aperture; dashed lines indicate galaxies with faint or marginal contamination by near neighbours. Red, green, cyan, blue, yellow and magenta denote the following redshift ranges: [0.2, 0.4], [0.4, 0.6], [0.6, 0.8], [0.8, 1.0] and [1.0, 1.2]. *Right:* the same plots normalised to a common 4 arcsecond magnitude. For objects with $I = 22.0$ a 4 arcsec diameter aperture was used and a magnitude correction of -0.243 applied (including the Moffat correction of 0.046.)

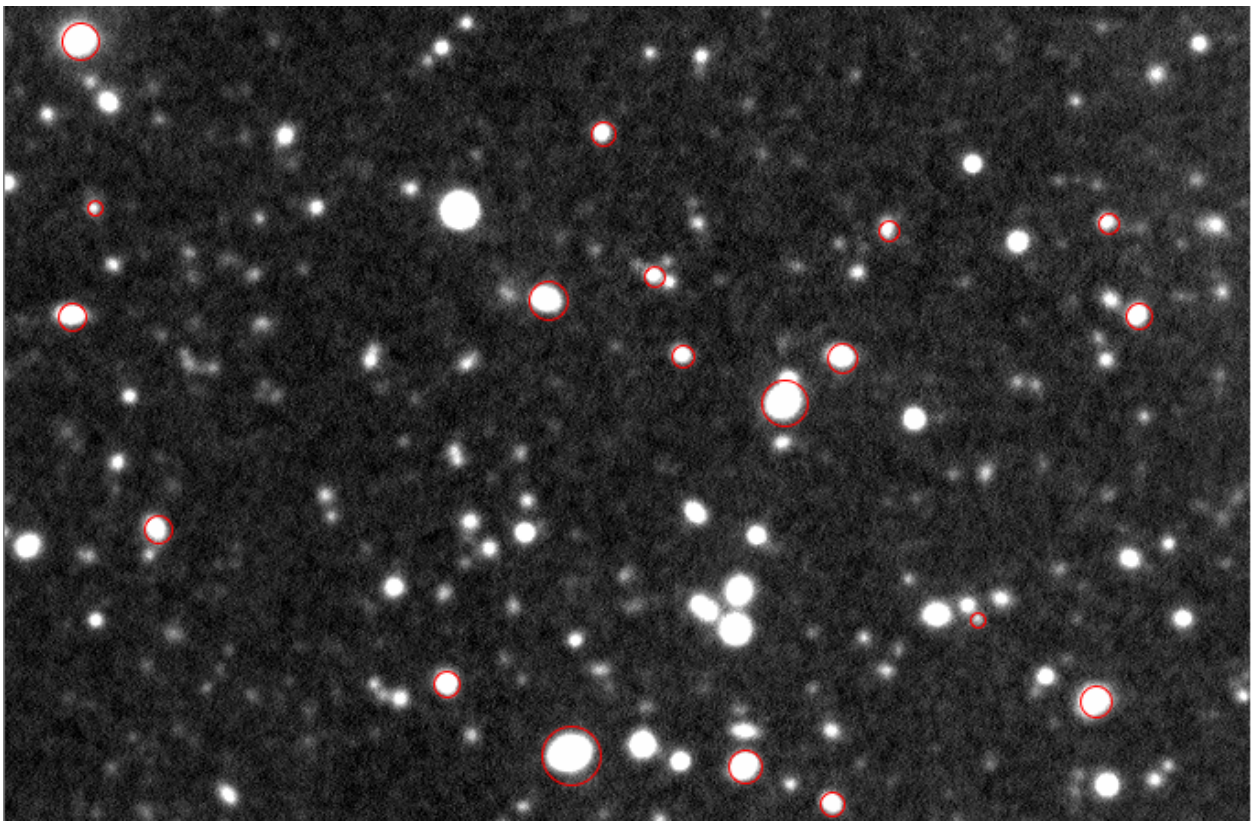

Fig. 43.—: **Showing the varying effective aperture sizes used.** The image is ∼3.5 arcmin across. Apertures are chosen to exclude light from neighbouring objects as far as is possible. A correction for light falling outside the aperture is then applied, determined using growth curves of magnitude with aperture diameter such as those shown in Figure 42.

Table 10. Numbers of spectroscopic redshifts in the Boötes field at different redshifts (includes quasars).

$z_{\rm min}$	$z_{\rm max}$	bright red $I <= 21$	faint red $I > 21$	bright blue $I <= 21$	faint blue $I > 21$	bright red and blue $I <= 21$	faint red and blue $I > 21$
0	0.2	1840	0	5391	39	7231	39
0.2	0.4	3325	6	5606	39	8931	45
0.4	0.6	2032	11	3111	64	5143	75
0.6	0.8	674	35	1090	119	1764	154
0.8	1	133	108	417	228	550	336
1	1.2	5	124	221	301	226	425
1.2	1.4	0	55	197	253	197	308
1.4	∞	0	19	865	469	865	488

Table 11. Aperture diameters and magnitude corrections including Moffat point spread function correction as applied to all wavebands except J for which slightly different corrections are applied because of the larger point spread function.

I (4 arcsecond) (mag)	aperture diameter to include most of light (arcsecond)	aperture diameter used (arcsecond)	correction applied (mag)
23	4	3	-0.410
22	5	4	-0.243
21	6	6	-0.105
20	8	8	-0.070
19	10	10	-0.078
18	15	15	-0.061

Table 12. Approximate random and systematic errors in the template based photometric redshifts for $0.2 \leq z_{\rm phot} < 1.2$.

I	$\sigma_{\rm photz}$ red	$\sigma_{\rm photz}$ blue	systematic error red	systematic error blue
23.0	0.08	0.08	0.03	0.03
22.0	0.06	0.08	0.03	0.03
21.0	0.05	0.08	0.03	0.03
20.0	0.05	0.05	0.02	0.03
19.0	0.04	0.04	0.02	0.03
< 18.5	0.03	0.03	0.02	0.02

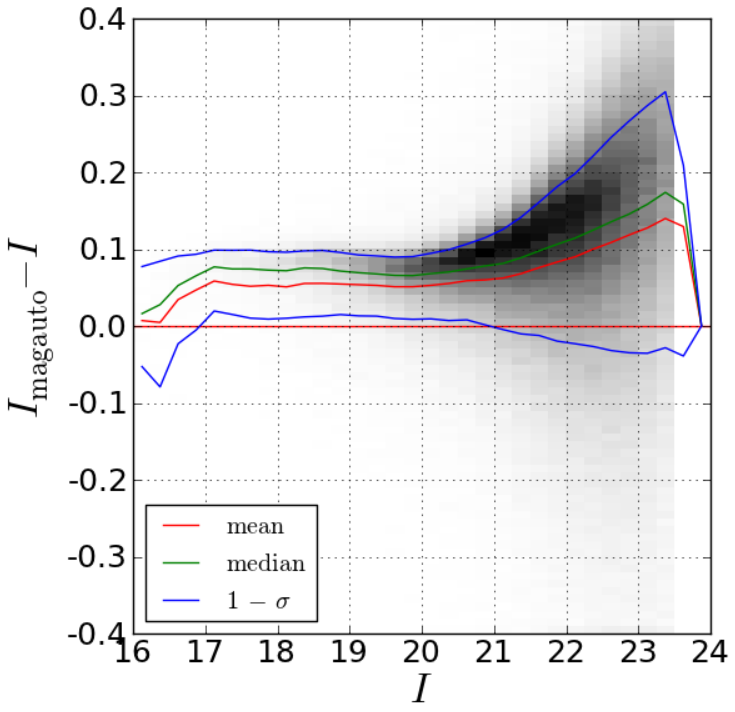

Fig. 44.—: **Our apparent magnitudes are** 0.08 **mag or more systematically brighter than those produced by MAGAUTO.** This is because our method of measuring apparent magnitudes more accurately measures the total light from galaxies, especially faint ones for which MAGAUTO does not use a PSF to correct for light beyond the aperture.

3.4. Photometric redshifts

3.4.1. Photometric redshifts using ANNz

Following Brown et al. (2007), we originally intended to use the photometric redshifts $z_{\rm phot}$ determined by Brown et al. (2007) using the empirical ANNz artificial neural network photometric redshift code (Firth et al. 2003; Collister & Lahav 2004). They trained the ANNz neural network using spectroscopic galaxies in the Bootes and Extended Groth Strip (EGS) fields with photometry in the NDWFS and IRAC filters. Seven inputs were used (B_w, R, I and the four IRAC channels) with 3 hidden layers, each containing 14 nodes. The training sample and validation samples were 50% of the available spectroscopic redshifts in the Boötes field and the EGS, and were extrapolated to fainter magnitudes by making copies of brighter galaxies (with small changes to the photometry to account for colour-magnitude relations). Approximately 20 000 spectroscopic redshifts were used, with the bulk of the redshifts for Boötes and the EGS coming from AGES and DEEP2 respectively.

To assess the accuracy of these photometric redshifts we compared them with available spectroscopic redshifts $z_{\rm spec}$. For $I < 20$ galaxies we used the well defined SDSS and AGES samples, while for fainter galaxies there is an ad-hoc collection of spectra from Gemini, Keck, Mayall and MMT. Additional spectroscopic redshifts were available in the Extended Groth Strip (EGS), including a well defined sample of faint $I > 20$ galaxies. However, there are differences between the imaging available in the EGS and in Boötes as the EGS does not have NEWFIRM J, H, K_s imaging. Figure 45 is a plot of the redshift errors we obtained.

Our luminosity functions for blue galaxies and for all galaxies based on ANNz redshifts were found to exhibit significant differences from other results in the literature. We attempted to resolve this inconsistency by a variety of means: investigating different photometric aperture sizes and the corresponding magnitude corrections, trying different K-correction techniques, varying the definition of the red-blue cut, and correcting the photometric redshifts for red galaxies and for blue in different I magnitude ranges using a number of gaussian type corrections centred on redshifts where the discrepancy with spectroscopic redshifts was greatest. None of these exhaustive investigations removed the discrepancy with other results in the literature for blue galaxies.

Eventually, when we plotted histograms for different galaxy colours and apparent magnitude ranges of the numbers of objects with different redshifts (Figure 46), we found that the ANNz redshifts for fainter blue galaxies ($I \gtrsim 20$) exhibited a significant ($\leq 30\%$) dip in numbers at $z_{\rm phot} \sim 0.55$. This deficiency in galaxy numbers was also very clearly visible in any binned colour-redshift plots that we made. We concluded that ANNz redshifts were either being systematically shifted out of the range $0.5 \lesssim z_{\rm phot} \lesssim 0.7$ into the bins above and below, or

that ANNz was not producing valid redshifts for some galaxies, or a combination of both. No evidence of this had been seen in our ($z_{\rm phot} - z_{\rm spec}$) against $z_{\rm spec}$ plots however.

We suspected that the available spectroscopic redshifts used to train the ANNz code might not be adequately spanning the range of real blue galaxies in some colour-colour spaces. We therefore produced colour-colour plots distinguishing galaxies with and without spectroscopic redshifts and these did in fact reveal that the available spectroscopic galaxies did not fully span the region in all colour-colour spaces occupied by our sample at some redshifts. We concluded that this was the cause of the implausible drop in ANNz $z_{\rm phot}$ values at $z \sim 0.55$ (Figure 47a). It is clear from this that a much more representative set of spectroscopic galaxies is needed for the ANNz method to be useful for blue galaxies. We therefore decided to investigate whether template based photometric redshifts would be more reliable.

3.4.2. Template fit photometric redshifts

Template fit photometric redshifts were derived by Michael Brown using the new set of ∼125 template SEDs in Brown et al. (2013). Unlike ANNz redshifts, template based photometric redshifts are not based on comparisons with spectroscopic redshifts, but depend on having as fully representative a set of template galaxy SEDs as possible. We were fortunate to have available the most complete and accurate set of galaxy templates yet available for this purpose. Photometric redshifts were determined by performing a least squares fit of computed colours for redshifted template galaxies to observed colours, derived from photometry in the optical $B_w, R, I, y, J, HandK_s$ wavebands and infrared IRAC photometry at 3.6, 4.5, 5.8 and 8.0 μm. A step size of $\Delta z = 0.01$ was used when determining the photometric redshifts, and the template that provided the best fit to the photometry was used to estimate the redshift. Because of the lack of J and K_s photometry in the EGS it was not possible to take advantage of the large number of spectroscopic redshifts of faint galaxies in this field to correct the template based photometric redshift values.

Plots of ($z_{\rm phot} - z_{\rm spec}$) (Figure 48) show the systematic errors in $z_{\rm phot}$ at different redshifts, based on comparisons with available $z_{\rm spec}$ values. Table 10 gives the numbers of the latter.

We expected that our template based $z_{\rm phot}$ values would be relatively free of systematic errors for $z_{\rm phot} \lesssim 0.8$ where the galaxies in our sample would differ little from a sample of nearby galaxies. Figure 48 confirms this using the large sample of $z_{\rm spec}$ values available at $z < 0.8$. For $z_{\rm phot} > 0.8$ we expected that there might be systematic errors due to the increasingly different stellar compositions of galaxies at these earlier epochs, and also due to the fainter apparent magnitudes involved. Plots of ($z_{\rm phot} - z_{\rm spec}$) for red, blue and all galaxies do in fact

show evidence of systematic errors, most significantly that $z_{\rm phot}$ is underestimated by ~ 0.07 at $z_{\rm phot} \sim 1$.

Importantly, however, as Figure 47b and Table 10 show, relatively few spectroscopic redshifts were available beyond $z \sim 0.8$, so the true systematic errors must remain relatively uncertain. In this context we note that claims have frequently been made in the literature for the high accuracy of photometric redshifts based on comparison with small numbers of spectroscopic redshifts. While these claims may be true, they may equally be more a reflection of the precise sample of galaxies selected for spectroscopic observation. For example, if only the brightest galaxies are selected, these can be expected to have more accurate photometric redshifts because of their smaller photometric uncertainties, and this will give an unduly optimistic picture of the overall photometric redshift accuracy.

Table 12 lists estimates of random and systematic errors for both red and blue galaxies of different apparent I magnitude. Figure 48b suggests that the largest systematic error is an approximately Gaussian shaped underestimate of amplitude ~ 0.07 centred close to $z_{\rm phot} = 1.0$. Because this systematic error is centred on the boundary between the redshift bins $0.8 \leq z_{\rm phot} < 1.0$ and $1.0 \leq z_{\rm phot} < 1.2$, a 5% error in $z_{\rm phot}$ can make a significantly larger percentage difference to the numbers of galaxies assigned to each bin. We made an approximate correction for this largest systematic error using a least squares fit to the data plus a Gaussian error (Figures 48b, 48c).

As we explain in §3.10, whether we apply this correction or not does not materially alter our main conclusions concerning the evolution of luminosity density and the mass of massive red galaxies. The effect of applying the correction on the measured Schechter parameters ϕ^* and M^* and the total luminosity density (Figures 75, 76 and 77) is discussed there.

Because of the uncertainty regarding what systematic redshift correction should be be applied (if any) we retained the uncorrected redshifts for our measurements of luminosity function evolution. We consider the redshifts for red galaxies to be reliable for the whole of our redshift range, i.e. $0.2 \leq z < 1.2$. We take the redshifts of blue galaxies to be reliable up to $z = 1.0$ but uncertain for $1.0 \leq z < 1.2$, and therefore base our conclusions for blue galaxies on the range $0.2 \leq z < 1.0$.

3.4.3. Comparison of ANNz and template fit photometric redshifts

Comparing Figures 45 and 48 we see that the ANNz redshifts mostly have smaller random errors ($\sigma z_{\rm phot} \sim 0.05$) than the template based ones ($\sigma z_{\rm phot} \sim 0.1$). Both types of redshift have systematic errors $\Delta z_{\rm phot}$ less than ± 0.02 over almost all the range $0.2 \leq z < 0.8$.

Above $z = 0.8$ the systematic errors seem to increase, but as already noted the number of spectroscopic redshifts is much less (Table 10) and may not be representative so the systematic errors are uncertain. Nevertheless, it is worth noting than both plots indicate redshift overestimates beyond $z = 1.2$ (especially the ANNz values). These would mean significant numbers of galaxies being incorrectly redshifted out of our last redshift bin.

We have already noted the implausible dip in ANNz photometric redshift numbers for fainter blue galaxies at $z \sim 0.55$. Figure 46 indicates that template based photometric redshifts also exhibit localised variations in numbers as well as considerable aliasing. However, both of these occur over narrower ranges than the dip in ANNz numbers at $z \sim 0.55$ and largely average out over redshift bins of width 0.2, so they should only affect our results to a small extent.

Cosmic variance cannot be the cause of the dips in numbers because they are larger than the 5% cosmic variance error that we estimate below in §3.9.2. Nor cannot it be the cause of the apparent aliasing with the template based photometric redshifts, because if it was this aliasing would also be visible with the ANNz redshifts.

For the preceding reasons we used template based photometric redshifts rather than ANNz ones, and have confidence in these over our whole redshift range $0.2 \leq z < 1.2$ for red galaxies and over the restricted range $0.2 \leq z < 1.0$ for blue galaxies (and all galaxies combined).

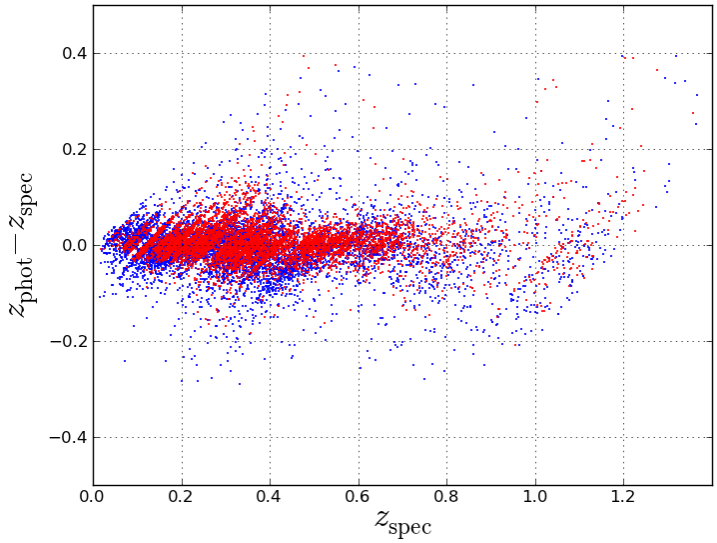

(a)

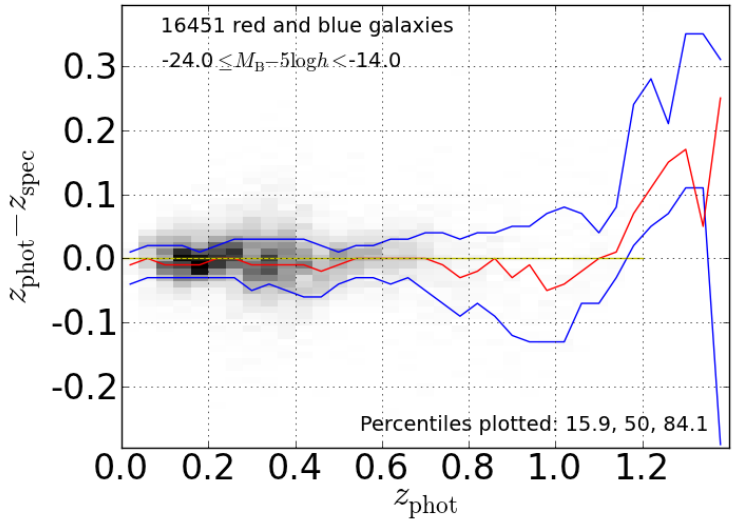

(b)

Fig. 45.—: **Systematic errors in our ANNz photometric redshifts.** (a) errors as a function of spectroscopic redshift, plotted as points, blue galaxies first, then red galaxies, (b) errors as a function of photometric redshift, plotted in bins. We did not use the ANNz photometric redshifts, choosing to use template based ones instead for reasons explained in the text. [The red curves in (b) denote the median error and the blue ones the $1-\sigma$ deviation.]

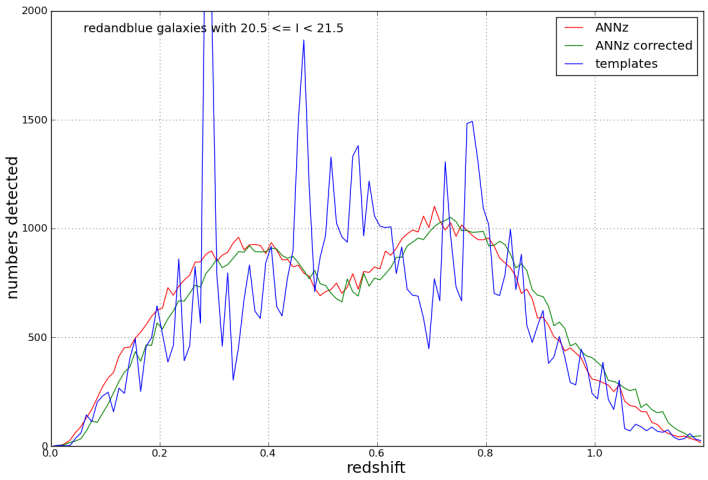

Fig. 46.—: **The anomalous drop in photometric redshift numbers for blue galaxies at $z \sim 0.55$ resulting from the ANNz code.** We did not find a remedy for this and as a result chose to determine our photometric redshifts by template fitting instead. Although template based photometric redshifts show considerable aliasing and localised variations in numbers, both of these occur over narrower ranges than the dip in ANNz numbers at $z \sim 0.55$ and largely average out over redshift bins of width 0.2 mag, so affecting our results to a lesser extent.

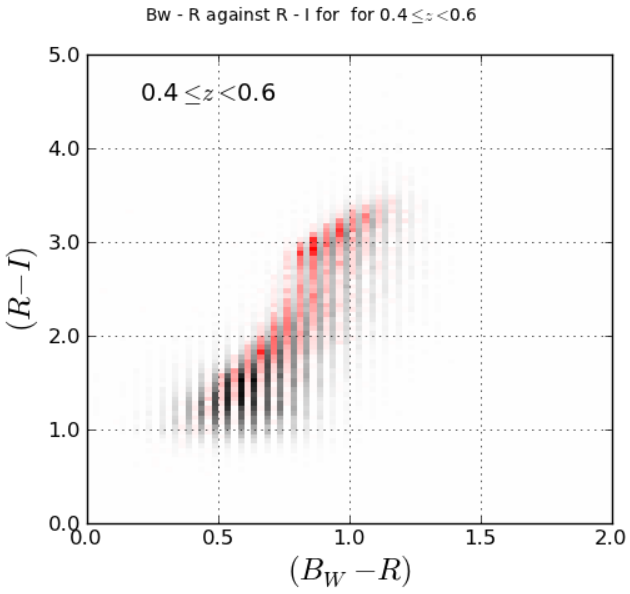

(a)

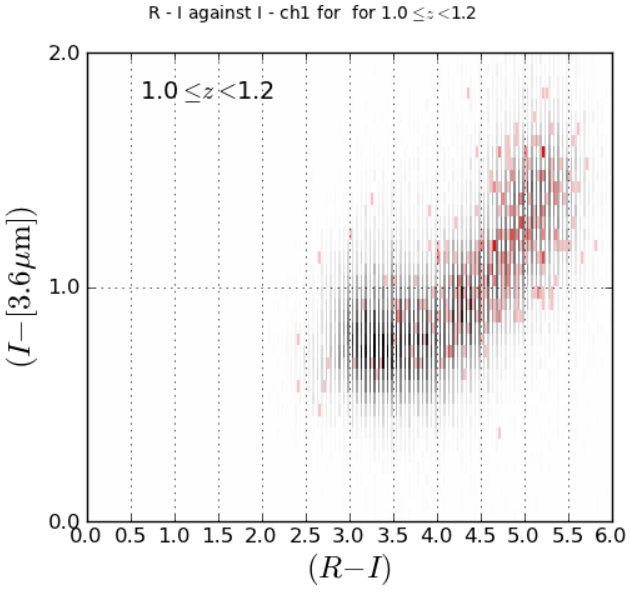

(b)

Fig. 47.—: **Examples of our checks on comparison spectroscopic redshift coverage using colour-colour plots.** The red and black bin densities indicate the distributions of spectroscopic and photometric redshifts respectively. *Top:* At some redshifts such as $z \sim 0.5$ the galaxies with spectroscopic redshifts do not fully span the sample range in colour-colour space. Individual bins are plotted twice, once for spectroscopic redshifts and once for photometric ones. *Bottom:* At redshifts $z > 0.8$ only a few spectroscopic redshifts are available.

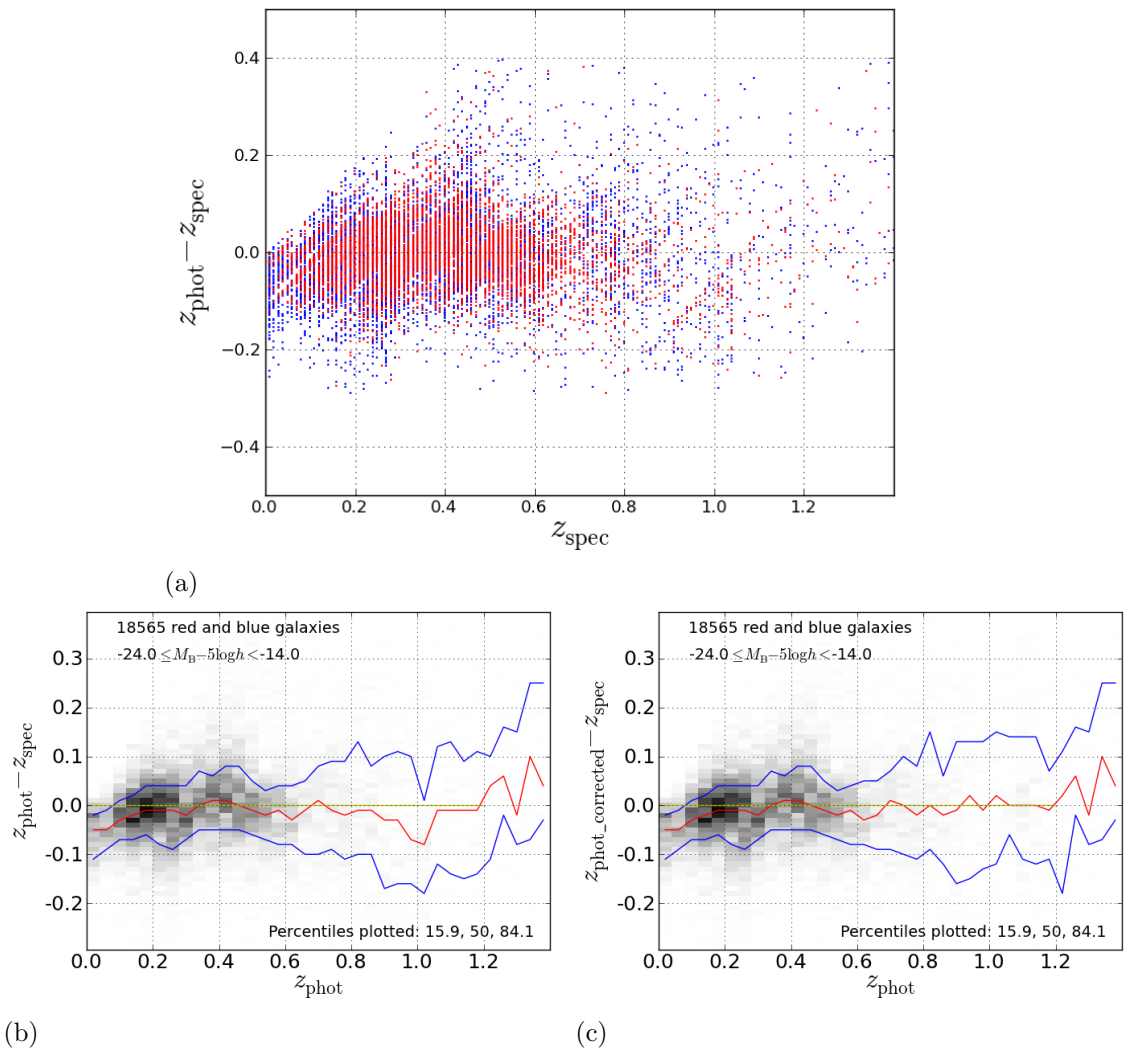

Fig. 48.—: **Systematic errors in our template based photometric redshifts.** (a) errors as a function of spectroscopic redshift, plotted as points, blue galaxies first, then red galaxies, (b) errors as a function of photometric redshift, plotted in bins, (c) errors after applying a correction at $z \sim 1.0$. We chose to use the uncorrected redshifts in preference to the corrected ones for reasons explained in the text. [The red curves in (b) and (c) denote the median error and the blue ones the $1-\sigma$ deviation.]

3.5. Sample selection

As already noted in 3.3, regions surrounding very extended galaxies and saturated stars were removed from our field, and this occurred before our initial sample was generated. We then applied the cuts summarised in Tables 13 and 14 in order to restrict our sample to galaxies with good quality data.

3.5.1. Sample completeness

Our primary magnitude cuts are $I < 23.5$ and [3.6 μm] < 20.5, which provide us with a highly complete sample with reliable photometric redshifts (§3.4). All objects in our sample have good NDWFS, NEWFIRM and IRAC imaging. We correct for I-band non-detections using the method in Brown et al. (2007) which is described below in (§3.8). Having done this we find that our 3.6 μm sample incompleteness is less than 0.8% for the absolute magnitude ranges that we fit Schechter functions to (§3.9).

3.5.2. Excluding stars

Because stellar properties are well defined, stars form a tight sequence in $(B_{\rm w} - R)$ versus $(I - [3.6\mu m])$ colour-colour space and could therefore be excluded using the simple cut shown in Figure 49a.

As confirmation of the effectiveness of this cut in removing stars, we also plotted the difference in measured I-band magnitude when using apertures of diameter 2 and 3 arcsecond (Figure 49b). Objects classified as stars by our colour cut appear as a thin horizontal locus of constant magnitude difference identical to that to be expected for point sources with our chosen point spread function, confirming that they are indeed stars (or possibly quasars, but we exclude these with the further cut in §3.5.3). Although the numbers involved were small, we additionally removed objects for which the difference in I-band magnitudes was more than 0.4 mag for the 2 and 3 arcsecond diameter measurement apertures.

3.5.3. Excluding AGN

AGN were excluded by the three cuts in $([3.6\mu m] - [4.5\mu m])$ versus $([5.8\mu m] - [8.0\mu m])$ colour-colour space shown in Figure 50 and Tables 13 and 14. These cuts are similar to those used by Stern et al. (2005) to select *for* AGN, rather than to exclude them as we

do; however, we have raised their middle cut by 0.2 mag to prevent it removing significant numbers of galaxies which do not have AGN. Our cuts do result in a small number of AGN not being excluded that should be, and for this reason any galaxies classified as AGN by AGES and/or SDSS are also excluded. Figure 50 also shows that our template galaxies would not be excluded by our cuts.

Table 13. Cuts used to select objects and separate red and blue galaxies.

cut number	purpose of cut	cuts
1	exclude faint I-band objects	$I > 23.5$
2	exclude objects with faint near infrared	$[3.6\mu\mathrm{m}] > 20.5$
3	exclude stars, [see Figure 49a]	$(R - I) > 0.25 + 0.5(I - [3.6\mu\mathrm{m}])$
4	exclude stars, [see Figure 49b]	$I_{2\mathrm{arcsecond}} - I_{3\mathrm{arcsecond}} \leq 0.4$
5	exclude AGN	$([3.6\mu\mathrm{m}] - [4.5]) > 0.18 + 0.2([5.8] - [8.0])$
	(using modified	and $([5.8] - [8.0]) > 0.6$
	Stern et al. (2005) cuts	and $([3.6\mu\mathrm{m}] - [4.5]) > 0.6 + 2.5([5.8] - [8.0] - 1.6)$
6	exclude further AGN identified by SDSS and AGES	
7	restrict abs mag range	$-24.0 \leq M_{\mathrm{B}} < -14.0$
8	red-blue separation	$(M_{\mathrm{U}} - M_{\mathrm{B}}) > 0.165 - 0.18z - 0.03(M_{\mathrm{B}} + 19.5)$

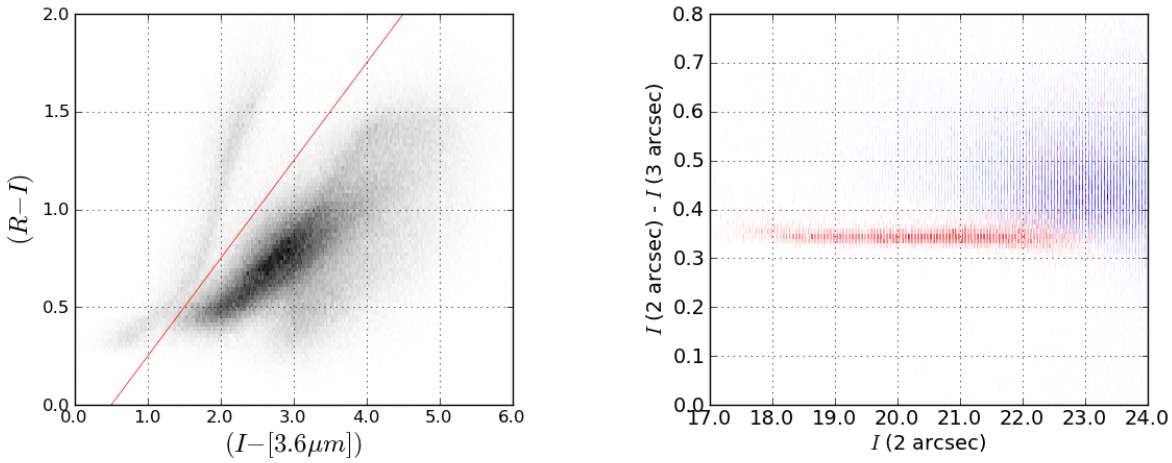

(a) (b)

Fig. 49.—: **Excluding stars.** (a) The colour-colour cut $(R - I) \geq -0.25 + 0.5(I - [3.6\mu m])$ effectively removes stars from the sample, except for a small amount of overlap withg very blue galaxies with $(I - [3.6\mu\text{m}]) \leq 2.0$. (b) The I- magnitude difference measured using apertures of diameter 2 arcsecond and 3 arcsecond is plotted against the 2 arcsecond magnitude. Red bins are stars as defined by the cut in (a) while blue bins are galaxies (i.e the remainder). For objects brighter than $I = 21.0$ this plot produces a very clear separation between stars, which are point sources, and galaxies, which are extended sources.

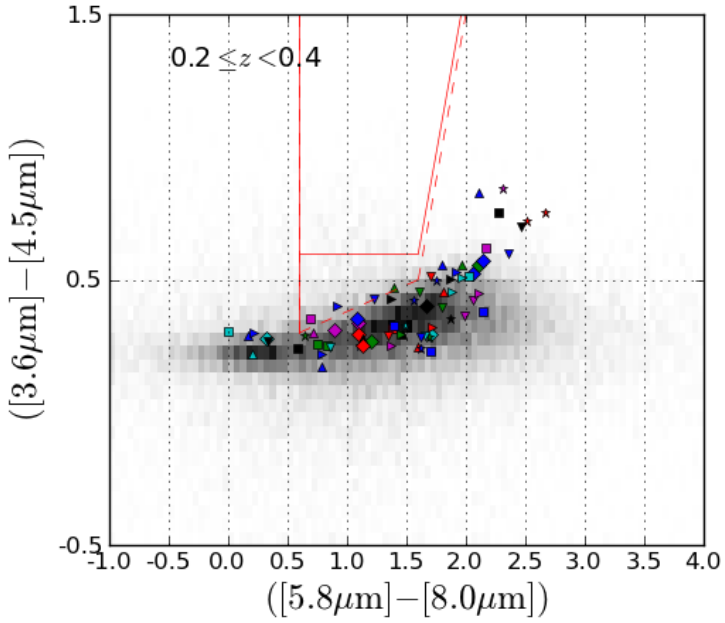

Fig. 50.—: **Excluding AGN.** AGN are removed using the IRAC colour-colour cuts shown by the three solid red lines. These are modifications of the cuts (dashed lines) used by Stern et al. (2005) to select *for* AGN rather than to exclude them. As an example, we show the redshift bin, $0.2 \leq z_{\rm phot} < 0.4$. The coloured markers indicate our template galaxies at $z_{\rm phot} = 0.3$. The galaxies appearing significantly redder than the template locus have artificially high red colours due to noise in the 8.0 μm band.

Table 14. Numbers of objects removed by the cuts.

-	initially	cut 1	cut 2	cut 3	cut 4	cut 5	cut 6	cut 7	cut 8	cut 9
			incomplete			stars	stars	AGN	known	
-	-	duplicates	$Bw, R, I, [3.6\mu\mathrm{m}]$	r'$I > 23.5$'	$[3.6\mu\mathrm{m}] > 20.5$	by colour cut	by profile	by cut	AGN	$-24 \leq M_\mathrm{B} < -14$
NUMBERS REJECTED BY CUT										
$0 \leq z < 0.2$	-	1173	3244	161085	37636	16952	1375	636	6	8124
$0.2 \leq z < 0.4$	-	1424	2190	66239	37526	13947	579	715	8	41
$0.4 \leq z < 0.6$	-	834	1373	45939	24693	7947	286	380	13	606
$0.6 \leq z < 0.8$	-	291	2083	85488	24058	4079	79	252	18	510
$0.8 \leq z < 1$	-	119	2008	88116	15713	3293	60	346	20	474
$1 \leq z < 1.2$	-	83	1243	63028	3219	969	79	450	20	740
$1.2 \leq z < inf$	-	264	11235	408287	25995	9541	520	7854	50	98514
$0.2 \leq z < 1.2$		2751	8897	348810	105209	30235	1083	2143	79	2371
$0 \leq z < inf$		4188	23376	918182	168840	56728	2978	10633	135	109009
NUMBERS REMAINING AFTER CUT										
$0 \leq z < 0.2$	263351	262178	258934	97849	60213	43261	41886	41250	41244	33120
$0.2 \leq z < 0.4$	187119	185695	183505	117266	79740	65793	65214	64499	64491	64450
$0.4 \leq z < 0.6$	149054	148220	146847	100908	76215	68268	67982	67602	67589	66983
$0.6 \leq z < 0.8$	194147	193856	191773	106285	82227	78148	78069	77817	77799	77289
$0.8 \leq z < 1$	181042	180923	178915	90799	75086	71793	71733	71387	71367	70893
$1 \leq z < 1.2$	120679	120596	119353	56325	53106	52137	52058	51608	51588	50848
$1.2 \leq z < inf$	569432	569168	557933	149646	123651	114110	113590	105736	105686	7172
$0.2 \leq z < 1.2$	832041	1660636	1637260	719078	550238	493510	490532	479899	479764	370755
$0 \leq z < inf$	1664824	829290	820393	471583	366374	336139	335056	332913	332834	330463
TOTAL REMOVED AFTER CUT										
	402066	406254	429630	1347812	1516652	1573380	1576358	1586991	1587126	1696135
TOTAL										
	2066890	2066890	2066890	2066890	2066890	2066890	2066890	2066890	2066890	2066890

3.6. Calculation of absolute U, B and V magnitudes

We use the method described in Chapter 2, calculating the absolute magnitude M_W in a waveband W from a polynomial fit to a plot of $(M_W + D_M) - m_Z$ against $(m_Y - m_Z)$, where m_Y and m_Z are the observed apparent magnitudes in two appropriately chosen wavebands and D_M is the distance modulus. Figure 51 shows the restframe and observed optical spectra of four template galaxies with representative SEDs in relation to our optical filters. Table 15 lists the observed colours $(m_Y - m_Z)$ that we used at different redshifts and Figures 52 to 58 show sample polynomial fits at six redshifts.

Although we do not use absolute V-band magnitudes in the determination of B-band luminosity functions we include them here for convenience as they are needed for determining stellar mass functions (Chapter 4).

Table 15. The observed colours used to determine absolute U, B and V magnitudes.

restframe waveband M_W	effective wavelength μm	redshift range	colour $(m_Y - m_Z)$
U	0.361	0.0 to 0.8	$(B_w - R)$
U	0.361	0.8 to 1.2	$(R - I)$
B	0.441	0.0 to 0.4	$(B_w - R)$
B	0.441	0.4 to 0.8	$(R - I)$
B	0.441	0.8 to 1.2	$(I - J)$
V	0.551	0.0 to 0.46	$(R - I)$
V	0.551	0.46 to 1.2	$(I - J)$

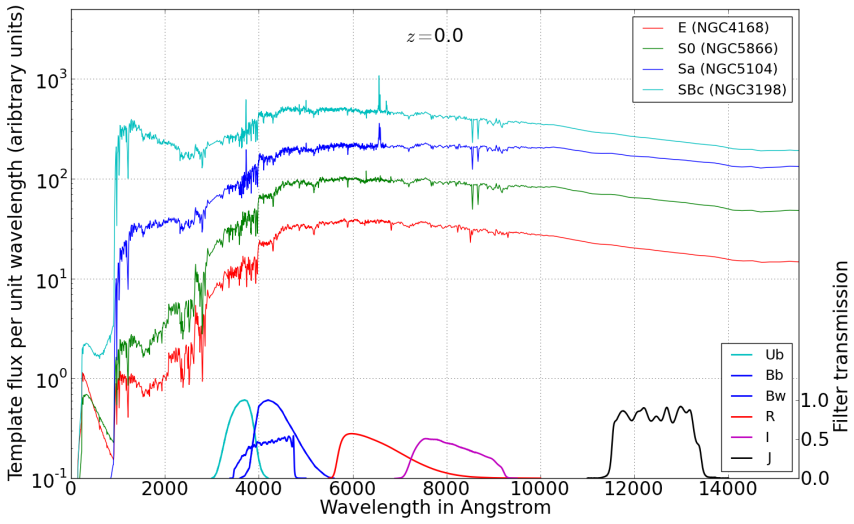

(a)

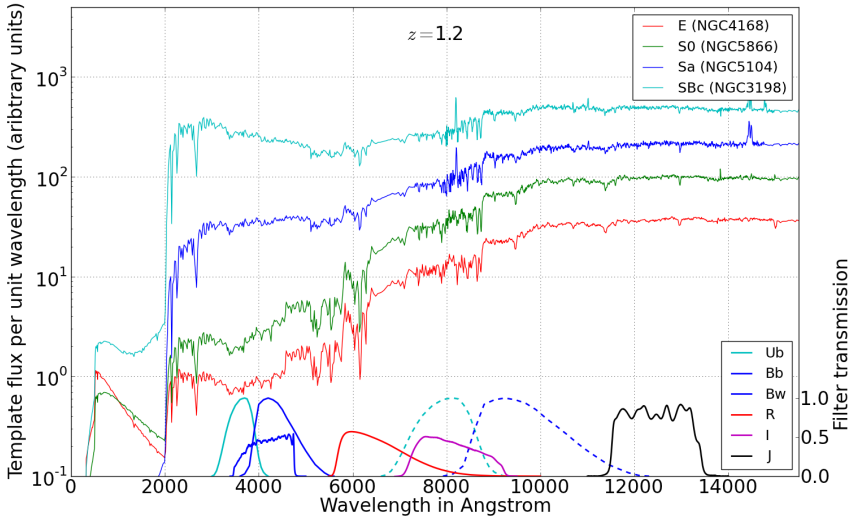

(b)

Fig. 51.—: **The restframe and observed optical spectra of four template galaxies with representative SEDs.** *Top:* The SEDs at $z = 0$ (offset artificially for clarity) together with the restframe Bessell B and U-bands in relation to the NDWFS B_w, R and I filters, and the NEWFIRM J filter; *bottom:* observed SEDs from galaxies at $z = 1.2$ with the same representative restframe SEDs. The redshifted restframe B and U-band filters are shown dashed in the lower figure. Over the redshift range of interest, $0.2 \leq z \leq 1.2$, the part of the SED sampled by the restframe U-band moves from being observed through the Bw filter to being observed through the I-band filter. Similarly the restframe B-band moves from the Bw waveband to beyond the I waveband.

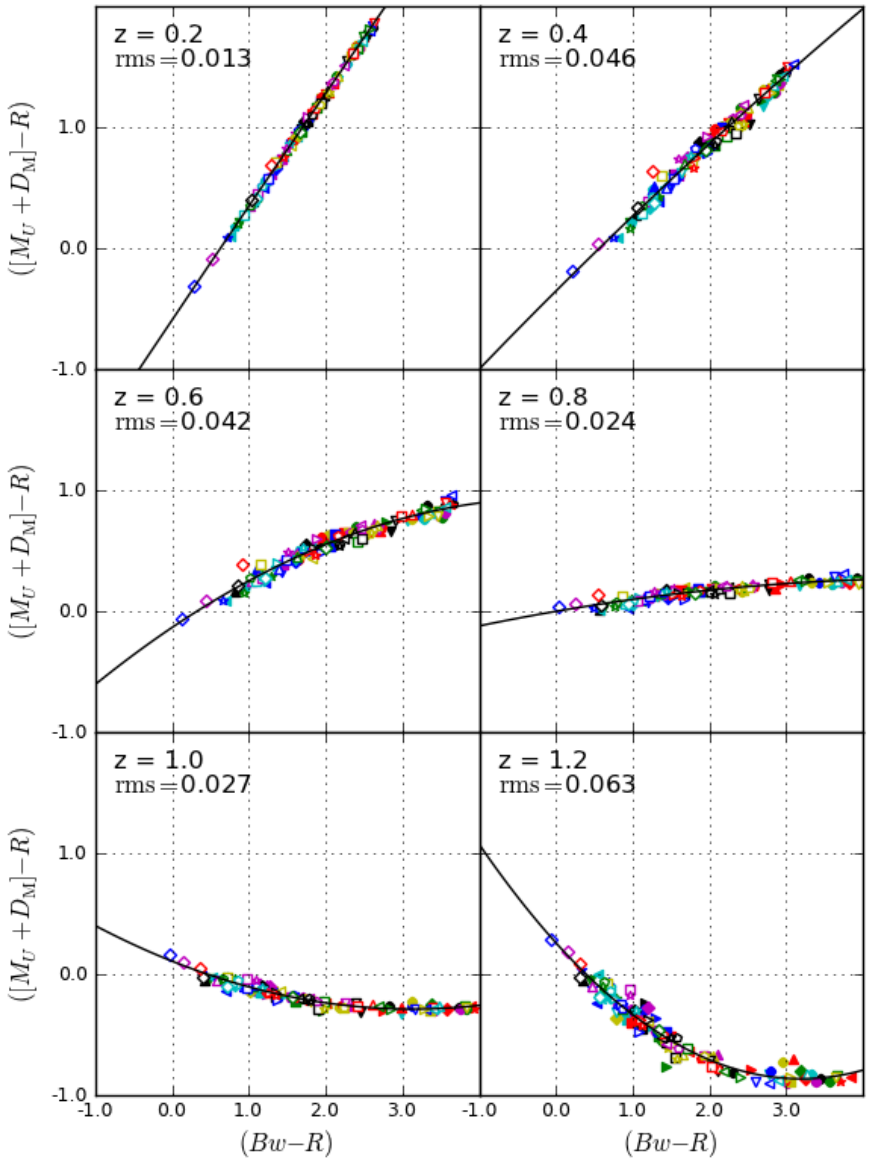

Fig. 52.—: **Evolution of the second order polynomial used to determine absolute U magnitudes from observed $(Bw - R)$ colour between $z = 0$ to $z = 0.8$.**

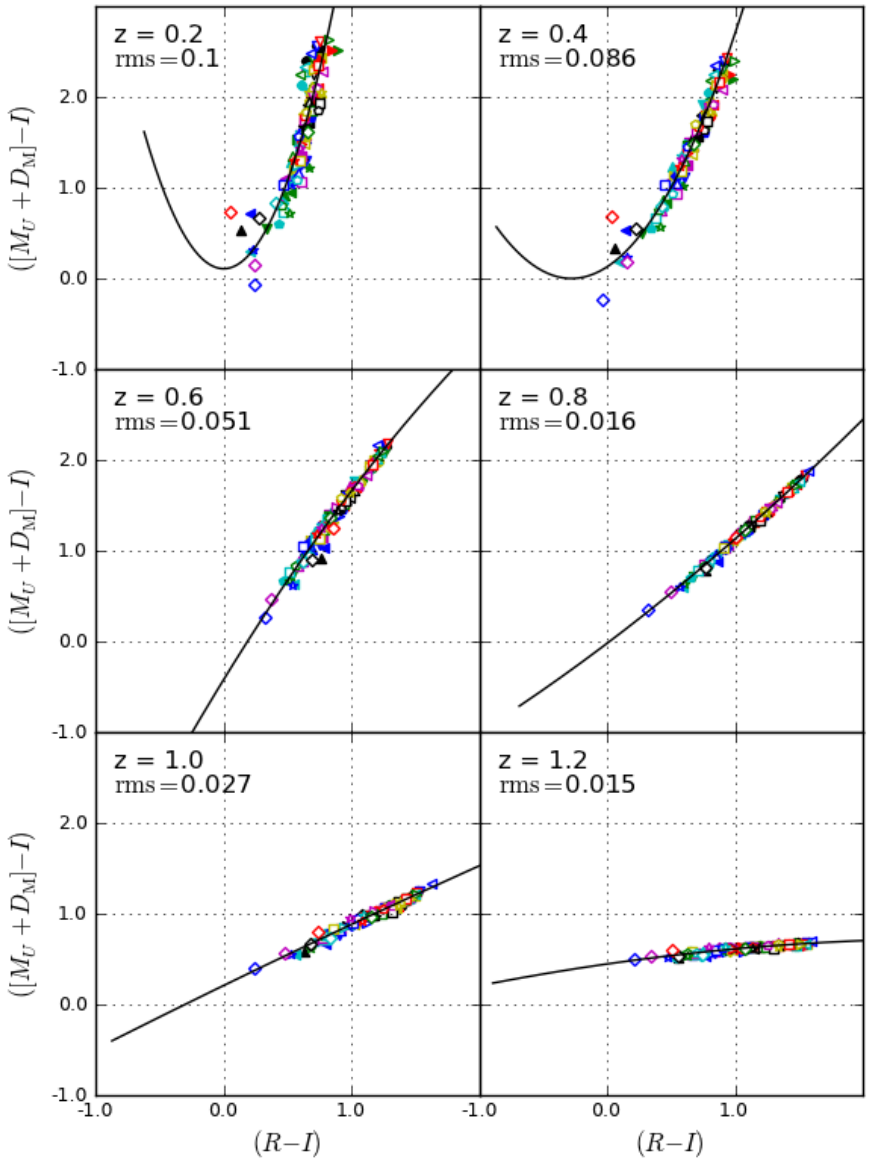

Fig. 53.—: **Evolution of the second order polynomial used to determine absolute U magnitudes from observed $(R - I)$ colour between $z = 0.8$ to $z = 1.2$.**

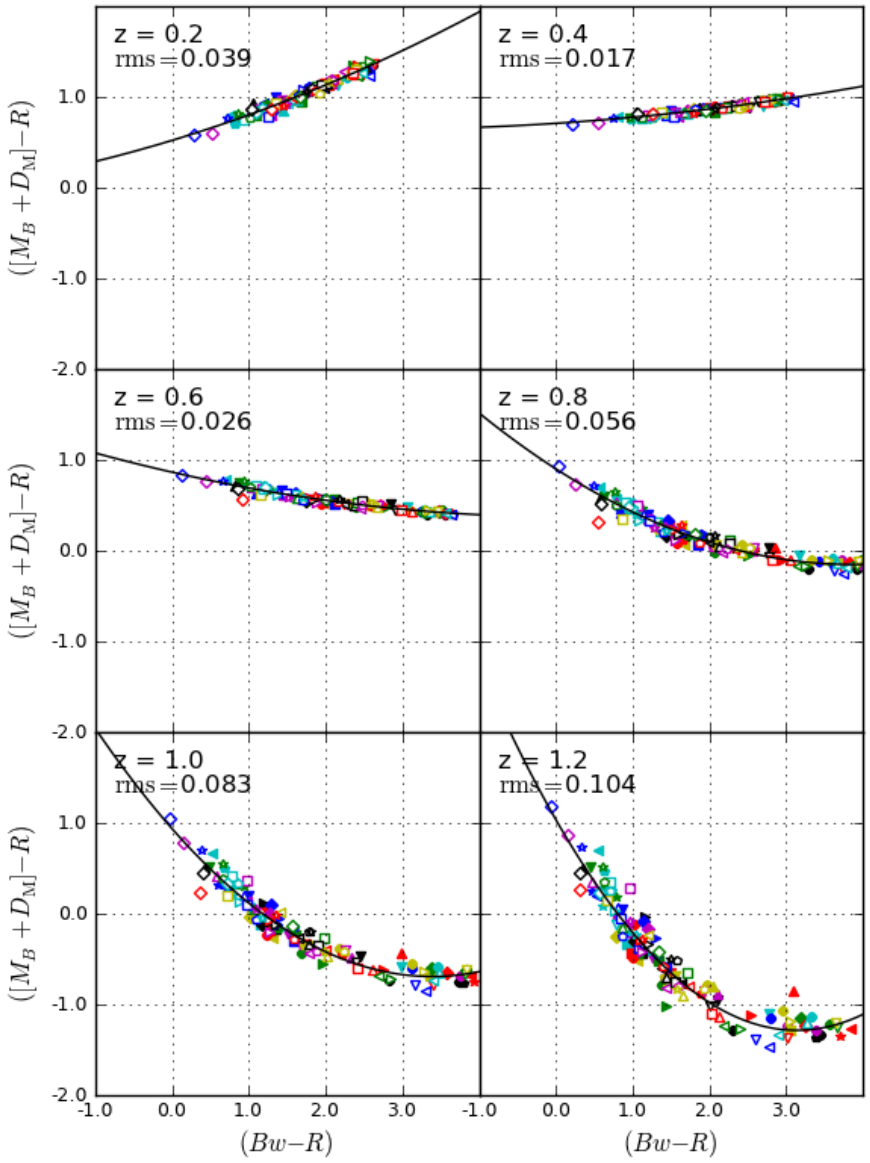

Fig. 54.—: **Evolution of the second order polynomial used to determine absolute B magnitudes from observed $(Bw - R)$ colour between $z = 0$ to $z = 0.8$.**

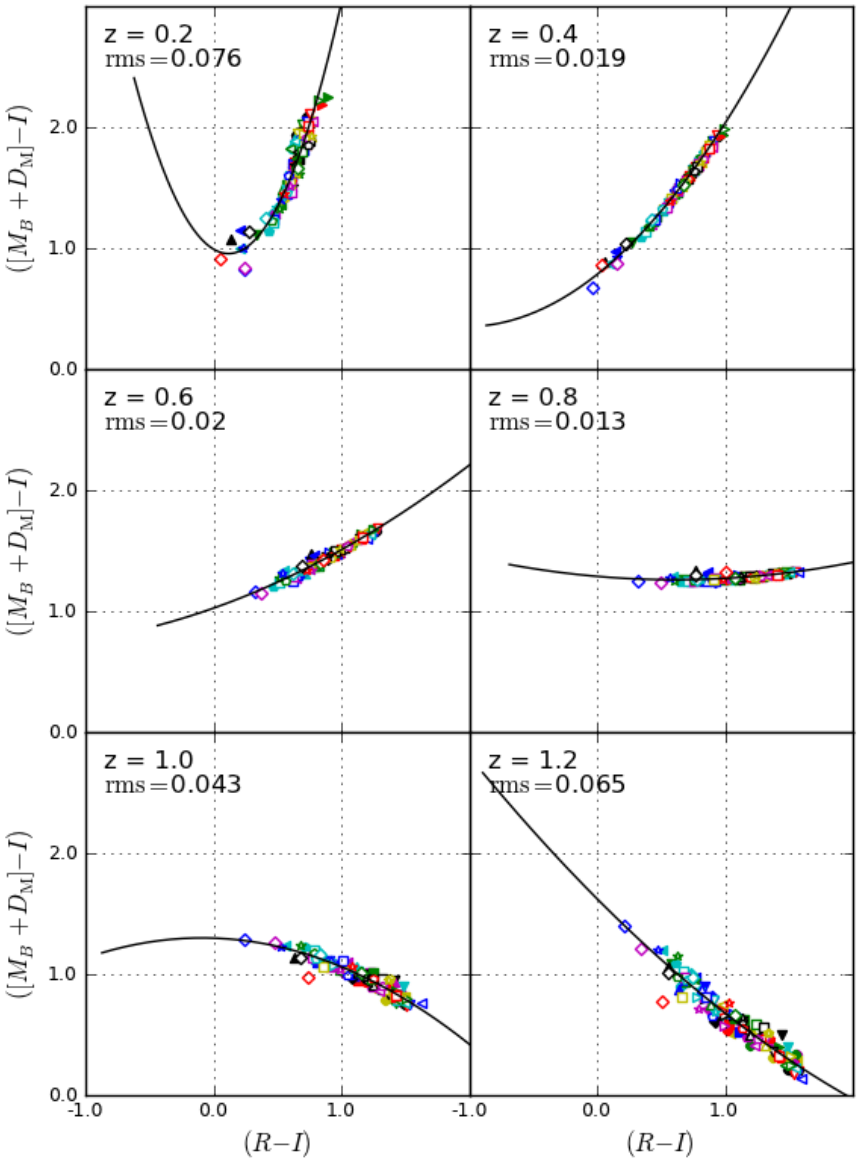

Fig. 55.—: **Evolution of the second order polynomial used to determine absolute B magnitudes from observed $(R-I)$ colour between $z = 0.4$ to $z = 0.8$.**

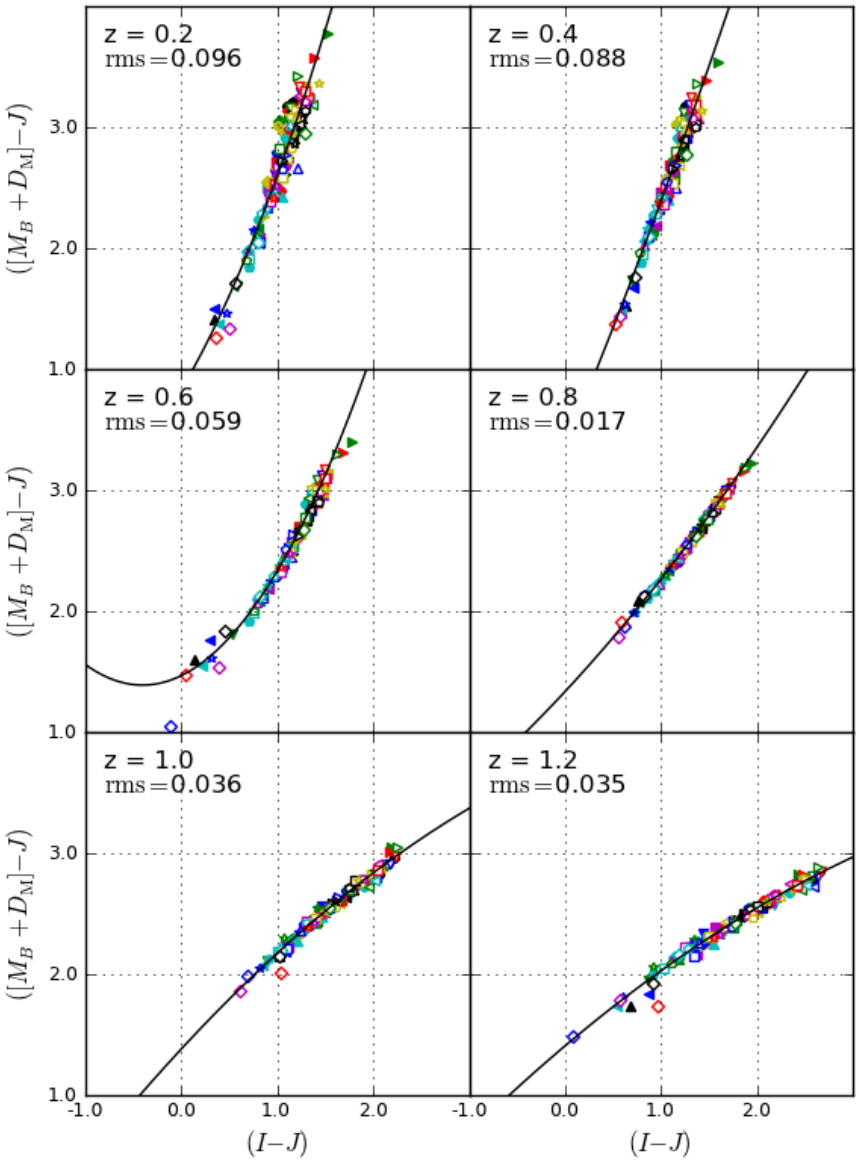

Fig. 56.—: **Evolution of the second order polynomial used to determine absolute B magnitudes from observed $(I - J)$ colour between $z = 0.8$ to $z = 1.2$.**

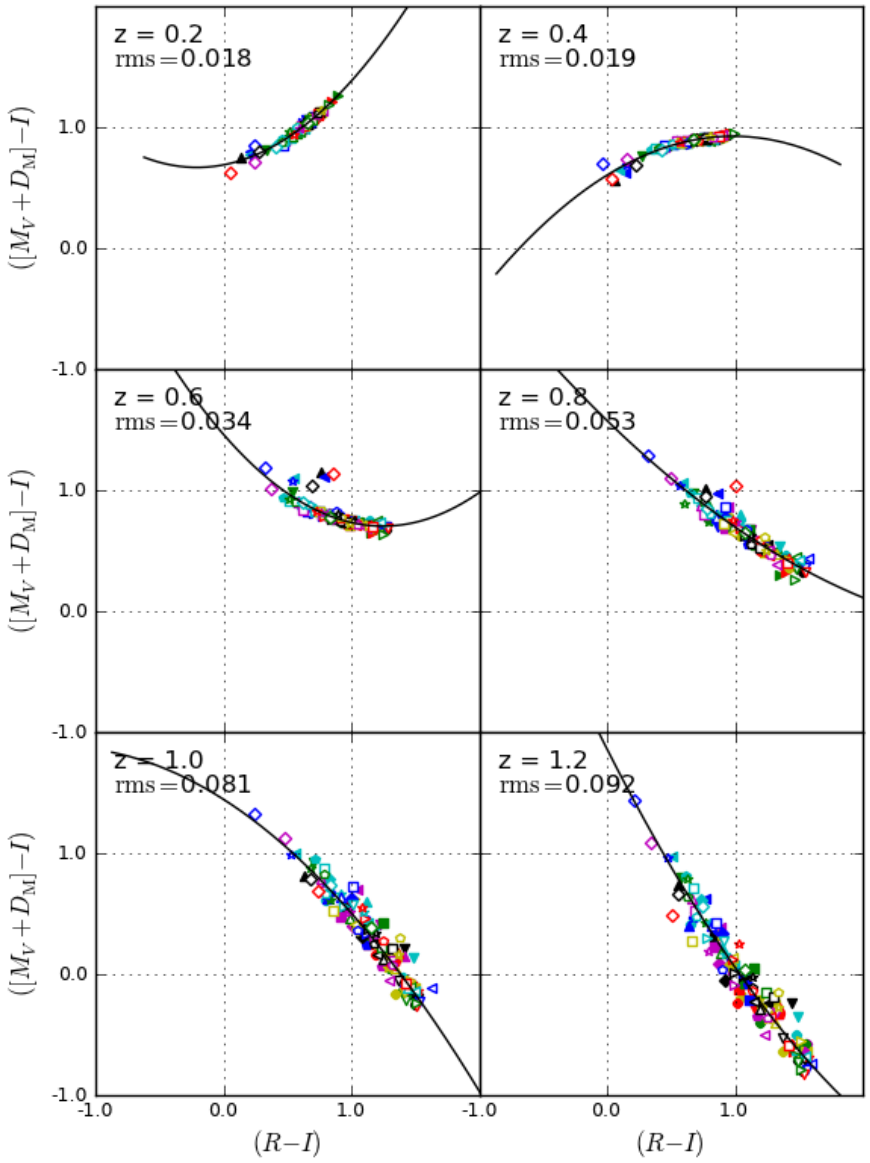

Fig. 57.—: **Evolution of the second order polynomial used to determine absolute V magnitudes from observed $(R-I)$ colour between $z = 0$ to $z = 0.46$.**

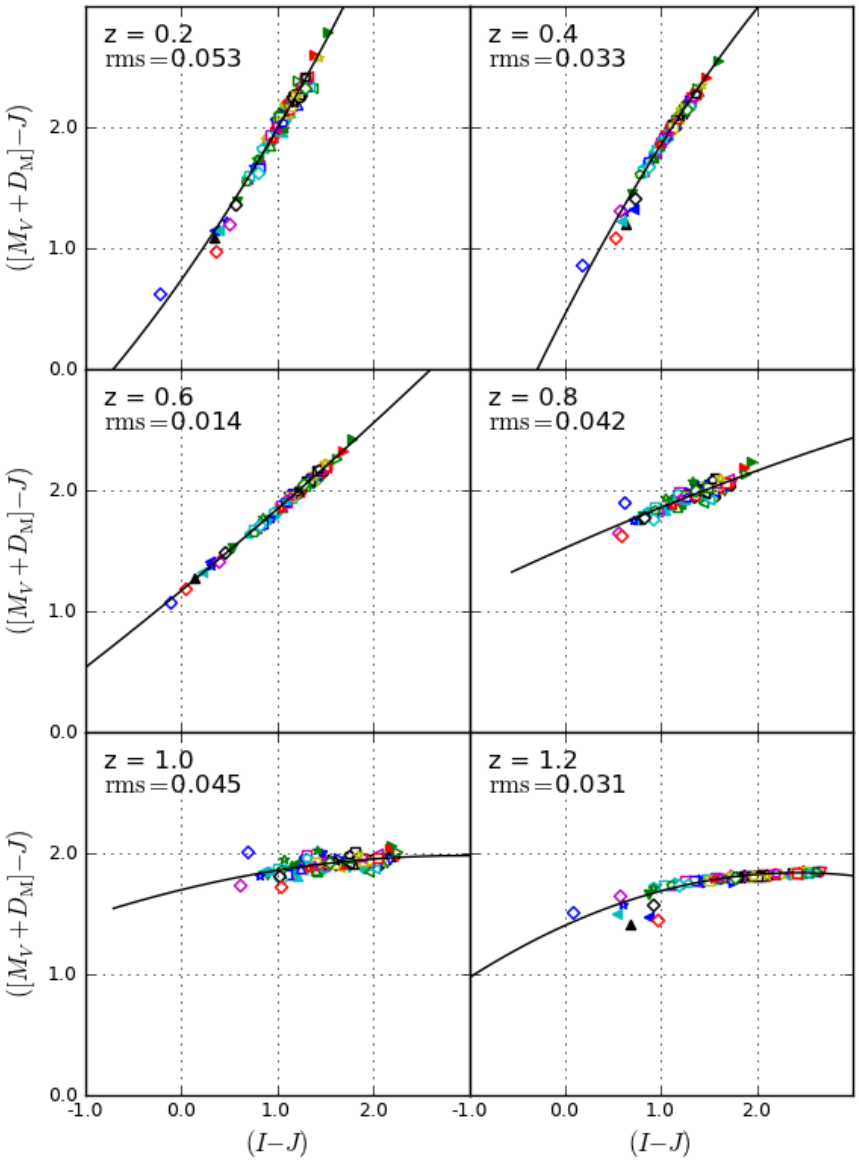

Fig. 58.—: **Evolution of the second order polynomial used to determine absolute V magnitudes from observed $(I - J)$ colour between $z = 0.46$ to $z = 1.2$.**

3.7. Separating red and blue galaxies

As Figure 59 shows, bimodality is evident beyond $z = 1$ on a $(M_{\rm U} - M_{\rm B})$ versus $M_{\rm B}$ colour-magnitude plot. We separated red and blue galaxies using an evolving empirical cut through the centre of the green valley, the position of which was determined for each redshift bin from histograms of galaxy colours at a range of absolute magnitudes. This resulted in our definition of a red galaxy as one for which:

$$(M_{\rm U} - M_{\rm B}) > 0.165 - 0.18z - 0.03(M_{\rm B} + 19.5). \quad (31)$$

In their determinations of B band luminosity functions, Willmer et al. (2006) and Faber et al. (2007) used a similar but redshift independent $(M_{\rm U} - M_{\rm B})$ versus $M_{\rm B}$ cut, which was approximately 0.05 mag above our own: $(M_{\rm U} - M_{\rm B}) > 0.617 - 0.032(M_{\rm B} + 21.52) - 0.52$ (when converted from AB to Vega magnitudes). Bell et al. (2004) used a redshift-dependent red-blue cut based on a plot of $(M_{\rm U} - M_V)$ versus M_V, and Brown et al. (2007) used a very similar cut, but we prefer to use $(M_{\rm U} - M_{\rm B})$ versus $M_{\rm B}$ because it gives clearer bimodality with our data set.

We checked the dependence of our measured Schechter luminosity function parameters (§3.9) on the exact position of the red-blue cut. We found that varying the cut up by 0.05 mag, or down by 0.05 mag (Table 16), made less than 16% difference to the space density parameter ϕ^* or the luminosity density $j_{\rm B}$ in the case of red galaxies, and less than 6% difference in the case of blue galaxies. For the characteristic magnitude parameter M^* and the the measured magnitude (§3.10.3) of the very brightest galaxies $M^{\rm fixed}$ the variations were no more than 0.06 mag, and generally much less, especially for red galaxies.

As an additional check on our red-blue cut at redshifts $z \sim 0.8$ and beyond, we also plotted observed $(B_w - R)$ and $(R - I)$ colours against redshift. At $z \sim 0.3$, the redshifted restframe U and B wavebands lie between the observed B_w and R-bands, and at $z \sim 0.8$ they coincide with the observed R and I-bands. We therefore expect restframe $(M_{\rm U} - M_{\rm B})$ bimodality to be reflected in observed $(B_w - R)$ bimodality at lower redshifts and $(R - I)$ bimodality at higher redshifts. Figure 60 shows that this is indeed the case.

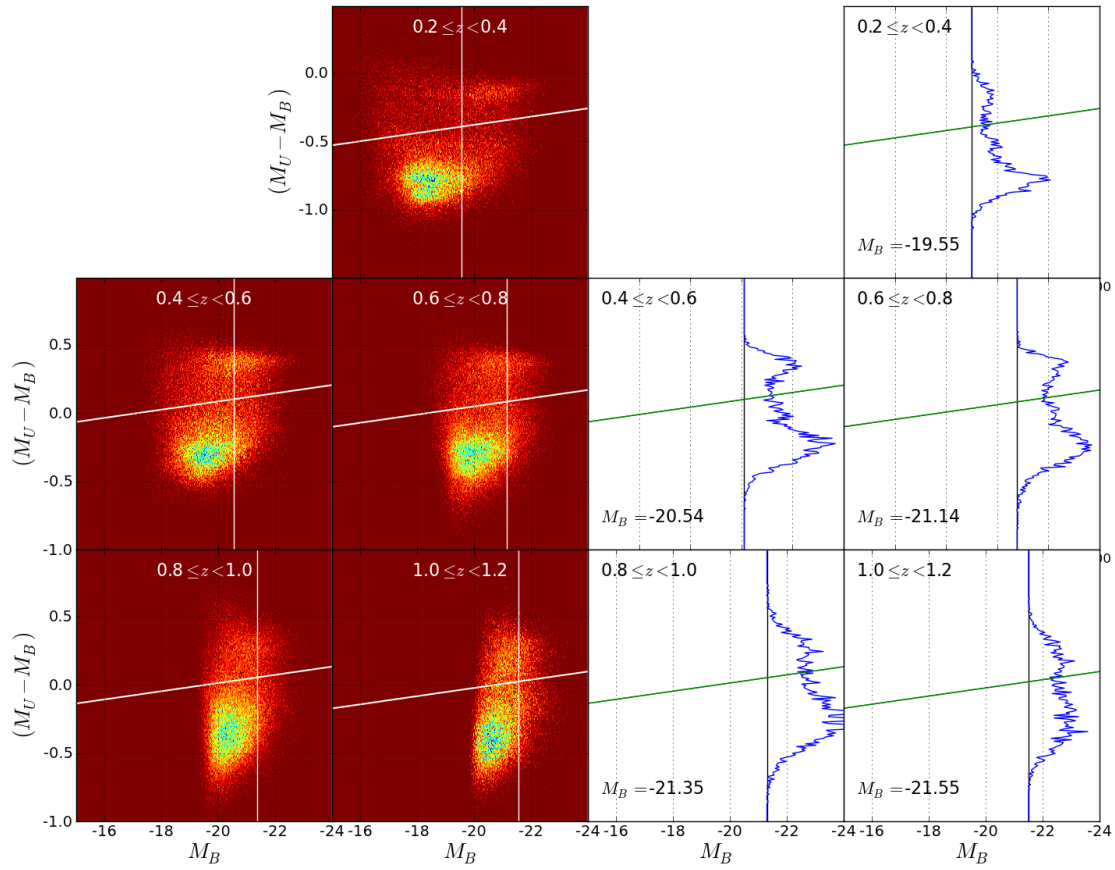

Fig. 59.—: **How an evolving cut in the $(M_{\rm U} - M_{\rm B})$ versus $M_{\rm B}$ plane is used to separate red and blue galaxies.** The cut is given by Equation 31). The histograms on the right show graphically how the position of the green valley was determined and indicate that bimodality is present even in the highest redshift bin.

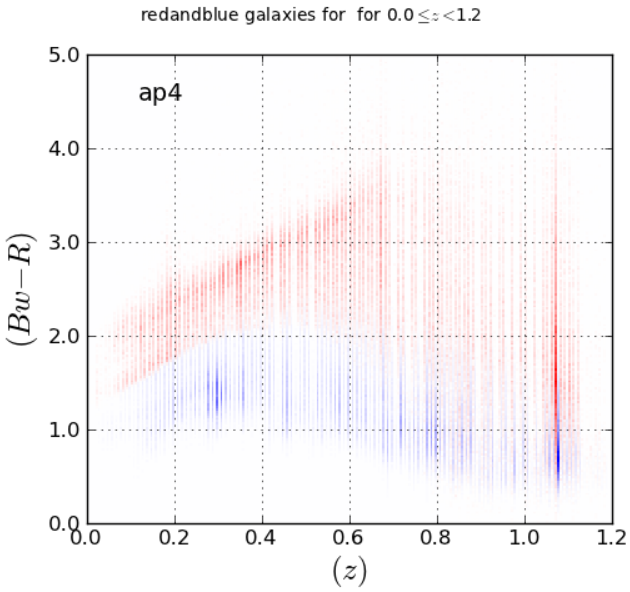

(a)

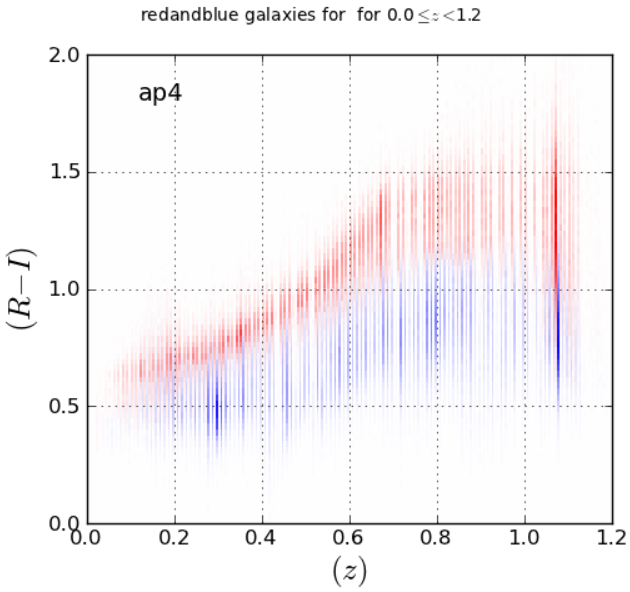

(b)

Fig. 60.—: **Confirming that our restframe colour-magnitude separation of red and blue galaxies also separates the sample in apparent colour redshift plots.** The red and blue bins correspond to galaxies classified as red and blue by our evolving restframe colour-magnitude plot. We observe that this red /blue separation agrees with the observed bimodality in $(B_w - R)$ colour at lower redshifts (*top*) and $(R - I)$ bimodality at higher redshifts (*bottom*). [Each colour-redshift bin is plotted twice, once for red galaxies and once for blue.]

Table 16. Numbers of red and blue galaxies resulting from our preferred restframe $(M_U - M_B)$ versus M_B colour-magnitude cut and cuts 0.02 mag above and below.

	red -	blue -	all -	red cut up 0.02 mag	blue cut up 0.02 mag	all cut up 0.02 mag	red cut down 0.02 mag	blue cut down 0.02 mag	all cut down 0.02 mag
$0 \leq z < 0.2$	7741	13452	21193	7317	13876	21193	8243	12950	21193
$0.2 \leq z < 0.4$	13703	46200	59903	13021	46882	59903	14412	45491	59903
$0.4 \leq z < 0.6$	21070	49988	71058	20138	50920	71058	21998	49060	71058
$0.6 \leq z < 0.8$	21413	60039	81452	20354	61098	81452	22527	58925	81452
$0.8 \leq z < 1$	19886	71122	91008	18759	72249	91008	21081	69927	91008
$1 \leq z < 1.2$	11327	33983	45310	10701	34609	45310	11960	33350	45310
$1.2 \leq z <$ inf	227	604	831	207	624	831	242	589	831
all redshifts	95367	275388	370755	90497	280258	370755	100463	270292	370755
$0.2 <= z < 1.2$	87399	261332	348731	82973	265758	348731	91978	256753	348731

3.8. Completeness correction

At the apparent magnitudes of interest the completeness is largely determined by source confusion rather than objects being lost in background noise. Brown et al. (2007) measured the completeness for red galaxies in the Boötes field by adding mock galaxies to their catalogue and then attempting to recover them. They found the completeness, as a function of observed I-magnitude, was well described by $C_I(I) = 1 - 0.05(I - 21.0)$ for $21.0 < I \leq 23.5$ and $C_I(I) = 1$ for $I \leq 21.0$. We assume that the same formula applies when blue galaxies are included. Our apparent magnitude limit of $I = 23.5$ [for which $C_I(23.5) = 0.875$] is designed to ensure completeness of better than 85%.

For any given absolute magnitude there will be galaxies at a range of different redshifts, and these will have different apparent magnitudes, depending on how far way they are. However, the completeness correction as a function of absolute magnitude can be determined, if, in any particular redshift bin, the galaxies are binned by both absolute magnitude M and apparent magnitude I.

In any particular bin $\Delta M \Delta I$, the completeness is a function $C_I(I)$ of the apparent magnitude I only. If there are $n(M, I)$ galaxies in a particular bin, the true number of galaxies in the bin, allowing for the additional undetected ones, will be $n(M, I)$, where:

$$n(M, I) = \frac{n(M, I)}{C_I(I)}. \tag{32}$$

The true number of galaxies in each absolute magnitude bin ΔM, including undetected ones, was then computed by dividing the total observed number by the absolute magnitude completeness factor $C_M(M)$ given by the following equation, where the sum is over bins of width $\Delta I = 0.25$:

$$C_M(M) \; = \; \sum_I n(M, I) \; \Big/ \; \sum_I n(M, I)/C_I(I). \tag{33}$$

We found that the completeness as a function of absolute magnitude varied between 88% and 100%.

3.9. Determination of luminosity functions

As a first approximation to the luminosity function, we calculated the (completeness corrected) space densities of red galaxies, blue galaxies, and all galaxies combined, in each of

five redshifts bins between $z = 0.2$ and $z = 1.2$ using the $1/V_{\max}$ best fit method (Schmidt 1968). Our results are shown in Figures 61 to 63 and Table 18, together with results from the prior literature. All space densities have been converted to the values that would be obtained assuming a Hubble Constant of $H_0 = 100h$ km s^{-1} Mpc^{-1} where $h = 1$.

3.9.1. Maximum likelihood fits for Schechter functions

The following derivation is based on that in Marshall (1983), but has been amended to treat objects in different redshift ranges separately. Furthermore, Marshall's analysis is in terms of luminosities, whereas magnitudes have been used here.

For any given range, $z_{\min} \leq z < z_{\max}$, and a range of absolute magnitudes, $M_{\min} \leq M < M_{\max}$, construct an array of small elements $\Delta z \Delta M$ in redshift-magnitude space.

Number the elements using the index i, and let (z_i, M_i) be the centre of the ith element.

Let $\rho(z, M)$ be the density of galaxies per steradian in (z, M) space and Ω the survey solid angle in steradians. Then:

$$\mu_i = \rho(z_i, M_i)\Omega\Delta z\Delta M g(z_i, M_i). \tag{34}$$

is the mean rate [per unit area in (z, M) space] at which galaxies are detected and $g(z_i, M_i)$ is the completeness for absolute magnitude M_i at redshift z_i.

Assuming that the absolute magnitudes of adjacent galaxies are not correlated, we have a Poisson distribution in (z, M) space, so that the probability of finding exactly m galaxies in element $\Delta z \Delta M$ at (z_i, M_i) is:

$$P_m = \frac{1}{m!}{\mu_i}^m e^{-\mu_i}$$

Given sufficiently small elements $\Delta z \Delta M$, the probability of more than one galaxy in any one element can be ignored, and we just need to consider the probabilities P_0 and P_1 of either no galaxies or exactly one:

$$P_0 = e^{-\mu_i}, \qquad P_1 = \mu_i e^{-\mu_i}. \tag{35}$$

We will use the index j to denote all values of i where a galaxy is present and k for all those where no galaxy is present. Then, given any observed distribution of galaxies amongst the

elements in (z, M) space, the probability of this distribution occurring entirely by chance based on the Poisson probabilities given by (35) is:

$$P(\text{obs}) = \prod_{\text{obs } j} \mu_j e^{-\mu_j} \prod_k e^{-\mu_k}$$

$$P(\text{obs}) = \prod_{\text{obs } j} \mu_j \prod_{\text{all } i} e^{-\mu_i}. \tag{36}$$

In the case of the Schechter function, $\rho(z, M)$ contains three parameters, ϕ^*, M^* and α, which we will denote by a, b, c for simplicity. The aim is to determine the values of these parameters from the data using the maximum likelihood method.

Given a specific set of values for the parameters, a, b, c , say, we can calculate the probability of the observed distribution in (z, M) space, and this is called the likelihood function:

$$L(a, b, c) \equiv P(\text{obs}|a, b, c). \tag{37}$$

Writing the dependence of μ_i explicitly, we have:

$$L(a, b, c) = \prod_{\text{obs } j} \mu_j(a, b, c) \prod_{\text{all } i} e^{-\mu_i(a,b,c)}. \tag{38}$$

The maximum likelihood method finds the values of (a, b, c) which maximise L.

It is simpler, however, to minimise:

$$S = -2 \ln L. \tag{39}$$

Then:

$$S(a, b, c) = -2 \sum_{\text{obs } j} \ln[\mu_j(a, b, c)] - 2 \sum_{\text{all } i} \ln[e^{-\mu_i(a,b,c)}]. \tag{40}$$

Using (34) we have:

$$\mu_i(a, b, c) = g(z_i, M_i)\rho(z_i, M_i; a, b, c))\Omega \Delta z \Delta M. \tag{41}$$

and so:

$$S(a,b,c) = -2\sum_{\text{obs } j} \ln[g(z_j,M_j)\rho(z_j,M_j;a,b,c)\Omega\Delta z\Delta M] + 2\sum_{\text{all } i} g(z_i,M_i)\rho(z_i,M_i;a,b,c)\Omega\Delta z\Delta M. \tag{42}$$

Now let $\phi(z,M)$ be the space density per unit comoving volume of galaxies with redshift z and absolute magnitude M so that:

$$\rho(z,M;a,b,c)\Delta z\Delta M = \phi(z,M;a,b,c)\Delta V\Delta M. \tag{43}$$

and:

$$\rho(z,M;a,b,c) = \phi(z,M;a,b,c)\frac{dV}{dz}. \tag{44}$$

Substituting (44) in (42):

$$\begin{aligned} S(a,b,c) = &-2\sum_{\text{obs } j} \ln[g(z_j,M_j)\phi(z_j,M_j;a,b,c)\frac{dV}{dz}\Omega\Delta z\Delta M] \\ &+ 2\Omega\int_{z_{min}}^{z_{max}} \frac{dV}{dz}dz \int_{M_{min}}^{M_{max}} g(z,M)\phi(z,M;a,b,c)dM \end{aligned}$$

$$\begin{aligned} S(a,b,c) = &-2\sum_{\text{obs } j} \ln[g(z_j,M_j)\phi(z_j,M_j;a,b,c) - 2N\ln\left[\frac{dV}{dz}\Omega\Delta z\Delta M\right] \\ &+ 2\Omega\int_{z_{min}}^{z_{max}} \frac{dV}{dz}dz \int_{M_{min}}^{M_{max}} g(z,M)\phi(z,M;a,b,c)dM \end{aligned}$$

where N is the total number of galaxies observed. Ignoring the middle term which is independent of a,b,c, we need to minimise the following quantity by varying a,b and c:

$$T(a,b,c) = -2\sum_{\text{obs } j} \ln[g(z_j,M_j)\phi(z_j,M_j;a,b,c)] + 2\Omega\int_{z_{min}}^{z_{max}} \frac{dV}{dz}dz \int_{M_{min}}^{M_{max}} g(z,M)\phi(z,M;a,b,c)dM. \tag{45}$$

Departing from Marshall et al (1983), we will now ignore variations of $\phi(z_i, M_i; a, b, c)$ and $g(z, M)$ within each redshift bin. We can do this as the luminosity function evolves little within the redshift bins that we are using. We write:

$$T(a,b,c) = -2\sum_{\text{obs } j} \ln[g(z_j, M_j)\phi(z_i, M_j; a, b, c)] + 2\Omega\Delta V \int_{M_{min}}^{M_{max}} g(z, M)\phi(\bar{z}, M; a, b, c)dM. \tag{46}$$

where the comoving volume between redshifts z_{min} and z_{max} is:

$$\Delta V = \int_{z_{min}}^{z_{max}} \frac{dV}{dz} dz. \tag{47}$$

As explained in §1.6, the luminosity function of galaxies is usually parameterised by the Schechter function (Schechter 1976). We repeat here for convenience from its formulation in terms of absolute magnitudes (Equation 2):

$$\phi_M\,(M)\,dM = -0.4 \ln 10 \phi^* 10^{-0.4(\alpha+1)(M-M^*)} \exp(-10^{-0.4(M-M^*)})dM. \tag{48}$$

Here ϕ^* is a normalising factor, M^* corresponds roughly to the transition from a power law luminosity function to an exponential one, and α determines the slope of the power law variation at the faint end.

Using the Schechter function parameterisation:

$$\phi(M; a, b, c) = -0.4 \ln 10 \phi^* 10^{-0.4(\alpha+1)(M-M^*)} \exp(-10^{-0.4(M-M^*)}). \tag{49}$$

the quantity to be minimised is:

$$T(a,b,c) = -2\sum_{\text{obs } j} \ln[g(z_j, M_j)\phi(M_j; a, b, c) + 2\Omega\Delta V \int_{M_{min}}^{M_{max}} g(\bar{z}, M)\phi(M; a, b, c)dM. \tag{50}$$

where ϕ is given by (49).

To minimise computing time, the maximum likelihood calculations were performed in two stages. First, a three dimensional grid of side 40 steps was used, centred on the Schechter parameter values for the $1/V_{\max}$ fits to the luminosity function. The maximum likelihood

values obtained from this were then used to provide the centre of a second grid of side 80 steps with increments ten times smaller.

We used the binned luminosity functions as starting points for more accurate calculations of the luminosity functions using the maximum likelihood method (e.g. Marshall et al. 1983). This method avoids the systematic errors arising from random errors when the slope of the luminosity function is steep, which causes more galaxies to be assigned to one side of an absolute magnitude bin than the other. Figures 67 to 69 show the evolution of our maximum likelihood Schechter functions from redshift $z \sim 1.1$ to $z \sim 0.3$.

3.9.2. Cosmic variance

Despite the large volume of our sample, we expect the largest source of error to be cosmic variance (Brown et al. 2007). We illustrate this in Figure 70 where we have plotted the spatial distribution for red and blue galaxies separately which are brighter than $M_B = -19$ and lie between redshift 0.8 and 1.0. Even at these distances the largest structures such as filaments and voids are comparable in size with the width of our sample area and can therefore give rise to significant cosmic variance. The clustering of red galaxies is seen to be stronger than that for blue galaxies. A large filamentary structure is visible at coordinates (219, 34.8).

To estimate the effect of covariance on our measurements we chose nine subfields, each 0.7 deg square, or 16.9 times smaller than our total field area, as shown in Figure 71. We then repeated our determinations of luminosity function evolution for each, and measured the standard deviations of our parameters. We chose non-contiguous subfields in order to minimise correlation between subfields due to structures such as clusters, filaments and voids overlapping two subfields. Assuming no such correlation we would expect the numbers of galaxies in given redshift and absolute magnitude bins to be Poisson variables and the standard deviation of the whole field to be $\sqrt{16.9}$ times smaller than that between the individual subfields. However, the true errors are likely to be slightly larger as clustering features such as filaments may extend across more than one of our subfields, even though they are smaller than the whole Boötes field.

3.9.3. Choice of absolute magnitude range for determining a Schechter function fit

At the bright end we exclude galaxies in bins for which the binned space density is less than $10^{-5}\mathrm{Mpc}^{-3}$ from our maximum likelihood fits. At the faint end we restrict ourselves in each redshift bin to plotting space densities in absolute magnitude bins whose completeness for our faint I magnitude limit $I < 23.5$ at the far end of the redshift bin is within 2σ of the median (97.7%), as determined from plots of $M_B + D_\mathrm{M} - I$ against redshift for all, red and blue galaxies (Figure 72).

Space densities for faint galaxies become increasingly hard to determine accurately at higher redshifts where sample completeness drops rapidly and apparent magnitudes and photometric redshifts become increasingly uncertain. For this reason, α, which determines the faint end slope of the Schechter function, becomes increasingly hard to measure as redshift increases. We therefore adopted fixed α values of -0.5, -1.3 and -1.1, for red, blue and all galaxies respectively, based on their varying values in the lower redshift bins ($0.2 \leq z < 0.6$) when α is treated as a free parameter.

Furthermore when space densities can only be measured for a small number of bins at the bright end, an extra one or two points can greatly alter the shape of the curve at fainter magnitudes. This is illustrated in Figure 73 where we plot the luminosity functions for blue galaxies using a linear scale on the vertical axis in order to show the true space densities. We see that adding two extra absolute mangitude bins at the faint end makes a big difference to the space density given by a Schechter function fit at faint magnitudes. As the five panels show the potential error is much greater at higher redshifts where there are fewer data points.

A large difference in space density at the faint end also means a big difference to the measured luminosity density, because this is effectively the area under the luminosity curve weighted by galaxy luminosity, as given by Equation (3): $j = \phi^* L^* \Gamma(\alpha + 2)$. The potential error is particularly great for blue galaxies because (as explained in section §1.6) blue galaxy luminosity functions have large negative faint end slopes (e.g. $\alpha = -1.3$ and for this reason the majority of the light comes for galaxies fainter than L^*.

Figure 73 shows why Schechter functions fits at high redshifts are highly sensitive to the precise absolute magnitude range considered. The left hand plots fit Schechter functions to our preferred ranges of absolute magnitude values for blue galaxies with α of -1.3. The right hand plots use faint end cut-off values 0.5 mag fainter. Using a linear scale on the vertical axis rather than the usual logarithmic one shows clearly why varying the number of absolute magnitude bins can make a big difference to the measured Schechter parameters (Figure 79). When there are only a few points at the high luminosity an extra one or two points

can greatly alter the shape of the curve at fainter magnitudes. The luminosity density is the area under the curve weighted by galaxy luminosity and therefore it is also sensitive to the faint end cut off value when only a few data points are available (Figure 80).

We also checked that our $[3.6\mu\mathrm{m}] < 20.5$ cut did not eat into the sample for absolute magnitudes brighter than the faint end limits we use for Schechter fitting. Figure 74 illustrates how this is not the case, using the example redshift bin $0.4 \leq z < 0.6$, even though it would be if we used a faint end absolute magnitude limit corresponding to our $I = 23.5$ limit.

In addition, a Schechter function does not necessarily provide a good fit over the whole range of absolute magnitudes. This is particularly the case for faint red galaxies, the number of which is underestimated by a Schechter function, as demonstrated by Blanton et al. (2005a) for SDSS galaxies and Madgwick et al. (2002) for 2dFGRS galaxies.

3.10. *B*-and luminosity function results and discussion

3.10.1. The evolution of space density and luminosity density

Figures 61 to 63 show our binned $1/V_{\rm max}$ luminosity functions for all, red and blue galaxies respectively, as well as results from previous studies using a variety of surveys. We only plot bins for which 97.7% of the measured absolute magnitudes have observed I-magnitudes of 23.5 or brighter. The space density of $\sim L^*$ (i.e. $\sim M^*$) galaxies near the "knee" of the luminosity function increases rapidly with time for red galaxies but hardly at all for blue. Blue galaxies are more numerous than red at all redshifts, but the difference is particularly marked for faint galaxies, as red galaxies show a marked downturn in space density at faint magnitudes (per unit magnitude, but not per unit luminosity), whereas the space density of blue galaxies continues rising steeply towards fainter magnitudes. We plot the low redshift luminosity functions from SDSS (Blanton 2006) in all bins to provide a fixed reference. This shows clearly how the distribution of luminosities is fading, with the blue galaxy distribution fading faster than the red.

Figures 64 to 66 show the maximum likelihood Schechter fits to our data using constant α values of of -0.5, -1.3 and -1.1 (continuous lines), as well as our binned $1/V_{\rm max}$ space densities (data points), using a separate plot for each redshift bin. Figures 67 to 69 display the same data with all redshift bins on a single plot to make the evolution of the luminosity functions more apparent. Table 20 lists the maximum likelihood values of ϕ^* and M^* for both fixed and varying α. The evolution of ϕ^* and M^* for fixed α is shown in graphical form in Figures 75 and 76. All quantities are expressed terms of units for which $h = 1$. In Figure 68 we begin to see the same upturn in the number of very faint red galaxies below $M_{\rm B} - 5\log h \sim 18.5$ that has been reported by other authors (e.g. Blanton et al. 2005a; Madgwick et al. 2002).

Integrating (49) over M gives the following formula for the total luminosity density in the B-band:

$$j_{\rm B} = \phi^* L^* \Gamma(\alpha + 2). \tag{51}$$

where $L^* = L_\odot 10^{-0.4(M^* - M_\odot)}$ and $L_\odot$ and $M_\odot$ are the luminosity and absolute magnitude of the Sun. We plot our maximum likelihood luminosity densities in Figure 77 and include them in Table 20.

Red galaxies increase in space density by a factor of ~ 2 from $z \sim 1.1$ to $z \sim 0.1$ but their luminosity density changes relatively little. By contrast, the space density of blue galaxies changes very little, but their luminosity density decreases by a factor of ~ 2. For both types

of galaxy the characteristic magnitude M^* fades, by 0.6 mag for red galaxies and by 0.9 mag for blue.

We interpret these observations as follows. Red galaxies are largely quiescent, i.e. lack significant star formation, so their luminosity is dominated by old stellar populations which are gradually fading The luminosity of blue galaxies is dominated by short lived bright blue stars so that as their star formation rates decrease their luminosities decrease. Eventually blue galaxies cease star formation altogether and cross the green valley to become quiescent red galaxies. The red galaxy luminosity function fades as the stars within red galaxies fade passively. However, it does not fade as fast as it would just due to passive evolution, because galaxies in the blue cloud migrating to the red sequence when they cease to form stars offset the decrease in luminosity due to passive fading. The bright end of the blue galaxy luminosity function fades much more rapidly than that for red galaxies because of "downsizing", whereby more massive galaxies cease to form stars sooner than less massive ones.

3.10.2. The evolution of luminosity density

In the absence of mergers and blue galaxies becoming red galaxies, a quiescent red galaxy population would decrease in luminosity due to passive evolution by an amount which we can estimate using a Bruzual & Charlot (2003) stellar population synthesis model with formation redshift $z_{\rm form} = 4$ and exponential decay of star formation with time constant $\tau = 0.6$ Gyr. Such a model matches the colour and size evolution of red galaxies well (Brown et al. 2007) and it predicts passive fading in the B-band of $\mu = 1.24$ mag per unit redshift. This is equivalent to a rate of change in the stellar mass to light ratio $\Upsilon(z) = m(z)/j(z)$ of $d\Upsilon/dz = 0.4 \ln 10 \, \mu \Upsilon$. Here $j(z)$, $m(z)$ are the comoving luminosity and stellar mass densities respectively for red galaxies. Given a value for the stellar mass to light ratio at any redshift z_0 we can determine its value at any other redshift z_1:

$$\Upsilon(z_1) = \Upsilon(z_0) 10^{\mu(z_1 - z_0)}. \tag{52}$$

The decrease in red galaxy luminosity density due to stellar fading is offset by the transfer of stellar mass from the blue population to the red population when star formation ceases, and by mergers. Equation (52) enables us to calculate the ratio of red galaxy stellar mass density at any redshift z_1 to that at any other z_0 using our measurements of red galaxy luminosity density at these redshifts:

$$\frac{m(z_1)}{m(z_0)} = \frac{j(z_1)}{j(z_0)} 10^{\mu(z_1 - z_0)}. \quad (53)$$

We plot the resulting change in red galaxy stellar mass in Figure 81 and conclude that the stellar mass in red galaxies increased due to mergers and the conversion of blue galaxies to red by a factor of ~ 4 from $z \sim 1.1$ to $z \sim 0.1$. Increasing or decreasing our assumed passive fading rate by 0.2 from 1.24 mag per unit redshift affects this value by $\sim 20\%$.

3.10.3. The evolution of highly luminous galaxies

Because of the steepness of the bright end of the luminosity function, and the statistically small samples involved, the space density at a fixed absolute magnitude cannot be used to accurately measure the evolution of the space density of the brightest galaxies from plots such as those in Figures 67 to 69. However, it is possible to accurately measure the evolution of the magnitude $M^{\rm fixed}$ corresponding to a fixed space density, and we choose to do this for a space density of $10^{-3.5} h^3\,{\rm Mpc}^{-3}\,{\rm mag})^{-1}$, Our results are shown in Figure 82 and Table 20.

The luminosity of the most luminous blue galaxies fades by ~ 0.7 mag from $z \sim 1.1$ to $z \sim 0.1$. Highly luminous red galaxies fade ~ 0.4 mag, and our results show that the rate of fading increases with time, most fading occurring after $z \sim 0.6$. As discussed in §3.1.2 and shown in Figure 39, Bell et al. (2004) demonstrated that there are insufficient highly luminous blue galaxies at $z \sim 1.0$ to produce any significant change in the density of highly luminous $\sim 4L^*$ red galaxies by the cessation of star formation. We therefore assume that the observed changes in $M^{\rm fixed}$ for red galaxies correspond to changes in the luminosity of a fixed population of highly luminous red galaxies. These changes must be almost entirely due to a combination of passive evolution and mergers, and making allowance for the rate of passive evolution we can estimate the rate of change of mass due to mergers. We use Equation (53), taking j to represent the luminosity of an individual massive red galaxy, and writing it in the form:

$$\frac{m(z_1)}{m(z_0)}) = 10^{-0.4[M(z_1) - M(z_0)] + \mu(z_1 - z_0)}. \quad (54)$$

where $M(z)$ is the absolute magnitude of the galaxy at redshift z.

The resulting change in stellar mass for highly luminous red galaxies is shown in Figure 82. We conclude that it approximately doubled from $z \sim 1.1$ to $z \sim 0.1$. Increasing or decreasing

our assumed passive fading rate by 0.2 from 1.24 mag per unit redshift affects this value by $\sim 20\%$. We conclude that most of the stellar mass in $\sim 4L^*$ red galaxies at $z = 0.1$ was already in place at $z = 0.5$ and half of it was in place at $z = 1.1$. We interpret the increase in mass of highly luminous red galaxies as the result of minor mergers.

The situation for highly luminous blue galaxies is much more difficult to interpret, as new star formation and accretion by mergers can both produce brightening, while passive fading and reduction or cessation of star formation can result in fading.

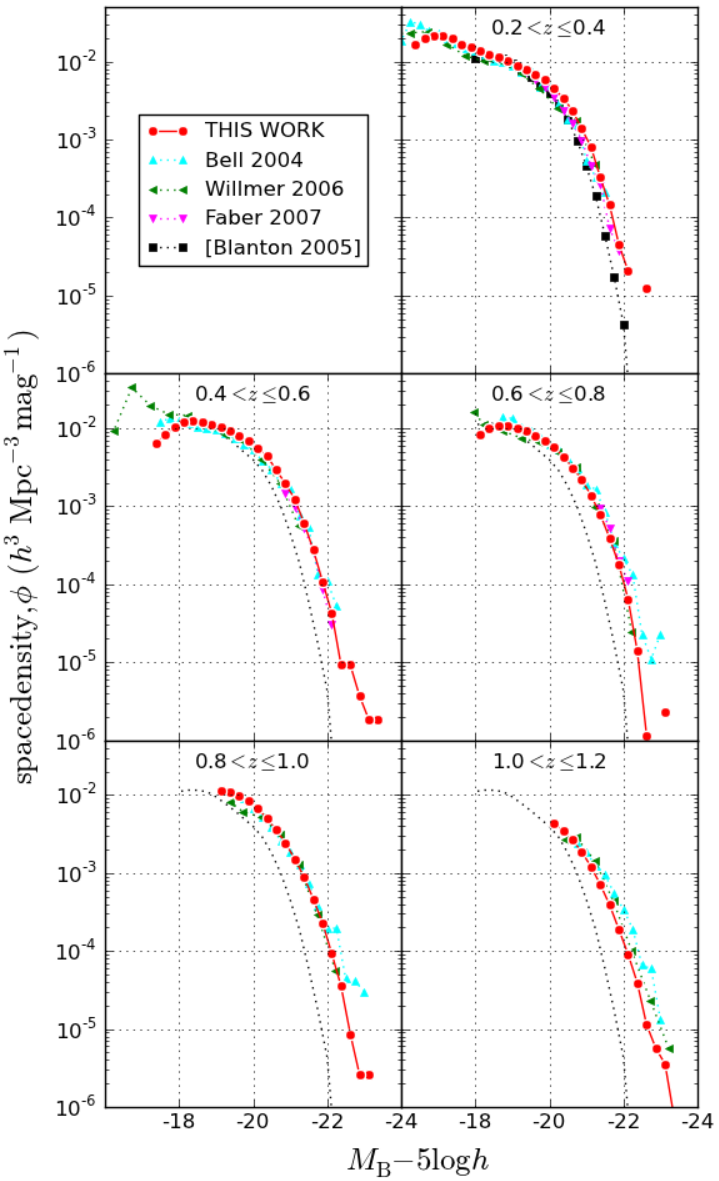

Fig. 61.—: **Binned B-band space densities for all galaxies in bins of width 0.1 mag.** The space density for all $\sim L^*$ galaxies increases and the luminosity of the brightest galaxies decreases as they evolve. Also shown for comparison are the results from Willmer et al. (2006, DEEP2), Bell et al. (2004) and Cool et al. (2012, AGES) which are in broad agreement with ours. The local luminosity function of SDSS galaxies from Blanton (2006) is shown in every panel to provide a reference. Our curves are much smoother due to the large sample size.

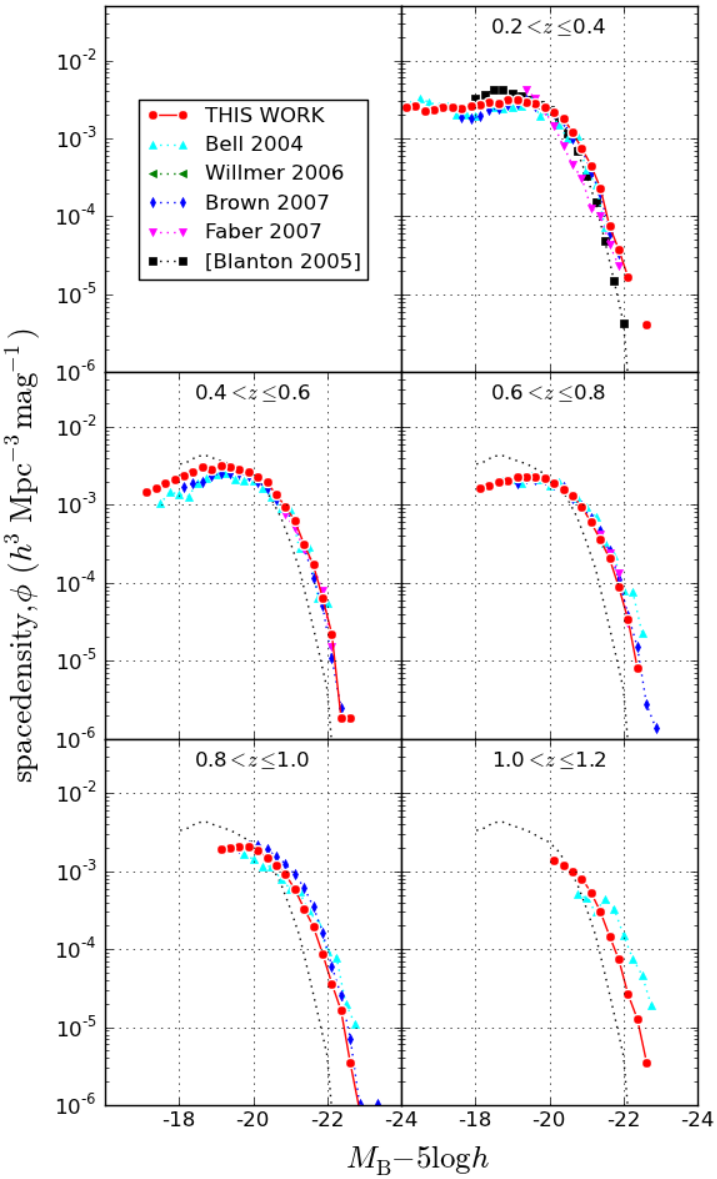

Fig. 62.—: **Binned B-band space densities for red galaxies.** The space density of red $\sim L^*$ galaxies increases and the luminosity of the brightest red galaxies decreases as they evolve. The luminosity function of red galaxies turns over at fainter magnitudes indicating a decrease in space density. Also shown for comparison are the results from Bell et al. (2004), Willmer et al. (2006, DEEP2), Brown et al. (2007) and Cool et al. (2012, AGES). The local luminosity function of SDSS galaxies from Blanton (2006) is shown in every panel to provide a reference. Our results are in broad agreement with the others except that our brightest galaxies are fainter by ∼0.3 mag at $z \sim 1.1$.

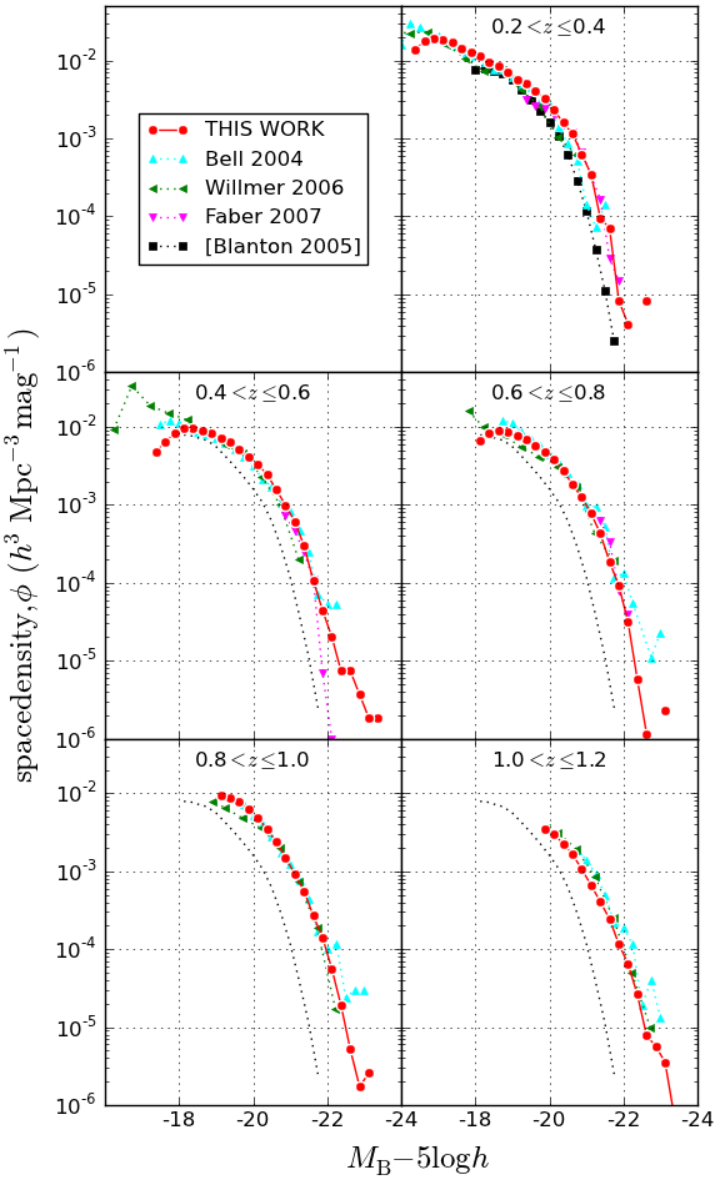

Fig. 63.—: **Binned B-band space densities for blue galaxies.** The space density of blue $\sim L^*$ galaxies increases and the luminosity of the brightest blue galaxies decreases as they evolve. The luminosity function of blue galaxies continues rising towards fainter magnitudes so that faint galaxies make a much larger contribution to the total luminosity density than for red galaxies. Also shown for comparison are the results from Bell et al. (2004), Willmer et al. (2006, DEEP2) and Cool et al. (2012, AGES). The local luminosity function of SDSS galaxies from Blanton (2006) is shown in every panel to provide a reference. Our results are in broad agreement with the others.

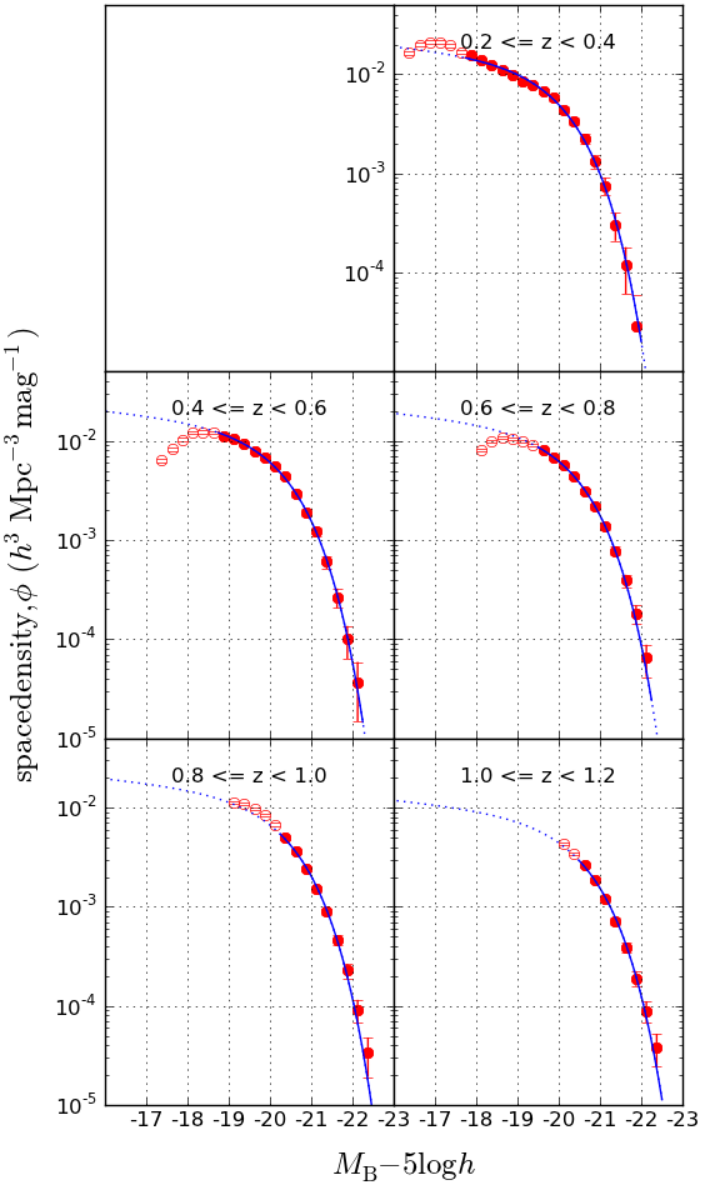

Fig. 64.—: **Evolution of the Bessell B-band Schechter function for all galaxies, showing separate plots for different redshift bins.** The circles denote comoving space densities for the various absolute magnitude bins. Filled circles denote the range of absolute magnitudes used to perform the maximum likelihood fit. Open circles denote data for very faint galaxies which are expected to be reliable on the basis of apparent I and [3.6μm] magnitudes, but which are not represented adequately by a Schechter function. The error bars show $1-\sigma$ Poisson errors for the numbers in each bin.

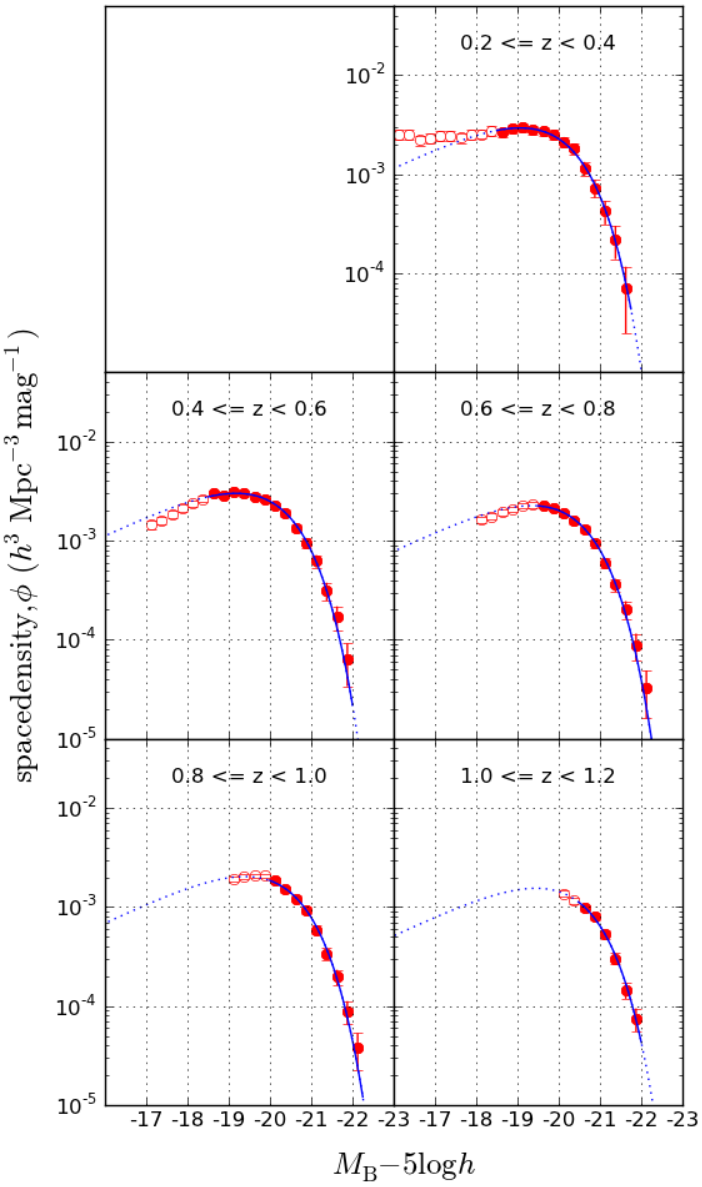

Fig. 65.—: **As Figure 64, but for red galaxies.**

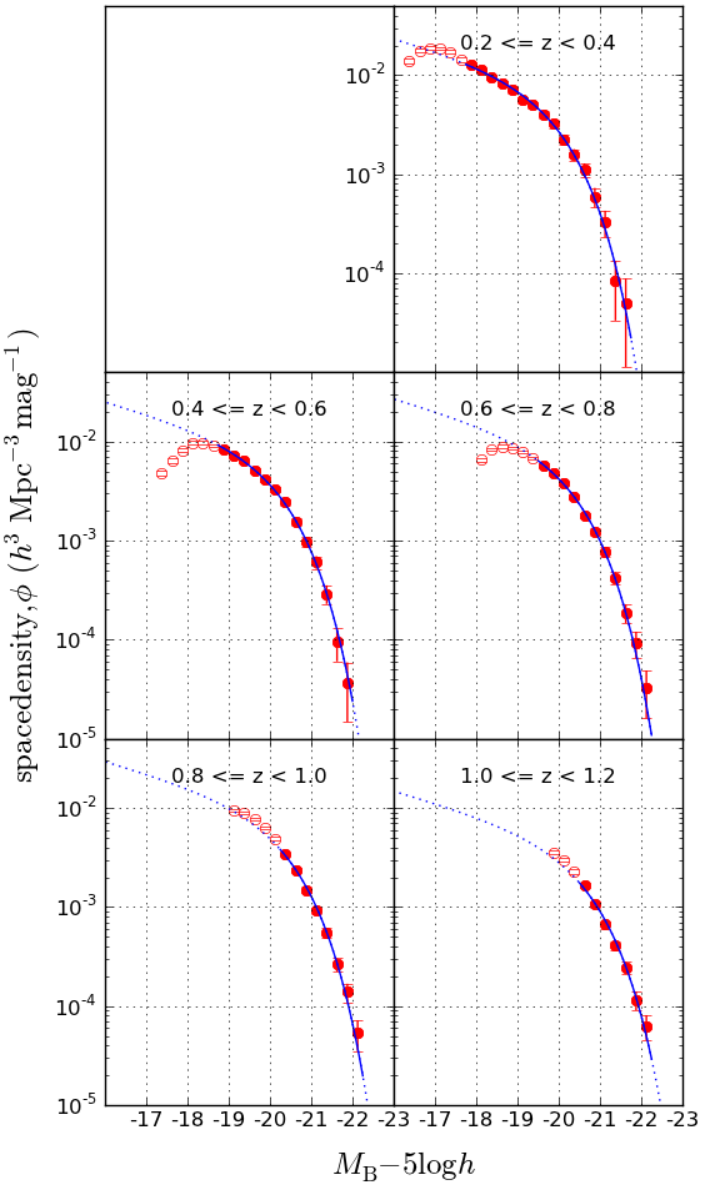

Fig. 66.—: **As Figure 64, but for blue galaxies.**

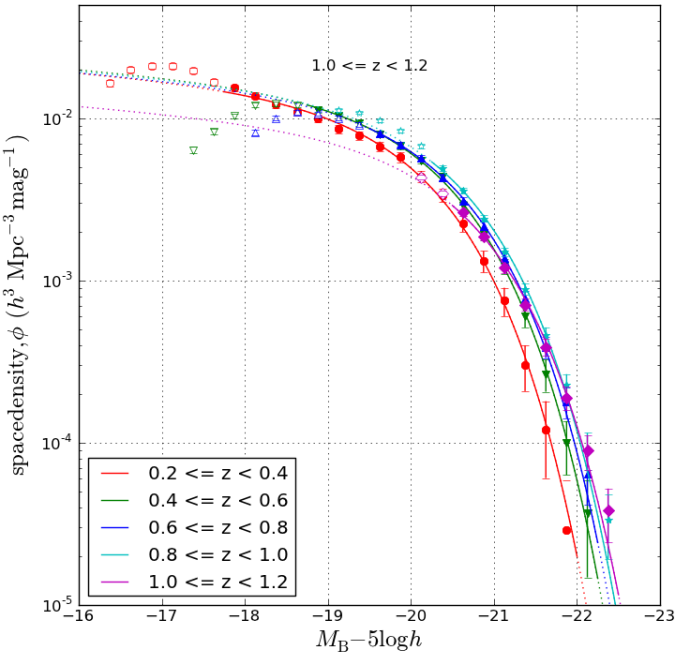

Fig. 67.—: **Evolution of the Bessell B-band Schechter function for all galaxies, showing all redshift bins on one plot.** The symbols denote comoving space densities for the various absolute magnitude bins. Filled symbols denote the range of absolute magnitudes used to perform the maximum likelihood fit. Open symbols denote data for very faint galaxies which are expected to be reliable on the basis of apparent I and $[3.6\mu\mathrm{m}]$ magnitudes, but which are not represented adequately by a Schechter function. The error bars show $1-\sigma$ Poisson errors for the numbers in each bin.

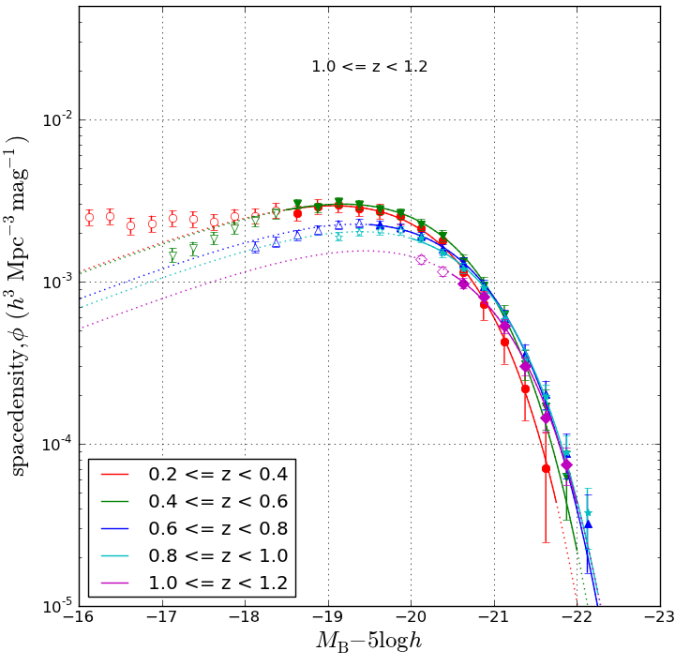

Fig. 68.—: **As Figure 67, but for red galaxies.**

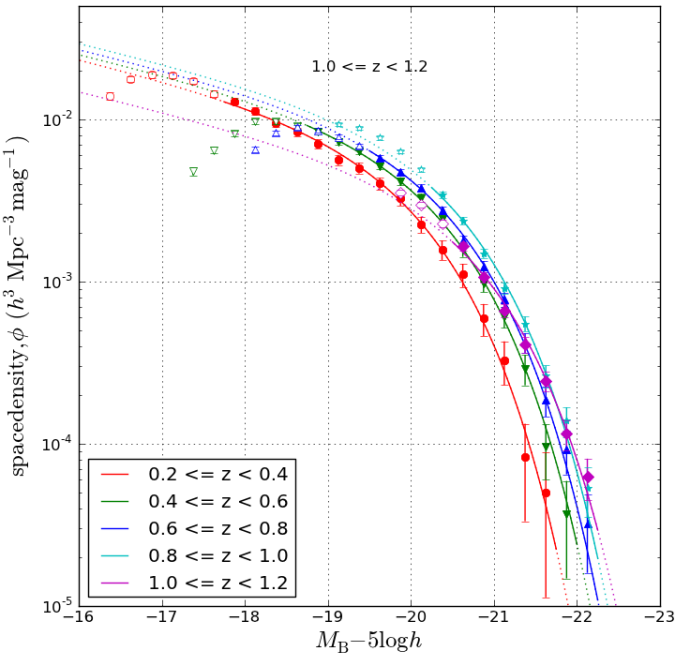

Fig. 69.—: **As Figure 67, but for blue galaxies.**

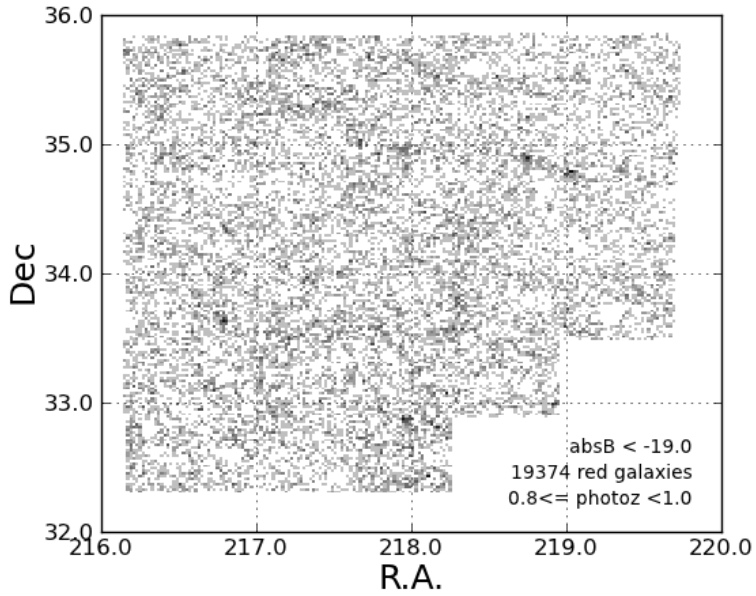

(a)

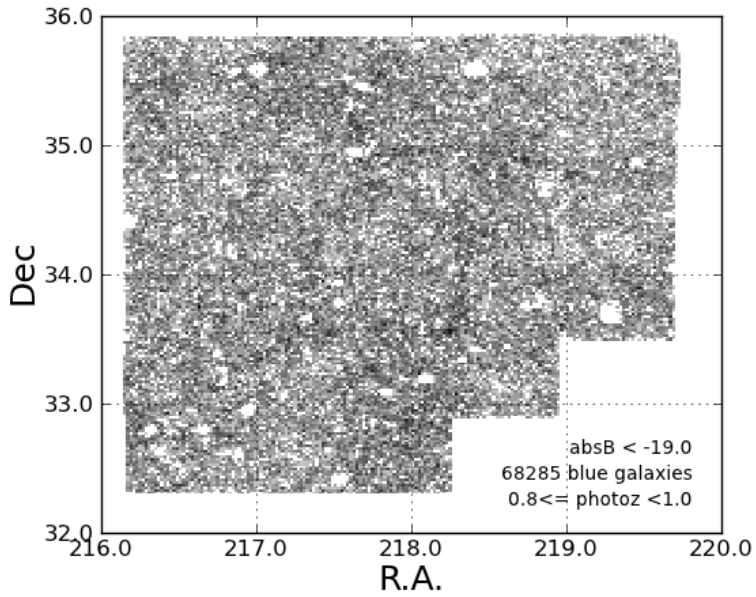

(b)

Fig. 70.—: **Cosmic variance is a significant source of error despite the large area of our sample.** Coordinate plots for galaxies brighter than $M_B = -19$ for redshifts between 0.8 and 1.0. *Top:* red galaxies, *bottom:* blue galaxies. Even at these distances the largest structures such as filaments and voids are comparable is size with the width of our sample area and can therefore give rise to significant cosmic variance.

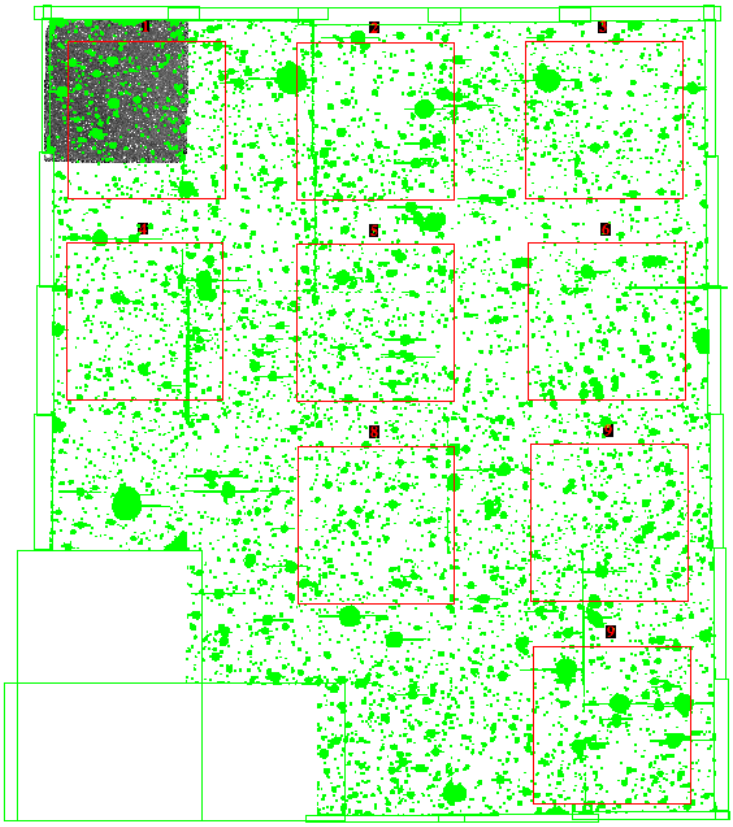

Fig. 71.—: **The nine subfields used to estimate cosmic variance.** Subfields are shown by red rectangles. Green areas are drilled regions around bright stars and very extended objects that are excluded from our sample. The dark rectangle is one of the 27 separate fields imaged by the Boötes Survey.

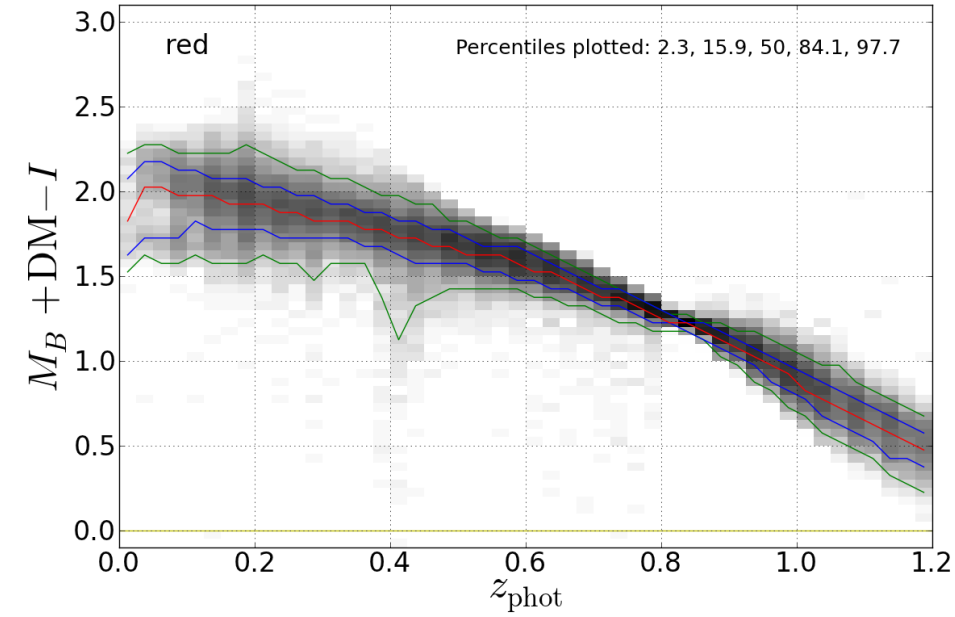

(a)

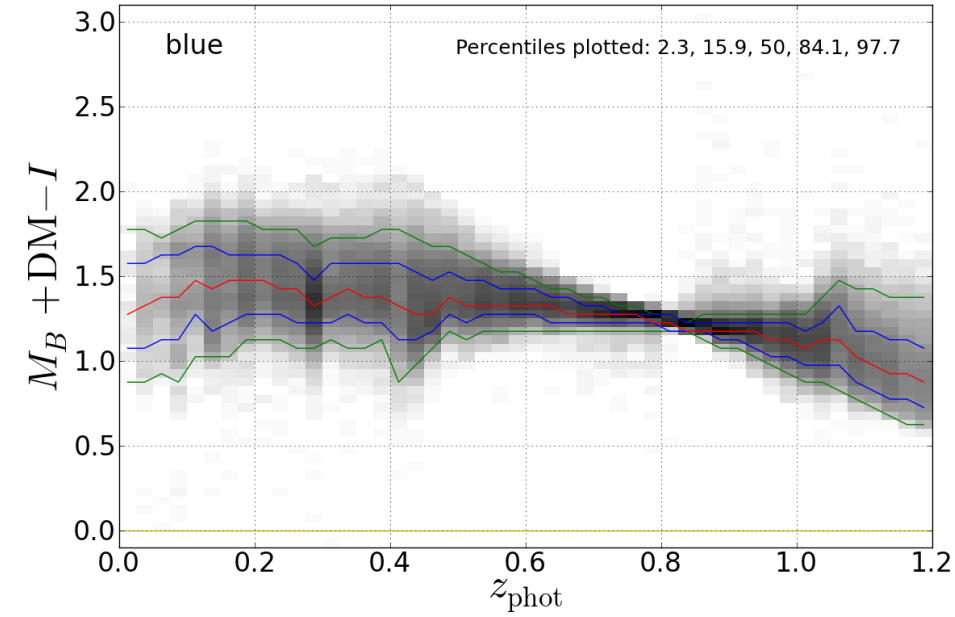

(b)

Fig. 72.—: **Binned plots of $M_B + D_{\mathrm{M}} - I$ against redshift enable the faint absolute magnitude cut-off corresponding to our faint apparent magnitude limit of $I = 23.5$ to be determined.** *Top:* red galaxies; *bottom:* blue galaxies. The red, blue and green lines denote the median and the 1-σ and 2-σ percentiles. We only plot our binned luminosity functions for galaxies brighter than the 2-σ faint limit. (D_{M} is the distance modulus.)

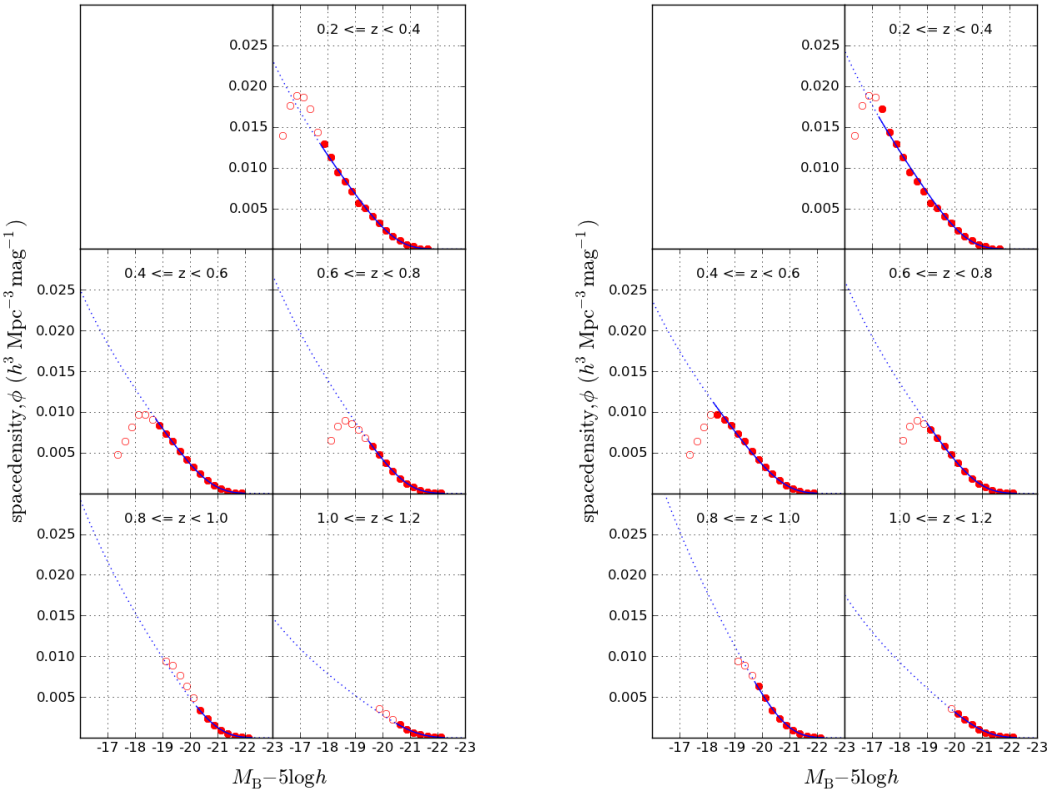

(a) (b)

Fig. 73.—: **Showing why Schechter functions fits at high redshifts are highly sensitive to the precise M_B range considered.** Using a linear scale on the vertical axis rather than the usual logarithmic one shows clearly why varying the number of absolute magnitude bins can make a big difference to the measured Schechter parameters and luminosity density. When there are only a few points at the high luminosity an extra one or two points can greatly alter the shape of the curve at fainter magnitudes. These plots are for blue galaxies only with a fixed value for α of -1.3. The luminosity density is the area under the curve weighted by galaxy luminosity. *Left:* using our preferred faint end M_B cut-off values. *Right:* using cut-off values 0.5 mag fainter.

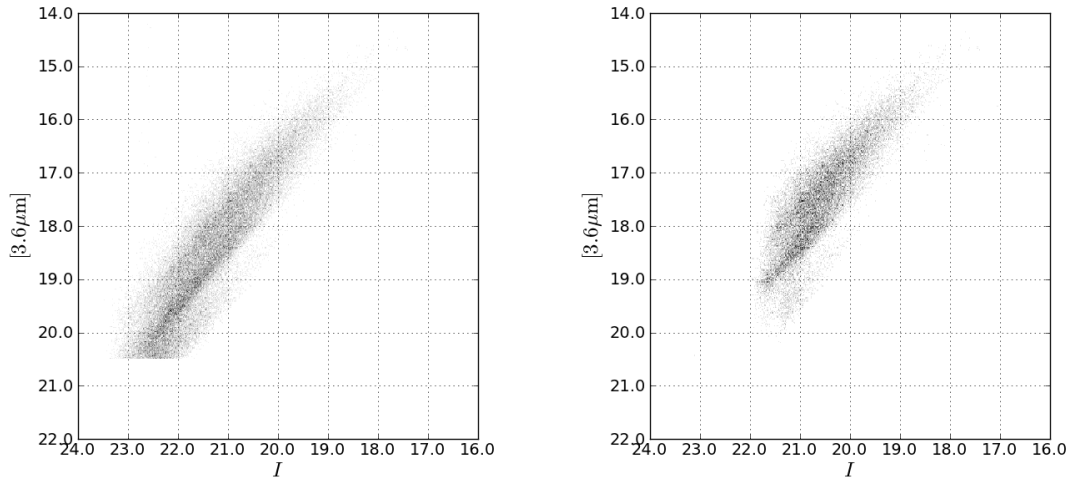

(a) (b)

Fig. 74.—: **The effect of our 3.6 μm cut on the sample.** *Left:* The [3.6μm] cut significantly reduces the number of fainter blue objects in the sample when an $M_B - 5\log h = -17.31$ faint end limit based on $I < 23.5$ is used. *Right:* The [3.6μm] cut does not affect the sample when the $M_B - 5\log h = -18.75$ faint end limit for fitting a Schechter function is used.

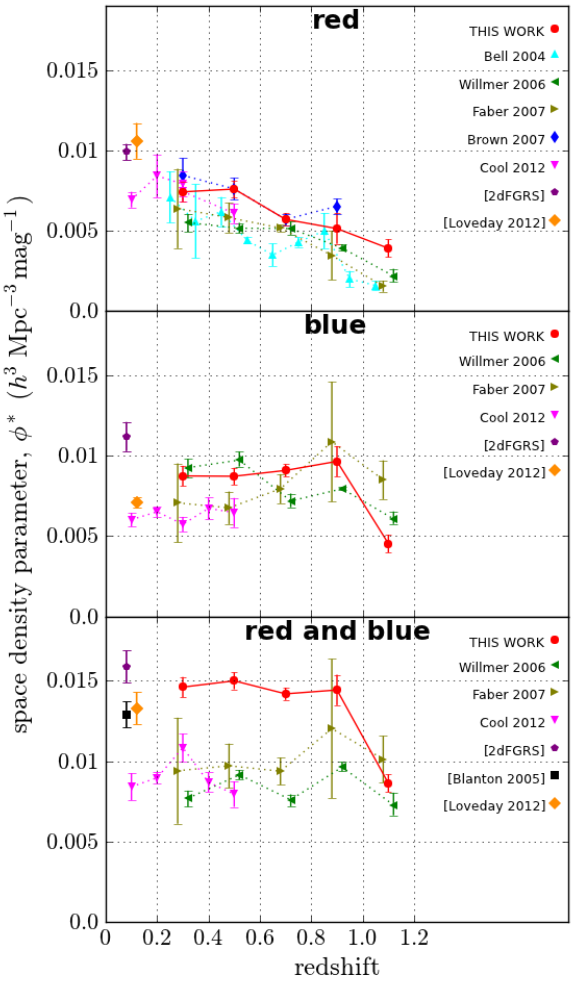

Fig. 75.—: **Evolution from $z = 1.1$ to $z = 0.3$ of the B-band maximum likehihood Schechter parameter ϕ^* which measures normalises the space density.** Separate plots are shown for red, blue and all galaxies (red data points), assuming fixed alpha values of -0.5, -1.3 and -1.1 respectively. ϕ^* measures the space density of L^* galaxies so the space density of red galaxies doubles while that of blue galaxies hardly changes. (We discount the point at $z = 1.1$ because blue galaxy $z_{\rm phot}$ values are unreliable at this redshift). Also shown for comparison are the results from Bell et al. (2004), Brown et al. (2007), Faber et al. (2007, COMBO-17), Willmer et al. (2006, DEEP2) and Cool et al. (2012, AGES). The low redshift results from Loveday et al. (2012, GAMA), Madgwick et al. (2002, 2dFGRS) and Blanton et al. (2005a, SDSS) are also shown and indicated by [square brackets]. Error bars on our results show errors due to cosmic variance. Error bars on results from the literature are as published.

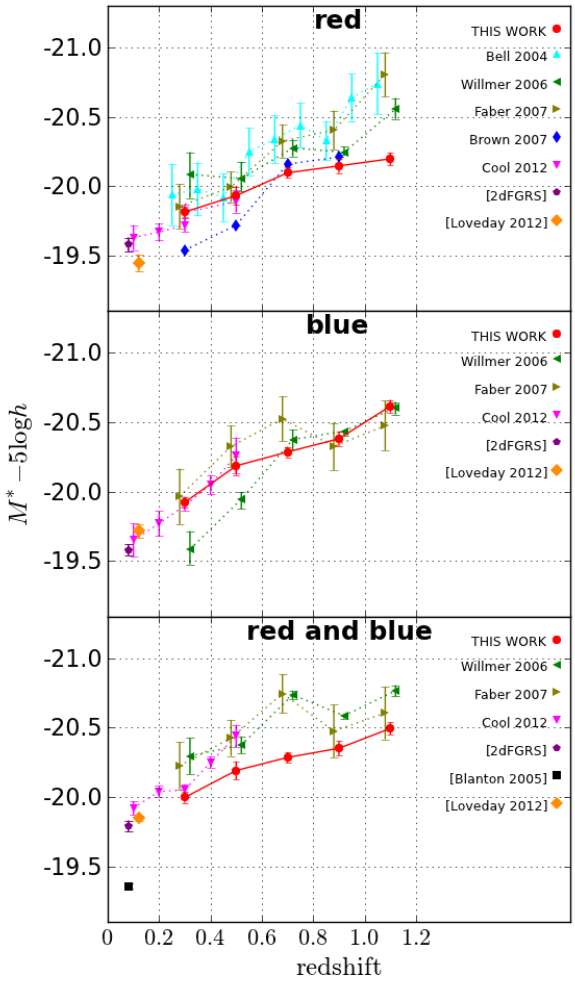

Fig. 76.—: **Evolution from $z = 1.1$ to $z = 0.3$ of the B-band maximum likehihood Schechter parameter $M^* - 5\log h$, the characteristic absolute magnitude.** Separate plots are shown for red, blue and all galaxies (red data points), assuming fixed alpha values of -0.5, -1.3 and -1.1 respectively. $M^* - 5\log h$ for red galaxies fades less than for blue (0.6 as opposed to 0.9 mag per unit redshift). (We discount the point at $z = 1.1$ because blue galaxy $z_{\rm phot}$ values are unreliable at this redshift). Also shown for comparison are the results from Bell et al. (2004), Brown et al. (2007), Faber et al. (2007, COMBO-17), Willmer et al. (2006, DEEP2) and Cool et al. (2012, AGES). The low redshift results from Loveday et al. (2012, GAMA), Madgwick et al. (2002, 2dFGRS) and Blanton et al. (2005a, SDSS) are also shown and indicated by [square brackets]. Error bars on our results show errors due to cosmic variance. Error bars on results from the literature are as published.

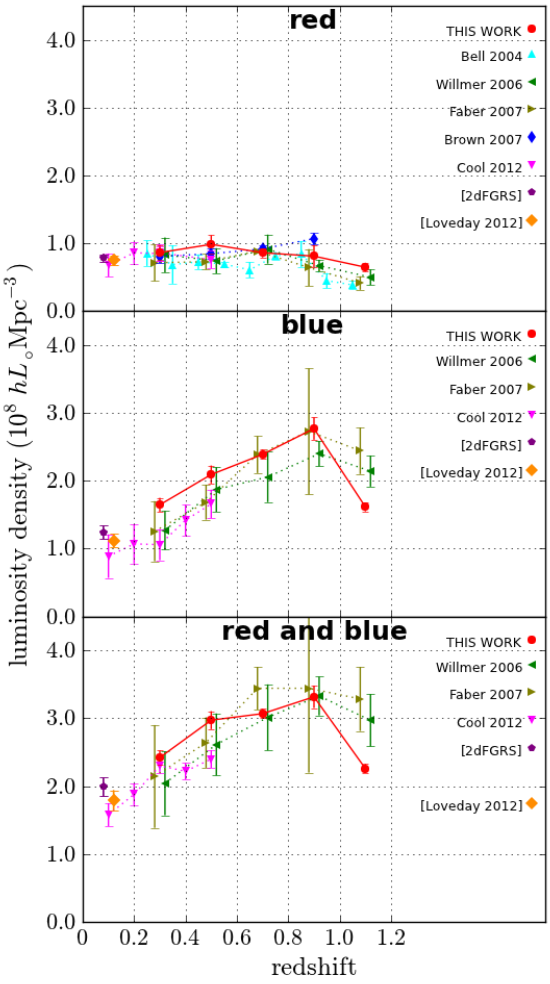

Fig. 77.—: **Evolution from $z = 1.1$ to $z = 0.3$ of the B-band luminosity density.** Separate plots are shown for red, blue and all galaxies (red data points), assuming fixed alpha values of -0.5, -1.3 and -1.1 respectively. The luminosity density of red galaxies hardly changes while that of blue galaxies approximately halves from $z = 0.9$ to $z = 0.3$ (we discount the point at $z = 1.1$ because blue galaxy z_{phot} values are unreliable at this redshift). Also shown for comparison are the results from Bell et al. (2004), Brown et al. (2007), Faber et al. (2007, COMBO-17), Willmer et al. (2006, DEEP2) and Cool et al. (2012, AGES). The low redshift results from Loveday et al. (2012, GAMA), Madgwick et al. (2002, 2dFGRS) and Blanton et al. (2005a, SDSS) are also shown and indicated by [square brackets]. Error bars on our results show errors due to cosmic variance. Error bars on results from the literature are as published.

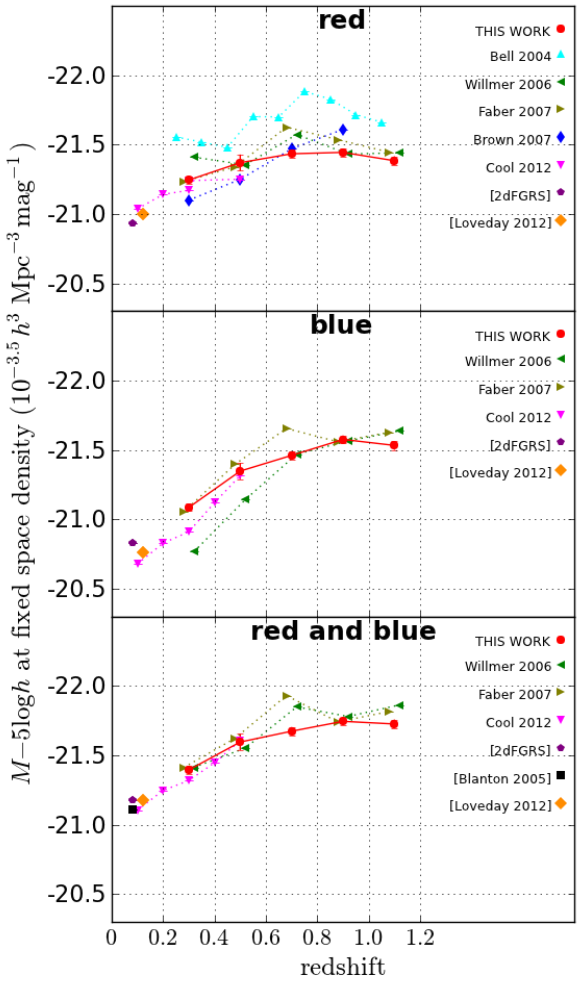

Fig. 78.—: **Evolution of the bright end of the B-band luminosity function from $z = 1.1$ to $z = 0.3$.** The luminosity evolution of the brightest galaxies is indicated by the value of $M_{\rm B} - 5\log h$ at which the space density is $10^{-3.5}h^3\,{\rm Mpc}^{-3}\,{\rm mag}^{-1}$. Separate plots are shown for red, blue and all galaxies (red data points), assuming fixed alpha values of -0.5, -1.3 and -1.1 respectively. The luminosity corresponding to the most massive galaxies fades less rapidly for red galaxies than for blue (0.4 as opposed to 0.7 mag per unit redshift). (We discount the point at $z = 1.1$ because blue galaxy $z_{\rm phot}$ values are unreliable at this redshift). Also shown for comparison are the results from Bell et al. (2004), Brown et al. (2007), Faber et al. (2007, COMBO-17), Willmer et al. (2006, DEEP2) and Cool et al. (2012, AGES). The low redshift results from Loveday et al. (2012, GAMA), Madgwick et al. (2002, 2dFGRS) and Blanton et al. (2005a, SDSS) are also shown and indicated by [square brackets]. Error bars on our results show errors due to cosmic variance.

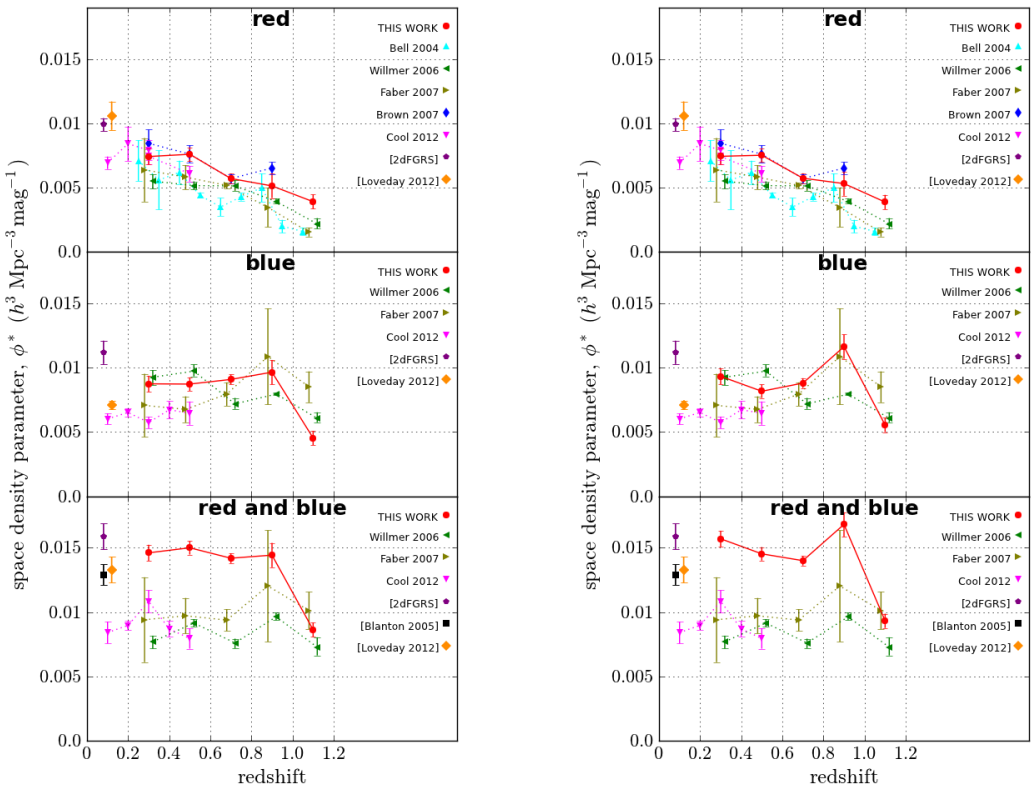

(a) (b)

Fig. 79.—: **The effect on the measured blue space density parameter ϕ^* of including two extra absolute magnitude bins at the faint end..** When there are only a few measured space densities at the bright end, the measured value of ϕ^* is sensitive to the exact absolute magnitude range. *Left:* using our preferred faint end M_B cut-off values. *Right:* using cut-off values 0.5 mag fainter.

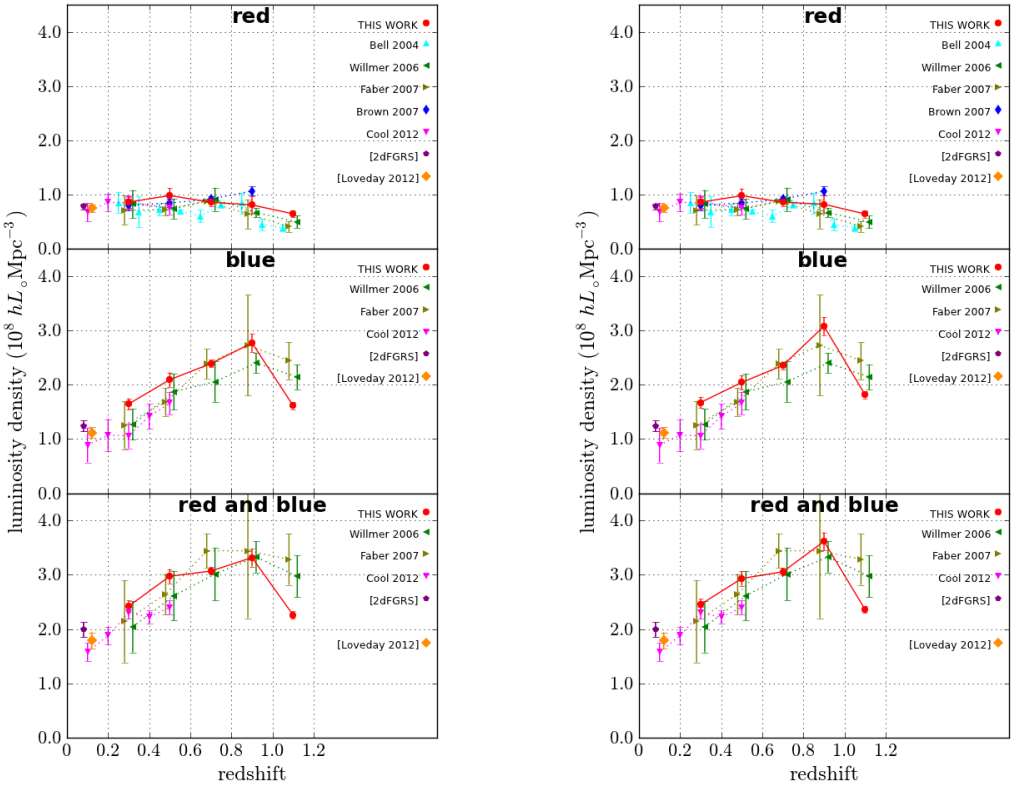

(a) (b)

Fig. 80.—: **The effect on the measured blue luminosity density of including two extra absolute magnitude bins at the faint end.** When there are only a few measured space densities at the bright end, the measured value of the luminosity density is sensitive to the exact absolute magnitude range. *Left:* using our preferred faint end M_B cut-off values. *Right:* using cut-off values 0.5 mag fainter.

Table 17. Binned Bessell B-band luminosity functions for all galaxies.

$M_B - 5\log h$		Luminosity Function ($10^{-3}h^3\,\mathrm{Mpc}^{-3}\,\mathrm{mag}^{-1}$)				
Min	Max	$0.2 \le z < 0.4$	$0.4 \le z < 0.6$	$0.6 \le z < 0.8$	$0.8 \le z < 1.0$	$1.0 \le z < 1.2$
-23.50	-23.25	-	-	-	-	0.001 ± 0.001
-23.25	-23.00	-	-	0.002 ± 0.002	0.002 ± 0.001	0.003 ± 0.001
-23.00	-22.75	-	0.002 ± 0.002	-	0.003 ± 0.001	0.005 ± 0.002
-22.75	-22.50	-	0.004 ± 0.003	0.001 ± 0.001	0.007 ± 0.002	0.011 ± 0.003
-22.50	-22.25	-	0.007 ± 0.004	0.013 ± 0.004	0.034 ± 0.005	0.038 ± 0.005
-22.25	-22.00	-	0.037 ± 0.008	0.065 ± 0.009	0.091 ± 0.009	0.089 ± 0.008
-22.00	-21.75	0.029 ± 0.011	0.100 ± 0.014	0.181 ± 0.014	0.227 ± 0.014	0.190 ± 0.012
-21.75	-21.50	0.121 ± 0.022	0.266 ± 0.022	0.390 ± 0.021	0.461 ± 0.020	0.391 ± 0.017
-21.50	-21.25	0.303 ± 0.036	0.603 ± 0.033	0.779 ± 0.030	0.888 ± 0.028	0.711 ± 0.023
-21.25	-21.00	0.753 ± 0.056	1.231 ± 0.048	1.372 ± 0.040	1.505 ± 0.036	1.198 ± 0.030
-21.00	-20.75	1.322 ± 0.074	1.924 ± 0.060	2.174 ± 0.050	2.419 ± 0.046	1.866 ± 0.037
-20.75	-20.50	2.252 ± 0.097	2.908 ± 0.073	3.107 ± 0.060	3.585 ± 0.056	2.631 ± 0.044
-20.50	-20.25	3.375 ± 0.118	4.358 ± 0.090	4.345 ± 0.071	4.933 ± 0.066	3.437 ± 0.051
-20.25	-20.00	4.381 ± 0.135	5.524 ± 0.101	5.703 ± 0.082	6.769 ± 0.078	4.348 ± 0.058
-20.00	-19.75	5.768 ± 0.155	6.782 ± 0.112	6.907 ± 0.090	8.433 ± 0.088	-
-19.75	-19.50	6.741 ± 0.167	7.955 ± 0.121	8.039 ± 0.098	9.779 ± 0.095	-
-19.50	-19.25	7.838 ± 0.180	9.376 ± 0.132	9.154 ± 0.105	10.886 ± 0.101	-
-19.25	-19.00	8.599 ± 0.189	10.399 ± 0.139	10.048 ± 0.111	11.265 ± 0.103	-
-19.00	-18.75	9.979 ± 0.204	11.275 ± 0.145	10.654 ± 0.115	-	-
-18.75	-18.50	10.998 ± 0.214	12.094 ± 0.151	10.904 ± 0.117	-	-
-18.50	-18.25	12.246 ± 0.226	12.345 ± 0.154	10.037 ± 0.113	-	-
-18.25	-18.00	13.789 ± 0.240	12.074 ± 0.153	8.187 ± 0.103	-	-
-18.00	-17.75	15.475 ± 0.255	10.341 ± 0.142	-	-	-
-17.75	-17.50	16.710 ± 0.265	8.308 ± 0.128	-	-	-
-17.50	-17.25	19.635 ± 0.289	6.393 ± 0.113	-	-	-
-17.25	-17.00	21.164 ± 0.301	-	-	-	-
-17.00	-16.75	21.113 ± 0.302	-	-	-	-
-16.75	-16.50	19.871 ± 0.295	-	-	-	-
-16.50	-16.25	16.477 ± 0.270	-	-	-	-

Table 18. Binned Bessell B-band luminosity functions for red galaxies.

$M_B - 5\log h$		Luminosity Function ($10^{-3}h^3\,\mathrm{Mpc}^{-3}\,\mathrm{mag}^{-1}$)				
Min	Max	$0.2 \le z < 0.4$	$0.4 \le z < 0.6$	$0.6 \le z < 0.8$	$0.8 \le z < 1.0$	$1.0 \le z < 1.2$
-23.00	-22.75	-	-	-	0.001 ± 0.001	-
-22.75	-22.50	-	0.002 ± 0.002	-	0.003 ± 0.002	0.004 ± 0.002
-22.50	-22.25	-	0.002 ± 0.002	0.008 ± 0.003	0.016 ± 0.004	0.014 ± 0.003
-22.25	-22.00	-	0.022 ± 0.006	0.032 ± 0.006	0.038 ± 0.006	0.026 ± 0.004
-22.00	-21.75	0.025 ± 0.010	0.063 ± 0.011	0.088 ± 0.010	0.089 ± 0.009	0.075 ± 0.007
-21.75	-21.50	0.071 ± 0.017	0.170 ± 0.018	0.204 ± 0.015	0.197 ± 0.013	0.146 ± 0.010
-21.50	-21.25	0.220 ± 0.030	0.312 ± 0.024	0.358 ± 0.020	0.337 ± 0.017	0.302 ± 0.015
-21.25	-21.00	0.424 ± 0.042	0.624 ± 0.034	0.596 ± 0.026	0.591 ± 0.023	0.533 ± 0.020
-21.00	-20.75	0.727 ± 0.055	0.952 ± 0.042	0.937 ± 0.033	0.924 ± 0.028	0.803 ± 0.024
-20.75	-20.50	1.147 ± 0.069	1.345 ± 0.050	1.309 ± 0.039	1.209 ± 0.033	0.977 ± 0.027
-20.50	-20.25	1.799 ± 0.086	1.921 ± 0.060	1.583 ± 0.043	1.504 ± 0.037	1.158 ± 0.030
-20.25	-20.00	2.124 ± 0.094	2.251 ± 0.064	1.909 ± 0.047	1.864 ± 0.041	1.372 ± 0.033
-20.00	-19.75	2.523 ± 0.102	2.624 ± 0.070	2.150 ± 0.050	2.067 ± 0.043	-
-19.75	-19.50	2.718 ± 0.106	2.790 ± 0.072	2.245 ± 0.051	2.064 ± 0.044	-
-19.50	-19.25	2.814 ± 0.108	2.985 ± 0.074	2.297 ± 0.052	2.031 ± 0.044	-
-19.25	-19.00	2.967 ± 0.111	3.095 ± 0.076	2.247 ± 0.052	1.898 ± 0.042	-
-19.00	-18.75	2.917 ± 0.110	2.874 ± 0.073	2.085 ± 0.051	-	-
-18.75	-18.50	2.647 ± 0.105	3.016 ± 0.075	1.936 ± 0.049	-	-
-18.50	-18.25	2.755 ± 0.107	2.626 ± 0.070	1.758 ± 0.047	-	-
-18.25	-18.00	2.548 ± 0.103	2.363 ± 0.067	1.638 ± 0.046	-	-
-18.00	-17.75	2.523 ± 0.102	2.136 ± 0.064	-	-	-
-17.75	-17.50	2.339 ± 0.099	1.853 ± 0.060	-	-	-
-17.50	-17.25	2.440 ± 0.101	1.604 ± 0.057	-	-	-
-17.25	-17.00	2.469 ± 0.102	1.460 ± 0.054	-	-	-
-17.00	-16.75	2.287 ± 0.099	-	-	-	-
-16.75	-16.50	2.215 ± 0.098	-	-	-	-
-16.50	-16.25	2.541 ± 0.105	-	-	-	-
-16.25	-16.00	2.508 ± 0.105	-	-	-	-

Table 19. Binned Bessell B-band luminosity functions for blue galaxies.

$M_B - 5\log h$		Luminosity Function ($10^{-3}h^3\,\mathrm{Mpc}^{-3}\,\mathrm{mag}^{-1}$)				
Min	Max	$0.2 \leq z < 0.4$	$0.4 \leq z < 0.6$	$0.6 \leq z < 0.8$	$0.8 \leq z < 1.0$	$1.0 \leq z < 1.2$
-23.50	-23.25	-	-	-	-	0.001 ± 0.001
-23.25	-23.00	-	-	0.002 ± 0.002	0.002 ± 0.001	0.003 ± 0.001
-23.00	-22.75	-	0.002 ± 0.002	-	0.002 ± 0.001	0.005 ± 0.002
-22.75	-22.50	-	0.002 ± 0.002	0.001 ± 0.001	0.003 ± 0.002	0.007 ± 0.002
-22.50	-22.25	-	0.006 ± 0.003	0.005 ± 0.002	0.017 ± 0.004	0.024 ± 0.004
-22.25	-22.00	-	0.015 ± 0.005	0.032 ± 0.006	0.053 ± 0.007	0.063 ± 0.007
-22.00	-21.75	-	0.037 ± 0.008	0.093 ± 0.010	0.139 ± 0.011	0.115 ± 0.009
-21.75	-21.50	0.050 ± 0.014	0.096 ± 0.013	0.186 ± 0.015	0.264 ± 0.015	0.245 ± 0.013
-21.50	-21.25	0.083 ± 0.019	0.292 ± 0.023	0.421 ± 0.022	0.551 ± 0.022	0.409 ± 0.017
-21.25	-21.00	0.329 ± 0.037	0.607 ± 0.033	0.776 ± 0.030	0.915 ± 0.028	0.664 ± 0.022
-21.00	-20.75	0.594 ± 0.050	0.972 ± 0.042	1.237 ± 0.038	1.495 ± 0.036	1.064 ± 0.028
-20.75	-20.50	1.105 ± 0.068	1.563 ± 0.054	1.798 ± 0.046	2.376 ± 0.046	1.654 ± 0.035
-20.50	-20.25	1.575 ± 0.081	2.437 ± 0.067	2.762 ± 0.057	3.429 ± 0.055	2.279 ± 0.041
-20.25	-20.00	2.257 ± 0.097	3.273 ± 0.078	3.793 ± 0.067	4.905 ± 0.066	2.976 ± 0.048
-20.00	-19.75	3.246 ± 0.116	4.159 ± 0.088	4.757 ± 0.075	6.366 ± 0.076	3.543 ± 0.052
-19.75	-19.50	4.023 ± 0.129	5.166 ± 0.098	5.794 ± 0.083	7.715 ± 0.084	-
-19.50	-19.25	5.024 ± 0.145	6.391 ± 0.109	6.857 ± 0.091	8.855 ± 0.091	-
-19.25	-19.00	5.631 ± 0.153	7.304 ± 0.117	7.801 ± 0.098	9.366 ± 0.094	-
-19.00	-18.75	7.061 ± 0.171	8.401 ± 0.126	8.569 ± 0.103	-	-
-18.75	-18.50	8.350 ± 0.186	9.078 ± 0.131	8.968 ± 0.106	-	-
-18.50	-18.25	9.490 ± 0.199	9.720 ± 0.137	8.279 ± 0.103	-	-
-18.25	-18.00	11.240 ± 0.217	9.711 ± 0.137	6.549 ± 0.092	-	-
-18.00	-17.75	12.952 ± 0.233	8.206 ± 0.127	-	-	-
-17.75	-17.50	14.371 ± 0.246	6.455 ± 0.113	-	-	-
-17.50	-17.25	17.194 ± 0.270	4.789 ± 0.098	-	-	-
-17.25	-17.00	18.695 ± 0.283	-	-	-	-
-17.00	-16.75	18.826 ± 0.286	-	-	-	-
-16.75	-16.50	17.656 ± 0.278	-	-	-	-
-16.50	-16.25	13.936 ± 0.248	-	-	-	-

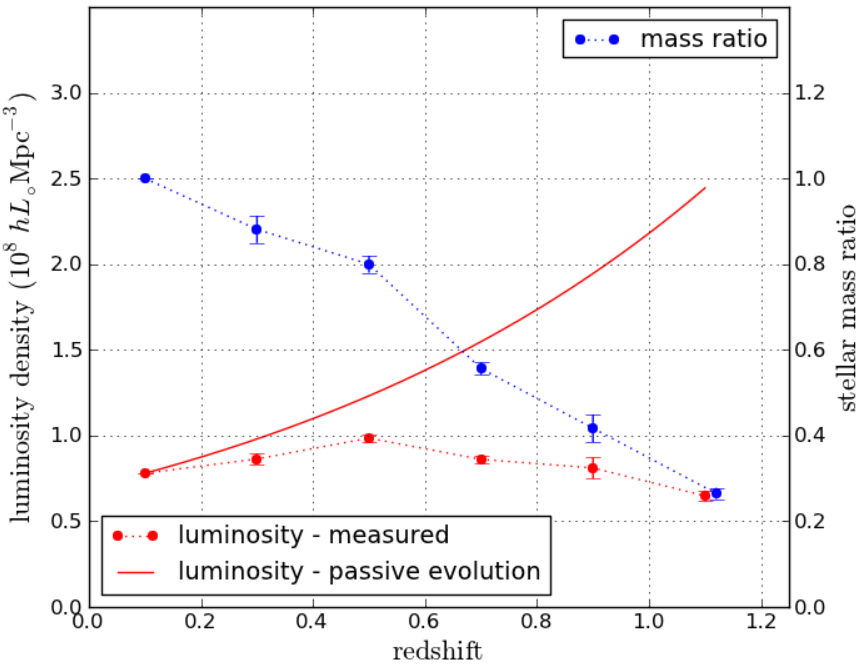

Fig. 81.—: **Our measurements of luminosity density indicate that the red galaxy population quadruples in stellar mass from $z = 1.1$ to $z = 0.1$.** (*left axis and red points*) luminosity density of all red galaxies; (*right axis and blue points*) stellar mass of all red galaxies relative to $z = 0.1$. The continuous red line shows how a passively stellar population would fade to produce the same luminosity at $z = 0.1$. The point at $z = 0.1$ is for 2dFGRS (Madgwick et al. 2002). Error bars on our results show errors due to cosmic variance. Error bars on results from the literature are as published.

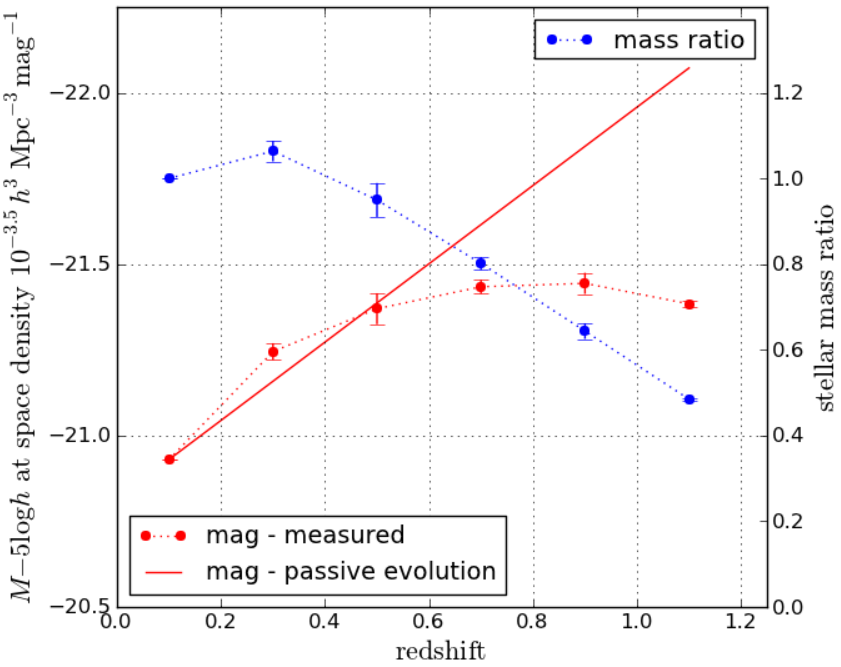

Fig. 82.—: **Highly luminous ($\sim 4L^*$) red galaxies approximately double in mass from $z = 1.1$ to $z \sim 0.5$, but then grow relatively little to $z = 0.1$.** (*left axis and red points*) absolute magnitude $M_\mathrm{B} - 5\log h$ of red galaxies at a fixed comoving space density of $10^{-3.5} h^3\,\mathrm{Mpc}^{-3}\,\mathrm{mag}^{-1}$; (*right axis and blue points*) evolution of the stellar mass of highly luminous red galaxies relative to $z = 0.1$. The continuous red line shows how a passively stellar population would fade to produce the same luminosity at $z = 0.1$. The point at $z = 0.1$ is for 2dFGRS (Madgwick et al. 2002). Error bars on our results show errors due to cosmic variance. Error bars on results from the literature are as published.

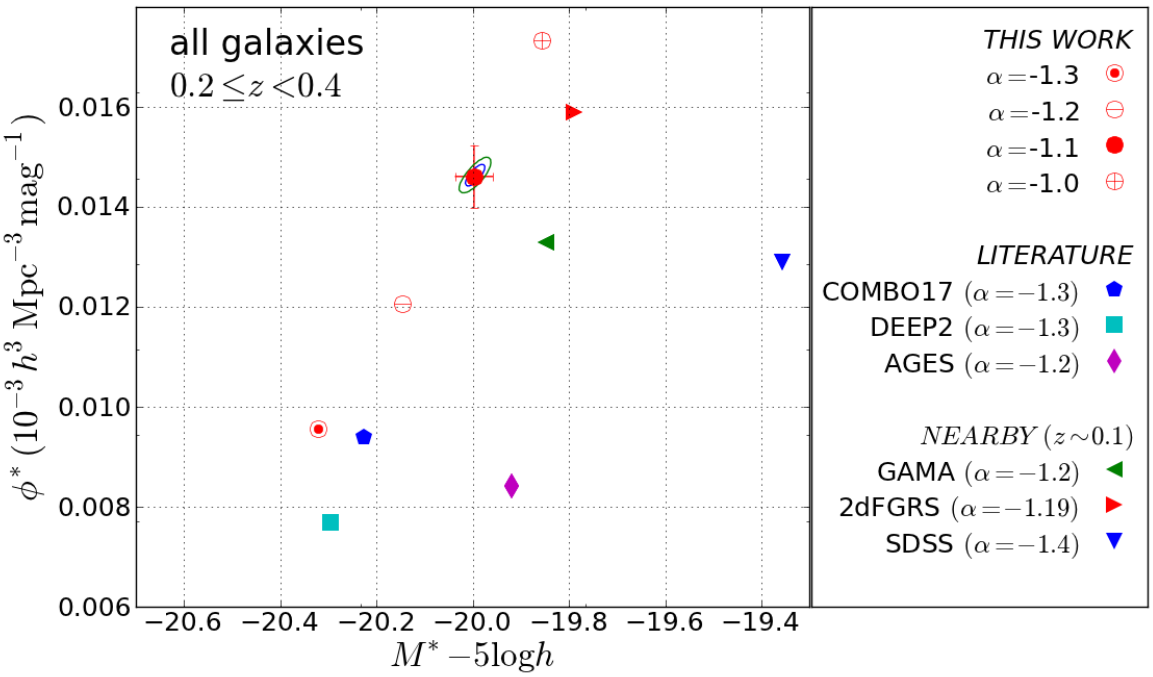

Fig. 83.—: **Random errors in our measurements of ϕ^* and M^* for all galaxies at $0.2 \leq z < 0.4$.** The solid red circle shows our maximum likelihood values using our preferred α value of -1.1; error bars show likely random error due to cosmic variance estimated using subfields, contours show 68% and 95% confidence limits for the maximum likelihood fit. Also shown are results obtained using data from the COMBO-17, DEEP2 and AGES surveys by the following authors respectively (assumed α values in parentheses): Willmer et al. (2006, $\alpha = -1.3$), Faber et al. (2007, $\alpha = -1.3$) and Cool et al. (2012, $\alpha = -1.2$) The large effect that the assumed value of α has on the maximum likelihood values ϕ^* and M^* can be seen from the additional points plotted for our data using $\alpha = -1.0, 1.2$ and 1.3. The latter giving similar values to Willmer et al. (2006) and Faber et al. (2007) who both use $\alpha = -1.3$. Low redshift ($z \sim 0.1$) values from the GAMA, 2dFGRS and SDSS surveys are also shown (Loveday et al. 2012; Madgwick et al. 2002; Blanton et al. 2005a, respectively)

.

3.10.4. Comparison with the literature and sources of error

As can be seen from Figures 61 to 63 and 75 to 78, our results are for the most part in broad agreement with previous authors. In particular, our results line up well with those from low redshift surveys including 2dFGRS, SDSS and GAMA.

We find that the stellar mass in red galaxies as a whole has approximately quadrupled from $z \sim 1.1$ to $z \sim 0.1$. This is a larger rate of growth than that quoted by some prior authors who report that it has approximately doubled from $z \sim 1$ to $z \sim 0$ (e.g. Mortlock et al. 2011; Brown et al. 2007). For highly luminous red galaxies we find a doubling of stellar mass from $z \sim 1.1$ to $z \sim 0.1$. Other authors have found that 80% of the stellar mass at $z \sim 0$ was already in place by $z \sim 1$ (e.g. Mortlock et al. 2011; Brown et al. 2007). We believe that our very large galaxy sample and accurate photometry provide us with more accurate measurements than has previously been possible.

The three Schechter parameters ϕ^*, M^* and α are highly degenerate. In particular, if we fix alpha, the measured values of ϕ^* and M^* depend critically on the value of alpha adopted. This is clearly demonstrated in Figure 83 which shows results for red and blue galaxies combined using values for α of -1.3, -1.2, -1.1 and -1.0. Our preferred value is $\alpha = -1.1$ and this results in very different values for ϕ^* and M^* to Willmer et al. (2006) and Faber et al. (2007) using DEEP2 and COMBO-17 data. However, if we adopt their value of $\alpha = -1.3$ the discrepancy (also visible in the lower panel of Figure 75) disappears. Figure 103 in Chapter 4 specifically compares three Schechter function fits for the K-band luminosity function using different α values and further illustrates the degeneracy between ϕ^*, M^* and α.

The luminosity density for red galaxies is largely insensitive to the assumed value for alpha because for these galaxies $\alpha = -0.5$ the gamma function $\Gamma(\alpha + 2)$ in (51) has a minimum at $\alpha = -0.5$, and 90% of the luminosity density is due to galaxies with luminosities close to M^*. For blue galaxies the upturn in the faint end of the luminosity function is reflected in a much larger negative value for alpha ($\alpha \sim -1.3$). Because $\Gamma(\alpha + 2)$ climbs very steeply as α decreases to -1.0 and beyond, the luminosity density given by (51) depends critically on the exact value adopted for α because a substantial proportion of the total blue galaxy luminosity density is contributed by galaxies fainter than M^*. (For example, as shown in Figure 5 80% of the light for red galaxies with $\alpha = -0.5$ and $M^* - 5 \log h = -20.0$ comes from galaxies between ~ 1.3 mag fainter than M^* and ~ 1.2 mag brighter, while for blue galaxies with $\alpha = -1.3$ and $M^* - 5 \log h = -20.0$ it comes from galaxies between ~ 2.8 mag fainter and ~ 0.6 mag brighter).

The largest random source of error in the luminosity function at all redshifts is cosmic variance (§3.9). We illustrate the importance of this and statistical errors in performing the

maximum likelihood fits to the Schechter parameters for an example redshift bin $0.2 \leq z < 0.4$ in Figure 83. As one progresses to higher redshifts the statistical error decreases (because the numbers of galaxies in a redshift bin increases), while the cosmic variance error remains important.

We expect our apparent magnitudes, calculated as in §3.3, to be more accurate than the SExtractor MAGAUTO values as used by many other authors. Our apparent magnitudes are 0:08 mag or more systematically brighter than those produced by MAGAUTO (Figure 44) because our method of measuring apparent because our method of measuring apparent magnitudes more accurately measures the total light from galaxies, especially faint ones for which MAGAUTO does not use a PSF to correct for light beyond the aperture.

We also investigated the effect of the random photometric redshift errors shown in Table 12 on our maximum likelihood luminosity functions. We also investigated the effect of the random photometric redshift errors on our maximum likelihood luminosity functions. We did this by convolving Gaussian functions representing the random photometric redshift errors with our measured Schechter functions, and found that the change in magnitude at any fixed space density was less than 0.01 mag, except for the bright end of the luminosity function in the lowest redshift bin ($0.2 \leq z < 0.4$). However, 95% of bright galaxies in this redshift range have spectroscopic redshifts, which we use in preference to photometric ones when available, so our errors remain less than 0.01 mag at all redshifts.

Table 20. B-band Schechter function parameters for fixed and varying α values based on our results.

z	α	ϕ^* $h^3\,\mathrm{Mpc}^{-3}\,\mathrm{mag}^{-1}$	$M^* - 5\log h$	$M\left(10^{-3.5}\right) - 5\log h$	j_B $h\,L_\odot\,\mathrm{Mpc}^{-3}$
Red galaxies - varying α					
0.3	-0.5	$4.12 \pm 0.31 \times 10^{-3}$	-20.86 ± 0.07	-21.83 ± 0.04	$1.50 \pm 0.10 \times 10^{8}$
0.5	-0.5	$5.50 \pm 0.16 \times 10^{-3}$	-20.55 ± 0.07	-21.68 ± 0.07	$1.40 \pm 0.46 \times 10^{8}$
0.7	-0.5	$6.86 \pm 0.14 \times 10^{-3}$	-20.12 ± 0.05	-21.51 ± 0.04	$1.06 \pm 0.22 \times 10^{8}$
0.9	-0.5	$5.12 \pm 0.29 \times 10^{-3}$	-20.37 ± 0.06	-21.55 ± 0.04	$1.03 \pm 0.25 \times 10^{8}$
1.1	-0.5	$3.87 \pm 0.39 \times 10^{-3}$	-20.35 ± 0.05	-21.44 ± 0.03	$0.75 \pm 0.47 \times 10^{8}$
Red galaxies - $\alpha = -0.5$					
0.3	-0.5	$7.43 \pm 0.31 \times 10^{-3}$	-19.82 ± 0.07	-21.25 ± 0.04	$0.86 \pm 0.10 \times 10^{8}$
0.5	-0.5	$7.60 \pm 0.16 \times 10^{-3}$	-19.93 ± 0.07	-21.37 ± 0.07	$0.99 \pm 0.46 \times 10^{8}$
0.7	-0.5	$5.71 \pm 0.14 \times 10^{-3}$	-20.10 ± 0.05	-21.43 ± 0.04	$0.86 \pm 0.22 \times 10^{8}$
0.9	-0.5	$5.14 \pm 0.29 \times 10^{-3}$	-20.15 ± 0.06	-21.44 ± 0.04	$0.81 \pm 0.25 \times 10^{8}$
1.1	-0.5	$3.91 \pm 0.39 \times 10^{-3}$	-20.20 ± 0.05	-21.38 ± 0.03	$0.65 \pm 0.47 \times 10^{8}$
Blue galaxies - varying α					
0.3	-1.2	$2.74 \pm 0.45 \times 10^{-3}$	-20.88 ± 0.06	-21.48 ± 0.04	$3.03 \pm 0.43 \times 10^{8}$
0.5	-1.2	$7.52 \pm 0.39 \times 10^{-3}$	-20.47 ± 0.07	-21.59 ± 0.07	$2.58 \pm 1.18 \times 10^{8}$
0.7	-1.2	$7.71 \pm 0.40 \times 10^{-3}$	-20.43 ± 0.05	-21.53 ± 0.04	$2.91 \pm 0.74 \times 10^{8}$
0.9	-1.2	$10.85 \pm 0.23 \times 10^{-3}$	-20.34 ± 0.05	-21.61 ± 0.04	$2.88 \pm 0.19 \times 10^{8}$
1.1	-1.2	$3.37 \pm 0.39 \times 10^{-3}$	-20.89 ± 0.06	-21.56 ± 0.05	$5.69 \pm 0.56 \times 10^{8}$
Blue galaxies - $\alpha = -1.3$					
0.3	-1.2	$8.75 \pm 0.45 \times 10^{-3}$	-19.92 ± 0.06	-21.09 ± 0.04	$1.65 \pm 0.43 \times 10^{8}$
0.5	-1.2	$8.73 \pm 0.39 \times 10^{-3}$	-20.19 ± 0.07	-21.35 ± 0.07	$2.09 \pm 1.18 \times 10^{8}$
0.7	-1.2	$9.09 \pm 0.40 \times 10^{-3}$	-20.29 ± 0.05	-21.46 ± 0.04	$2.39 \pm 0.74 \times 10^{8}$
0.9	-1.2	$9.66 \pm 0.23 \times 10^{-3}$	-20.38 ± 0.05	-21.58 ± 0.04	$2.77 \pm 0.19 \times 10^{8}$
1.1	-1.2	$4.54 \pm 0.39 \times 10^{-3}$	-20.62 ± 0.06	-21.53 ± 0.05	$1.62 \pm 0.56 \times 10^{8}$
All galaxies - varying α					
0.3	-1	$6.17 \pm 0.56 \times 10^{-3}$	-20.92 ± 0.05	-21.93 ± 0.04	$3.81 \pm 0.27 \times 10^{8}$
0.5	-1	$11.80 \pm 0.47 \times 10^{-3}$	-20.60 ± 0.07	-21.90 ± 0.07	$3.92 \pm 1.47 \times 10^{8}$
0.7	-1	$14.33 \pm 0.04 \times 10^{-3}$	-20.36 ± 0.04	-21.75 ± 0.04	$3.53 \pm 0.78 \times 10^{8}$
1.1	-1	$15.58 \pm 0.44 \times 10^{-3}$	-20.38 ± 0.05	-21.80 ± 0.04	$3.78 \pm 0.28 \times 10^{8}$
1.1	-1	$7.27 \pm 0.62 \times 10^{-3}$	-20.72 ± 0.05	-21.78 ± 0.04	$3.88 \pm 0.87 \times 10^{8}$
All galaxies - $\alpha = -1.1$					
0.3	-1	$14.61 \pm 0.56 \times 10^{-3}$	-20.00 ± 0.05	-21.40 ± 0.04	$2.42 \pm 0.27 \times 10^{8}$
0.5	-1	$15.00 \pm 0.47 \times 10^{-3}$	-20.19 ± 0.07	-21.60 ± 0.07	$2.97 \pm 1.47 \times 10^{8}$
0.7	-1	$14.19 \pm 0.40 \times 10^{-3}$	-20.29 ± 0.04	-21.67 ± 0.04	$3.07 \pm 0.78 \times 10^{8}$
1.1	-1	$14.43 \pm 0.44 \times 10^{-3}$	-20.35 ± 0.05	-21.75 ± 0.04	$3.32 \pm 0.28 \times 10^{8}$
1.1	-1	$8.63 \pm 0.62 \times 10^{-3}$	-20.49 ± 0.05	-21.73 ± 0.04	$2.26 \pm 0.87 \times 10^{8}$

3.11. Summary

We measured evolution of the B-band luminosity function from $z = 1.2$ to $z = 0.2$ based on data from an $\sim$8 deg^2 field in Boötes.

$BwRIJHKs$ optical and near infrared photometry from the NDWFS and NEWFIRM surveys and photometry in the Spitzer IRAC 3.6, 4.5, 5.8 and 8.0 μm infrared bands enabled absolute magnitudes to be calculated in the U, B and V-wavebands, and cuts to be applied to exclude stars and AGN, and to limit the sample to objects with plausible photometry for galaxies.

We employed template based photometric redshifts calculated by Michael Brown, based on the $\sim$125 new galaxy SED templates in Brown et al. (2013). At first we had made use of his photometric redshifts based on the ANNz artificial neural network code, but after much investigation these were abandoned because they were found to produce an implausible drop in blue galaxy numbers around $z = 0.45$.

We developed a new method of determining total apparent magnitudes from observed magnitudes measured using photometric apertures with a range of diameters from 1 to 20 arcsec. We produced empirically determined growth curves of measured magnitude with aperture diameter for isolated galaxies in order to determine the optimum aperture diameter and the corresponding magnitude correction for light falling outside the aperture. We expected our total magnitudes to be more accurate than previously used methods (e.g. MAGAUTO which is known to underestimate total galaxy magnitudes).

Absolute magnitudes were calculated in the U, B and V-wavebands using the new K-correction method in Chapter 2.

We used both the $1/V_{\rm max}$ and maximum likelihood methods to determine Schechter function fits to the B-band luminosity function in five redshift bins between $z = 0.2$ and $z = 1.2$. Our measurements were compared with those from other studies (Bell et al. 2004; Brown et al. 2007; Willmer et al. 2006; Faber et al. 2007; Cool et al. 2012), and in the low redshift Universe with Madgwick et al. (2002); Blanton et al. (2005a); Loveday et al. (2012). We found good agreement, despite the fact that we separated "red" and "blue" galaxies using an evolving cut in restframe $(M_U - M_B)$ versus M_B colour-magnitude space whereas other authors have used a variety of other methods.

Evolution of the Schechter parameters M^* and ϕ^* giving the characteristic magnitude and space density of the luminosity function was measured for both varying and fixed values of the faint end slope parameter α. Because of the difficulty of measuring faint end slopes at higher redshifts because of sample incompleteness we adopted fixed values corresponding to

$0.2 \leq z < 0.6$. These were -1.1, -0.5 and -1.3 respectively for all, red and blue galaxies. We demonstrated the degeneracy of the three Schechter parameters and showed that this had little effect on either the total B-band luminosity density (obtained by integrating the Schechter function) or the measured evolution of highly luminous galaxies (which we determined by measuring evolution of the absolute magnitude corresponding to a fixed space density).

Blue galaxies are more numerous than red at all redshifts and are present in rapidly increasing numbers as one goes to fainter magnitudes (faint end slope parameter $\alpha = -1.3$) whereas the numbers of red galaxies show a downturn and decrease rapidly at fainter magnitudes ($\alpha = -0.5$). The characteristic space density ϕ^* for blue $\sim L^*$ galaxies hardly changed from $z \sim 1$ to the present while that of red galaxies doubled. The characteristic luminosity $\sim L^*$ of blue galaxies faded more (0.9 mag) than that of red (0.6 mag).

The total luminosity density j_B of blue galaxies halved from $z = 0.9$ to the present, while that of red galaxies changed little from $z = 1.1$ to the present. (Our results for blue galaxies at $1.0 \leq z < 1.2$ are uncertain because of indeterminate systematic redshift errors.) By comparing the fading of luminosity density in our red galaxy sample with that to be expected on the basis of passive evolution alone (i.e. no mergers and no star formation), we inferred that the stellar mass in red galaxies quadrupled from $z = 1.1$ to the present, most of this increase occurring since $z \sim 0.6$.

Using a similar comparison with the fading to be expected from passive evolution alone, we also concluded that highly luminous red galaxies approximately doubled in mass from $z = 1.1$ to the present.

Our results are consistent with "downsizing" in which more massive, luminous blue galaxies cease star formation and move to the red sequence sooner than less massive ones. This results in a decrease in the characteristic magnitude M^* of blue galaxies and an increase in the space density of red galaxies. Migration of galaxies from the blue cloud to the red sequence largely offsets the decrease in red galaxy luminosity density caused by stellar fading. The luminosity density of blue galaxies on the other hand decreases much more rapidly due to a combination of downsizing and the loss of galaxies to the red sequence.

4. EVOLUTION OF THE K-BAND INFRARED LUMINOSITY FUNCTION AND THE GALAXY STELLAR MASS FUNCTION

4.1. Introduction

4.1.1. Optical and infrared luminosities and their relation to stellar mass to light ratios

Measurement of the K-band luminosity function is of particular importance because it is often argued that it can provide better estimates of the stellar mass function than optical wavebands. Bell & de Jong (2001) showed that there is a tight relationship between optical and near infrared stellar mass to light (M/L) ratios and restframe optical colour, such as $(M_B - M_R)$. Their Figure 1(d) (reproduced in Figure 84) showed that in optical wavebands (M/L) varies by a factor $\sim$7 between different types of galaxies whereas in near infrared bands such as the K-band it only varies by a factor $\sim$2, although the scatter is greater in infrared wavebands.

However, Bell & de Jong (2001) was based on the predictions of theoretical stellar population synthesis (SPS) models alone (Bell & Bower 2000), and these did not include the full range of observed metallicities. In a development of their work, Bell et al. (2003) estimated stellar mass to light ratios by fitting PEGASE (Fioc & Rocca-Volmerange 1997) models to observed $ugriz$ magnitudes from the Sloan Digital Sky Survey (SDSS York et al. 2000; Stoughton et al. 2002) and K magnitudes from 2MASS (Skrutskie et al. 2006) for $\sim$20 000 galaxies. Figure 85, taken from the Appendix to Bell et al. (2003), shows their plots of B-band and K-band (M/L) ratios as a function of restframe $(M_B - M_R)$ colour. The appendix to their paper provides a table of parameters for calculating mass to light ratios in the $grizJHK$-bands as linear functions of restframe SDSS colours, and for determining $BVRIJHK$ mass to light ratios from restframe $(B-V)$ and $(B-R)$ colours. Bell et al. (2003) assumed a modification of the Salpeter (1955) initial stellar mass function in their SPS models that had fewer faint low mass stars and this modification lowered their computed stellar mass to light ratios by $\sim$30%.

The M/L ratio for blue galaxies shows greater scatter in the K-band than in the B-band and this is due to variation in metallicity (Bell et al. 2003), but the uncertainties in stellar M/L ratios are still only $\sim$0.2 dex in the K-band for blue galaxies and $\sim$0.1 dex for red. In the B-band the uncertainties are $\sim$0.1 dex for both red and blue galaxies. Despite the increased scatter for blue galaxies the K-band is often preferred for estimating stellar mass to light ratios because of the much smaller range of M/L values amongst galaxy types. In essence this narrow range is because the restframe K-band samples the part of galaxy spectra which consists mainly of black body emission in the Rayleigh-Jeans tail from stars, with little contribution from absorption and emission lines (Figure 86). Over the whole redshift

range $0 \leq z \leq 1.2$ the J, Ks, 3.6 μm and 4.5 μm filters sample the same relatively featureless part of the SED. We choose to use apparent magnitudes in these wavebands to determine our absolute K-band magnitudes following the method described in Chapter 2.

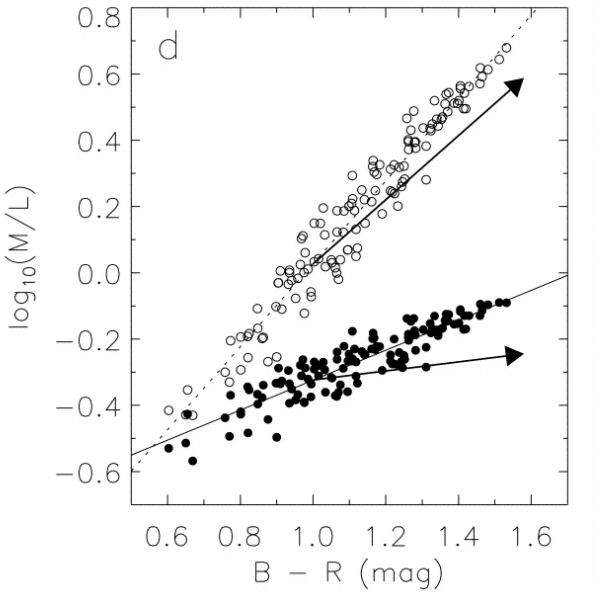

Fig. 84.—: **Showing that stellar mass to light (M/L) ratios are tightly correlated with optical restframe colour.** *Upper points and line:* B-band; *lower points and line:* K-band. The range of (M/L) ratios is ∼7 in the B-band but only ∼2 in the K-band, making the latter waveband a better choice for determining stellar masses from stellar luminosities. This figure is reproduced from Figure 1d of Bell & de Jong (2001) who used a range of SPS models from Bell & Bower (2000) to calculate their (M/L) ratios. (The long arrows show the effect of dust reddening and are largely parallel to the plotted data.)

Recently Taylor et al. (2011) have argued against the conventional wisdom that galaxy masses are determined more accurately using near infrared restframe colours than using optical ones. Using data from GAMA they showed (their Figure 11) that fitting $ugrizYJHK$ optical + infrared photometry to Bruzual & Charlot (2003) (BC03) models *cannot* accurately predict near infrared observed magnitudes, and results in magnitude offsets $\sim$+0.08 in the $zJHK$ bands as well as offsets $\sim$-0.08 in the r and i bands. When they used a mock SED catalogue (their Figure A1) the model fits to the simulated near infrared observations were found to be near perfect, showing that the model fitting was not in error. This demonstrated that the failure of BC03 models to accurately reproduce near infrared spectra was due to the inadequacy of the existing SED libraries at near infrared wavelengths. They concluded that until improved SED libraries are available, optical wavebands are preferable to near infrared ones for determining stellar masses.

In addition Taylor et al. (2011) showed that this conclusion was not specific to the use of BC03 models. A similar conclusion was reached using Maraston (2005) models and the Bruzual (2007) modification to BC03 models which included thermally pulsing asymptotic giant branch (TP-AGB) stars. The systematic offets in the infrared were different with these models, so providing further evidence of the inability of currently available stellar population synthesis models to accurately reproduce observed infrared SEDs. The inclusion of TP-AGB stars when only optical photometry was fitted did not result in an under-prediction of near infrared fluxes, as would be expected, but an over-prediction in the same way as when BC03 models were used without TP-AGB stars. TP-AGB components cannot therefore be the cause of the systematic errors in the near infrared, as has been suggested.

Taylor et al. (2011) investigated in detail the dependence of i-band stellar M/L ratios on restframe $(g-i)$ colour as predicted by BC03 models, and concluded that it is possible to derive stellar mass estimates that are accurate to within a factor of ≤ 2 using g and i-band photometry alone.

To further justify this statement they also plotted the stellar M/L ratio against restframe $(g-i)$ colour for GAMA galaxies, and varied in turn either the stellar formation ages, or the metallicities, or the star-forming histories used in their SPS models. They found that the relationship between M/L and $(g-i)$ changed remarkable little, because the variation of M/L ratio with each of these parameters is largely parallel to the overall trend (their Figure 11). Furthermore, as noted by previous authors, e.g. Bell & de Jong (2001); Bell et al. (2003), the dust reddening vector was also largely parallel to the overall trend of M/L with $(g-i)$ colour, so that that dust reddening also had little effect on the M/L - $(g-i)$ relationship.

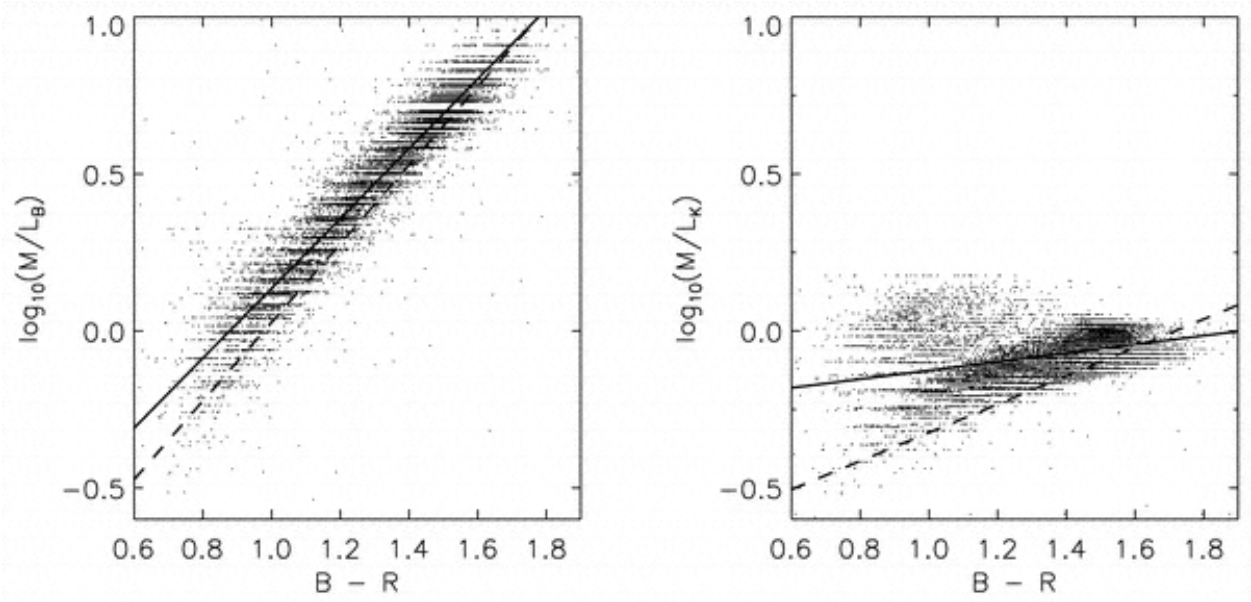

Fig. 85.—: **Plots of stellar mass to light ratios from the appendix to Bell et al. (2003), showing that the range of stellar mass to light ratios is smaller in the K-band than in the B-band.** *Left:* B-band; *right:* K-band. The data points are calculated using PEGASE SPS models fitted to $ugrizK$ magnitudes and the solid line is a least squares best fit. The dashed line is a fit to the purely theoretical SPS models used in Bell & de Jong (2001) whose predictions differ significantly from the newer ones in Bell et al. (2003) who include a realistic spread in metallicity.

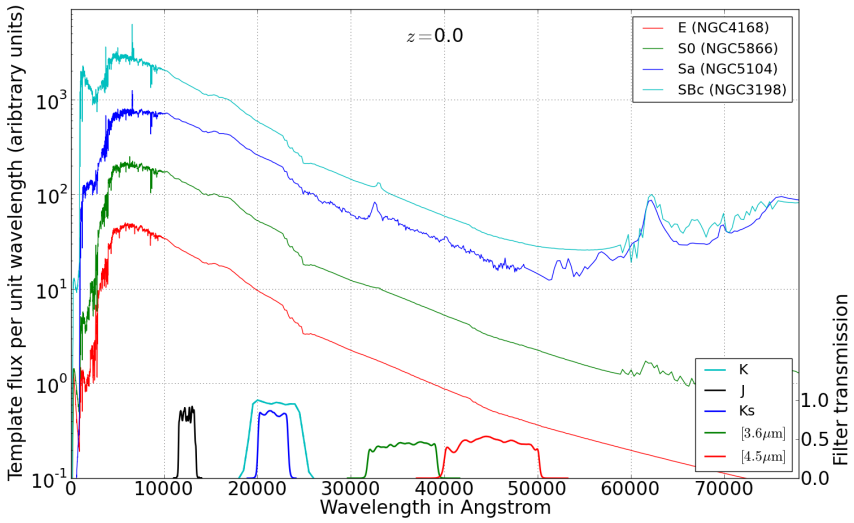

(a)

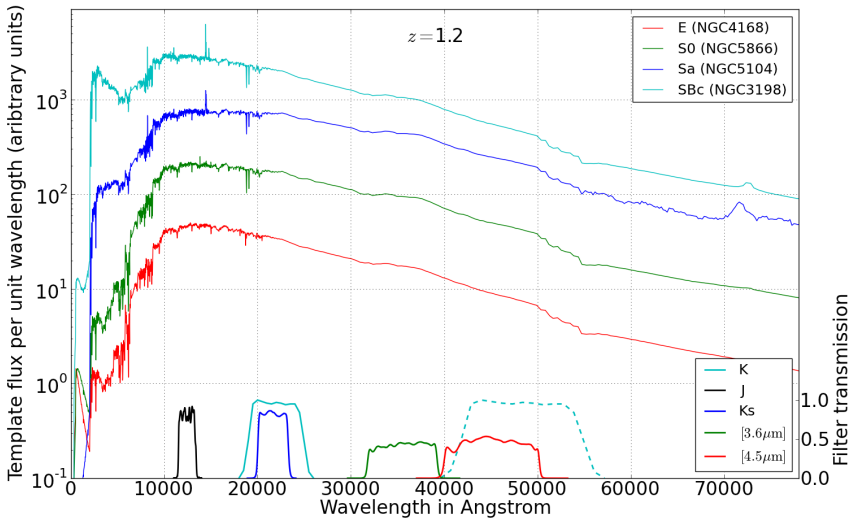

(b)

Fig. 86.—: **The observed near infrared spectra of four template galaxies with representative SEDs.** *Top:* The SEDs at $z = 0$ (offset artificially for clarity) in relation to the Johnson J and K filters, the NEWFIRM Ks filter, and the IRAC 3.6 and 4.5 μm filters; *bottom:* observed SEDs from galaxies at $z = 1.2$ with the same representative restframe SEDs. The redshifted restframe K-band filter is shown dashed in the lower figure. The restframe K-band samples a part of each galaxy spectrum consisting largely of black body emission in the Rayleigh-Jeans tail of stars, with little contribution from absorption and emission lines.

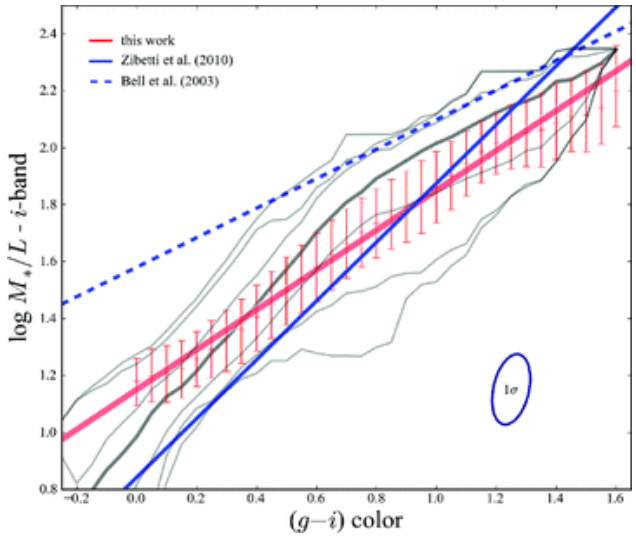

Fig. 87.—: **Comparing the i-band stellar mass relationships given in Bell et al. (2003) and Taylor et al. (2011).** The solid red line shows the relationship derived by Taylor et al. (2011) who used only optical photometry for fitting their SPS models. The dashed blue line shows the relationship from Bell et al. (2003) who also fitted K-band photometry. Also shown as a solid blue line, but not referred to here, is the fit based on Zibetti et al. (2009). This is Figure 13 of Taylor et al. (2011) where further explanation of the figure will be found. AB system colours are used.

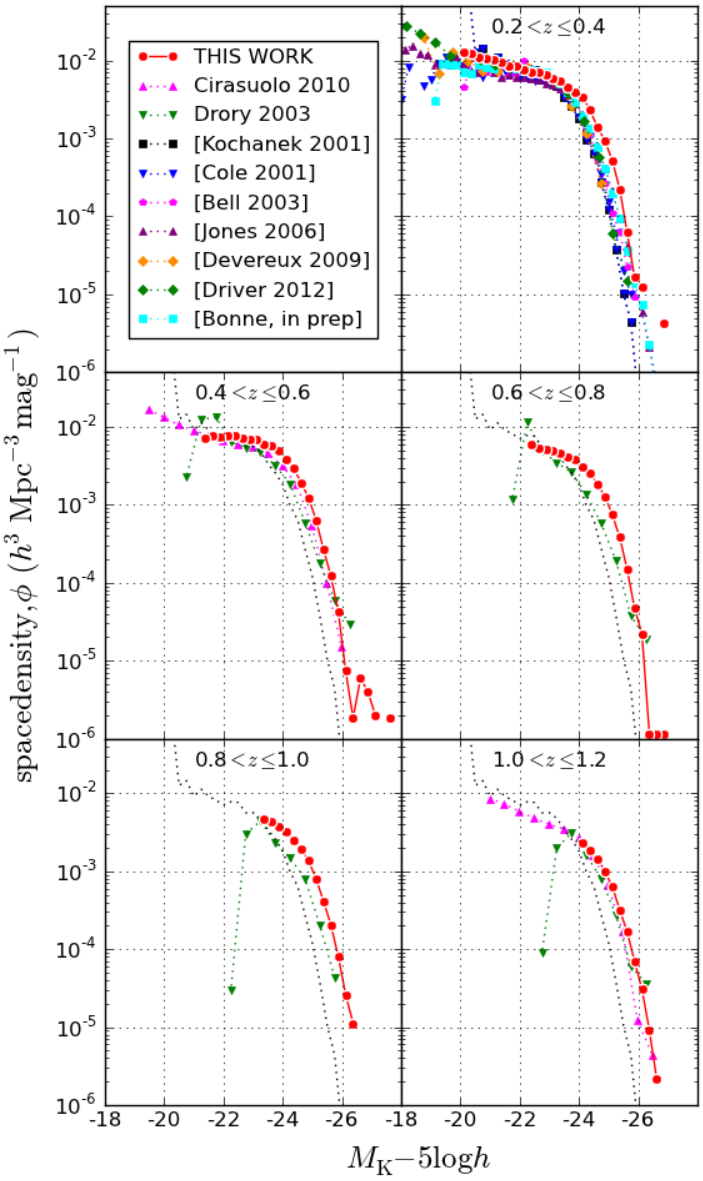

Fig. 88.—: **Binned K-band space densities for all galaxies in bins of width 0.1 mag.** The space density of all $\sim L^*$ galaxies increases and the luminosity of the brightest galaxies decreases as they evolve. Our luminosity functions (red points) are in broad agreement with others in the literature, but tend to indicate higher space densities. Luminosity functions for the low redshift Universe are labelled using square brackets. To provide a fixed reference results from Kochanek et al. (2001) are shown as black dotted lines in the lower four panels.

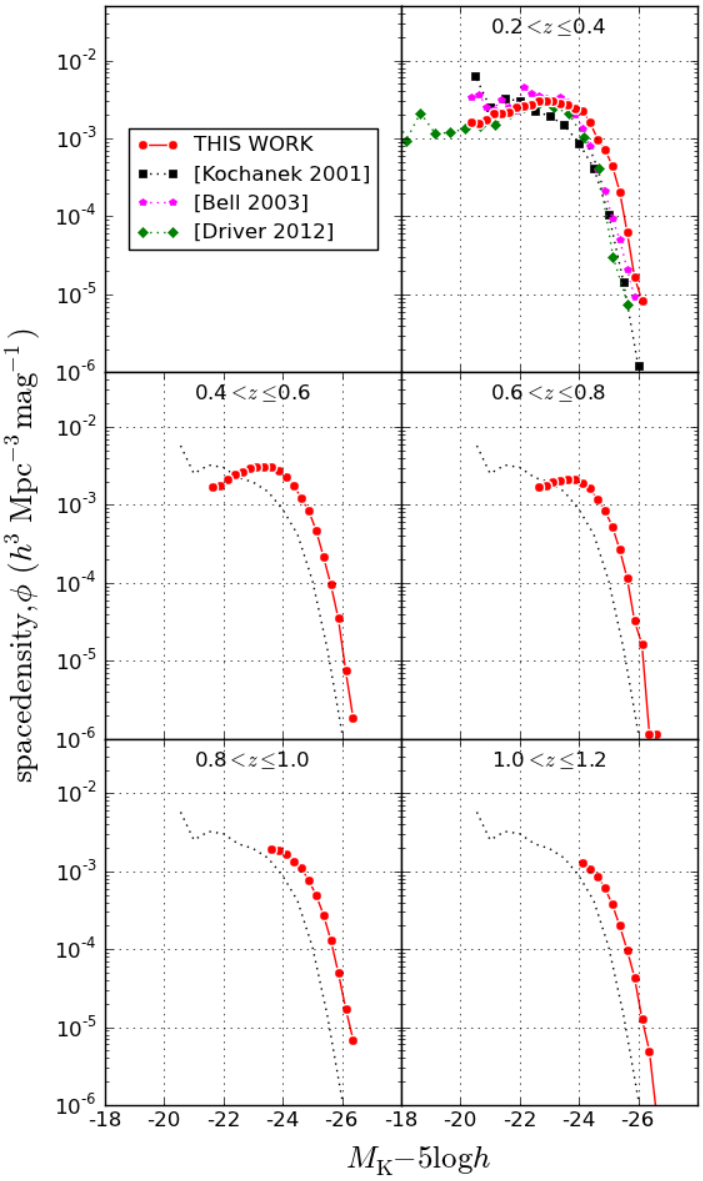

Fig. 89.—: **Binned K-band space densities for red galaxies.** The space density of red $\sim L^*$ galaxies increases and the luminosity of the brightest red galaxies decreases as they evolve. The luminosity function of red galaxies turns over at fainter magnitudes indicating a decrease in space density. Luminosity functions for the low redshift Universe are labelled using square brackets. To provide a fixed reference results from Kochanek et al. (2001) are shown as black dotted lines in the lower four panels.

For all the preceding reasons Taylor et al. (2011) argued strongly for the use of the restframe optical $(g-i)$ colour in conjunction together with a restframe optical magnitude such as i for the determination of stellar masses. However, it needs to be noted that they used SDSS optical data and UKIDSS infrared data, and the latter may well have calibration errors due to a non-linearity issue with the UKIDSS detectors.

Based on optical photometry alone from GAMA, they obtained the relation $\log(M/L_i) = -0.68+0.70(M_g-M_i)$ between the stellar M/L ratio and restframe $(g-i)$ AB colour. Using the Vega magnitude system this becomes:

$$\log(M/L_i) = -0.48 + 0.70(M_g - M_i). \tag{55}$$

This is offset from, and has steeper slope than, the i-band stellar M/L relation $\log(M/L_i) = -0.152 + 0.518(M_g - M_i)$ provided by Bell et al. (2003) who included K-band photometry in their model fitting as well as $ugriz$. According to the preceding arguments from Taylor et al. (2011) this relation should be less accurate because near infrared photometry has been used in the model fitting. Figure 87, taken from Taylor et al. (2011), compares the two relationships.

It is clear from the discussion in this section that the stellar masses of galaxies are highly model dependent, unlike their luminosities which are reliably determined by observations. Because different studies use different models to determine stellar mass to light ratios there is considerable variation in conclusions regarding the absolute value of stellar masses. In terms of understanding how galaxies evolve, however, it is the rate of change of stellar mass that is the most important consideration, and in this respect measurements based on different model assumptions agree much more closely.

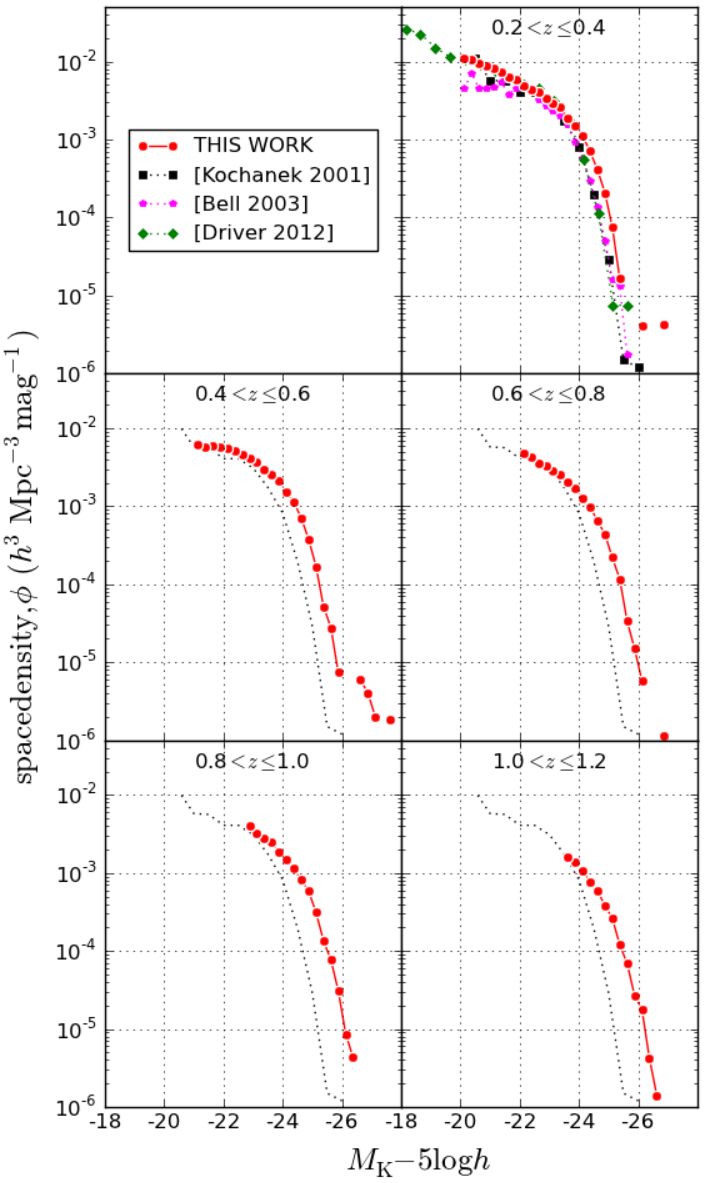

Fig. 90.—: **Binned K-band space densities for blue galaxies.** The space density of blue $\sim L^*$ galaxies increases and luminosity of the brightest blue galaxies decreases as they evolve. The luminosity function of blue galaxies continues rising towards fainter magnitudes so that faint galaxies make a much larger contribution to the total luminosity density than for red galaxies. Luminosity functions for low redshift are labelled using square brackets. To provide a fixed reference results from Kochanek et al. (2001) are shown as black dotted lines in the lower four panels.

4.1.2. Infrared luminosity functions in the literature

We summarise the essential features of several key studies of K-band galaxy luminosity functions in Table 21. We note the trend towards fainter limiting K-band magnitudes and correspondingly larger sample sizes as the available telescope technology has advanced.

Most of the prior studies used spectroscopic redshifts and determined the K-band luminosity density of the low redshift Universe, i.e. $z \leq 0.2$. At these low redshifts we expect cosmic variance to be a potential source of significant systematic error except for the very largest sample sizes. Sample sizes vary from a few hundred to over 110 000 for Jones et al. (2006) who used data from 6dFGS covering almost half the sky. Different studies have subdivided their samples into early and late galaxies in different ways, for example colour, morphology from visual inspection, central concentration index, emission line strength.

Loveday (2000) used a sample of 345 galaxies imaged using the Cerro Tololo Interamerican Observatory 1.5-m telescope and found that a Schechter function provided a good fit to the luminosity function of $z < 0.04$ galaxies. They divided their sample into emission line (ELG) and non-emission line (non-ELG) galaxies on the basis of the equivalent width of the H_α line, and found little difference in the shape of the luminosity function, although there was a hint that ELG galaxies had a value for M* roughly 1 mag fainter than that for non-ELGs

Many studies of the local K-band galaxy luminosity function (e.g. Cole et al. 2001; Kochanek et al. 2001) have used data from the Two Micron All Sky Survey (2MASS, Skrutskie et al. 2006). 2MASS surveyed the whole sky in the near infrared J, H and $K_{\rm S}$-bands to depths of 15.8, 15.1, and 14.3 mag (Vega) respectively, achieving a $1-\sigma$ photometric uncertainty of 0.03 mag. Because 2MASS is relatively shallow it necessitated the use of models to estimate the total flux from extended sources. Even so we expect that surveys based on 2MASS may underestimate the true luminosity of galaxies because the faint outer parts of extended sources become lost in the sky background.

One of the first key studies with samples of a few thousand was Kochanek et al. (2001) who used a sample of 4192 galaxies covering 6960 deg^2 from the 2MASS Second Incremental Release Catalogue of Extended Sources (Jarrett et al. 2000). They morphologically subdivided their sample into early and late galaxies using visual estimates of the Hubble T-stage, the numerical galaxy classification scheme used in the RC3 Catalogue (de Vaucouleurs et al. 1991). They used $\mu_{Ks} = 20\,\mathrm{mag\,arcsecond}^{-1}$ isophotal magnitudes in the range $7 < Ks < 11.25$ mag and obtained luminosity functions for absolute magnitudes brighter than $Ks = -20.25$.

Table 21. K-band luminosity functions in the literature.

Approx mean redshift	Galaxy types	number of galaxies	α	ϕ^* ($\mathrm{Mpc}^{-3}\,\mathrm{mag}^{-1}$)	$M^* - 5\log h$	j_K ($L_\odot\,\mathrm{Mpc}^{-3}$)
Loveday 2000	(Cerro Tololo Interamerican Observatory 1.5-m telescope, $Ks < 12$, spectroscopic redshifts)					-
¡0.04	all	345	-1.16	12.0×10^{-3}	-23.58	
0.05	ELG	134	-1.3	1.0×10^{-3}	-23.5	
0.05	non-ELG	138	-1.2	11.0×10^{-3}	-22.5	
Kochanek et al. 2001	(2MASS, $Ks < 11.25$, spectroscopic redshifts)					-
0.05	all	3878	-1.09	11.6×10^{-3}	-23.39	7.67×10^{8}
0.05	early	1781	-0.92	4.5×10^{-3}	-23.53	3.08×10^{8}
0.05	late	2097	-0.87	10.1×10^{-3}	-22.98	4.06×10^{8}
Cole et al. 2001	(2MASS+2dFGRS, $Ks < 13.2$, spectroscopic redshifts)					-
0.04	all	5683	-0.96	10.8×10^{-3}	-23.44	5.66×10^{8}
Bell et al. 2003	(2MASS, $K < 13.5$, spectroscopic (SDSS) redshifts)					-
0.078	all	6282	-0.77	14.3×10^{-3}	-23.29	5.8×10^{8}
Drory et al. 2003	(MUNICS, $K < 19.5$, photometric redshifts)					-
0.5	all	5000	-1.09	10.15×10^{-3}	-23.66	6.58×10^{8}
0.7	all	between all	-1.09	9.57×10^{-3}	-23.76	6.84×10^{8}
0.9	all	four redshift	-1.09	8.99×10^{-3}	-23.87	7.08×10^{8}
1.1	all	bins	-1.09	8.41×10^{-3}	-23.97	7.3×10^{8}
Pozzetti et al. 2003	(K20, $Ks < 20$, spectroscopic redshifts)					-
0.5	all	132	-1.25	1.78×10^{-3}	-24.87	4.08×10^{8}
1	all	170	-0.98	2.91×10^{-3}	-24.77	4.91×10^{8}
Huang et al. 2003	(AAO KRS, $K < 16$, spectroscopic redshifts)					-
0.138	all	1056	-1.38	14×10^{-3}	-23.7	12.88×10^{8}
Jones et al. 2006	(6dFGS, $K < 12.75$, spectroscopic redshifts)					-
0.054	all	113988	-1.16	7.48×10^{-3}	-23.83	6.03×10^{8}
Arnouts et al. 2007	(SWIRE+VVDS,+CFHTLS+UKIDSS UDS, $K < 20$, mostly photometric redshifts)					-
0.3	all	2180	-1.1	12.22×10^{-3}	-23.97	9.96×10^{8}
0.5	all	2680	-1.1	10.2×10^{-3}	-23.96	8.24×10^{8}
0.7	all	3336	-1.1	9.8×10^{-3}	-24.09	8.91×10^{8}
0.9	all	4545	-1.1	12.3×10^{-3}	-24.21	12.5×10^{8}
1.1	all	3027	-1.1	8.02×10^{-3}	-24.35	9.26×10^{8}
1.35	all	3077	-1.1	7.46×10^{-3}	-24.31	8.31×10^{8}
-	-	-	-	- -	-	
0.3	red	514	-0.6	5.19×10^{-3}	-24.04	3.76×10^{8}
0.5	red	617	-0.3	4.29×10^{-3}	-23.68	2.29×10^{8}
0.7	red	767	-0.3	3.76×10^{-3}	-23.86	2.36×10^{8}
0.9	red	1117	-0.3	4.61×10^{-3}	-23.96	3.17×10^{8}
1.1	red	669	0	2.62×10^{-3}	-23.99	2.03×10^{8}
1.35	red	468	0.3	1.2×10^{-3}	-23.97	1.06×10^{8}
-	-	-	-	- -	-	
0.3	blue	1666	0.3	6.94×10^{-3}	-23.96	6.8×10^{8}
0.5	blue	2063	0.5	6.47×10^{-3}	-23.95	6.29×10^{8}
0.7	blue	2569	0.7	6.44×10^{-3}	-24.08	7.06×10^{8}
0.9	blue	3428	0.9	8.22×10^{-3}	-24.19	9.96×10^{8}
1.1	blue	2358	1.1	5.8×10^{-3}	-24.32	7.93×10^{8}
1.35	blue	2609	1.35	6.06×10^{-3}	-24.32	8.29×10^{8}
Devereux et al. 2009	(2MASS, $K < 10$, spectroscopic redshifts)					-
0.03	all	1345	-0.94	11.5×10^{-3}	-23.41	5.8×10^{8}
0.03	E	142	-0.03	1.76×10^{-3}	-23.42	0.81×10^{8}
0.03	S0-Sbc	893	-0.18	15.7×10^{-3}	-22.49	3.4×10^{8}
0.03	Sc-Scd	246	-1.41	1.59×10^{-3}	-23.33	0.8×10^{8}
Smith et al. 2009	(SDSS+UKIDSS, $K < 16$, spectroscopic redshifts)					-
0.05	all	40111	-0.81	16.6×10^{-3}	-23.19	6.31×10^{8}
Cirasuolo et al. 2010	(UKDSS UDS, $K < 23$, photometric redshifts)					-
0.3	all	3254	-1.07	9.44×10^{-3}	-23.82	7.01×10^{8}
0.5	all	5883	-1.07	8.65×10^{-3}	-23.94	7.16×10^{8}

Kochanek et al. (2001) found that the luminosity density of local late type galaxies was slightly ($\times 1.17$) higher than that of early types, early types being brighter ($M_K = -23.53$ as opposed to $M_K = -22.98$) but less numerous ($0.45 \times 10^{-2}\, h^3\, \mathrm{Mpc}^{-3}$ as opposed to $1.01 \times 10^{-2}\, h^3\, \mathrm{Mpc}^{-3}$). Unlike some previous morphologically typed optical surveys (e.g. Loveday et al. 1992; Marzke et al. 1998) they found that both early and late type galaxies have similarly shaped luminosity functions with $\alpha \sim -0.9$. They pointed out that this is in sharp contrast with surveys that divide early and late types on the basis of colour - these show steepening of the faint end slope for late type galaxies.

We used the local luminosity functions of Kochanek et al. (2001) as a benchmark in our plots showing the evolution of luminosity functions at higher redshifts (Figures 88 to 90).

Cole et al. (2001) also used 2MASS but combined it with data from the Two Degree Field Galaxy Redshift Survey (2dFGRS, Norberg et al. 2002; Madgwick et al. 2002) to obtain a fainter and incomplete but larger catalogue containing 17 713 galaxies with measured redshifts. They measured the local J and K-band luminosity functions. The results of Cole et al. (2001) and Kochanek et al. (2001) are in agreement. According to Kochanek et al. (2001), the Cole et al. (2001) survey should have smaller statistical errors but larger systematic errors.

Bell et al. (2003) combined K-band infrared photometry from 2MASS with optical *ugriz* photometry and spectroscopic redshifts from SDSS and used the resulting sample of over 6000 galaxies to determine luminosity functions in the corresponding restframe wavebands, i.e. *ugrizK*. They recognised that 2MASS is biased against low surface brightness galaxies and they took steps to correct for this. Their sample was morphologically split into early and late subsamples in a relatively crude manner with the use of an r-band concentration index.

Spectroscopic studies of the low redshift K-band luminosity function using data other than 2MASS include Jones et al. (2006) ($\sim$110 000 6dFGS galaxies covering almost half the sky) and Driver et al. (2012) (7638 galaxies from the GAMA survey). Surveys tracing evolution of the K-band luminosity function have mostly used photometric redshifts (Drory et al. 2003; Arnouts et al. 2007; Cirasuolo et al. 2010). The exception is Pozzetti et al. (2003) who made use of spectroscopic redshifts to determine the luminosity function at redshifts of 0.5, 1.0 and 1.5, but their sample sizes were only $\sim$150.

Drory et al. (2003) traced evolution of the K-band luminosity function since $z \sim 1.1$ using a sample size of $\sim$5000 with photometric redshifts and data from the Munich Near Infrared Cluster Survey (MUNICS, Drory et al. 2001). Cirasuolo et al. (2010) used deep spectroscopy and photometry from the UKIRT Infrared Deep Sky Survey Ultra Deep Survey (UKIDSS UDS) and Arnouts et al. (2007) additionally used 3.6, 4.5, 5.6, 8.0 and 24μm IRAC pho-

Table 21—Continued

Approx mean redshift	Galaxy types	number of galaxies	α	ϕ^* ($\mathrm{Mpc}^{-3}\,\mathrm{mag}^{-1}$)	$M^* - 5\log h$	j_K ($L_\odot\,\mathrm{Mpc}^{-3}$)
0.7	all	5831	-1.07	7.78×10^{-3}	-24.03	7.02×10^{8}
0.9	all	5652	-1.07	6.89×10^{-3}	-24.11	6.7×10^{8}
1.1	all	6351	-1.07	6.02×10^{-3}	-24.18	6.26×10^{8}
Hill et al. 2010	(MGC+SDSS+UKIDSS, $K < 15.7$, spectroscopic redshifts)					-
0.05	all	1785	-0.96	15.6×10^{-3}	-23.36	6.98×10^{8}
Driver et al. 2012	(GAMA, $K < 14.9$, spectroscopic redshifts)					-
0.05	all	7638	-1.03	11×10^{-3}	-23.53	6.1×10^{8}
0.05	ellipticals	-	-0.31	5.8×10^{-3}	-23.16	2.02×10^{8}
0.05	spirals	-	-1.17	7×10^{-3}	-23.45	4.06×10^{8}
Bonne et al. 2013	(2MASS, $K < 10.75$, mostly photometric redshifts)					-
0.06	all	13321	-1.22	7.24×10^{-3}	-23.83	5.83×10^{8}
This work	(NEWFIRM+SDWFS, $K < 20$?, mostly photometric redshifts)					-
0.3	all	-	-1.1	8.75×10^{-3}	-24.16	9.06×10^{8}
0.5	all	-	-1.1	9.1×10^{-3}	-24.29	10.68×10^{8}
0.7	all	-	-1.1	6.9×10^{-3}	-24.37	8.68×10^{8}
0.9	all	-	-1.1	7.36×10^{-3}	-24.35	9.15×10^{8}
1.1	all	-	-1.1	5.67×10^{-3}	-24.35	7×10^{8}
-	-	-	-	- -	-	
0.3	red	-	-0.5	7.77×10^{-3}	-23.77	4.68×10^{8}
0.5	red	-	-0.5	7.81×10^{-3}	-23.84	5.03×10^{8}
0.7	red	-	-0.5	5.45×10^{-3}	-24.02	4.15×10^{8}
0.9	red	-	-0.5	5.02×10^{-3}	-24.04	3.87×10^{8}
1.1	red	-	-0.5	3.85×10^{-3}	-24.05	3.01×10^{8}
-	-	-	-	- -	-	
0.3	blue	-	-1.3	4.26×10^{-3}	-23.95	4.45×10^{8}
0.5	blue	-	-1.3	3.93×10^{-3}	-24.31	5.69×10^{8}
0.7	blue	-	-1.3	3.24×10^{-3}	-24.27	4.54×10^{8}
0.9	blue	-	-1.3	3.49×10^{-3}	-24.35	5.27×10^{8}
1.1	blue	-	-1.3	2.41×10^{-3}	-24.38	3.74×10^{8}

tometry from the SWIRE survey (Lonsdale et al. 2003), $u'g'r'i'z'$ optical photometry from the Canada-France-Hawaii Telescope Legacy Survey (CFHTLS) and spectroscopy and deep $BVRI$ photometry from the VIMOS VLT Deep Survey (VVDS Le Fèvre et al. 2005) .

UKIDSS (Lawrence et al. 2007) surveyed 7500 square degrees of the Northern sky in the J, H and K wavebands to a depth of $K = 18.3$, three magnitudes deeper than 2MASS. It is a near infrared counterpart to the Sloan survey, and is made up of five separate surveys including the Ultra Deep Survey (UDS) which reaches a depth of $K = 23$ over an area of 0.77 square degrees.

4.1.3. Parameterisation of the stellar mass function using a Schechter function

As found by Cole et al. (2001), stellar mass functions can be parameterised using the Schechter function (Schechter 1976). The comoving number space density ϕ at any given redshift as a function of mass M is then:

$$\phi_M\,(M)\,dM = \left(\frac{\phi^*}{M^*}\right)\left(\frac{M}{M^*}\right)^{\alpha}\exp\left(\frac{-M}{M^*}\right)dM. \tag{56}$$

Here ϕ^* is a normalising factor, the characteristic mass M^* corresponds roughly to the transition from a power law luminosity function to an exponential one, and α determines the slope of the power law variation at the low mass end.

Because of the large range of observed galaxy masses it is more useful to write (56) in terms of logarithms of mass relative to the Sun's mass: $\mu = \log_{10}(M/M_{\odot})$. Writing $\mu^* = \log_{10}(M^*/M_{\odot})$ we obtain:

$$\phi_\mu(\mu)d\mu = (\phi^* \ln 10)\,10^{(\alpha+1)(\mu-\mu^*)}\exp(-10^{(\mu-\mu^*)})d\mu. \tag{57}$$

The space density at $M = M^*$ (or $\mu = \mu^*$) is $\phi^* \ln 10$ or $2.30\phi^*$, so ϕ^* effectively measures the space density of galaxies per unit $\log_{10} M$ at the characteristic mass.

The total stellar mass density ρ_M can be calculated by integrating (56) over all masses M to give:

$$\rho_M = \phi^* M^* \Gamma(\alpha + 2). \tag{58}$$

4.2. Stellar mass functions in the literature

Cole et al. (2001) provided the first estimate of the galactic stellar mass function derived directly from near infrared data and found that it was fairly well fitted by the same Schechter functional form as luminosity functions. Their stellar mass functions were based on J and Ks-band photometry from 2MASS, together with spectroscopic redshifts from 2dFGRS and b_J-band photometry from automated scans of UK Schmidt Telescope plates. J-band stellar M/L ratios were estimated by generating a grid of BC03 models with different metallicities and star formation histories and finding the one with the nearest match to the observed $(b_J - Ks)$ and $(J - Ks)$ colours. Separate stellar mass functions were obtained using Kennicutt and Salpeter initial mass functions in the BC03 models (Kennicutt 1983; Salpeter 1955) and these showed significant differences, the Salpeter initial mass function resulting in greater numbers of more massive galaxies with the most massive galaxies being consderably more massive. Cole et al. (2001) concluded that uncertainty in the initial mass function (IMF) was their greatest source of potential error. They also estimated that stellar mass in the Universe made up a fraction $1.6 \pm 0.24 \times 10^{-3}\,\Omega_c/h$ using a Kennicutt IMF or $2.9 \pm 0.43 \times 10^{-3}\,\Omega_c/h$ using a Salpeter IMF, Ω_c being the critical density of the Universe.

As well as producing J and K-band luminosity functions and tables of stellar mass to light ratios (§4.1.1), Bell et al. (2003) also determined stellar mass functions for all their sample galaxies as well as for early and late type galaxies separately, based on K-band luminosities from 2MASS and i-band luminosities from SDSS. They subdivided their sample of 6283 galaxies into early and late types based on a simple morphological concentration index and produced separate stellar mass functions for each. In agreement with previous work they found that the characteristic luminosity and mass of early type galaxies is larger than that for later types, and that the faint end slope for later types is steeper than that for early types. They estimated that at least one half and possible three quarters of the stellar mass of the Universe is in early type galaxies and gave an estimated upper limit to the stellar mass density in the low redshift Universe of $2.0 \pm 0.6 \times 10^{-3}\,\Omega_c/h$.

Arnouts et al. (2007) used their measurements of how K-band total luminosity density has evolved since $z = 2$ to determine how the stellar mass function has evolved over the same period. They used stellar mass to light ratios obtained by fitting BC03 models with Salpeter IMFs to optical and infrared photometry for a spectroscopic subsample and found that the stellar M/L_K ratio for all galaxies increased over time according to the following linear relation: $\log(M/L_K) = -0.30z + 0.03$ with global rms $\sigma = 0.22$. Dividing their sample into active/blue and quiescent/red subsamples on the basis of SED fitting they found the following relations: $\log(M/L_K) = -0.27z + 0.05$ (active/blue, $\sigma = 0.21$) and $\log(M/L_K) = -0.18z + 0.04$ (quiescent/red, $\sigma = 0.15$). They attributed the increase in stellar M/L over

time to the reduction in star formation rates since $z = 2$ and the resulting decrease in the proportion of highly luminous young blue stars.

Arnouts et al. (2007) found a major build-up in the quiescent population from $z \sim 2$ to $z \sim 1.2$ with its stellar mass increasing by a factor of 10, but from $z \sim 1.2$ to the present ($\sim$8 Gyr) they found that it increased by a factor of only $\sim$2. The stellar mass density of active galaxies was found to have been relatively constant since $z \sim 1.2$. These results suggest that between $z \sim 2$ and $z \sim 1.2$ an increasing proportion of galaxies have ended their star formation and moved to the red sequence. These conclusions are in agreement with those from their measurements of K-band luminosity function evolution which support the idea that a large fraction of galaxies was already assembled by $z \sim 1.2$, with 80% of the present day active population and 50% of the quiescent population already in place by this time.

Borch et al. (2006) analysed a sample of $\sim$25 000 galaxies from the COMBO-17 survey over the redshift interval $0.2 < z < 1.0$ using SPS models fitted to the photometry from 5 broadband and 12 medium band filters to estimate stellar mass to light ratios. They found that at all redshifts below $z = 1$ more than 60% of massive galaxies with $M^* > 10^{11} M_\odot$ are quiescent while blue galaxies dominate at lower masses. They found that the total stellar mass density of the Universe has roughly doubled since $z \sim 1$. However, the integrated stellar mass of blue galaxies has not significantly changed, the majority of the growth of stellar mass occurring in red sequence galaxies.

Bundy et al. (2006) measured the mass-dependent evolution of more than 8000 field galaxies for $0.4 < z < 1.4$ using spectroscopic redshifts from the DEEP2 survey, and supplemented these with photometric redshifts in order to test the completeness of their main spectroscopic sample. They calculated galaxy masses from Ks-band photometry obtained at Palomar Observatory by fitting Bruzual & Charlot (2003) to $BRIK$ colours (BRI photometry being provided by the Canada-France-Hawaii Telescope (CFHT). They attempted to quantify "downsizing" in blue star-forming galaxies, whereby the most massive luminous galaxies cease to form stars earlier than less massive ones, and showed that it showed little dependence on environment, except for the most massive galaxies, so suggesting that it was governed by internal rather than external processes. Bundy et al. (2006) also compared the effect of separating galaxies by restframe $(M_U - M_B)$ colour, star formation rate based on the [O II] line, and morphology.

Ilbert et al. (2010) used a sample of almost 200 000 galaxies covering an area of 2 deg^2 from the Cosmic Evolution Survey (COSMOS) (Scoville et al. 2007) to measure the evolution of the stellar mass function and stellar mass density from $z = 2$ to $z = 0.2$. The large area and sample size minimised cosmic variance. Accurate photometric redshifts were derived

with the *Le Phare* software (Arnouts et al. 2002; Ilbert et al. 2006a) using photometry in 31 bands ranging from the ultraviolet to the mid-infrared measured by a range of terrestrial and space telescopes. They subdivided their sample morphologically using high resolution HST/ACS images (Koekemoer et al. 2007) but also subdivided them by $(NUV - r)$ colour, and investigated various subsamples that they labelled quiescent, red sequence, red elliptical, blue elliptical and elliptical. Stellar masses were determined from K-band stellar M/L ratios derived using SPS models from a BC03 library fitted to all their available photometry, including that at 24 μm. One conclusion of this study was that $z \sim 1$ was an epoch of transition in the stellar mass assembly of quiescent galaxies, with stellar mass density increasing by a factor of $\sim$12 (1.1 dex) in the $\sim$2.5 Gyr from $z \sim 1.75$ to $z \sim 0.9$, but a factor of only $\sim$2 (0.3 dex) in the $\sim$6 Gyr from then to $z \sim 0.1$. Another was that the mass density of massive star-forming galaxies became less than that of massive elliptical galaxies after $z \sim 1$, indicating the latter could no longer be forming by "wet" mergers between massive star-forming galaxies (i.e. mergers which trigger further star formation resulting in depletion of available gas for further star formation).

Ilbert et al. (2013) used a sample of 220 000 galaxies from the first data release of the UltraVISTA survey (McCracken et al. 2012) to measure evolution of the stellar mass function for star-forming and quiescent galaxies between $z = 4$ and $z = 0.2$. UltraVISTA is an ultra-deep, near-infrared survey with the new VISTA survey telescope of the European Southern Observatory (ESO). Over the course of 5 years, UltraVISTA will repeatedly image the COSMOS field in 5 bands resulting in three key surveys: an ultra-deep broad-band (Y, J, H, Ks) survey covering 0.73 deg^2, a deep broad-band (Y, J, H, Ks) survey covering the full 1.5 deg^2 field, and a narrow-band survey covering the same region as the ultra-deep broadband survey. Ilbert et al. (2013) used 30-band photometric redshifts. They separated their sample into star-forming and quiescent subsamples based on $(NUV - r^+)$ and $(r^+ - J)$ colours which cleanly separate dusty star-forming galaxies and quiescent galaxies. They found that the low mass end of the stellar mass function of star-forming galaxies has evolved more rapidly than the high mass end, this fall being attributed to star formation in galaxies more massive than $\sim 10^{10.8}\,M_\odot$ being quenched. No significant evolution of the high mass end of the stellar mass function of quiescent galaxies was seen, but they saw a flattening of the faint end slope with time. Over the whole mass range the comoving density of quiescent galaxies increased by a factor of $\sim$40 (1.6 dex) from $z \sim 3$ to $z \sim 1$, but then by less than $\sim$1.6 (0.2 dex) from $z \sim 1$ to the present.

Baldry et al. (2012) measured the low-redshift stellar mass function using a sample of 5210 galaxies from GAMA covering an area of 143 deg^2. They used a density-corrected maximum volume method to correct for fluctuations in space density. They obtained their i-band stellar mass to light ratios from $(g - i)$ colours using the prescription $\log(M/L_i) = a + b(g - i)$ and

compared the resulting stellar mass functions when the values of a and b were taken from Bell et al. (2003) and Taylor et al. (2011).

Moustakas et al. (2013) used a sample of ∼40 000 galaxies with redshifts in the range $0.2 < z < 1.0$ from five fields totalling ∼5.5 deg^2 from the PRIMUS spectroscopic survey (Coil et al. 2011; Cool et al. 2013). PRIMUS is the largest faint galaxy spectroscopic redshift survey carried out to date, providing redshifts accurate to $\delta z/(1+z) < 0.005$ for 125 000 galaxies covering more than 9 deg^2 out to $z = 1$, and focusing on regions with deep Spitzer, optical, GALEX and X-ray data. In addition Moustakas et al. (2013) analysed ∼170 000 galaxies from SDSS at $0.01 < z < 0.2$ which they compared with PRIMUS in order to minimise systematic errors in their evolutionary measurements. They developed their own code *iSEDfit* to fit SPS models to observed photometry in order to derive physical properties of galaxies including stellar mass (Moustakas et al. 2013, Appendix A). Their photometry consisted of the FUV and NUV wavebands from the GALEX Deep Imaging Survey and optical and near infrared wavebands from several surveys including SDSS, SWIRE, COSMOS, and Spitzer/IRAC. They divided their sample into star-forming and quiescent subsamples using an evolving cut in a plot of star formation rate (SFR) against stellar mass

Moustakas et al. (2013) found that the stellar mass function for all galaxies has evolved relatively little from $z = 1$, although they did see evidence for mass assembly downsizing, e.g. an increase by a factor of ∼1.3 in the space density of $\sim 10^{10} M_\odot$ galaxies since $z \sim 0.6$, but a change of less than 10% in the space density of massive galaxies with $M > 10^{11} M_\odot$ since $z \sim 1$. For star-forming galaxies they found little change in the space density of $\sim 10^{10} M_\odot$ galaxies since $z \sim 0.6$, and a decrease by a factor of ∼0.5 in the space density of massive galaxies with $M > 10^{11} M_\odot$ since $z \sim 1$. For quiescent galaxies the space density has increased by a factor of ∼2-3 since since $z \sim 0.6$, while the space density of massive red galaxies with $M > 10^{11} M_\odot$ has remained relatively constant since $z \sim 1$. From their results they concluded that the more massive star-forming galaxies see their star formation quenched first and that the bulk of the build up of quiescent galaxy stellar mass occurs at masses of around $M > 10^{10.8} M_\odot$. They also concluded that mergers did not appear to be a dominant channel for the stellar mass buildup of galaxies at $z < 1$, even among massive ($> 10^{11} M_\odot$) quiescent galaxies.

4.3. Measuring evolution of the K-band luminosity function

We measured evolution of the K-band luminosity function using the same sample as for the B-band luminosity function (Chapter 3). We used the same photometric redshifts, the same evolving red-blue cut, and the same $B_W RIJ$ and 3.6, 4.5, 5.8 and 8.0 μm matched aperture photometry. In addition we used photometry from the NDWFS Ks-band (K short), and the same best fit aperture sizes and corrections as for the other wavebands.

We calculated absolute K-band magnitudes using the method described in Chapter 2, just as we did for the U and B-bands (Chapter 3). Because of the uniformity of photometry, sample and method we are able to make direct comparisons between our optical B-band and near infrared K-band measurements. We also calculated V-band absolute magnitudes (Chapter 3) in order that we could determine stellar mass functions for both the V and K-bands using stellar mass to light ratios based on $(M_B - M_V)$ colours, as given in Bell et al. (2003). These are based on SPS models with a modified Salpeter (1955) stellar IMF.

As shown in Figures 93 and 94 and in Table 22, we used second order polynomials in $(Ks - [3.6\mu\mathrm{m}])$ colour to determine absolute K-magnitudes between $z = 0$ and $z = 0.45$, and polynomials in $([3.6\mu\mathrm{m}] - [4.5\mu\mathrm{m}])$ colour to determine absolute K-magnitudes between $z = 0.45$ and $z = 1.2$.

Figure 86 shows the location of the restframe Johnson K-band, the observed NEWFIRM J and Ks filters, and the IRAC [3.6 μm] and [4.5 μm] filters, in relation to four representative "typical" template galaxies at $z = 0$ and $z = 1.2$. At $z = 0$ all the filters sample the relatively featureless part of each spectrum which is mostly due to emission in the Rayleigh-Jeans tail of stellar spectra. Emission from polycyclic aromatic hydrocarbons (PAHs) appears at longer wavelengths, while stellar emission and absorption features are largely at shorter wavelengths, except for the 1.6 μm stellar opacity feature dip. Even at $z = 1.2$ the filters mostly sample the relatively featureless Rayleigh-Jeans part of the spectrum.

The two template galaxies substantially redder in $(Ks - [3.6\mu m])$ colour than the others for $z < 0.8$ in Figure 93 are UGC5101 (open yellow pentagon) and IRAS03359+1523 (filled cyan triangle). SDSS images are shown in Figure 95. These two are also substantially redder in ([4.5 μm] - [3.6 μm]) colour in Figure 94. The first of these is classified as an

Table 22. The observed wavebands used at different redshifts.

restframe waveband	effective wavelength K	redshift range	observed waveband Y	effective wavelength Y	observed waveband Z	effective wavelength Z
K	2.20	0.2 to 0.45	Ks	2.17	[3.6 μm]	3.56
K	2.20	0.45 to 1.2	[3.6 μm]	3.56	[4.5 μm]	4.51

ultra-luminous infrared galaxy (luminosity $> 10^{12} L_{\odot}$) and the second as luminous infrared galaxy (luminosity $> 10^{12} L_{\odot}$). Both ULIRGs and LIRGs emit most of their energy in the infrared.

Figure 96 shows that the spectra of both these template galaxies exhibit substantial emission from hot (∼a few 100 K) dust in the near infrared, indicating the presence of a powerful AGN. SDSS images (Figure 94) reveal that UGC5101 has a tidal tail showing that it has recently experienced a significant merger or interaction, while IRAS03359+1523 consists of two interacting galaxies. In both cases a powerful AGN giving rise to excess emission from hot dust is likely to have been triggered by the galaxy interaction. These two outliers break the assumption that infrared light from galaxies is dominated by stellar emission.

It can be seen from Figure 93 that these two very red galaxies play a useful role in "anchoring" the colour-colour model used to determine absolute K-magnitudes. Then because the SEDs of nearly all the templates are very similar at the wavelengths being observed, colours can vary very little at certain redshifts, e.g. $(Ks - [3.6\mu\text{m}])$ colour at $z \sim 0.4$. Because the resulting colour range on the x-axis is so small, the fitted polynomial model would be highly indeterminate at this redshift, for the reasons explained in §2.5 and Figure 25, were it not for the two very red galaxy templates which effectively anchor it and constrain it to a well-determined relatively linear form. Similarly, in Figure 94 there is a very small range in ([3.6 μm] - [4.5 μm]) colour at $z > 0.8$ and the same two very red galaxies constrain the model very effectively. Were it not for the presence of these two anomalous template galaxies, other steps would need to be taken to artificially constrain the polynomial model and prevent it from assuming a highly indeterminate and potentially highly convex or concave parabolic shape when the observed colour range was small. It is both fortunate and fortuitous that this is not needed due to UGC5101 and IRAS03359+1523.

From the point of view of anchoring the best fit model curve it does not matter whether UGC5101 and IRAS03359+1523 are typical of highly luminous red galaxies. It is a different question as to whether other highly luminous infrared galaxies would lie close to the best fit model curves in Figures 93 and 94 or not. A larger sample of SEDs from such galaxies would be needed to answer this question and at present such a sample is not available. When using our method for determining absolute K-band magnitudes, it should therefore be born in mind that the values for ULIRGs and LIRGs may *possibly* but not necessarily be in error by a few tenths of a magnitude. It must be emphasised that this represents a worst case scenario and the present work does not suggest that such errors will be present.

We used the $1/V_{\text{max}}$ method to measure the K-band luminosity density of red, blue and all galaxies in five redshift bins of width 0.2 mag between $z = 0.2$ and $z = 1.2$. For each redshift bin we determined the faintest magnitude for which the sample would be complete down to

$I = 23.5$ from a plot of $(M_K + D_{\rm DM} - I)$ against redshift (Figure 92). We then used the maximum likelihood method described in detail in §3.9.1 to fit Schechter functions to the data over a range no wider than that over which the sample was complete to $I = 23.5$.

Initially we allowed the faint end slope parameter α to vary as well as the characteristic space density ϕ^* and magnitude M^*. Then, because α becomes increasingly poorly constrained as redshift increases, we kept α fixed at values corresponding to the lowest two redshift bins ($0.2 \leq z < 0.6$) and repeated the maximum likelihood calculations, allowing just ϕ^* and M^* to vary. The fixed α values we used were -0.5, -1.2 and -1.0 for red, blue and all galaxies respectively.

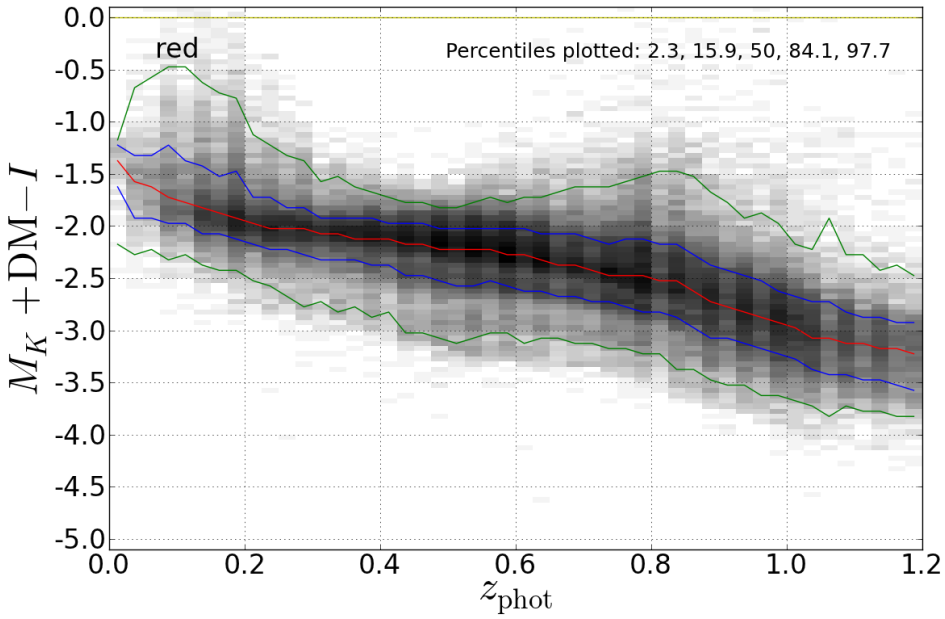

(a)

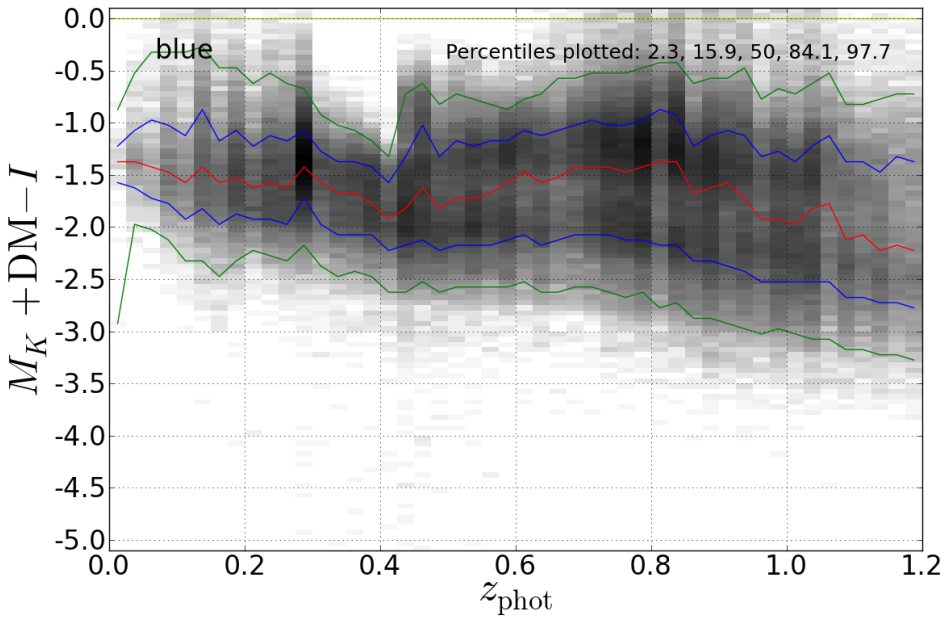

(b)

Fig. 91.—: **Binned plots of $M_K + D_{\mathrm{M}} - I$ against redshift enable the faint absolute magnitude cut-off corresponding to our faint apparent magnitude limit of $I = 23.5$ to be determined.** *Top:* red galaxies; *bottom:* blue galaxies. The red, blue and green lines denote the median and the 1-σ and 2-σ percentiles. We only plot our binned luminosity functions for galaxies brighter than the 2-σ faint limit. (D_{M} is the distance modulus.)

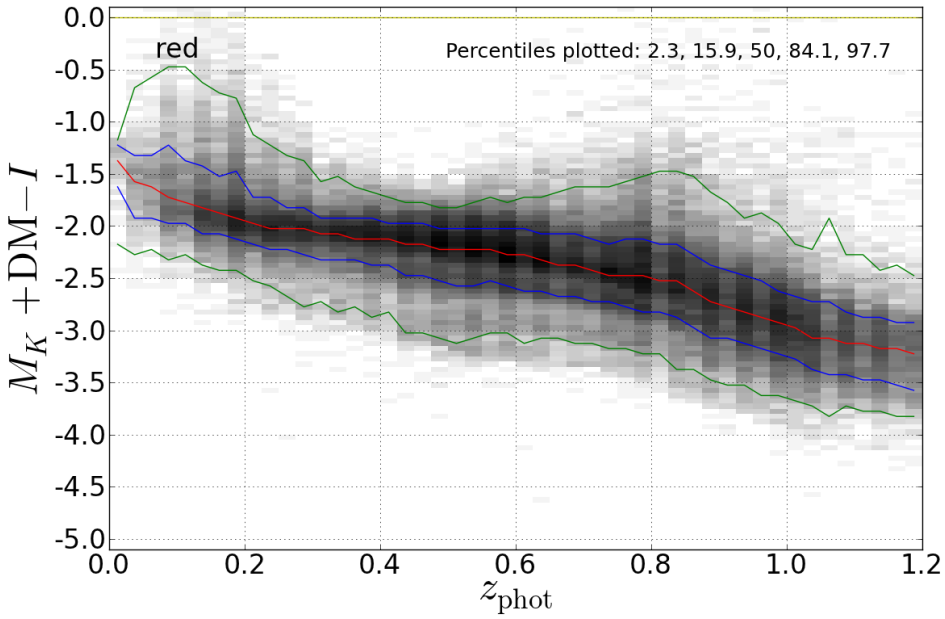

(a)

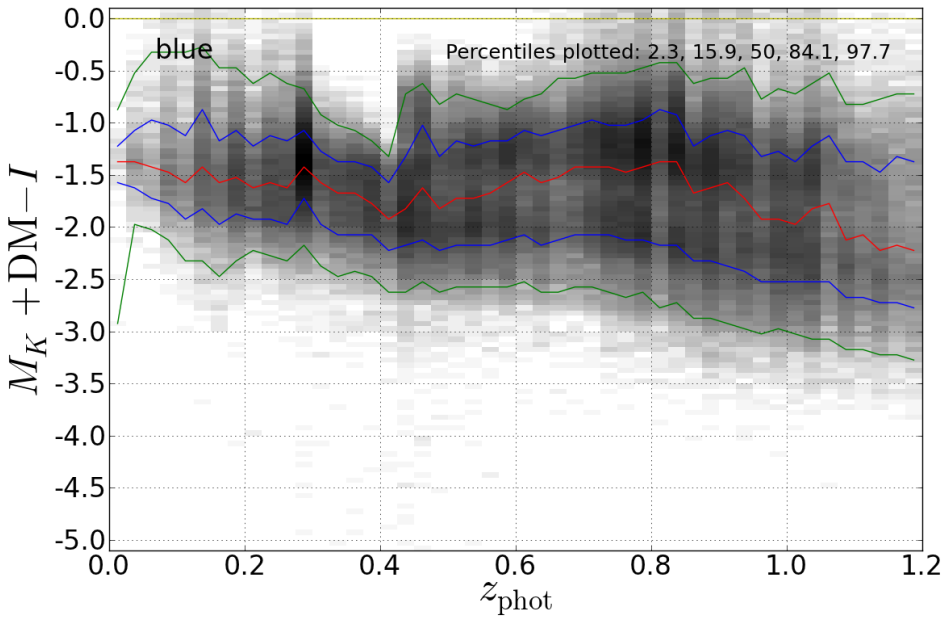

(b)

Fig. 92.—: **Binned plots of $M_K + D_{\mathrm{M}} - I$ against redshift enable the faint absolute magnitude cut-off corresponding to our faint apparent magnitude limit of $I = 23.5$ to be determined.** *Top:* red galaxies; *bottom:* blue galaxies. The red, blue and green lines denote the median and the 1-σ and 2-σ percentiles. We only plot our binned luminosity functions for galaxies brighter than the 2-σ faint limit. (D_{M} is the distance modulus.)

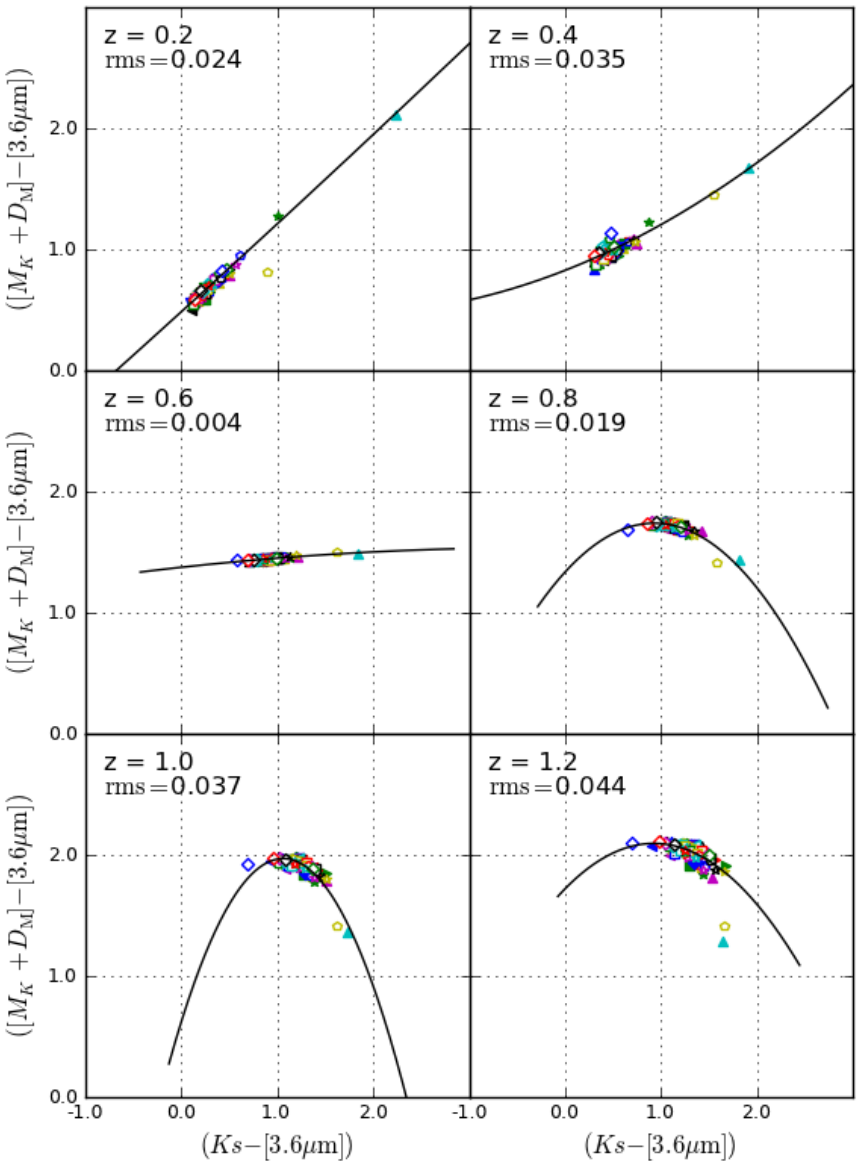

Fig. 93.—: **Determination of absolute K magnitudes between $z = 0$ and $z = 0.45$.** Evolution of the second order polynomial used to determine M_K from observed $(Ks - [3.6\mu m])$ colour from $z = 0$ to $z = 0.45$. The two galaxies substantially redder in $(Ks - [3.6\mu m])$ colour than the others for $z < 0.8$ are UGC5101 (open yellow pentagon) and IRAS03359+1523 (filled cyan triangle).

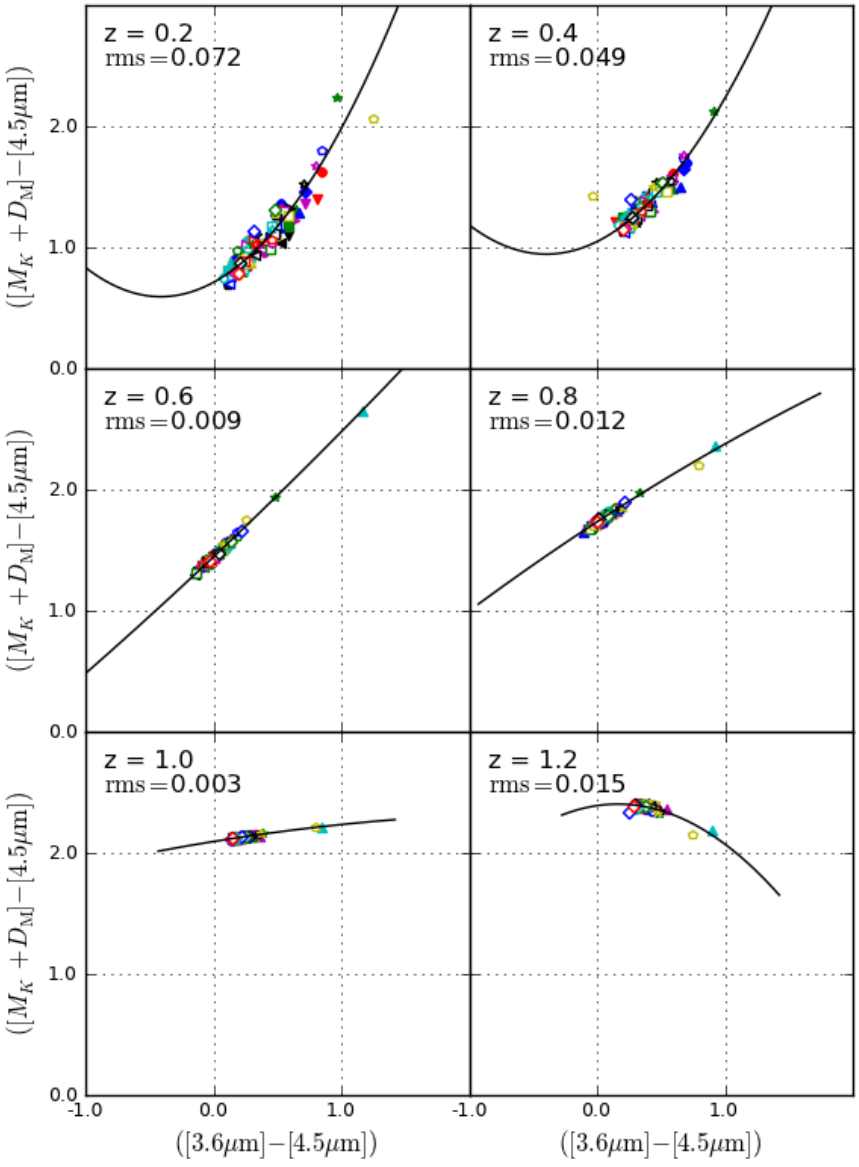

Fig. 94.—: **Determination of absolute K magnitudes for $z \geq 0.45$.** Evolution of the second order polynomial used to determine M_K from observed ([4.5] - [3.6 μm]) colour for $z \geq 0.45$. The two galaxies noticeably redder in $(Ks - [3.6\mu m])$ colour in Figure 93 are also substantially redder in ([4.5 μm] - [3.6 μm]) colour in this figure.

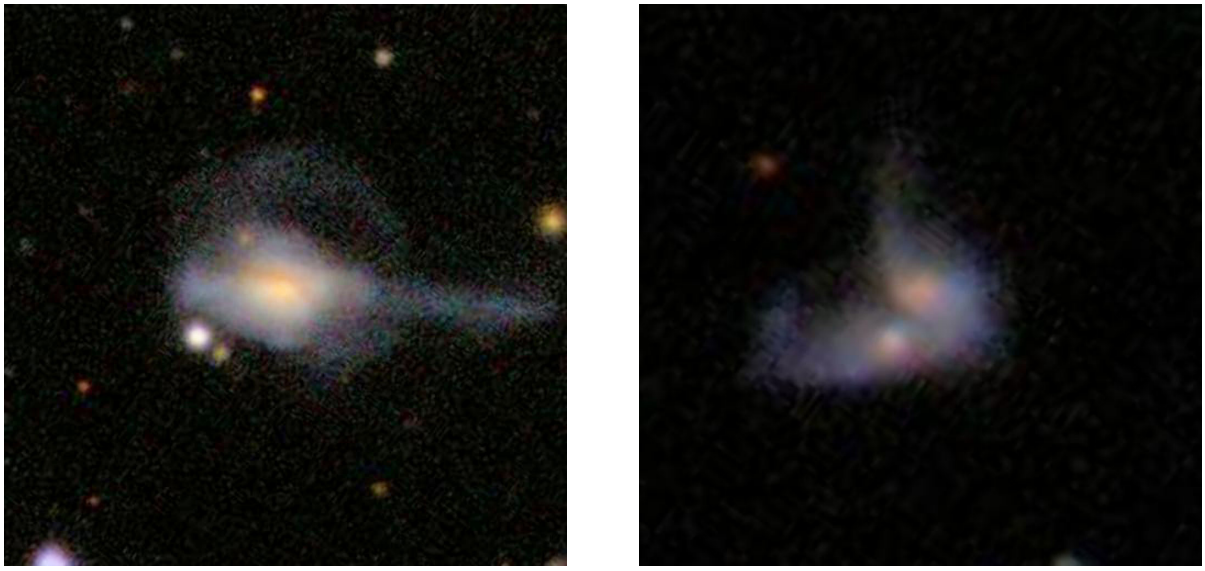

(a) (b)

Fig. 95.—: **SDSS images of the two unusually red galaxies in Figures 93 and 94.** *Left:* this image of UGC5101 shows a tidal tail indicating that it has recently experienced a significant merger or interaction; *right:* IRAS03359+1523 consists of two interacting galaxies.

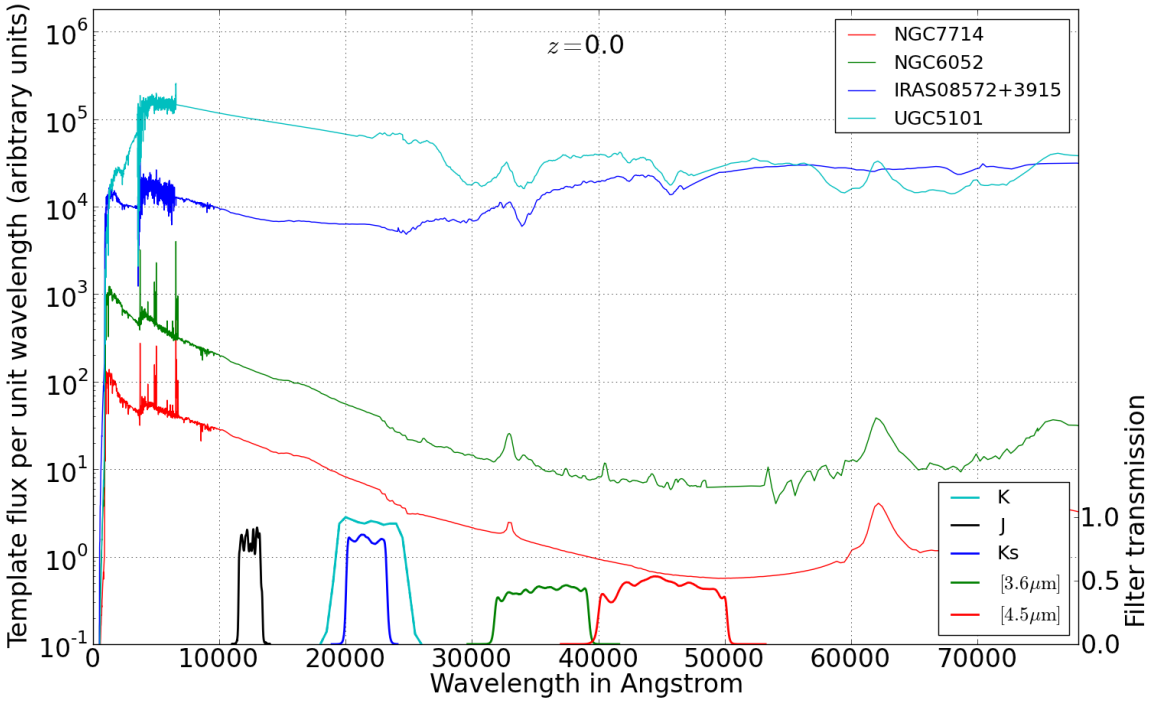

Fig. 96.—: **Spectra of the two unusually red galaxies in Figures 93 and 94.** UGC5101 and IRAS03359+1523 both show unusually high emission in the near infrared indicating the presence of dust heated to a few 100 K by a powerful AGN. Two more typical galaxies are shown for comparison: NGC7714 (SBb starburst) and NGC6052 (Sc).

4.4. K-band luminosity function results and discussion

4.4.1. The evolution of space density and luminosity density

Figures 88 to 90 show our binned $1/V_{\rm max}$ K-band luminosity functions for all, red and blue galaxies, as well as results from previous studies using a variety of surveys. To provide a reference we show the local luminosity functions of Kochanek et al. (2001) in each bin. We only plot bins for which 97.7% of the measured absolute magnitudes have observed I-magnitudes of 23.5 or brighter.

In the first $0.2 \leq z < 0.4$ redshift bin our absolute magnitudes are $\sim$0.3 mag brighter at the bright end of the luminosity function than many of those from the literature for the local Universe. Part of this difference will be due to evolution of the luminosity function, but we also expect our measured magnitudes to be brighter than those from studies such as Kochanek et al. (2001); Cole et al. (2001); Bell et al. (2003) and Bonne et al. (in prep.) which use 2MASS data. This is because, as already noted in §4.2, 2MASS underestimates the true luminosity of extended sources.

At higher redshifts, agreement with the evolving luminosity functions for all galaxies of Drory et al. (2003) and Cirasuolo et al. (2010) is somewhat uneven: being closer at some redshifts than others. Both these studies also use photometric redshifts as we do. Their sample sizes are much smaller than ours [$\sim$70 times smaller for Drory et al. (2003) and $\sim$10 times smaller for Cirasuolo et al. (2010)], so we expect random Poisson errors and cosmic variance to be much more significant, and it is indeed quite evident in the plots in Figures 88 to 90. By contrast, our luminosity functions show little no visible evidence of random variation from one absolute magnitude bin to the next and evolution between redshift bins is smooth.

To parameterise our luminosity functions and measure their evolution we fit Schechter functions (2). Figures 97 to 99 show the maximum likelihood fits to our data (continuous lines) as well as our binned $1/V_{\rm max}$ space densities (data points), using a separate plot for each redshift bin. Figures 100 to 102 display the same data with all redshift bins on a single plot to make the evolution of the luminosity functions more apparent. Figures 104 to 107 show how the Schechter parameters, the luminosity density and the magnitude of highly luminous galaxies evolve.

In the K-band, as in B, blue galaxies are more numerous than red at all redshifts, but the difference is particularly marked for faint galaxies, because red galaxies show a marked downturn in space density at faint magnitudes (per unit magnitude, but not per unit luminosity), whereas the space density of blue galaxies continues rising steeply towards fainter magnitudes. This is reflected in the values of the faint end steepness parameter α, $\sim$-0.5 for

red galaxies and ∼-1.2 for blue.

Figure 104 shows that the space density parameter ϕ^* for both red and blue galaxies increases by a factor of ~ 2 from $z \sim 1.1$ to $z \sim 0.3$ in the K-band. (In the B-band, ϕ^* double for red galaxies but hardly changes for blue).

Figure 105 shows that the characteristic K-band magnitude M^* fades by ∼0.3 mag for red galaxies and by ∼0.6 mag for blue from $z \sim 1.1$ to $z \sim 0.3$. These changes are smaller than those for the B-band: ∼0.6 mag and ∼0.9 mag respectively. This is to be expected because (as discussed in §3.10) the fading of individual $\sim L^*$ red galaxies is mainly due to the ageing of their old stellar populations, whereas the decrease in the characteristic luminosity L^* of blue galaxies is largely a result of more massive blue galaxies ceasing star formation earlier and migrating to the red sequence, leaving behind their less massive counterparts (downsizing).

4.4.2. The evolution of luminosity density

The total K-band luminosity density of red galaxies increases by a modest factor of ∼1.5 from $z \sim 1.1$ to $z \sim 0.3$, (compared with no change in the B-band), while that for blue galaxies shows hardly any change, (compared with a B-band decrease by a factor of ∼0.5). The red galaxy population grows in total luminosity due to the migration of galaxies from the blue cloud to the red sequence as they cease to form stars. In the B-band this growth is more than offset by the rapid fading of the old stellar populations in red galaxies and we see a decrease in total luminosity with time, but in the K-band we see an increase of total luminosity with time because stellar population fading is less rapid in the K-band than the B-band. The restframe K-band samples the Rayleigh-Jeans tail of galaxy SEDs which is dependent almost entirely on the surface temperatures of stars within a galaxy. We therefore expect to see less fading from the long-lived stellar populations in red galaxies than from the stellar populations of blue galaxies whose luminosity is dominated by highly luminous short-lived stars whose total luminosity will decrease as star formation rates decrease. Furthermore, the proportion of optically red galaxies that are dusty star-forming galaxies decreases with time and this means that a decreasing proportion of red galaxies will appear artificially brighter in the K-band relative to the B-band due to dust obscuration.

van der Wel et al. (2005) showed that the mass to light ratio of early type galaxies increases more slowly due to stellar fading in the K-band than in the B-band. (They find $d\ln(M/L_B)/dz = -1.46$, $d\ln(M/L_K)/dz = -1.18$, i.e. $\Delta z = -1$ produces a change of $\times 4.31$ in M/L_B and $\times 3.25$ in M/L_K). This implies, that for a given stellar mass, fading is less rapid in the K-band than in the B-band. When the increase in red stellar mass due

to migration from the blue cloud is taken into account, this explains the fact that the total K-band luminosity density j_K of red galaxies can increase by $\sim \times 1.5$ while the B-band luminosity density j_B shows hardly any change. A precise analysis would need to take account of the mass dependence of stellar mass to light ratio evolution for early type galaxies, which van der Wel et al. (2005) show is strong in the B-band and weaker in the K-band.

Luminosity density is relatively insensitive to the degeneracy amongst the Schechter parameters fitted to luminosity function data, as it is effectively the luminosity weighted area under the luminosity function. Figure 103 illustrates that while Jones et al. (2006) obtain a value for ϕ^* which is half that of Bell et al. (2003) and a faint end slope parameter α value is much less, both obtain luminosity density values that are similar to those Kochanek et al. (2001). Luminosity density, rather than the Schechter parameters, provides the measurement which is the most physically meaningful and therefore it is fortunate that it does not depend critically on the exact Schechter function parameters used to fit the data.

4.4.3. The evolution of highly luminous galaxies

In the K-band there is little evolution in the luminosity of the brightest ($\sim 4L^*$) red galaxies and modest fading of $\sim$0.7 mag in that for blue galaxies. By comparison, the B-band luminosity of the brightest red and blue galaxies fades by 0.4 mag and 0.7 mag respectively. As observed in §3.10, luminous red galaxies evolve by passive stellar fading and the acquisition of additional stellar mass through minor mergers, rather than by major mergers and the cessation of star formation in massive blue galaxies. The net result is little change in overall luminosity as the addition of new stars in minor mergers compensates for the fading of existing stars. Massive blue galaxies cease star formation earlier than less massive ones (downsizing) and move to the red sequence. This causes the bright end of the luminosity function for blue galaxies to move to fainter magnitudes.

Rather than use the argument based on comparing the observed rate of fading of luminosity with that to be expected from passive evolution alone, as in §3.10.2, we draw conclusions regarding the evolution of stellar mass density using the stellar mass to light ratios from Bell et al. (2003). These enable us to derive stellar mass functions from our K-band magnitudes and $(M_B - M_V)$ colours, as described in §4.1.1. Our results are presented in §4.6.2 below.

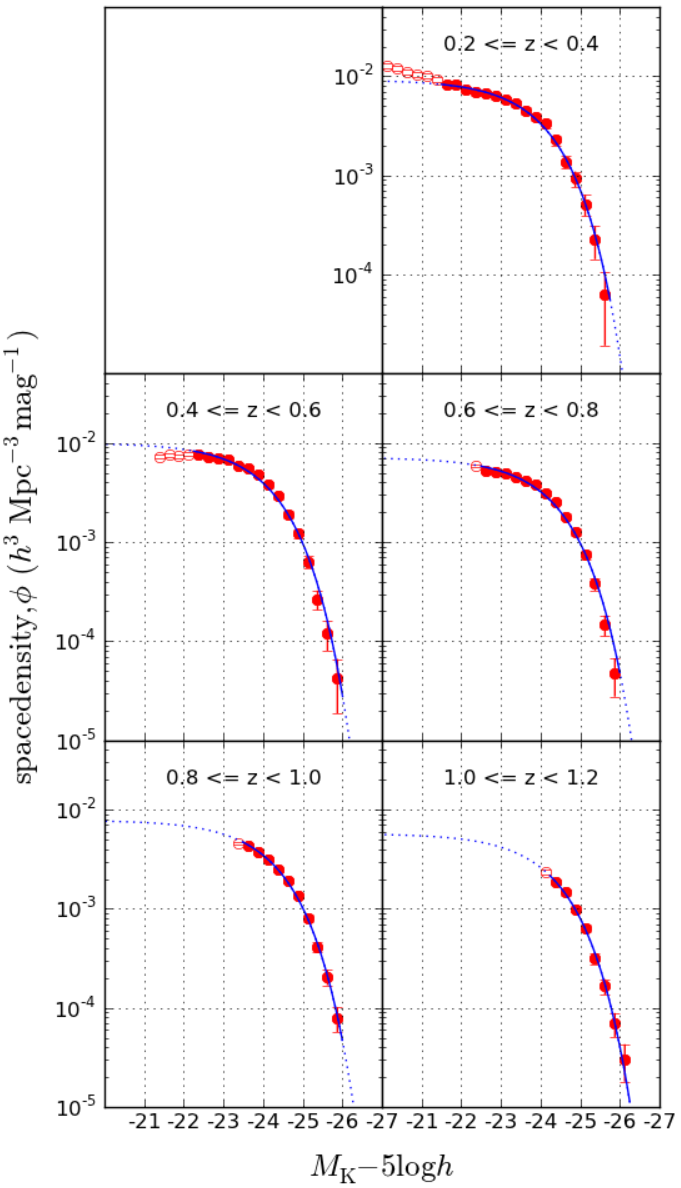

Fig. 97.—: **Evolution of the K-band Schechter function for all galaxies, showing separate plots for different redshift bins.** The circles denote comoving space densities for the various absolute magnitude bins, as shown in Table 23. Filled circles denote the range of absolute magnitudes used to perform the maximum likelihood fit. Open circles denote data for very faint galaxies which are expected to be reliable on the basis of apparent I and [3.6μm] magnitudes, but which are not represented adequately by a Schechter function. The error bars show $1-\sigma$ Poisson errors for the numbers in each bin.

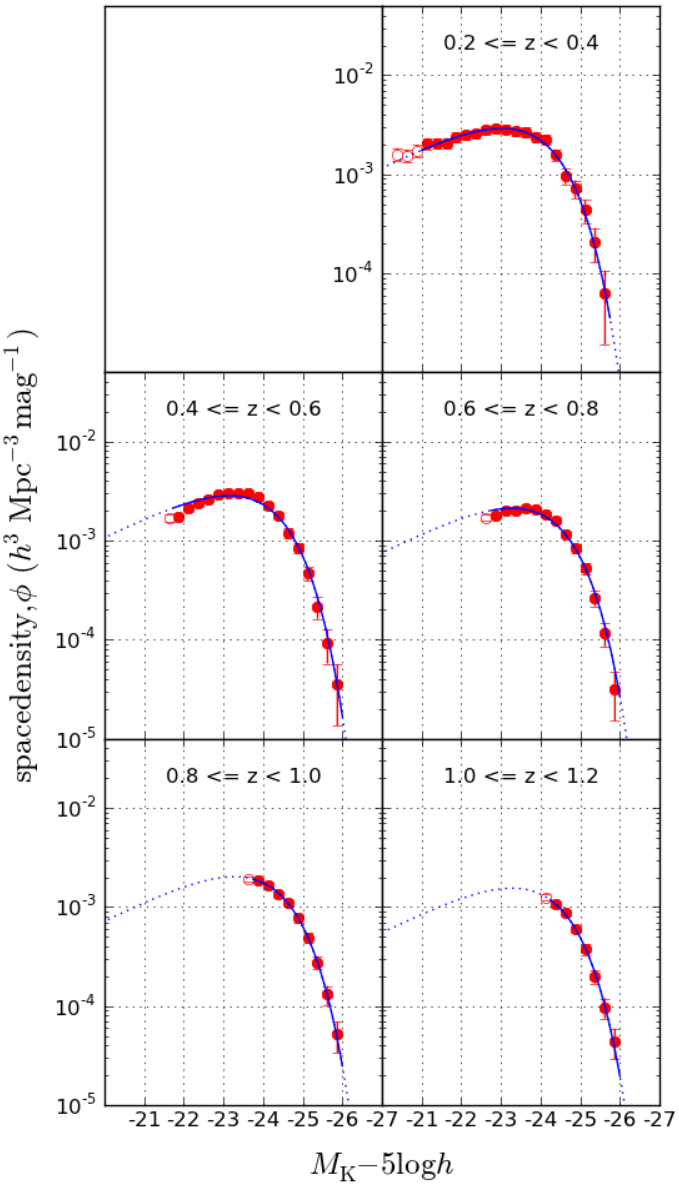

Fig. 98.—: **Evolution of the K-band Schechter function for red galaxies, showing separate plots for different redshift bins.** Data are tabulated in Table 24. Symbols are as in Figure 97.

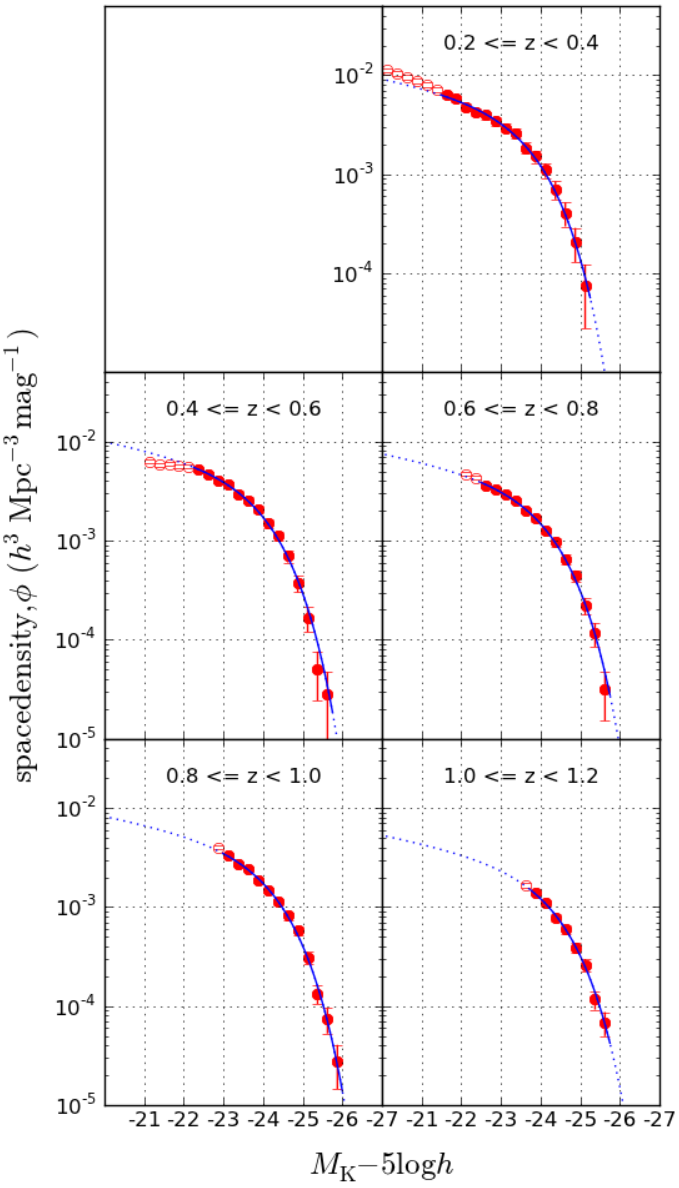

Fig. 99.—: **Evolution of the K-band Schechter function for blue galaxies, showing separate plots for different redshift bins**. Data are tabulated in Table 25. Symbols are as in Figure 97.

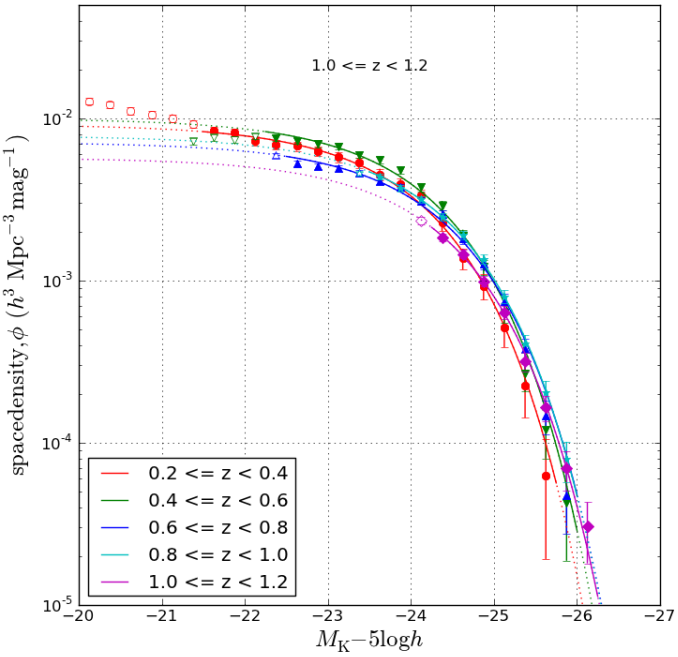

Fig. 100.—: **Evolution of the K-band Schechter function for all galaxies showing all redshift bins in one panel.** The symbols denote comoving space densities for the various absolute magnitude bins, as shown in Table 24. Filled symbols denote the range of absolute magnitudes used to perform the maximum likelihood fit. Open symbols denote data for very faint galaxies which are expected to be reliable on the basis of apparent I and [3.6μm] magnitudes, but which are not represented adequately by a Schechter function. Data are tabulated in Table 23. The error bars show $1-\sigma$ Poisson errors for the numbers in each bin.

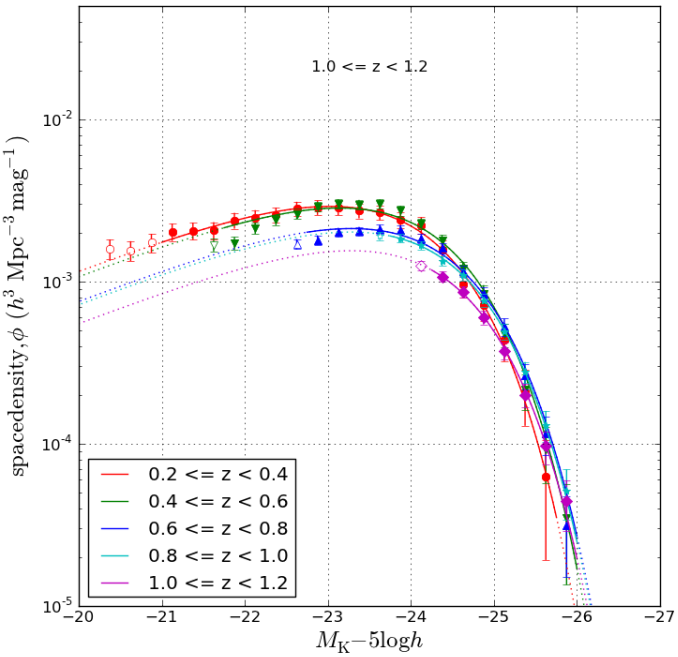

Fig. 101.—: **Evolution of the Johnson K-band Schechter function for red galaxies, showing all bins on one panel.** Symbols are as in Figure 100. Data are tabulated in Table 24.

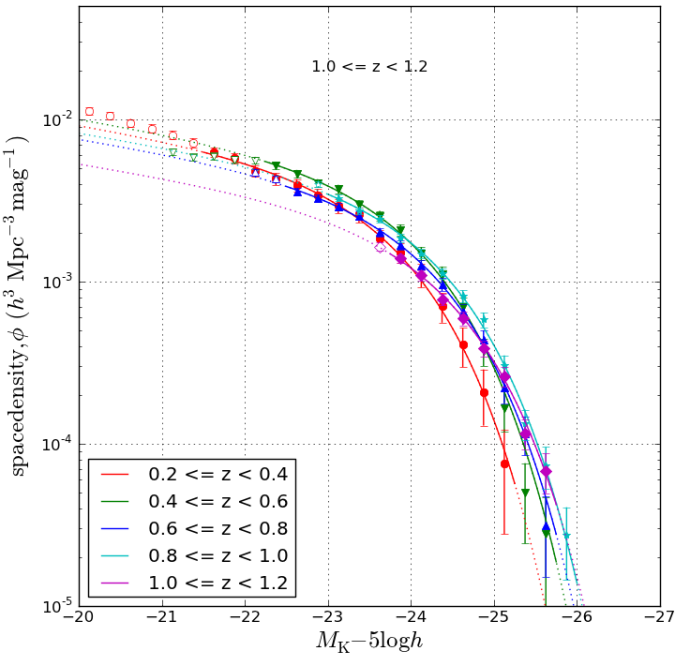

Fig. 102.—: **Evolution of the K-band Schechter function for blue galaxies, showing all redshift bins in one panel.** Symbols are as in Figure 100. Data are tabulated in Table 25.

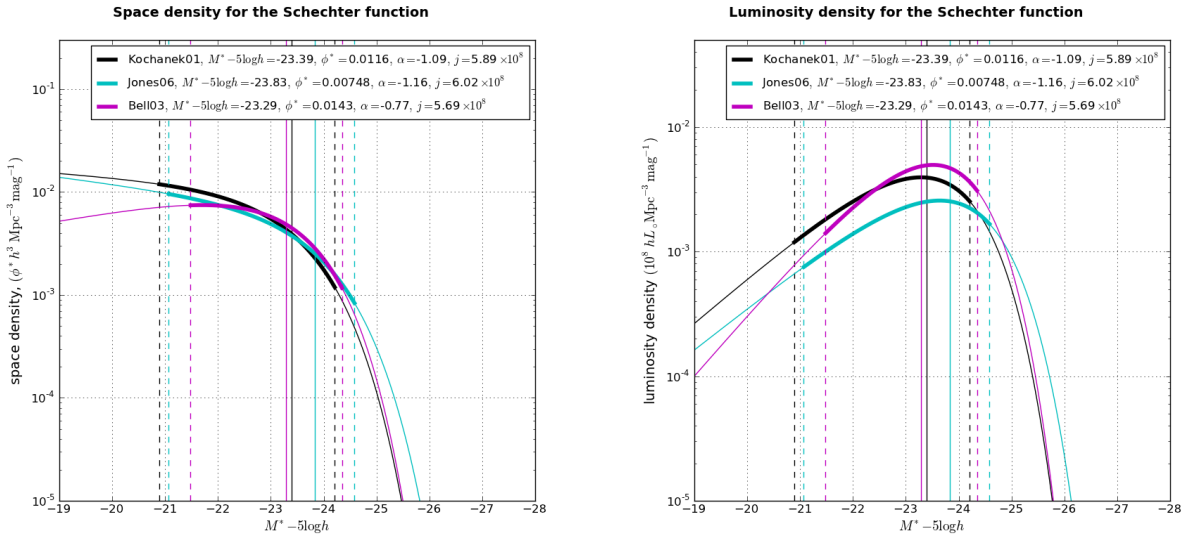

(a) (b)

Fig. 103.—: **Showing why different studies can obtain quite different values for the Schechter parameters yet arrive at very similar values for the luminosity density.** See text for explanation. *Left:* plots of the Schechter function using the parameters from Kochanek et al. (2001), Jones et al. (2006) and Bell et al. (2003); *right:* the corresponding plots of luminosity density per unit magnitude. The bold sections of the curves and dotted vertical lines indicate the magnitude ranges contributing the central 80% of the total luminosities. The solid vertical lines indicate the values of $M^* - 5\log h$.

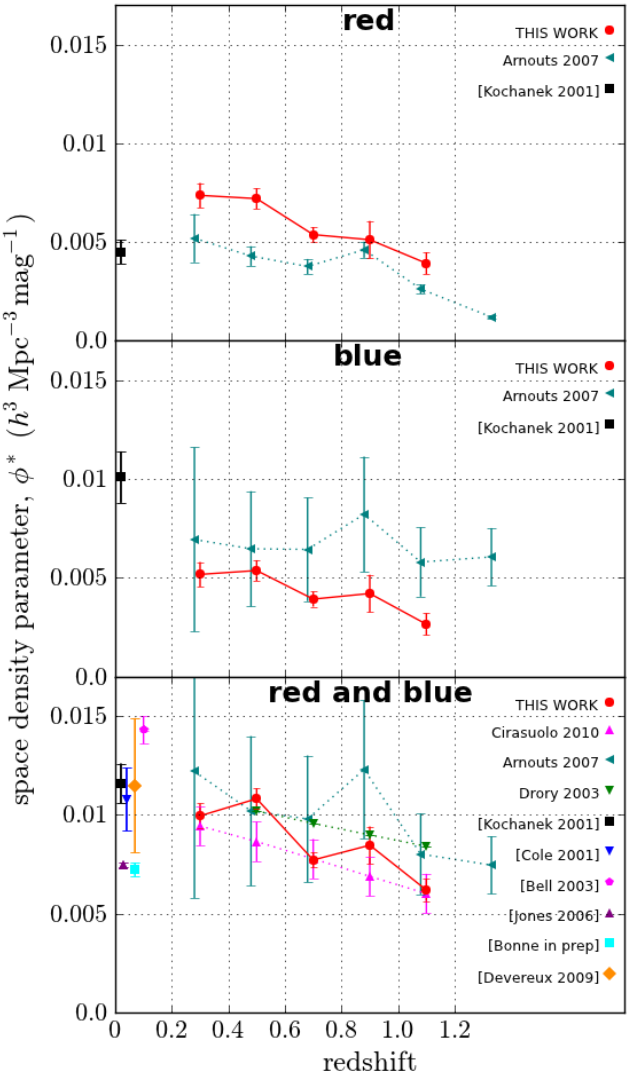

Fig. 104.—: **Evolution from $z = 1.1$ to $z = 0.3$ of the K-band maximum likehihood Schechter parameter ϕ^* which normalises the space density.** The space density of both red and blue $\sim L^*$ galaxies approximately doubled from $z \sim 1.1$ to $z \sim 0.3$. Separate plots are shown for red, blue and all galaxies (red data points), assuming fixed alpha values of -0.5, -1.2 and -1.0 respectively. Also shown for comparison are the results from Drory et al. (2003), Arnouts et al. (2007), Cirasuolo et al. (2010) and luminosity functions for the low redshift Universe from Cole et al. (2001), Kochanek et al. (2001), Bell et al. (2003), Jones et al. (2006), Devereux et al. (2009) and Bonne et al. (in prep.). Error bars on our results show errors due to cosmic variance. Error bars on results from the literature are as published.

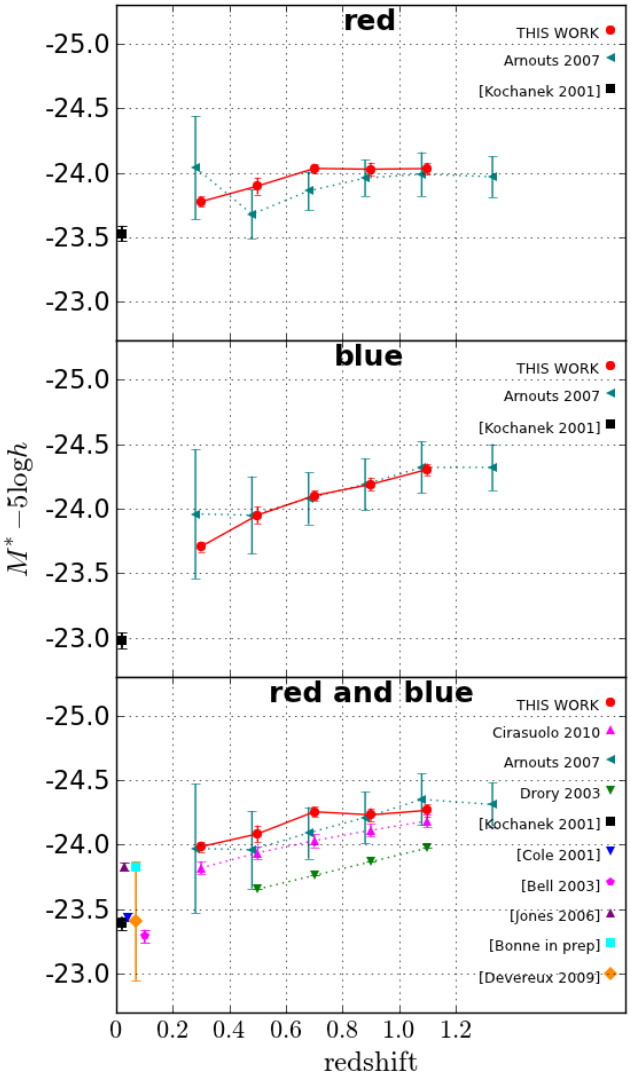

Fig. 105.—: **Evolution from $z = 1.1$ to $z = 0.3$ of the K-band maximum likehihood Schechter characteristic magnitude parameter $M^* - 5\log h$.** M^*_K faded faster from $z = 1.1$ to $z = 0.3$ for blue galaxies ($\Delta M^*_K \sim 0.6$ mag) than for red ($\Delta M^*_K \sim 0.3$ mag). Separate plots are shown for red, blue and all galaxies (red data points), assuming fixed alpha values of -0.5, -1.2 and -1.0 respectively. Also shown for comparison are the results from Drory et al. (2003), Arnouts et al. (2007), Cirasuolo et al. (2010) and luminosity functions for the low redshift Universe from Cole et al. (2001), Kochanek et al. (2001), Bell et al. (2003), Jones et al. (2006), Devereux et al. (2009) and Bonne et al. (in prep.). Error bars on our results show errors due to cosmic variance. Error bars on results from the literature are as published.

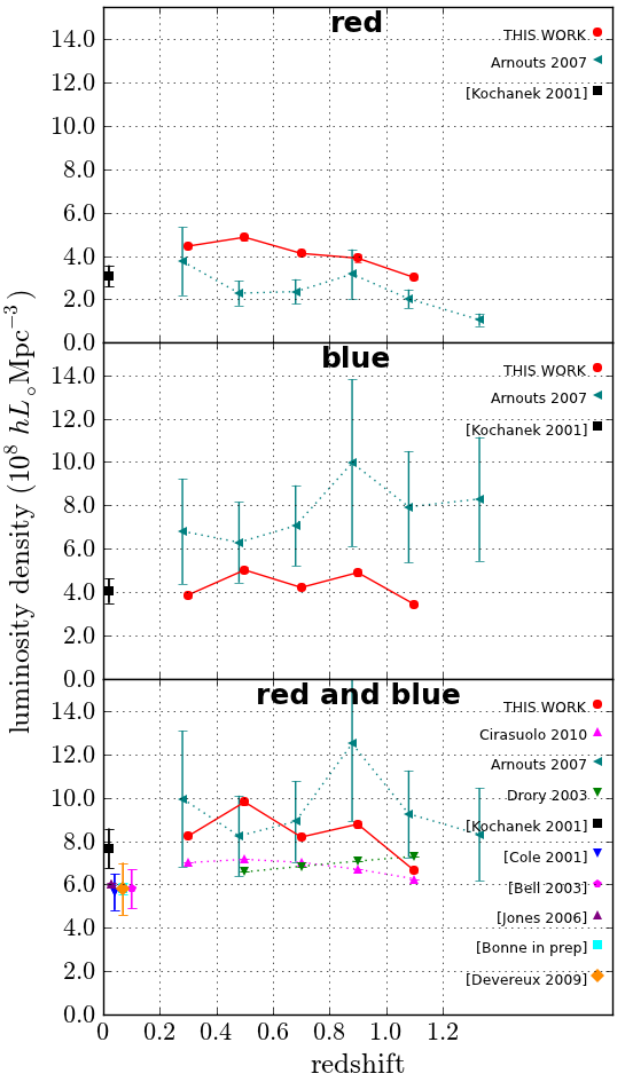

Fig. 106.—: **Evolution from $z = 1.1$ to $z = 0.3$ of the K-band luminosity density.** The K-band luminosity density of blue galaxies hardly changed from $z = 1.1$ to $z = 0.3$, while that of red galaxies increased by a factor of $\sim$1.5. Separate plots are shown for red, blue and all galaxies (red data points), assuming fixed alpha values of -0.5, -1.2 and -1.0 respectively. Also shown for comparison are the results from Drory et al. (2003), Arnouts et al. (2007), Cirasuolo et al. (2010) and luminosity functions for the low redshift Universe from Cole et al. (2001), Kochanek et al. (2001), Bell et al. (2003), Jones et al. (2006), Devereux et al. (2009) and Bonne et al. (in prep.). Error bars on our results show errors due to cosmic variance. Error bars on results from the literature are as published.

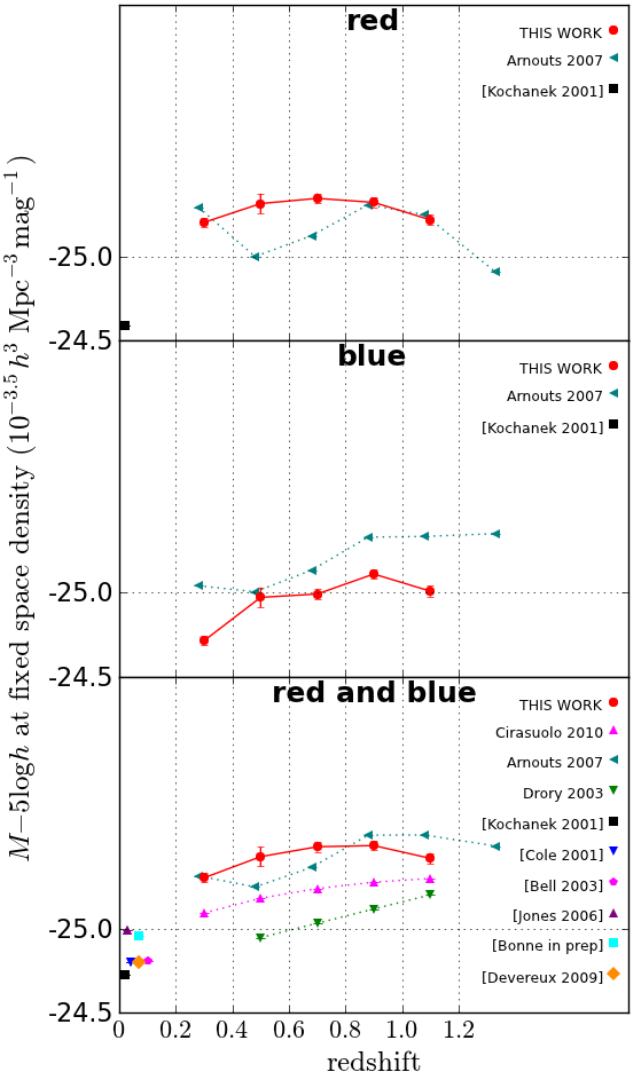

Fig. 107.—: **Evolution of the bright end of the K-band luminosity function.** The value of $M_{\rm K} - 5\log h$ corresponding to a space density is $10^{-3.5}h^3\,{\rm Mpc}^{-3}\,{\rm mag}^{-1}$ is used to monitor evolution of the luminosity of the brightest galaxies. This hardly changes from $z = 1.1$ to $z = 0.3$ for red galaxies. For blue galaxies it fades by $\sim$0.7 mag as a result of downsizing. Separate plots are shown for red, blue and all galaxies (red data points), assuming fixed alpha values of -0.5, -1.2 and -1.0 respectively. Also shown for comparison are the results from Drory et al. (2003), Arnouts et al. (2007), Cirasuolo et al. (2010) and luminosity functions for the low redshift Universe from Cole et al. (2001), Kochanek et al. (2001), Bell et al. (2003), Jones et al. (2006), Devereux et al. (2009) and Bonne et al. (in prep.).

Table 23. Binned Johnson K-band luminosity function for all galaxies.

$M_K - 5\log h$		Luminosity Function ($10^{-3}h^3\,\mathrm{Mpc}^{-3}\,\mathrm{mag}^{-1}$)				
Min	Max	$0.2 \le z < 0.4$	$0.4 \le z < 0.6$	$0.6 \le z < 0.8$	$0.8 \le z < 1.0$	$1.0 \le z < 1.2$
-28.00	-27.75	-	-	-	-	-
-27.75	-27.50	-	0.002 ± 0.002	-	-	-
-27.50	-27.25	-	-	-	-	-
-27.25	-27.00	-	0.002 ± 0.002	-	0.001 ± 0.001	-
-27.00	-26.75	0.004 ± 0.004	0.004 ± 0.003	0.001 ± 0.001	-	-
-26.75	-26.50	-	0.006 ± 0.003	0.001 ± 0.001	-	0.002 ± 0.001
-26.50	-26.25	-	0.002 ± 0.002	0.001 ± 0.001	0.009 ± 0.003	0.009 ± 0.003
-26.25	-26.00	0.012 ± 0.007	0.007 ± 0.004	0.022 ± 0.005	0.026 ± 0.005	0.031 ± 0.005
-26.00	-25.75	0.017 ± 0.008	0.042 ± 0.009	0.047 ± 0.007	0.079 ± 0.008	0.070 ± 0.007
-25.75	-25.50	0.062 ± 0.016	0.120 ± 0.015	0.147 ± 0.013	0.205 ± 0.013	0.165 ± 0.011
-25.50	-25.25	0.224 ± 0.031	0.266 ± 0.022	0.380 ± 0.021	0.411 ± 0.019	0.317 ± 0.015
-25.25	-25.00	0.512 ± 0.046	0.639 ± 0.034	0.746 ± 0.029	0.801 ± 0.026	0.637 ± 0.022
-25.00	-24.75	0.927 ± 0.062	1.216 ± 0.047	1.278 ± 0.038	1.354 ± 0.034	0.990 ± 0.027
-24.75	-24.50	1.371 ± 0.075	1.901 ± 0.059	1.812 ± 0.046	1.912 ± 0.041	1.456 ± 0.033
-24.50	-24.25	2.273 ± 0.097	2.902 ± 0.073	2.573 ± 0.055	2.465 ± 0.047	1.851 ± 0.037
-24.25	-24.00	3.333 ± 0.118	3.766 ± 0.083	3.103 ± 0.060	3.164 ± 0.053	2.343 ± 0.042
-24.00	-23.75	3.911 ± 0.127	4.815 ± 0.094	3.774 ± 0.066	3.715 ± 0.058	-
-23.75	-23.50	4.522 ± 0.137	5.554 ± 0.101	4.120 ± 0.069	4.362 ± 0.063	-
-23.50	-23.25	5.328 ± 0.149	5.961 ± 0.105	4.588 ± 0.074	4.598 ± 0.065	-
-23.25	-23.00	5.790 ± 0.155	6.746 ± 0.112	4.904 ± 0.076	-	-
-23.00	-22.75	6.280 ± 0.162	6.946 ± 0.113	5.062 ± 0.078	-	-
-22.75	-22.50	6.758 ± 0.168	7.254 ± 0.116	5.299 ± 0.080	-	-
-22.50	-22.25	6.871 ± 0.169	7.590 ± 0.119	5.907 ± 0.085	-	-
-22.25	-22.00	7.277 ± 0.174	7.735 ± 0.121	-	-	-
-22.00	-21.75	8.145 ± 0.184	7.393 ± 0.118	-	-	-
-21.75	-21.50	8.349 ± 0.186	7.615 ± 0.121	-	-	-
-21.50	-21.25	9.227 ± 0.196	7.230 ± 0.118	-	-	-
-21.25	-21.00	10.043 ± 0.205	-	-	-	-
-21.00	-20.75	10.526 ± 0.210	-	-	-	-
-20.75	-20.50	11.076 ± 0.216	-	-	-	-
-20.50	-20.25	12.124 ± 0.227	-	-	-	-
-20.25	-20.00	12.756 ± 0.233	-	-	-	-
-20.00	-19.75	-	-	-	-	-
-19.75	-19.50	-	-	-	-	-
-19.50	-19.25	-	-	-	-	-
-19.25	-19.00	-	-	-	-	-
-19.00	-18.75	-	-	-	-	-
-18.75	-18.50	-	-	-	-	-
-18.50	-18.25	-	-	-	-	-
-18.25	-18.00	-	-	-	-	-

Table 24. Binned Johnson K-band luminosity function for red galaxies.

$M_K - 5\log h$		Luminosity Function ($10^{-3}h^3\,\mathrm{Mpc}^{-3}\,\mathrm{mag}^{-1}$)				
Min	Max	$0.2 \le z < 0.4$	$0.4 \le z < 0.6$	$0.6 \le z < 0.8$	$0.8 \le z < 1.0$	$1.0 \le z < 1.2$
-26.75	-26.50	-	-	0.001 ± 0.001	-	0.001 ± 0.001
-26.50	-26.25	-	0.002 ± 0.002	0.001 ± 0.001	0.007 ± 0.002	0.005 ± 0.002
-26.25	-26.00	0.008 ± 0.006	0.007 ± 0.004	0.016 ± 0.004	0.017 ± 0.004	0.012 ± 0.003
-26.00	-25.75	0.017 ± 0.008	0.035 ± 0.008	0.031 ± 0.006	0.052 ± 0.007	0.044 ± 0.006
-25.75	-25.50	0.062 ± 0.016	0.092 ± 0.013	0.116 ± 0.012	0.131 ± 0.011	0.097 ± 0.008
-25.50	-25.25	0.208 ± 0.029	0.216 ± 0.020	0.264 ± 0.017	0.278 ± 0.015	0.200 ± 0.012
-25.25	-25.00	0.436 ± 0.043	0.472 ± 0.030	0.525 ± 0.025	0.494 ± 0.021	0.375 ± 0.017
-25.00	-24.75	0.719 ± 0.055	0.845 ± 0.039	0.838 ± 0.031	0.770 ± 0.026	0.601 ± 0.021
-24.75	-24.50	0.964 ± 0.063	1.203 ± 0.047	1.162 ± 0.037	1.098 ± 0.031	0.863 ± 0.025
-24.50	-24.25	1.571 ± 0.081	1.786 ± 0.057	1.609 ± 0.043	1.344 ± 0.035	1.073 ± 0.029
-24.25	-24.00	2.232 ± 0.096	2.275 ± 0.065	1.852 ± 0.046	1.679 ± 0.039	1.251 ± 0.031
-24.00	-23.75	2.398 ± 0.100	2.735 ± 0.071	2.090 ± 0.049	1.852 ± 0.041	-
-23.75	-23.50	2.672 ± 0.105	3.009 ± 0.075	2.108 ± 0.050	1.918 ± 0.042	-
-23.50	-23.25	2.739 ± 0.107	2.989 ± 0.074	2.040 ± 0.049	-	-
-23.25	-23.00	2.859 ± 0.109	3.019 ± 0.075	2.013 ± 0.049	-	-
-23.00	-22.75	2.868 ± 0.109	2.900 ± 0.073	1.802 ± 0.047	-	-
-22.75	-22.50	2.814 ± 0.108	2.621 ± 0.070	1.705 ± 0.046	-	-
-22.50	-22.25	2.578 ± 0.104	2.407 ± 0.067	-	-	-
-22.25	-22.00	2.483 ± 0.102	2.135 ± 0.064	-	-	-
-22.00	-21.75	2.386 ± 0.100	1.728 ± 0.058	-	-	-
-21.75	-21.50	2.074 ± 0.093	1.686 ± 0.057	-	-	-
-21.50	-21.25	2.058 ± 0.093	-	-	-	-
-21.25	-21.00	2.028 ± 0.092	-	-	-	-
-21.00	-20.75	1.737 ± 0.086	-	-	-	-
-20.75	-20.50	1.556 ± 0.081	-	-	-	-
-20.50	-20.25	1.596 ± 0.083	-	-	-	-

Table 25. Binned Johnson K-band luminosity function for blue galaxies.

$M_K - 5\log h$		Luminosity Function ($10^{-3}h^3\,\mathrm{Mpc}^{-3}\,\mathrm{mag}^{-1}$)				
Min	Max	$0.2 \le z < 0.4$	$0.4 \le z < 0.6$	$0.6 \le z < 0.8$	$0.8 \le z < 1.0$	$1.0 \le z < 1.2$
-27.75	-27.50	-	0.002 ± 0.002	-	-	-
-27.50	-27.25	-	-	-	-	-
-27.25	-27.00	-	0.002 ± 0.002	-	0.001 ± 0.001	-
-27.00	-26.75	0.004 ± 0.004	0.004 ± 0.003	0.001 ± 0.001	-	-
-26.75	-26.50	-	0.006 ± 0.003	-	-	0.001 ± 0.001
-26.50	-26.25	-	-	-	0.003 ± 0.001	0.004 ± 0.002
-26.25	-26.00	0.004 ± 0.004	-	0.006 ± 0.003	0.009 ± 0.003	0.018 ± 0.004
-26.00	-25.75	-	0.007 ± 0.004	0.016 ± 0.004	0.028 ± 0.005	0.026 ± 0.004
-25.75	-25.50	-	0.028 ± 0.007	0.031 ± 0.006	0.074 ± 0.008	0.068 ± 0.007
-25.50	-25.25	0.017 ± 0.008	0.050 ± 0.010	0.116 ± 0.012	0.134 ± 0.011	0.116 ± 0.009
-25.25	-25.00	0.075 ± 0.018	0.166 ± 0.018	0.221 ± 0.016	0.307 ± 0.016	0.262 ± 0.014
-25.00	-24.75	0.208 ± 0.029	0.371 ± 0.026	0.440 ± 0.023	0.584 ± 0.022	0.388 ± 0.017
-24.75	-24.50	0.407 ± 0.041	0.698 ± 0.036	0.649 ± 0.027	0.814 ± 0.027	0.593 ± 0.021
-24.50	-24.25	0.702 ± 0.054	1.116 ± 0.045	0.963 ± 0.033	1.122 ± 0.031	0.778 ± 0.024
-24.25	-24.00	1.101 ± 0.068	1.491 ± 0.052	1.251 ± 0.038	1.485 ± 0.036	1.092 ± 0.029
-24.00	-23.75	1.513 ± 0.079	2.080 ± 0.062	1.684 ± 0.044	1.863 ± 0.041	1.393 ± 0.032
-23.75	-23.50	1.849 ± 0.088	2.545 ± 0.069	2.012 ± 0.048	2.444 ± 0.047	1.645 ± 0.035
-23.50	-23.25	2.589 ± 0.104	2.972 ± 0.074	2.548 ± 0.055	2.745 ± 0.050	-
-23.25	-23.00	2.931 ± 0.110	3.727 ± 0.083	2.892 ± 0.058	3.280 ± 0.055	-
-23.00	-22.75	3.412 ± 0.119	4.046 ± 0.087	3.260 ± 0.062	3.988 ± 0.060	-
-22.75	-22.50	3.944 ± 0.128	4.633 ± 0.093	3.594 ± 0.065	-	-
-22.50	-22.25	4.293 ± 0.134	5.184 ± 0.098	4.312 ± 0.072	-	-
-22.25	-22.00	4.794 ± 0.141	5.599 ± 0.102	4.716 ± 0.076	-	-
-22.00	-21.75	5.759 ± 0.155	5.665 ± 0.103	-	-	-
-21.75	-21.50	6.275 ± 0.162	5.928 ± 0.106	-	-	-
-21.50	-21.25	7.169 ± 0.173	5.850 ± 0.106	-	-	-
-21.25	-21.00	8.015 ± 0.183	6.302 ± 0.110	-	-	-
-21.00	-20.75	8.789 ± 0.192	-	-	-	-
-20.75	-20.50	9.520 ± 0.200	-	-	-	-
-20.50	-20.25	10.528 ± 0.211	-	-	-	-
-20.25	-20.00	11.215 ± 0.219	-	-	-	-

Table 26. K-band Schechter function parameters for fixed α values based on our results.

z	α	ϕ^* $\mathrm{Mpc}^{-3}\,\mathrm{mag}^{-1}$	$M^* - 5\log h$	$M\left(10^{-3.5}\right) - 5\log h$	j_B $L_\odot\,\mathrm{Mpc}^{-3}$
Red galaxies - $\alpha = -0.5$					
0.3	-0.5	$7.70 \pm 0.31 \times 10^{-3}$	-23.76 ± 0.07	-25.20 ± 0.04	$4.59 \pm 0.01 \times 10^{8}$
0.5	-0.5	$7.29 \pm 0.16 \times 10^{-3}$	-23.89 ± 0.07	-25.32 ± 0.07	$4.91 \pm 0.46 \times 10^{8}$
0.7	-0.5	$5.38 \pm 0.14 \times 10^{-3}$	-24.04 ± 0.05	-25.35 ± 0.04	$4.13 \pm 0.22 \times 10^{8}$
0.9	-0.5	$5.10 \pm 0.29 \times 10^{-3}$	-24.03 ± 0.06	-25.32 ± 0.04	$3.89 \pm 0.25 \times 10^{8}$
1.1	-0.5	$3.94 \pm 0.39 \times 10^{-3}$	-24.03 ± 0.05	-25.22 ± 0.03	$3.02 \pm 0.47 \times 10^{8}$
Blue galaxies - $\alpha = -1.2$					
0.3	-1.2	$5.28 \pm 0.45 \times 10^{-3}$	-23.07 ± 0.06	-24.71 ± 0.04	$3.90 \pm 0.43 \times 10^{8}$
0.5	-1.2	$5.37 \pm 0.39 \times 10^{-3}$	-23.96 ± 0.07	-24.98 ± 0.07	$5.05 \pm 1.18 \times 10^{8}$
0.7	-1.2	$3.93 \pm 0.40 \times 10^{-3}$	-24.10 ± 0.05	-24.99 ± 0.04	$4.21 \pm 0.74 \times 10^{8}$
0.9	-1.2	$4.17 \pm 0.23 \times 10^{-3}$	-24.20 ± 0.05	-25.12 ± 0.04	$4.91 \pm 0.19 \times 10^{8}$
1.1	-1.2	$2.59 \pm 0.39 \times 10^{-3}$	-24.31 ± 0.06	-25.01 ± 0.05	$3.37 \pm 0.56 \times 10^{8}$
All galaxies - $\alpha = -1.0$					
0.3	-1.0	$10.27 \pm 0.56 \times 10^{-3}$	-23.97 ± 0.05	-25.30 ± 0.04	$8.42 \pm 0.27 \times 10^{8}$
0.5	-1.0	$10.92 \pm 0.47 \times 10^{-3}$	-24.09 ± 0.07	-25.43 ± 0.07	$9.92 \pm 1.47 \times 10^{8}$
0.7	-1.0	$7.71 \pm 0.40 \times 10^{-3}$	-24.26 ± 0.04	-25.49 ± 0.04	$8.22 \pm 0.78 \times 10^{8}$
1.1	-1.0	$8.47 \pm 0.44 \times 10^{-3}$	-24.23 ± 0.05	-25.50 ± 0.04	$8.79 \pm 0.28 \times 10^{8}$
1.1	-1.0	$6.19 \pm 0.62 \times 10^{-3}$	-24.27 ± 0.05	-25.42 ± 0.04	$6.64 \pm 0.87 \times 10^{8}$

4.5. Measuring evolution of the stellar mass function

We determined K and V-band stellar mass to light ratios from restframe $(M_B - M_V)$ colours using the following two relations from Bell et al. (2003) shown in Figure 85.

$$\begin{aligned} \log(M/L_V) &= -0.628 + 1.305(M_B - M_V), \\ \log(M/L_K) &= -0.206 + 0.135(M_B - M_V). \end{aligned} \tag{59}$$

The scatter in these correlations is $\sim$0.1 dex for $\log(M/L_V)$ and 0.1 to 0.2 dex for $\log(M/L_K)$ (the larger scatter being for galaxies with blue optical colours). The scatter is principally due to the spread in metallicities included by Bell et al. (2003) in their SPS models. They also estimate $\sim$25% systematic errors in stellar M/L ratios from the effects of dust and bursts of star formation. Relations (59) assume a modified Salpeter (1955) IMF. If other IMFs are used there will be an offset. For example, a Kennicutt IMF results in stellar M/L ratios 0.15 dex less.

We calculated individual galaxy masses based on both their K and their V-band absolute magnitudes, and used these masses to calculate stellar mass functions. As the majority of the literature presents K-band determined mass functions because of their perceived greater reliability (but see the discussion in §4.1.1 above), we did the same, showing results based on the V-band for comparison.

We used the $1/V_{\rm max}$ method to measure the mass density of red, blue and all galaxies in five redshift bins of width 0.2 mag between $z = 0.2$ and $z = 1.2$. For each redshift bin we determined the smallest mass for which the sample would be complete at our limiting magnitudes of $I = 23.5$ and [3.6μm] from plots of $(\log M - D_{\rm M} + I)$ (Figure 108) and $(\log M - D_{\rm M} + [3.6\mu{\rm m}])$ against redshift. We then fitted Schechter functions of the form of Equation 56 using just a range no larger than that over which the sample is complete. We found that at higher redshifts the parameter α, determining the slope of the low mass end of the stellar mass function, was even more indeterminate than for luminosity functions. Accordingly we used the same fixed α values as for the K-band luminosity function, as we found that these give a good fit to the stellar mass function in the lowest redshift bins. These values were $\alpha = -0.5, -1.2, -1.0$ for red, blue and all galaxies respectively.

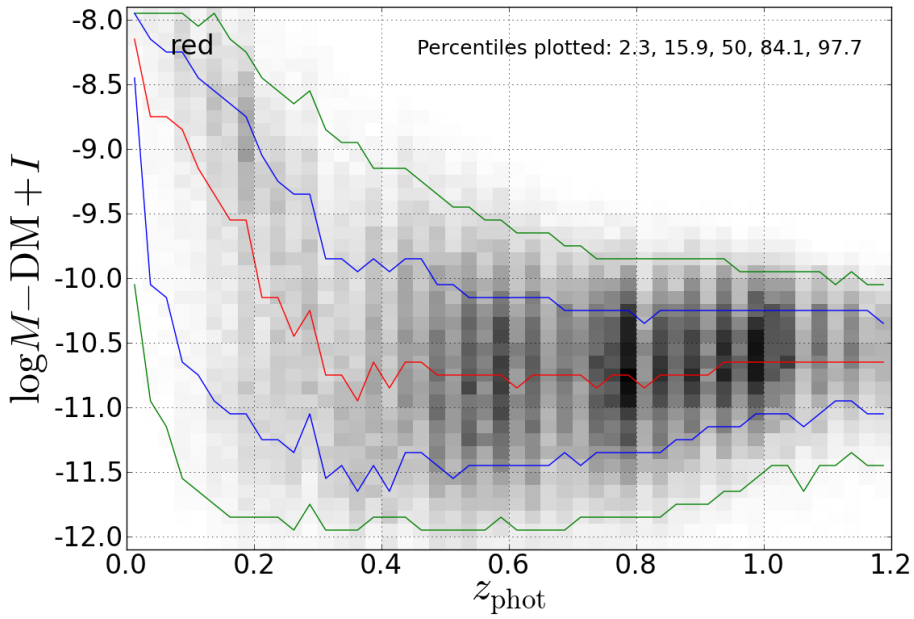

(a)

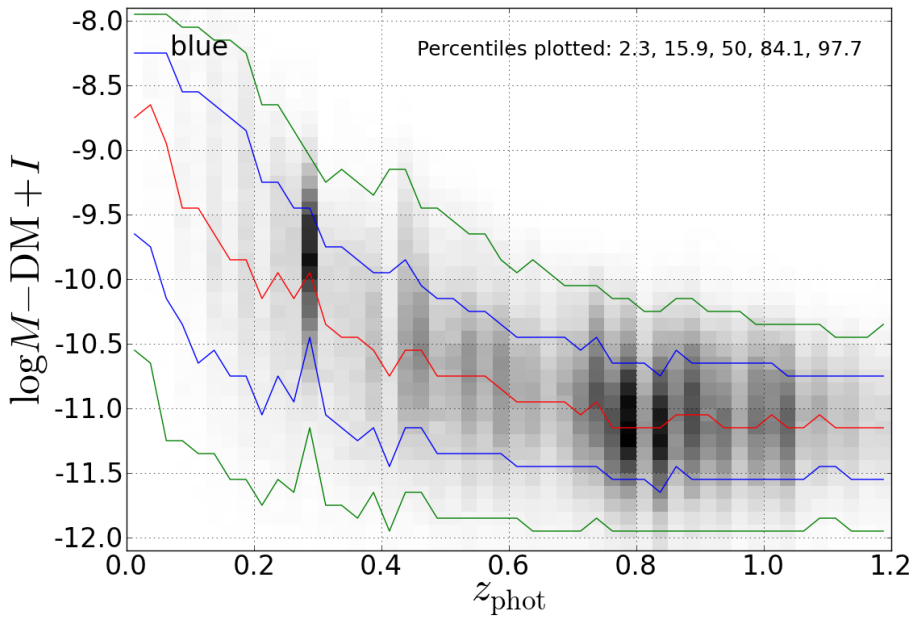

(b)

Fig. 108.—: **Binned plots of $\log M - D_{\mathrm{M}} + I$ against redshift enable the low mass cut-off corresponding to our faint apparent magnitude limit of $I = 23.5$ to be determined.** *Top:* red galaxies; *bottom:* blue galaxies. The red, blue and green lines denote the median and the 1-σ and 2-σ percentiles. We only plot our binned luminosity functions for masses greater than the 2-σ low mass limit. (M is galaxy mass, I is apparent I-band magnitude, D_{M} is distance modulus.)

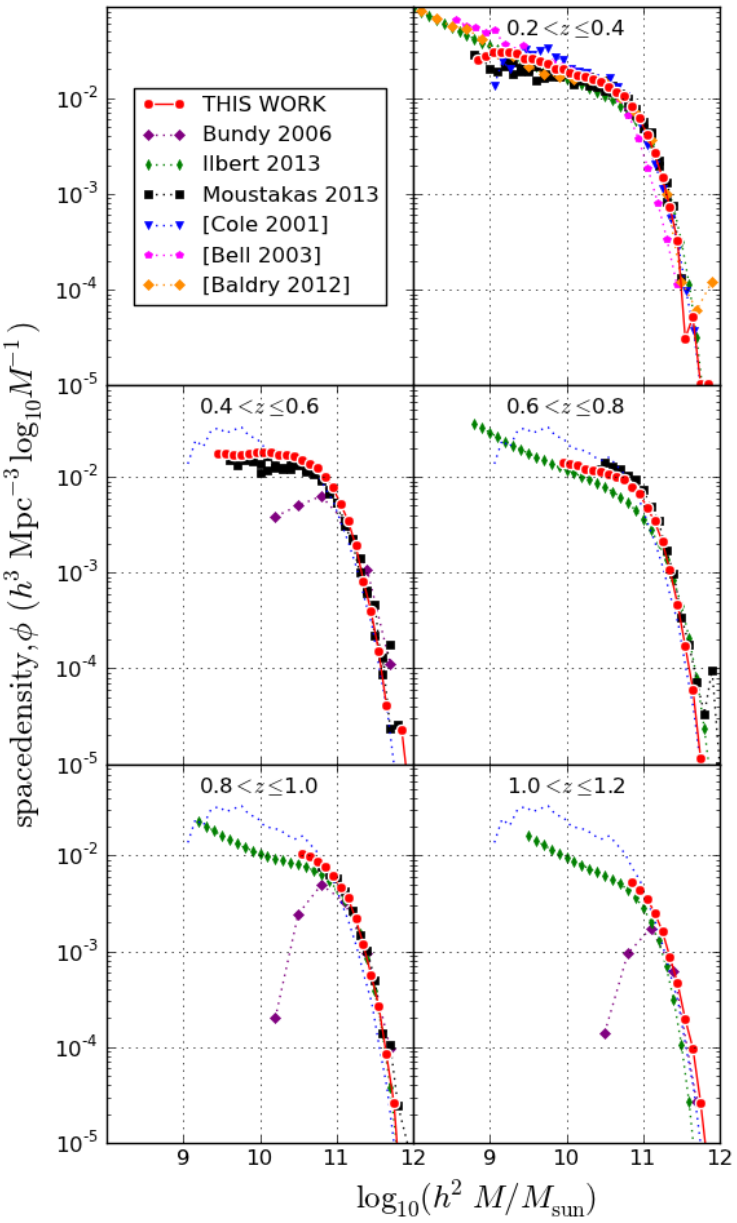

Fig. 109.—: **Binned mass functions for all galaxies based on K-band absolute magnitudes and stellar mass to light ratios from Bell et al. (2003).** We show the evolving mass functions from Bundy et al. (2006); Ilbert et al. (2013) and Moustakas et al. (2013) for comparison, as well as mass functions for the low redshift Universe from Cole et al. (2001), Bell et al. (2003) and Baldry et al. (2012). The Cole et al. (2001) mass function for all galaxies in the low redshift Universe is shown as a black dotted line to provide a fixed reference.

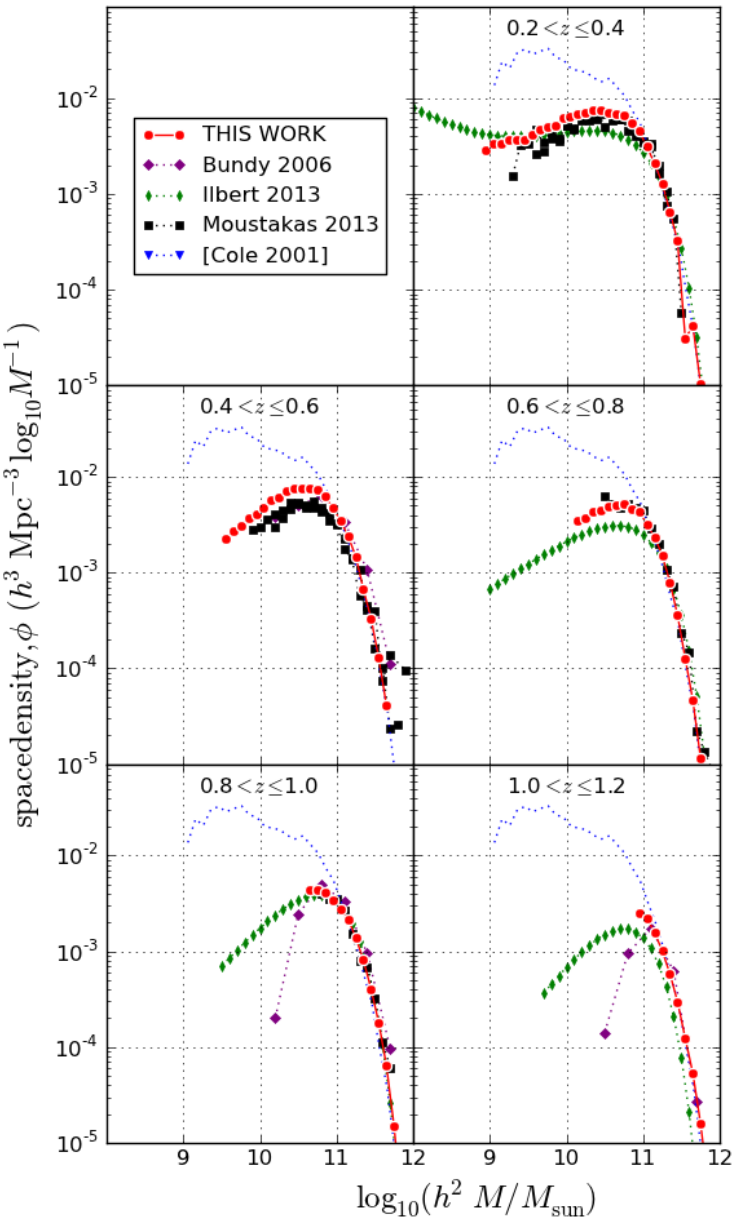

Fig. 110.—: **Binned mass functions for red galaxies based on K-band absolute magnitudes and stellar mass to light ratios from Bell et al. (2003).** We show the evolving mass functions from Bundy et al. (2006); Ilbert et al. (2013) and Moustakas et al. (2013) for comparison. The Cole et al. (2001) mass function for all galaxies in the low redshift Universe is shown as a black dotted line for $z > 04$ in order to provide a fixed reference.

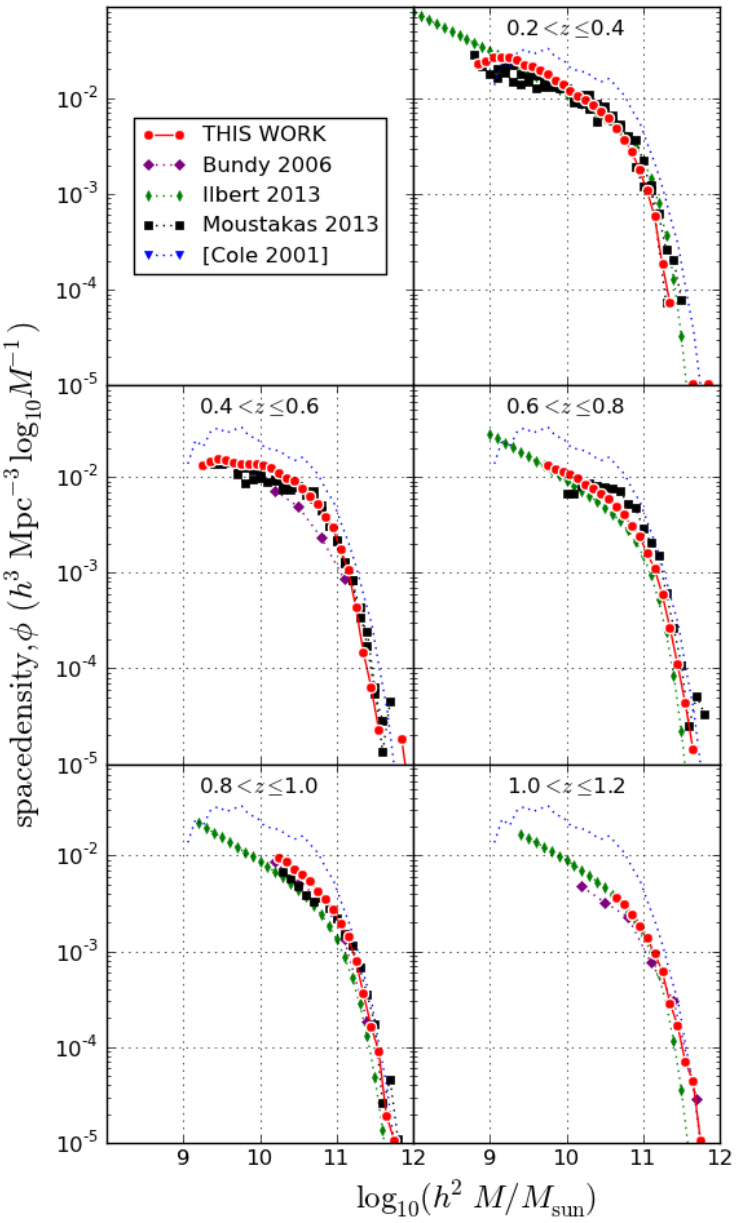

Fig. 111.—: **Binned mass functions for blue galaxies based on K-band absolute magnitudes and stellar mass to light ratios from Bell et al. (2003).** We show the evolving mass functions from Bundy et al. (2006); Ilbert et al. (2013) and Moustakas et al. (2013) for comparison. The Cole et al. (2001) mass function for all galaxies in the low redshift Universe is shown as a black dotted line to provide a fixed reference.

4.6. Stellar mass function results and discussion

Our binned $1/V_{\rm max}$ stellar mass functions for all, red, and blue galaxies based on K-band absolute magnitudes and $(M_B - M_V)$ colours are tabulated in Tables 27 to 29 and plotted in Figures 109 to 111, together with results from a number of previous studies using a variety of surveys. We only plot bins for which 97.7% of the measured masses correspond to observed I-magnitudes of 23.5 or brighter (Figure 108). To provide a fixed reference in the plots we show the local stellar mass function for all galaxies from Cole et al. (2001) in each bin. Our results lie within the range seen in the literature but show smoother variation than most due to the large size of our sample, which minimises both random (Poisson) errors and cosmic variance.

Results from different authors differ by $\sim \pm 0.2$ dex as one would expect from the different prescriptions used to calculate stellar mass to light ratios (e.g. the different stellar IMFs used in their SPS models). Our stellar masses are based on K-band stellar mass to light ratios calculated from $(B - V)$ observed colours, as given in Bell et al. (2003) and described in detail in §4.1.1. These stellar M/L ratios are based on SPS models with modified Salpeter (1955) stellar IMFs. Other authors use different IMFs and as noted in §4.2 this results in significant offsets in measured galaxy masses (e.g. Bundy et al. (2006); Ilbert et al. (2013) use a Chabrier (2003) IMF).

We also expect significant variations in the "red" and "blue" plots due to the range of different criteria used by different authors to differentiate star-forming and quiescent galaxies. As already noted in §4.2, Ilbert et al. (2013) separated their sample into star-forming and quiescent subsamples based on $(NUV - r^+)$ and $(r^+ - J)$ colours which cleanly separates dusty star-forming galaxies and quiescent galaxies. Moustakas et al. (2013) divided their sample into quiescent and star-forming on the basis of an evolving cut in a plot of star formation rate against stellar mass, star formation rates being derived from their *iSEDfit* SED modelling code which fitted SPS templates to their broad waveband photometry. We subdivided our sample on the basis of restframe $(M_U - M_B)$ colour. Particularly at higher redshifts this will result in dusty star-forming galaxies being classified as red. In the low redshift Universe Bell et al. (2003) subdivided their sample into star-forming and quiescent subsamples based on a morphological concentration index. Despite all this, our results for red and blue galaxies separately agree surprisingly well with the recent results of Ilbert et al. (2013) and Moustakas et al. (2013) except for the significantly lower space density seen by Ilbert et al. (2013) for all but the most massive galaxies at $z \sim 0.7$.

Initial inspection of Figures 109 to 111 shows that at at $M \sim M^*$ the space densities for all, red and blue galaxies increase by less than $\sim$0.2 dex from $z \sim 0.8$ to $z \sim 0.2$. Above $z \sim 0.8$ galaxies less massive than $h^2 M = 10^{10.5} M_\odot$ are fainter than our I-band magnitude limit of

23.5 and the luminosity function is undetermined except at the high mass end.

To parameterise our stellar mass functions and measure the evolution of total stellar mass density we fitted Schechter functions (56). Figures 112 to 114 show our maximum likelihood fits to our data (continuous lines) as well as our binned $1/V_{\rm max}$ space densities (data points), using a separate plot for each redshift bin. Figures 115 to 117 display the same data with all redshift bins on a single plot to make the evolution of the stellar mass functions more apparent. Table 30 tabulates evolution of the parameters.

The total mass density for blue galaxies includes a much larger contribution from faint galaxies than that for red galaxies because of the high faint-end slope (i.e. α value $\sim$-1 or less). (See the parallel discussion for total luminosity density in Figure 103 and §4.4). Our stellar mass function faint end limit rapidly increases as we go to higher redshifts (more rapidly than that for luminosity functions). The uncertainty in the total mass function for blue galaxies (and all galaxies by extension) therefore increases rapdily at higher redshifts, because we cannot be sure that the faint end slope (i.e. α value) does not evolve significantly (as we have assumed).

At the bright end we excluded galaxies in bins for which the binned space density was less than 10^{-5}Mpc^{-3} from our maximum likelihood fits, and at the faint end we excluded very faint galaxies because their apparent magnitudes and photometric redshifts will have larger uncertainties, and in the case of red galaxies because a simple Schechter function underestimates the number of these. Several authors (e.g. Baldry et al. 2012; Ilbert et al. 2013) have used a double Schechter function to parameterise the behaviour of the faint end of the stellar mass function:

$$\phi_M\left(M\right)dM = \left[\left(\frac{\phi_1^*}{M^*}\right)\left(\frac{M}{M^*}\right)_1^{\alpha} + \left(\frac{\phi_2^*}{M^*}\right)\left(\frac{M}{M^*}\right)_2^{\alpha}\right]\exp\left(\frac{-M}{M^*}\right)dM. \qquad (60)$$

Our data do not extend to sufficiently small masses to do this. As we are only using a simple Schechter function we cannot compare our Schechter parameters ϕ^*, M^* and α with those from the literature where a double Schechter fit has been used. Instead we compare our results for the total stellar mass density at different epochs with the literature as shown in Figure 118. There is a scatter of $\sim$0.08 dex (a factor of $\sim$1.2 either way) between the mass functions for all galaxies from different authors with our results lying at the upper end of the range. For the "red" and "blue" plots there is greater scatter than for all galaxies but this is to be expected because of the different methods used to separate galaxies into red and blue or quiescent and star-forming.

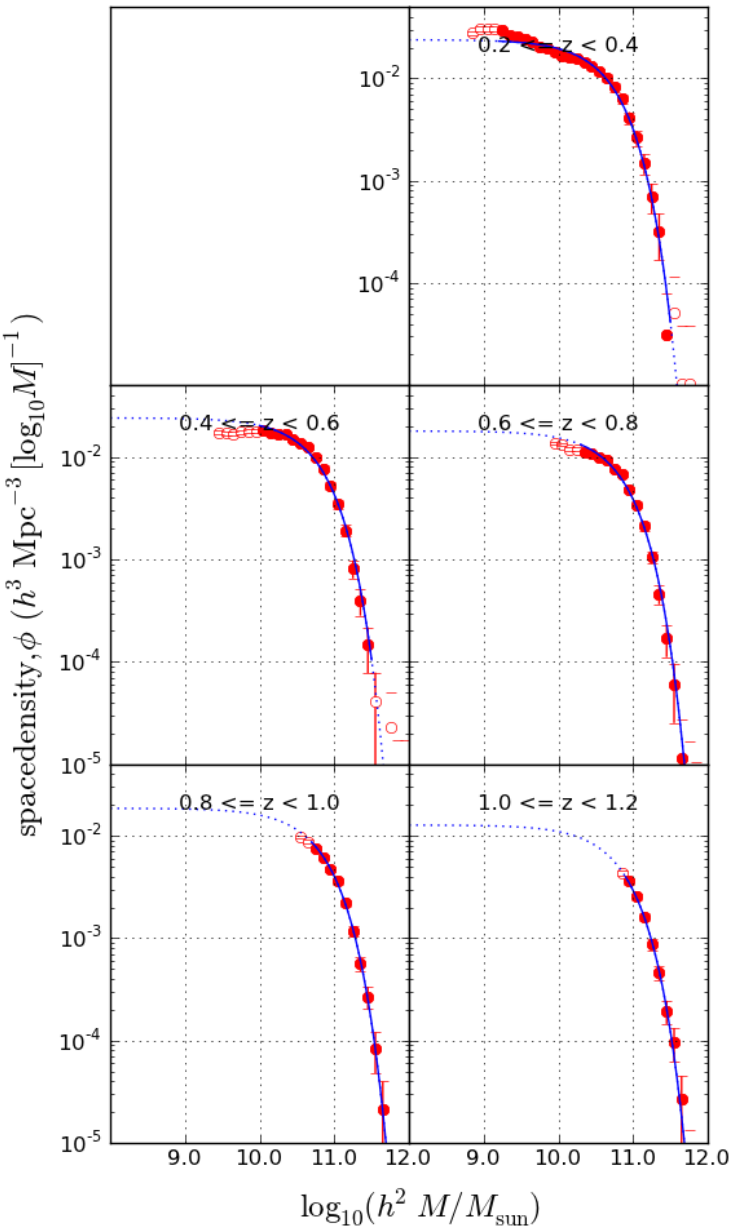

Fig. 112.—: **Stellar mass functions for all galaxies based on K-band absolute magnitudes, showing separate plots for different redshift bins.** The circles denote comoving space densities for the various mass bins, as shown in Table 28. Filled circles denote the mass range used to perform the maximum likelihood fit. Open circles denote data for very low mass galaxies which are expected to be reliable on the basis of apparent I and [3.6μm] magnitudes, but which are not represented adequately by a Schechter function. The error bars show $1-\sigma$ Poisson errors for the numbers in each bin.

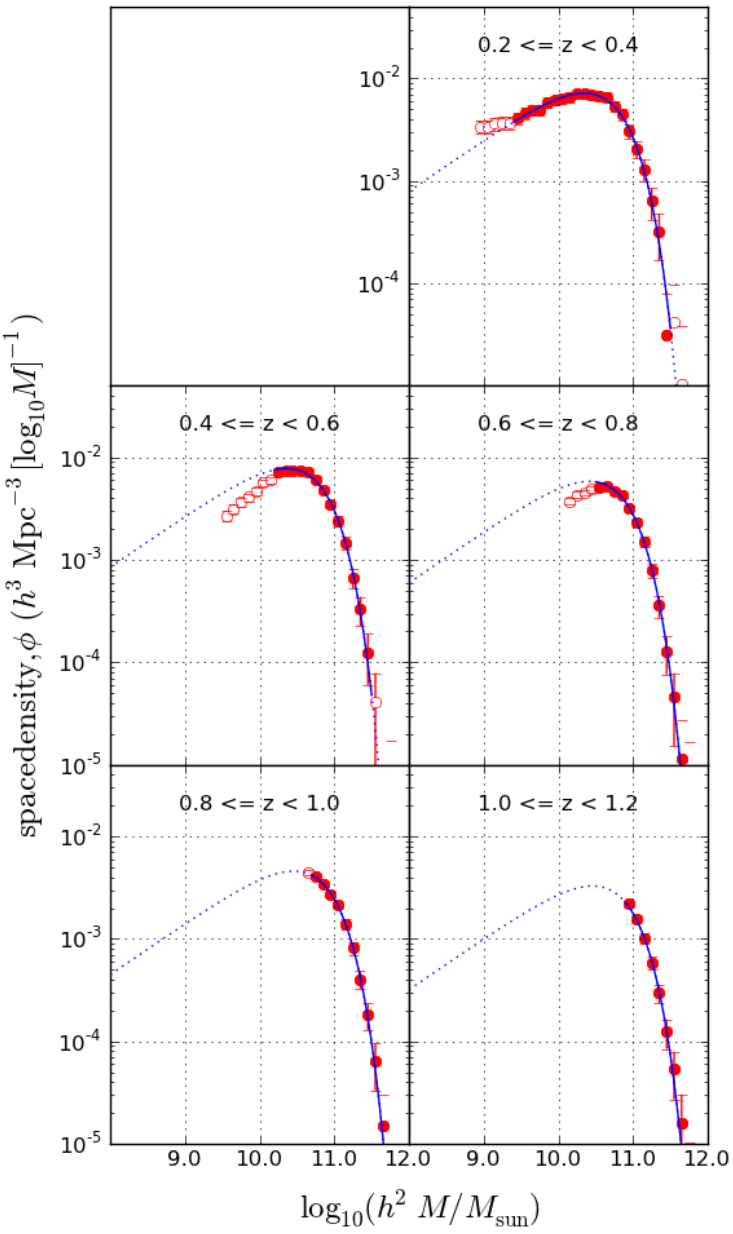

Fig. 113.—: **Stellar mass functions for red galaxies at different redshifts based on K-band absolute magnitudes.** Symbols are as in Figure 112.

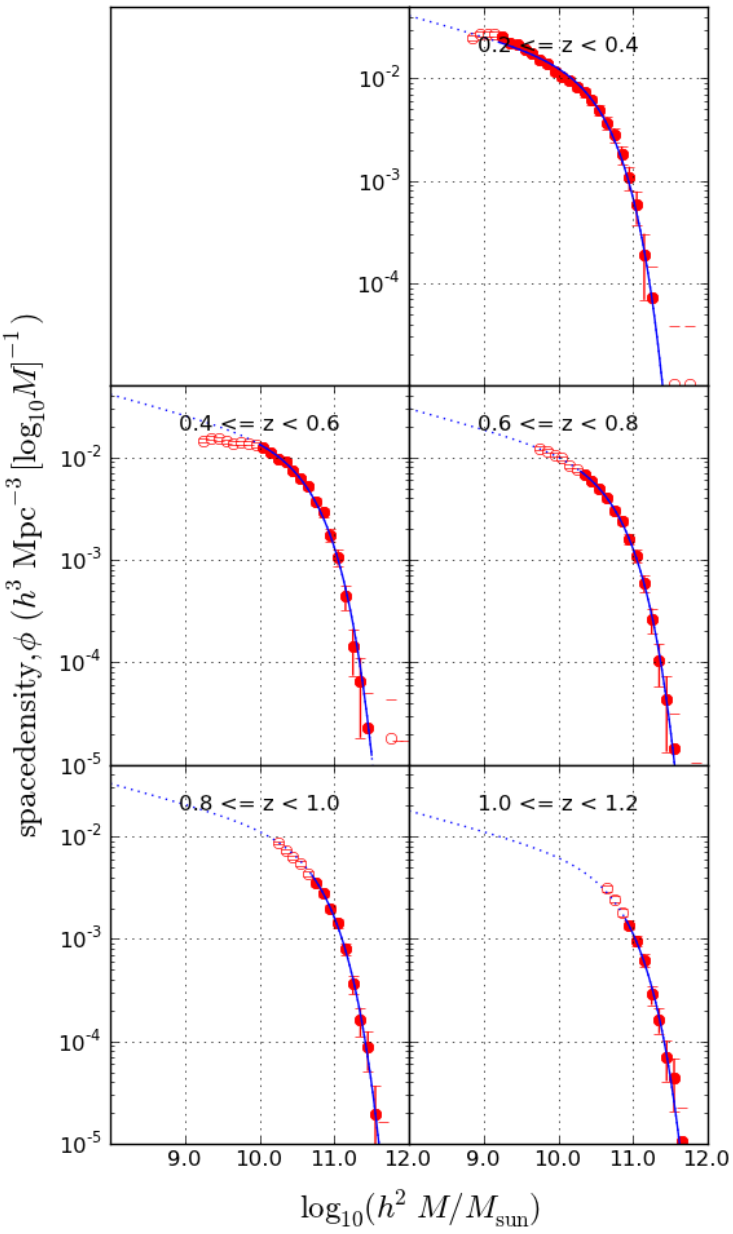

Fig. 114.—: **Stellar mass functions for blue galaxies at different redshifts based on K-band absolute magnitudes.** Symbols are as in Figure 112.

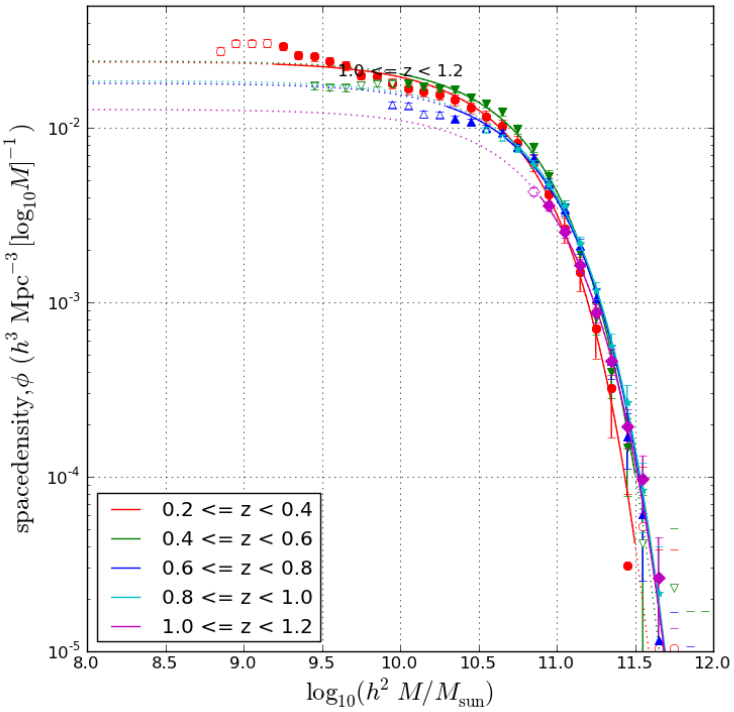

Fig. 115.—: **Evolution of the stellar mass functions for all galaxies based on K-band absolute magnitudes, showing all redshift bins in one panel.** The error bars show $1-\sigma$ Poisson errors for the numbers in each bin.

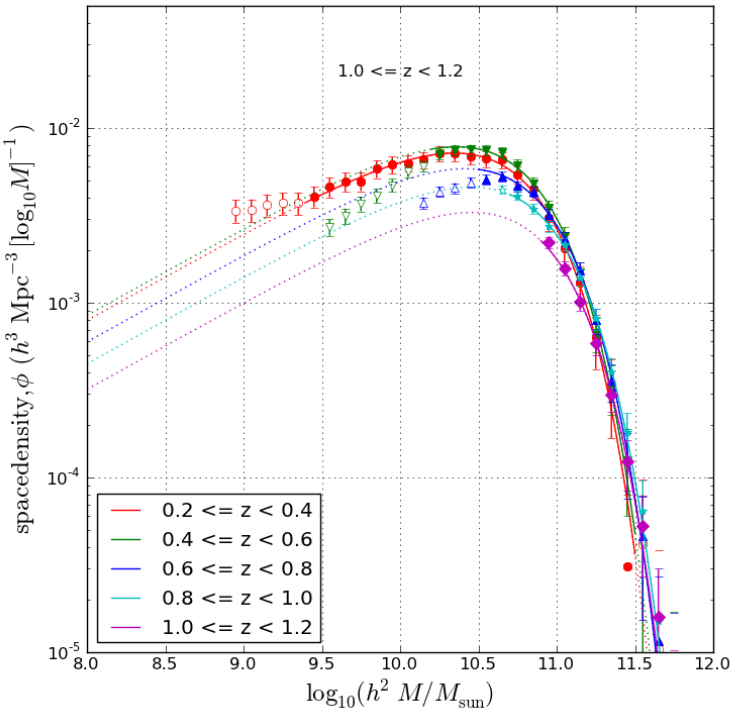

Fig. 116.—: **Evolution of the stellar mass functions for red galaxies based on K-band absolute magnitudes, showing all redshift bins in one panel.**

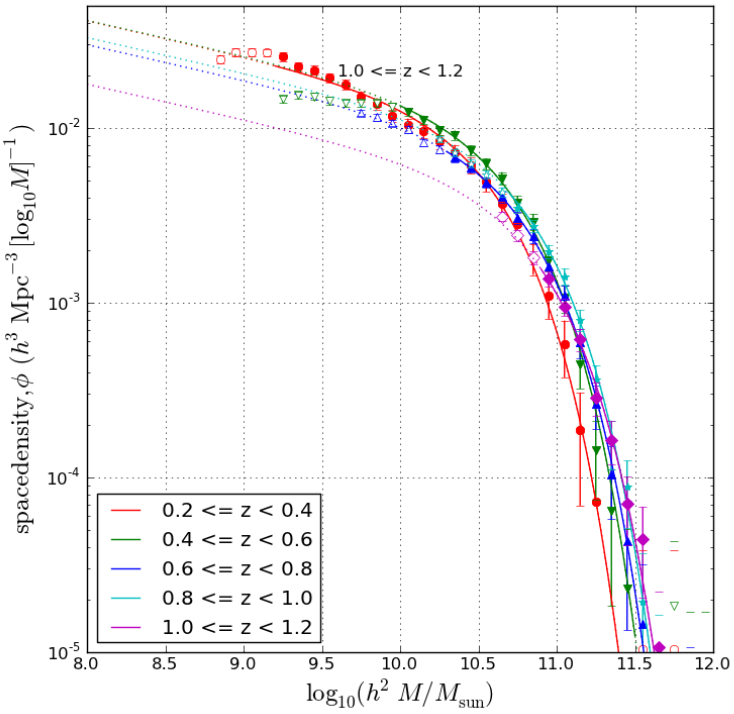

Fig. 117.—: **Evolution of the stellar mass functions for blue galaxies based on K-band absolute magnitudes, showing all redshift bins in one panel.**

4.6.1. The evolution of massive galaxies

Comparison of our binned luminosity functions in Figures 109 to 111 with the reference plot for all galaxies from Cole et al. (2001) shows that for all and red galaxies there is very little evolution (less than 0.1 dex) in the mass of the most massive galaxies throughout our redshift range. For blue galaxies some mass evolution is apparent, of the order of ∼0.2 dex (or ×1.6).

We quantify the evolution of the mass of the most massive galaxies by studying evolution of the mass corresponding to a fixed space density at the high mass end of the mass function (Figure 119). We measure a decrease of less than ∼-0.05 dex (×0.9) for red galaxies and ∼-0.2 dex (×0.6) for blue from $z \sim 0.9$ to $z \sim 0.3$. Note that only for red galaxies does evolution of this mass correspond to evolution of the mass of individual galaxies; massive blue galaxies eventually cease to form stars and become quiescent so no longer remain in the "blue" subsample, so the decrease in mass of the most massive galaxies is a result of this downsizing (§3.1.2).

We found in Chapter 3 that, based on evolution of the B-band luminosity function, massive red galaxies approximately doubled in mass from $z \sim 1.1$ to $z \sim 0.5$ and then changed little in mass until the present. There is clear tension between these results for massive red galaxies and those inferred from B-band luminosity functions. The latter conclusion assumes that B-band stellar mass to light ratios as a function of colour have not changed since $z \sim 1.1$. By contrast, the results in this chapter are based on assuming that stellar M/L ratios are a non-evolving linear function of $(B-V)$ colour alone, whereas in reality they will also depend on factors such as metallicity and galaxy mass. Resolution of the tension between the results for massive red galaxies in this chapter and the previous one will depend on improved modelling of evolving stellar M/L ratios.

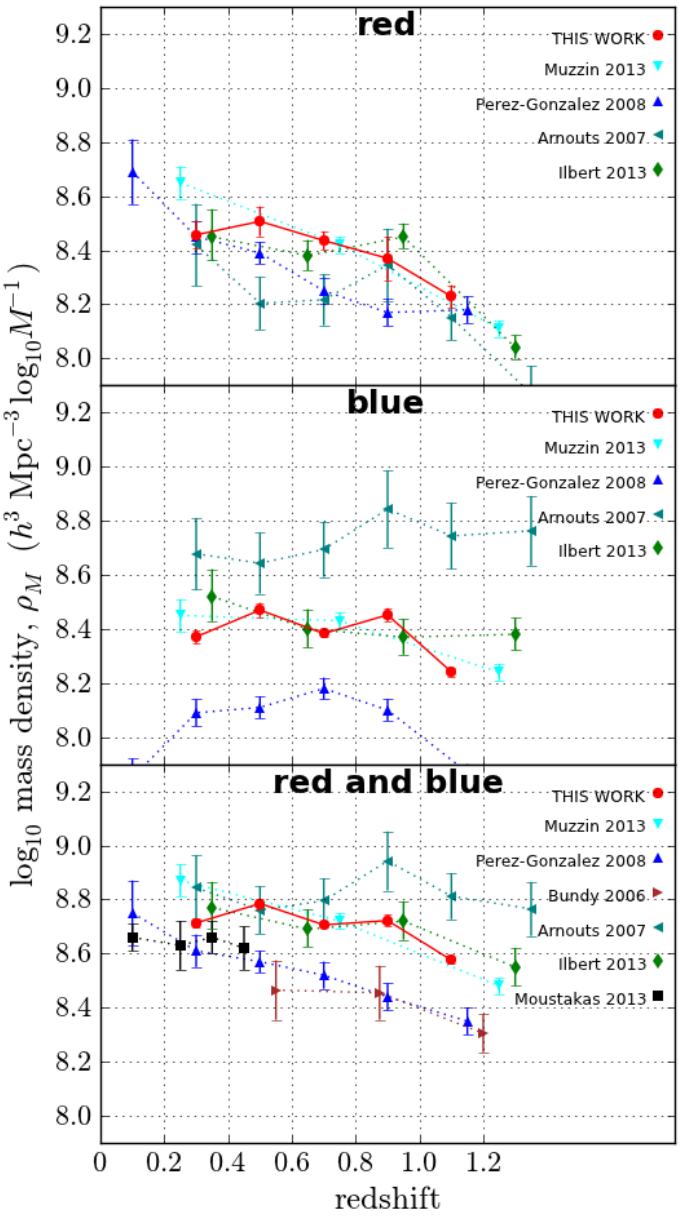

Fig. 118.—: **Evolution of the total mass density based on K-band absolute magnitudes.** From $z \sim 1.1$ to ~ 0.3 the mass density for all galaxies increases by a factor of $\sim$1.5, while for red and blue galaxies separately the increases are $\times$1.9 and $\times$1.4 respectively. Similar trends are seen by other authors. Error bars on our results show errors due to cosmic variance. Error bars on results from the literature are as published.

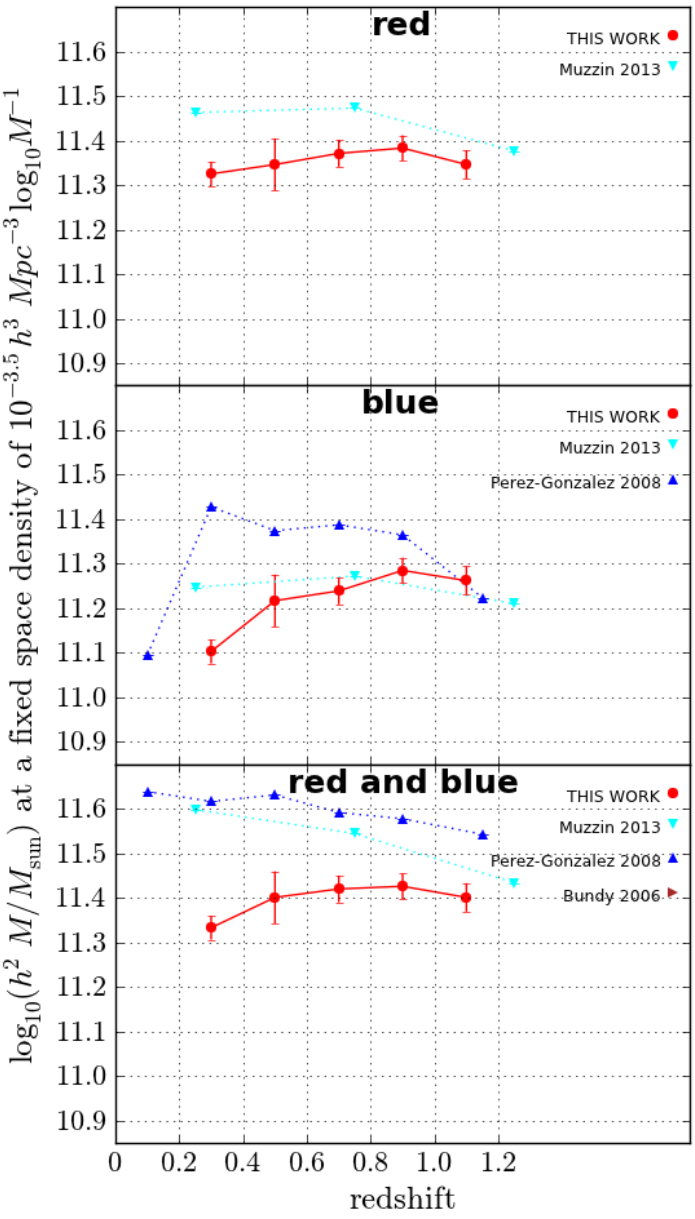

Fig. 119.—: **Evolution of very massive galaxies based on K-band absolute magnitudes.** The value of $h^2\ \log_{10} M/M_\odot$ corresponding to a fixed space density of $10^{-3.5}(h^3\mathrm{Mpc}^{-3}[\log_{10}M]^{-1})$ effectively monitors evolution of the most massive galaxies. Values from the literature have been computed using the published Schechter parameters when available. The mass of the most massive red galaxies has hardly changed from $z \sim 1.1$ to ~ 0.3, while the mass of the most massive blue galaxies has decreased by a factor of $\sim$0.6. Error bars on our results show errors due to cosmic variance. Error bars on results from the literature are as published.

4.6.2. The evolution of stellar mass density

Integrating the stellar mass functions using Equation 58 and our measured values of the Schechter parameters ϕ^*, M^* and α, we find that the stellar mass density evolves as shown in Figure 118. Selected results from the literature are shown for comparison.

Similar trends in total stellar mass density evolution are seen by most authors: a steady increase with time which is larger for red galaxies than for blue. We find that the stellar mass in all galaxies increases $\sim$0.17 dex (a factor of $\sim$1.5) from $z = 1.1$ to $z = 0.3$, with the increases for red and blue galaxies being respectively $\sim$0.28 dex (a factor of $\sim$1.9) and $\sim$0.15 dex (a factor of $\sim$1.4). These results are consistent with a scenario in which star formation is ceasing in star-forming galaxies causing them to become quiescent and move to the red sequence.

Once again we see a tension between these results for red galaxies and those inferred from evolution of the B-band luminosity function in Chapter 3 which show that the total mass density of red galaxies approximately quadrupled between $z \sim 1.1$ and the present.

4.7. The effect of assuming different stellar initial mass functions

As mentioned in §4.1.1, several authors (e.g. Cole et al. 2001; Bell et al. 2003) have pointed out that the use of different stellar initial mass functions in SPS models results in significantly different stellar mass to light ratios derived using those models. For example, in Cole et al. (2001) the effect of assuming a Kennicutt IMF (Kennicutt 1983) instead of a Salpeter one (Salpeter 1955) is to shift the galaxy stellar mass function by $\sim$0.3 dex towards smaller masses, i.e. the stellar mass to light ratio is decreased by a factor of $\sim$2. When calculating stellar mass functions it is important to quote the stellar IMF that has been used so that valid comparisons can be made between studies. We have used stellar mass to light ratios based on a Salpeter IMF with the "diet" modification described in Bell et al. (2003) that includes fewer faint low mass galaxies. Some other studies have used a standard Salpeter IMF, while many of the more recent studies have used a Chabrier (2003) IMF.

However, the *trend* in total mass density (as opposed to its absolute values) is relatively insensitive to the exact stellar IMF used to generate the stellar mass ratios, and to the restframe waveband used to determine stellar masses, because these two factors largely result in mass offsets rather than changes in gradient.

4.8. The effect of using optical instead of infrared mass to light ratios

We have also calculated stellar mass functions based on optical V-band stellar mass to light ratios, again taken from Bell et al. (2003) and calculated from $(B-V)$ observed colours. Comparison of Figures 120 and 109 shows that in the redshift range $0.6 < z < 1.0$ the stellar masses derived using the V-band are larger by $\sim$0.1 dex. Bell et al. (2003) found a similar small difference when they compared mass functions derived from K- and g-band luminosities. Very little difference is apparent when red galaxies alone are considered (Figures 121 and 110).

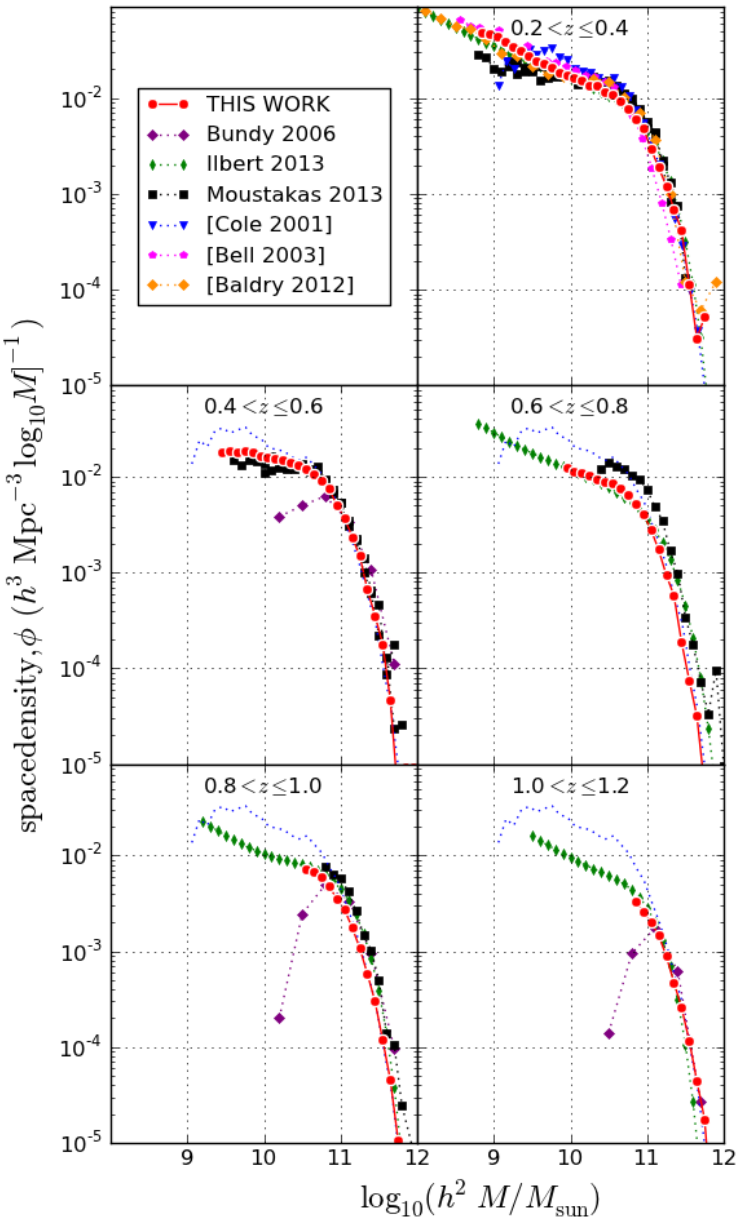

Fig. 120.—: **Binned mass functions for all galaxies based on V-band absolute magnitudes instead of K-band magnitudes.** These mass functions for all galaxies differ very little from those in Figure 109 which are based on K-band magnitudes. The Cole et al. (2001) mass function for all galaxies in the low redshift Universe is shown as a black dotted line for $z > 0.4$ in order to provide a fixed reference.

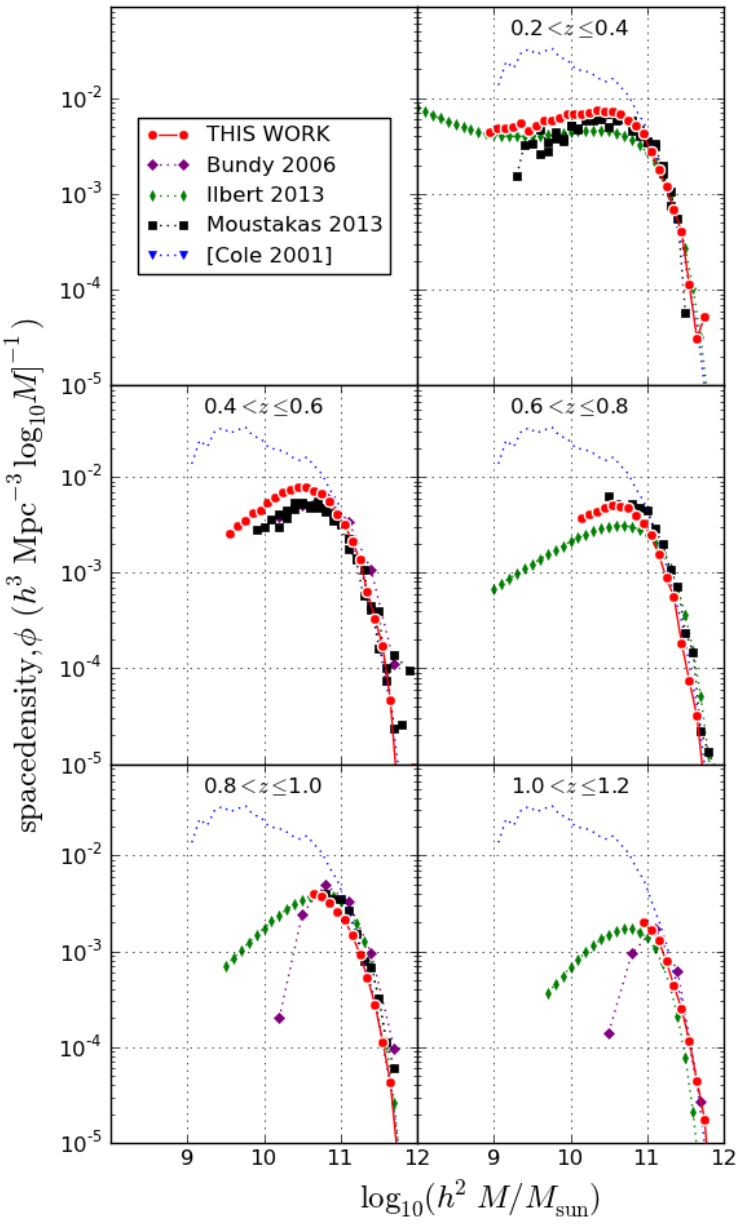

Fig. 121.—: **Binned mass functions for red galaxies only based on V-band absolute magnitudes instead of K-band magnitudes.** Comparison with Figure 110 shows that there is a small difference (∼0.1 dex) between mass functions based on K and V-band magnitudes when only red galaxies are included. The Cole et al. (2001) mass function for all galaxies in the low redshift Universe is shown as a black dotted line for $z > 0.4$ in order to provide a fixed reference.

Table 27. Binned stellar mass function for all galaxies.

$\log M$		Stellar Mass Function ($h^3\mathrm{Mpc}^{-3}\log_{10}M^{-1}$)				
Min	Max	$0.2 \leq z < 0.4$	$0.4 \leq z < 0.6$	$0.6 \leq z < 0.8$	$0.8 \leq z < 1.0$	$1.0 \leq z < 1.2$
8.80	8.90	27.605 ± 0.536	-	-	-	-
8.90	9.00	30.452 ± 0.562	-	-	-	-
9.00	9.10	30.473 ± 0.563	-	-	-	-
9.10	9.20	30.608 ± 0.564	-	-	-	-
9.20	9.30	29.268 ± 0.551	-	-	-	-
9.30	9.40	26.140 ± 0.521	-	-	-	-
9.40	9.50	25.538 ± 0.515	17.380 ± 0.283	-	-	-
9.50	9.60	23.927 ± 0.499	17.020 ± 0.280	-	-	-
9.60	9.70	22.660 ± 0.485	16.983 ± 0.280	-	-	-
9.70	9.80	20.062 ± 0.457	17.560 ± 0.285	-	-	-
9.80	9.90	19.605 ± 0.451	17.947 ± 0.288	-	-	-
9.90	10.00	17.933 ± 0.432	17.933 ± 0.288	13.619 ± 0.198	-	-
10.00	10.10	16.717 ± 0.417	18.039 ± 0.288	13.330 ± 0.196	-	-
10.10	10.20	16.114 ± 0.409	17.214 ± 0.282	11.970 ± 0.186	-	-
10.20	10.30	15.522 ± 0.402	16.799 ± 0.278	11.906 ± 0.186	-	-
10.30	10.40	14.421 ± 0.387	16.605 ± 0.277	11.285 ± 0.181	-	-
10.40	10.50	13.039 ± 0.368	14.958 ± 0.263	10.816 ± 0.177	-	-
10.50	10.60	11.595 ± 0.347	13.671 ± 0.251	9.986 ± 0.170	9.782 ± 0.145	-
10.60	10.70	10.244 ± 0.326	12.417 ± 0.239	9.306 ± 0.164	8.759 ± 0.137	-
10.70	10.80	8.218 ± 0.292	9.857 ± 0.213	7.709 ± 0.149	7.605 ± 0.128	-
10.80	10.90	6.296 ± 0.256	7.721 ± 0.189	6.734 ± 0.140	6.208 ± 0.116	4.333 ± 0.088
10.90	11.00	4.135 ± 0.207	5.258 ± 0.156	4.793 ± 0.118	4.716 ± 0.101	3.578 ± 0.080
11.00	11.10	2.629 ± 0.165	3.478 ± 0.127	3.422 ± 0.099	3.589 ± 0.088	2.527 ± 0.067
11.10	11.20	1.486 ± 0.124	1.923 ± 0.094	2.115 ± 0.078	2.192 ± 0.069	1.631 ± 0.054
11.20	11.30	0.706 ± 0.086	0.816 ± 0.061	1.056 ± 0.055	1.176 ± 0.050	0.871 ± 0.039
11.30	11.40	0.322 ± 0.058	0.397 ± 0.043	0.463 ± 0.037	0.566 ± 0.035	0.462 ± 0.029
11.40	11.50	0.031 ± 0.018	0.148 ± 0.026	0.171 ± 0.022	0.269 ± 0.024	0.195 ± 0.019
11.50	11.60	0.052 ± 0.023	0.042 ± 0.014	0.061 ± 0.013	0.084 ± 0.013	0.097 ± 0.013
11.60	11.70	0.010 ± 0.010	-	0.012 ± 0.006	0.022 ± 0.007	0.027 ± 0.007
11.70	11.80	0.010 ± 0.010	0.023 ± 0.010	0.006 ± 0.004	0.002 ± 0.002	0.005 ± 0.003
11.80	11.90	-	0.005 ± 0.005	0.003 ± 0.003	-	0.002 ± 0.002
11.90	12.00	-	0.005 ± 0.005	-	0.002 ± 0.002	-

Table 28. Binned stellar mass function for red galaxies.

$\log M$		Stellar Mass Function ($h^3\mathrm{Mpc}^{-3}\log_{10}M^{-1}$)				
Min	Max	$0.2 \leq z < 0.4$	$0.4 \leq z < 0.6$	$0.6 \leq z < 0.8$	$0.8 \leq z < 1.0$	$1.0 \leq z < 1.2$
8.90	9.00	3.377 ± 0.187	-	-	-	-
9.00	9.10	3.397 ± 0.188	-	-	-	-
9.10	9.20	3.636 ± 0.194	-	-	-	-
9.20	9.30	3.709 ± 0.196	-	-	-	-
9.30	9.40	3.709 ± 0.196	-	-	-	-
9.40	9.50	4.062 ± 0.205	-	-	-	-
9.50	9.60	4.592 ± 0.218	2.712 ± 0.112	-	-	-
9.60	9.70	4.935 ± 0.226	3.132 ± 0.120	-	-	-
9.70	9.80	4.956 ± 0.227	3.681 ± 0.130	-	-	-
9.80	9.90	5.829 ± 0.246	4.100 ± 0.138	-	-	-
9.90	10.00	6.161 ± 0.253	4.709 ± 0.147	-	-	-
10.00	10.10	6.286 ± 0.256	5.664 ± 0.162	-	-	-
10.10	10.20	6.577 ± 0.261	6.065 ± 0.167	3.732 ± 0.104	-	-
10.20	10.30	7.169 ± 0.273	7.112 ± 0.181	4.322 ± 0.112	-	-
10.30	10.40	7.169 ± 0.273	7.491 ± 0.186	4.527 ± 0.114	-	-
10.40	10.50	6.899 ± 0.268	7.518 ± 0.186	4.897 ± 0.119	-	-
10.50	10.60	6.681 ± 0.263	7.440 ± 0.185	5.091 ± 0.121	-	-
10.60	10.70	6.577 ± 0.261	7.246 ± 0.183	5.288 ± 0.124	4.446 ± 0.098	-
10.70	10.80	5.413 ± 0.237	6.125 ± 0.168	4.649 ± 0.116	4.121 ± 0.094	-
10.80	10.90	4.488 ± 0.216	4.806 ± 0.149	4.333 ± 0.112	3.450 ± 0.086	-
10.90	11.00	3.044 ± 0.178	3.505 ± 0.127	3.176 ± 0.096	2.748 ± 0.077	2.208 ± 0.063
11.00	11.10	2.047 ± 0.146	2.412 ± 0.105	2.326 ± 0.082	2.168 ± 0.068	1.576 ± 0.053
11.10	11.20	1.299 ± 0.116	1.481 ± 0.083	1.522 ± 0.066	1.395 ± 0.055	1.011 ± 0.042
11.20	11.30	0.634 ± 0.081	0.673 ± 0.056	0.793 ± 0.048	0.814 ± 0.042	0.584 ± 0.032
11.30	11.40	0.322 ± 0.058	0.332 ± 0.039	0.359 ± 0.032	0.405 ± 0.030	0.297 ± 0.023
11.40	11.50	0.031 ± 0.018	0.125 ± 0.024	0.127 ± 0.019	0.181 ± 0.020	0.124 ± 0.015
11.50	11.60	0.042 ± 0.021	0.042 ± 0.014	0.046 ± 0.012	0.065 ± 0.012	0.053 ± 0.010
11.60	11.70	0.010 ± 0.010	-	0.012 ± 0.006	0.015 ± 0.006	0.016 ± 0.005
11.70	11.80	-	0.005 ± 0.005	0.006 ± 0.004	0.002 ± 0.002	0.004 ± 0.003
11.80	11.90	-	-	-	-	0.002 ± 0.002

Table 29. Binned stellar mass function for blue galaxies.

$\log M$		Stellar Mass Function ($h^3\mathrm{Mpc}^{-3}\log_{10}M^{-1}$)				
Min	Max	$0.2 \leq z < 0.4$	$0.4 \leq z < 0.6$	$0.6 \leq z < 0.8$	$0.8 \leq z < 1.0$	$1.0 \leq z < 1.2$
8.80	8.90	24.759 ± 0.507	-	-	-	-
8.90	9.00	27.076 ± 0.530	-	-	-	-
9.00	9.10	27.076 ± 0.530	-	-	-	-
9.10	9.20	26.972 ± 0.529	-	-	-	-
9.20	9.30	25.559 ± 0.515	14.677 ± 0.260	-	-	-
9.30	9.40	22.431 ± 0.483	15.429 ± 0.267	-	-	-
9.40	9.50	21.475 ± 0.472	15.138 ± 0.264	-	-	-
9.50	9.60	19.335 ± 0.448	14.308 ± 0.257	-	-	-
9.60	9.70	17.725 ± 0.429	13.851 ± 0.253	-	-	-
9.70	9.80	15.107 ± 0.396	13.879 ± 0.253	12.259 ± 0.188	-	-
9.80	9.90	13.777 ± 0.378	13.847 ± 0.253	11.522 ± 0.183	-	-
9.90	10.00	11.772 ± 0.350	13.224 ± 0.247	10.665 ± 0.176	-	-
10.00	10.10	10.431 ± 0.329	12.375 ± 0.239	9.803 ± 0.168	-	-
10.10	10.20	9.538 ± 0.315	11.148 ± 0.227	8.238 ± 0.154	-	-
10.20	10.30	8.353 ± 0.295	9.686 ± 0.211	7.585 ± 0.148	8.675 ± 0.137	-
10.30	10.40	7.252 ± 0.274	9.114 ± 0.205	6.757 ± 0.140	7.259 ± 0.125	-
10.40	10.50	6.140 ± 0.253	7.440 ± 0.185	5.919 ± 0.131	6.270 ± 0.116	-
10.50	10.60	4.914 ± 0.226	6.231 ± 0.170	4.894 ± 0.119	5.426 ± 0.108	-
10.60	10.70	3.668 ± 0.195	5.171 ± 0.154	4.018 ± 0.108	4.313 ± 0.096	3.118 ± 0.074
10.70	10.80	2.805 ± 0.171	3.731 ± 0.131	3.061 ± 0.094	3.484 ± 0.087	2.427 ± 0.066
10.80	10.90	1.808 ± 0.137	2.915 ± 0.116	2.401 ± 0.083	2.758 ± 0.077	1.815 ± 0.057
10.90	11.00	1.091 ± 0.106	1.753 ± 0.090	1.617 ± 0.068	1.968 ± 0.065	1.370 ± 0.049
11.00	11.10	0.582 ± 0.078	1.065 ± 0.070	1.096 ± 0.056	1.421 ± 0.055	0.951 ± 0.041
11.10	11.20	0.187 ± 0.044	0.443 ± 0.045	0.593 ± 0.041	0.797 ± 0.041	0.620 ± 0.033
11.20	11.30	0.073 ± 0.027	0.143 ± 0.026	0.263 ± 0.028	0.362 ± 0.028	0.287 ± 0.023
11.30	11.40	-	0.065 ± 0.017	0.104 ± 0.017	0.161 ± 0.019	0.165 ± 0.017
11.40	11.50	-	0.023 ± 0.010	0.043 ± 0.011	0.088 ± 0.014	0.071 ± 0.011
11.50	11.60	0.010 ± 0.010	-	0.014 ± 0.006	0.019 ± 0.006	0.044 ± 0.009
11.60	11.70	-	-	-	0.006 ± 0.004	0.011 ± 0.004
11.70	11.80	0.010 ± 0.010	0.018 ± 0.009	-	-	0.002 ± 0.002
11.80	11.90	-	0.005 ± 0.005	0.003 ± 0.003	-	-
11.90	12.00	-	0.005 ± 0.005	-	0.002 ± 0.002	-

Table 30. Stellar mass functions.

z	α	ϕ^* ($h^3\mathrm{Mpc}^{-3}\log_{10}M^{-1}$)	$\log_{10} M^*/M_\odot$	$log_{10}M/M_\odot$ (at $\phi = 10^{-3.5}$)	mass density $h^3 M_\odot\,\mathrm{Mpc}^{-3}$
Red galaxies - using K-band					
0.3	-0.5	$7.27 \pm 0.29 \times 10^{-3}$	10.65 ± 0.16	11.33 ± 0.11	$8.46 \pm 0.01 \times 10^{8}$
0.5	-0.5	$7.90 \pm 0.16 \times 10^{-3}$	10.66 ± 0.18	11.35 ± 0.07	$8.51 \pm 0.05 \times 10^{8}$
0.7	-0.5	$5.92 \pm 0.14 \times 10^{-3}$	10.72 ± 0.12	11.37 ± 0.04	$8.44 \pm 0.03 \times 10^{8}$
0.9	-0.5	$4.64 \pm 0.29 \times 10^{-3}$	10.76 ± 0.15	11.38 ± 0.04	$8.37 \pm 0.04 \times 10^{8}$
1.1	-0.5	$3.33 \pm 0.36 \times 10^{-3}$	10.76 ± 0.11	11.35 ± 0.03	$8.23 \pm 0.08 \times 10^{8}$
Red galaxies - using V-band					
0.3	-0.5	$7.56 \pm 0.30 \times 10^{-3}$	10.62 ± 0.16	11.30 ± 0.11	$8.44 \pm 0.01 \times 10^{8}$
0.5	-0.5	$7.61 \pm 0.15 \times 10^{-3}$	10.65 ± 0.18	11.33 ± 0.07	$8.48 \pm 0.04 \times 10^{8}$
0.7	-0.5	$5.38 \pm 0.14 \times 10^{-3}$	10.65 ± 0.12	11.30 ± 0.04	$8.33 \pm 0.02 \times 10^{8}$
0.9	-0.5	$3.67 \pm 0.21 \times 10^{-3}$	10.73 ± 0.15	11.33 ± 0.04	$8.24 \pm 0.03 \times 10^{8}$
1.1	-0.5	$2.52 \pm 0.27 \times 10^{-3}$	10.77 ± 0.11	11.32 ± 0.03	$8.12 \pm 0.07 \times 10^{8}$
Blue galaxies - using K-band					
0.3	-1.2	$5.48 \pm 0.43 \times 10^{-3}$	10.57 ± 0.14	11.10 ± 0.10	$8.37 \pm 0.06 \times 10^{8}$
0.5	-1.2	$5.21 \pm 0.40 \times 10^{-3}$	10.69 ± 0.18	11.22 ± 0.07	$8.47 \pm 0.12 \times 10^{8}$
0.7	-1.2	$3.67 \pm 0.41 \times 10^{-3}$	10.75 ± 0.12	11.24 ± 0.04	$8.38 \pm 0.09 \times 10^{8}$
0.9	-1.2	$3.96 \pm 0.25 \times 10^{-3}$	10.79 ± 0.11	11.29 ± 0.04	$8.45 \pm 0.02 \times 10^{8}$
1.1	-1.2	$2.07 \pm 0.38 \times 10^{-3}$	10.86 ± 0.15	11.26 ± 0.03	$8.24 \pm 0.1 \times 10^{8}$
Blue galaxies - using V-band					
0.3	-1.2	$5.82 \pm 0.49 \times 10^{-3}$	10.33 ± 0.14	10.88 ± 0.10	$8.16 \pm 0.05 \times 10^{8}$
0.5	-1.2	$4.42 \pm 0.32 \times 10^{-3}$	10.52 ± 0.18	11.03 ± 0.07	$8.23 \pm 0.09 \times 10^{8}$
0.7	-1.2	$3.66 \pm 0.38 \times 10^{-3}$	10.49 ± 0.12	10.98 ± 0.04	$8.12 \pm 0.07 \times 10^{8}$
0.9	-1.2	$2.92 \pm 0.16 \times 10^{-3}$	10.59 ± 0.11	11.06 ± 0.04	$8.12 \pm 0.02 \times 10^{8}$
1.1	-1.2	$2.00 \pm 0.29 \times 10^{-3}$	10.58 ± 0.15	10.98 ± 0.03	$7.95 \pm 0.07 \times 10^{8}$
All galaxies - using K-band					
0.3	-1.0	$10.36 \pm 0.53 \times 10^{-3}$	10.70 ± 0.13	11.33 ± 0.10	$8.71 \pm 0.02 \times 10^{8}$
0.5	-1.0	$10.48 \pm 0.48 \times 10^{-3}$	10.76 ± 0.18	11.40 ± 0.07	$8.79 \pm 0.08 \times 10^{8}$
0.7	-1.0	$7.81 \pm 0.42 \times 10^{-3}$	10.81 ± 0.11	11.42 ± 0.04	$8.71 \pm 0.05 \times 10^{8}$
1.1	-1.0	$8.05 \pm 0.45 \times 10^{-3}$	10.82 ± 0.12	11.43 ± 0.04	$8.72 \pm 0.02 \times 10^{8}$
1.1	-1.0	$5.53 \pm 0.58 \times 10^{-3}$	10.83 ± 0.12	11.40 ± 0.03	$8.58 \pm 0.07 \times 10^{8}$
All galaxies - using V-band					
0.3	-1.0	$9.45 \pm 0.51 \times 10^{-3}$	10.65 ± 0.13	11.27 ± 0.10	$8.62 \pm 0.01 \times 10^{8}$
0.5	-1.0	$8.63 \pm 0.37 \times 10^{-3}$	10.73 ± 0.18	11.35 ± 0.07	$8.67 \pm 0.06 \times 10^{8}$
0.7	-1.0	$6.46 \pm 0.33 \times 10^{-3}$	10.72 ± 0.11	11.31 ± 0.04	$8.53 \pm 0.04 \times 10^{8}$
1.1	-1.0	$5.00 \pm 0.27 \times 10^{-3}$	10.78 ± 0.12	11.34 ± 0.04	$8.48 \pm 0.01 \times 10^{8}$
1.1	-1.0	$3.29 \pm 0.35 \times 10^{-3}$	10.82 ± 0.12	11.33 ± 0.03	$8.34x \pm 0.06 \times 10^{8}$

4.9. Summary

Using an identical sample with identical photometric redshifts, photometric apertures and methods to those used for the B-band luminosity function in Chapter 3 we measured evolution of the K-band luminosity function from $z = 1.2$ to $z = 0.2$. We then used this and K-band stellar mass to light ratios from Bell et al. (2003) to determine how the galaxy stellar mass function evolved.

Absolute K-band magnitudes were determined using our new K-correction method described in Chapter 2 and near infrared data from the NEWFIRM K_s-band and the IRAC 3.6 and 4.5 μm infrared bands. We quantified luminosity function evolution by fitting Schechter functions to binned luminosity functions in five equal redshift bins spanning the range $0.2 \leq z < 1.2$, employing both the $1/V_{\rm max}$ and maximum likelihood methods. Red and blue galaxies were differentiated using the same evolving cut in restframe $(M_U - M_B)$ versus M_B colour-magnitude space as for the B-band.

Our binned K-band luminosity functions are based on samples more than ten times larger than those of the previous studies of Drory et al. (2003), Arnouts et al. (2007) and Cirasuolo et al. (2010). The luminosity functions for the $0.2 \leq z < 0.4$ redshift bin are consistent with results for the low redshift Universe from several studies.

Evolution of the Schechter parameters M^* and ϕ^* giving the characteristic magnitude and space density of the luminosity function was measured for both varying and fixed values of the faint end slope parameter α. Because of the difficulty of measuring faint end slopes at higher redshifts because of sample incompleteness we adopted fixed values corresponding to $0.2 \leq z < 0.6$. These were -1.0, -0.5 and -1.2 respectively for all, red and blue galaxies (only slightly different from the optimum values of -1.1, -0.5 and -1.3 for the B-band). We measured the total K-band luminosity density by integrating the Schechter function and we measured evolution of highly luminous galaxies by measuring evolution of the absolute magnitude corresponding to a fixed space density.

As in the B-band, blue galaxies are more numerous than red in the K-band at all redshifts and are present in rapidly increasing numbers at faint magnitudes ($\alpha = -1.2$) whereas the numbers of red galaxies show a downturn and decrease rapidly at fainter magnitudes ($\alpha = -0.5$). From $z = 1.1$ to 0.3 the space density of both red and blue $\sim L^*$ galaxies approximately doubled. Over the same redshift range the characteristic luminosity $\sim L^*$ of blue galaxies faded more (0.6 mag) than that of red (0.3 mag), but the rate of fading is less than in the B-band, as is to be expected given that the restframe K-band samples the Rayleigh-Jeans tail of stellar spectra and is little affected by star formation.

The changes in total luminosity density j_K differed from those in the B-band in the manner

we would expect from the smaller rate of stellar fading in the K-band: the luminosity density of blue galaxies hardly changed from $z = 1.1$ to 0.3 but that of red galaxies increased by $\times 1.5$. Over the same redshift range the luminosity of highly luminous blue galaxies decreased by $\sim$0.7 mag while that of highly luminous red galaxies showed little change.

Our evolving binned mass functions are in good agreement with other studies (Ilbert et al. 2013; Moustakas et al. 2013) and consistent with those for the low redshift Universe (Cole et al. 2001; Bell et al. 2003; Baldry et al. 2012), except that they are systematically more massive by $\sim$2 to 3 dex. However, there are significant offsets (up to $\sim$0.4 dex) amongst values for total mass density from different studies, largely due to the use of different stellar initial mass functions for modelling stellar mass to light ratios and different ways of separating star-forming and quiescent galaxies, but significantly the measured rates of evolution of mass density are similar.

Evolution of the Schechter parameters M^* and ϕ^* giving the characteristic magnitude and space density of the mass function was measured for both varying and fixed values of the faint end slope parameter α. Because of the difficulty of measuring faint end slopes at higher redshifts because of sample incompleteness we adopted fixed values corresponding to $0.2 \leq z < 0.6$. These were -1.0, -0.5 and -1.2 respectively for all, red and blue galaxies, the same values we used for the K-band luminosity function.

We quantified mass function evolution by fitting Schechter functions using both the $1/V_{\rm max}$ and maximum likelihood methods. Integration of our mass functions indicates that the total stellar mass in blue galaxies has increased by a factor of $\sim$1.4 from $z \sim 1.1$ to $z \sim 0.3$ while that in red galaxies has increased by $\times \sim 1.9$. We find that the mass of the most massive blue galaxies decreases by a factor of $\sim$0.6, consistent with downsizing, while the mass of the most massive red galaxies hardly changed, indicating that they are evolving passively with minimal mass added through mergers.

There is a tension between these results and those based on evolution of the B-band luminosity function (Chapter 3) which imply that the mass density of red galaxies quadrupled while the mass of massive red galaxies doubled in mass from $z \sim 1.1$ to the present. We attribute these discrepancies to the evolution of stellar mass to light ratios and their dependence on factors such as metallicity and galaxy mass, neither of which we were able to take into account.

5. SUMMARY

5.0.1. Overview

We have used the largest galaxy sample to date to measure evolution of the B and K-band luminosity functions and to determine how the stellar mass in galaxies has changed over the last 8 Gyr (i.e. since $z = 1.2$). Our sample of ∼335 000 galaxies was split into red and blue subsamples using an evolving $(M_U - M_B)$ cut in restframe colour-magnitude space and we studied the subsamples separately as well as together. Our measurements improve on previous studies in three ways: a sample size which is ∼10 times larger than previous studies, a more accurate method of determining total apparent magnitudes, and a new method for measuring K-corrections which is both simpler and more accurate than previous methods.

5.0.2. An improved method of determining K-corrections

The absolute magnitude of a galaxy in a waveband W is calculated from its apparent magnitude in another waveband Z using a K-correction defined as $K_{WZ} = (M_W + D_M) - m_Z$. Using a new set of 125 empirical galaxy templates (Brown et al. 2013) we demonstrated that it is possible (at any given redshift) to model the dependence of the K-correction on a single suitably chosen observed colour $x = (m_Y - m_Z)$ using a second order polynomial in that colour: $K_{WZ} = ax^2 + bx + c$. Our method is much simpler than other available methods and more accurate in many cases.

We determined the observed SDSS colours that provide the greatest accuracy for determining absolute magnitudes in each of the Sloan *ugriz* wavebands. For each waveband we tabulated the coefficients a, b, c for the corresponding K-correction polynomials for redshifts in the range $0 < z < 0.5$ and make these publicly available. We compared our K-corrections with those from *kcorrect* using the sample of SDSS galaxies in the New York Value-Added Galaxy Catalogue and found that our method provided clearer separation between red and blue galaxies and a much tighter red sequence. Furthermore it did not generate the spurious cloud of extremely red galaxies at $z \sim 0.2$ which is produced by *kcorrect* but not seen in the low redshift Universe.

5.0.3. Measurement of the evolving B-band luminosity function and conclusions

Making use of our new K-correction method, we measured evolution of the B-band luminosity function from $z = 1.2$ to $z = 0.2$ based on data from an $\sim$8 deg^2 field in Boötes. This provided a sample $\sim$10 times larger than any previous study, so minimising cosmic variance. We measured absolute magnitudes in the U, B and V-wavebands using $B_W RI$ optical photometry from the NOAO Deep Wide Field Survey (NDWFS) and near infrared J-band data from the NEWFIRM Boötes Imaging Survey. Additional infrared photometry in the NEWFIRM H and K_s bands, and the Spitzer IRAC 3.6, 4.5, 5.8 and 8.0 μm bands was used to exclude stars and AGN, as well as to limit the sample to objects with plausible photometry for galaxies.

Photometric redshifts were calculated by Michael Brown, based on the $\sim$125 new galaxy templates of Brown et al. (2013). Initially photometric redshifts were calculated using the ANNz artificial neural network code, but after much investigation these were found to produce an implausible drop in blue galaxy numbers over a broad range of redshifts around $z = 0.45$ and these were therefore dropped in favour of template based photometric redshifts.

Comparison with available spectroscopic redshifts shows that for all galaxies these template based photometric redshifts have systematic errors less than $\sim$0.02 out to $z = 0.8$. From $z = 0.8$ to $z = 1.0$ the systematic errors are still relatively small, but beyond $z = 1.0$ an increasing systematic redshift overestimate is seen, particularly for blue galaxies. This is undoubtedly the main reason for the sudden drop in the measured space density of blue galaxies at $1.0 \leq z < 1.2$. This is because the Schechter function parameters are sensitively dependent on the exact space density values being fitted when data is only available for the brightest galaxies, as is the case at $z > 1$.

The number of available spectroscopic redshifts is relatively small beyond $z = 0.8$ and very small beyond $z = 1.0$, so our redshifts become a little uncertain in the second to last redshift bin ($0.8 \leq z < 1.0$) and much more uncertain in the highest redshift bin ($1.0 \leq z < 1.2$), in the case of blue galaxies. We therefore take our results for blue galaxies at $1.0 \leq z < 1.2$ as tentative, particularly those based on the B-band (Chapter 3), while noting nevertheless that whether we include this redshift bin or not does not materially alter our main conclusions regarding the rate of growth of galaxy luminosity and mass.

Total apparent magnitudes were estimated from measured magnitudes by locating isolated galaxies in each range of redshifts and then plotting growth curves of measured magnitude against photometric aperture diameter. From these curves the optimum aperture diameters and associated magnitude corrections for galaxies were determined. Our method is empirically based and we expect it to be more accurate than methods which involve assuming

particular surface brightness profiles, as some studies do.

We measured the luminosity functions of red, blue and all galaxies in five redshift bins of width 0.2 in the range $0.2 \leq z < 1.2$. Comparison of these with results from other studies (Bell et al. 2004; Brown et al. 2007; Willmer et al. 2006; Faber et al. 2007; Cool et al. 2012), and with low redshift Universe measurements (Madgwick et al. 2002; Blanton et al. 2005a; Loveday et al. 2012), showed good agreement, despite the fact that we separated "red" and "blue" galaxies using an evolving cut in restframe $(M_U - M_B)$ versus M_B colour-magnitude space whereas many authors used different criteria.

We parameterised luminosity function evolution by fitting Schechter functions to our binned luminosity functions, using both the $1/V_{\rm max}$ and maximum likelihood methods. Evolution of the Schechter parameters M^* and ϕ^* giving the characteristic magnitude and space density of the luminosity function was measured for both varying and fixed values of the faint end slope parameter α. Because of the difficulty of measuring faint end slopes at higher redshifts due to sample incompleteness we adopted fixed α values corresponding to those at $0.2 \leq z < 0.6$. These were α = -1.1, -0.5 and -1.3 respectively for all, red and blue galaxies. We demonstrated the degeneracy of the three Schechter parameters and showed that this had little effect on either the total B-band luminosity density (obtained by integrating the Schechter function) or the measured evolution of highly luminous galaxies (which we determined by measuring evolution of the absolute magnitude corresponding to a fixed space density).

We found that blue galaxies are more numerous than red at all redshifts and are present in rapidly increasing numbers as one goes to fainter magnitudes (faint end slope parameter $\alpha = -1.3$) whereas the numbers of red galaxies show a downturn and decrease rapidly towards fainter magnitudes ($\alpha = -0.5$) . The space density of blue $\sim L^*$ galaxies hardly changed from $z \sim 1$ to the present while that of red galaxies doubled. The characteristic luminosity $\sim L^*$ of blue galaxies faded more (0.9 mag) than that of red (0.6 mag).

The total luminosity density j_B of blue galaxies halved from $z = 0.9$ to the present, while that of red galaxies hardly changed from $z = 1.1$ to the present. (Our results for blue galaxies at $1.0 \leq z < 1.2$ are uncertain because of indeterminate systematic redshift errors.) By comparing the fading of luminosity density in our red galaxy sample with that to be expected on the basis of passive evolution alone (i.e. no mergers and no star formation), we inferred that the stellar mass in red galaxies quadrupled from $z = 1.1$ to the present. However, Bell et al. (2004) and Brown et al. (2007) made use of a similar argument and concluded that the total luminosity density j_B for red galaxies at least doubled from $z \sim 1$ to the present. van der Wel et al. (2005) found that this became a factor of four rather than two when they used their own measured rate of stellar M/L evolution rather than that

predicted by Bruzual & Charlot (2003) models, as used by Bell et al. (2004) and Brown et al. (2007). This explains the discrepancy between their results and ours.

Using a similar comparison with the fading to be expected from passive evolution alone, we also concluded that highly luminous red galaxies approximately doubled in mass from $z = 1.1$ to the present.

Our results are consistent with the scenario in which more massive and luminous blue galaxies cease star formation and move to the red sequence sooner than less massive ones ("downsizing"), so resulting in a decrease in the characteristic magnitude M^* of blue galaxies and an increase in the space density of red galaxies. The total luminosity density of blue galaxies decreases as more massive galaxies cease star formation and move to the red sequence, while that of red galaxies changes little because the increase in luminosity due to migration from the blue cloud almost balances the decrease due to stellar fading.

5.0.4. Measurement of the evolving K-band luminosity function and conclusions

Using an identical sample and methods to those used for the B-band luminosity function, we measured evolution of the K-band luminosity function from $z = 1.2$ to $z = 0.2$. Our K-corrections were based on the NEWFIRM near infrared K_s-band and the IRAC 3.6 and 4.5 μm infrared bands. As with the B-band, we parameterised luminosity function evolution by fitting Schechter functions to our binned luminosity functions in five redshift bins of width 0.2 spanning the range $0.2 \leq z < 1.2$, analysing red, blue and all galaxies separately, and then using both the $1/V_{\rm max}$ and maximum likelihood methods.

Our binned K-band luminosity functions were based on samples at least ten times larger than those of the previous studies of Drory et al. (2003); Arnouts et al. (2007) and Cirasuolo et al. (2010) giving smaller random Poisson errors and cosmic variance errors. The luminosity functions for the $0.2 \leq z < 0.4$ redshift bin are also consistent with results for the low redshift Universe from (Kochanek et al. 2001; Cole et al. 2001; Blanton 2006), except that our magnitudes are $\sim$0.3 mag brighter. We attribute much of this difference to the fact that many studies use 2MASS data which is known to underestimate the luminosity of extended objects. Because of the difficulty of measuring faint end slopes at higher redshifts where space densities are only available for more luminous galaxies we adopted fixed values of -1.0, -0.5 and -1.2 for the faint end slope parameter α, these values corresponding to those for the first two redshift bins (i.e. $0.2 \leq z < 0.6$) when α was allowed to vary as a free parameter.

As in the B-band, blue galaxies are more numerous than red in the K-band at all redshifts

and are present in rapidly increasing numbers at faint magnitudes (faint end slope parameter $\alpha = -1.2$) whereas the numbers of red galaxies show a downturn and decrease rapidly towards fainter magnitudes ($\alpha = -0.5$).

From $z = 1.1$ to 0.3 the parameter ϕ^* giving the space density of both red and blue $\sim L^*$ galaxies approximately doubled. Over the same redshift range the characteristic luminosity $\sim L^*$ of blue galaxies faded more (0.6 mag) than that of red (0.3 mag). This rate of fading was less than that in the B-band, as was to be expected given that the restframe K-band samples the Rayleigh-Jeans tail of stellar spectra and is little affected by star formation. This expectation is in agreement with the measurements of van der Wel et al. (2005) for early type galaxies, who found that stellar mass to light ratios increased more slowly due to stellar fading in the K-band than in the B-band. (They find $d\ln(M/L_B)/dz = -1.46$, $d\ln(M/L_K)/dz = -1.18$, i.e. $\Delta z = -1$ produces a change of $\times 4.31$ in M/L_B and $\times 3.25$ in M/L_K). van der Wel et al. (2005) also point out that stellar mass to light ratios for early type galaxies evolve at a rate which varies with galaxy mass, this mass dependence being stronger in the B-band and weaker in the K-band. A more detailed analysis would need to take these factors into account.

Over the same redshift range, the K-band luminosity of highly luminous blue galaxies decreased by $\sim$0.7 mag while that of highly luminous red galaxies showed little change. In the B-band the decrease in luminosity for massive blue galaxies was similar to that in the K-band, as would be expected if the decrease was mainly due to downsizing. For massive red galaxies, however, the fading was $\sim$0.4 mag in the B-band and very little in the K-band, and this is what one would expect from the slower rate of increase of stellar mass to light ratios in the K-band, (i.e. the slower rate of increase of stellar light to mass ratios).

5.0.5. Measurement of the evolving stellar mass function of galaxies

We derived galaxy mass functions from our infrared K-band luminosity functions by assuming the stellar mass to light ratios given in Bell et al. (2003) as linear functions of restframe $(M_B - M_V)$ colour, M_B and M_V being as determined previously. Our evolving binned mass functions are in good agreement with other studies (Ilbert et al. 2013; Moustakas et al. 2013) and consistent with those for the low redshift Universe (Cole et al. 2001; Bell et al. 2003; Baldry et al. 2012). We quantified mass function evolution by fitting Schechter functions to our mass functions in five redshift bins of width 0.2 spanning the range $0.2 \leq z < 1.2$, analysing red, blue and all galaxies separately, and then using both the $1/V_{\rm max}$ and maximum likelihood methods.

Integration of our mass functions indicated that the total stellar mass in blue galaxies in-

creased by a factor of ∼1.4 from $z \sim 1.1$ to $z \sim 0.3$ while that in red galaxies has increased by $\times \sim 1.9$. The increase for red galaxies is less than that inferred from evolution of the B-band luminosity density j_B, which was $\times \sim 4$. However, in deriving our mass functions we did not take account of the evolution of stellar mass to light ratios as described in van der Wel et al. (2005), which is $\times 3.25$ for all galaxies taken together. Taking this value at face value we would obtain mass density increases of $\times 4.2$ and $\times 5.2$ respectively, but this is far too simplistic because a more accurate analysis would need to take account of the evolution of stellar mass to light ratios and their dependence on factors such as metallicity and galaxy mass, not just the colour dependence of average stellar M/L ratios.

There are significant offsets (up to ∼0.4 dex) between values for total stellar mass density from different studies. However, these can be attributed to the use of different stellar initial mass functions for modelling stellar mass to light ratios and different ways of separating star-forming and quiescent galaxies (e.g. by restframe colour, star formation rate, morphology). Despite these offsets, the rates of change of stellar mass density are broadly similar in the various studies, and it is these rates of change which are of key significance for understanding galaxy evolution, not the absolute mass density values themselves.

We found that the mass of the most massive blue galaxies decreased by a factor of ∼0.6 from $z \sim 1.1$ to the present, consistent with downsizing. The mass of the most massive red galaxies hardly changed in mass over our redshift range indicating that they evolved passively with minimal mass added through mergers. This differs from our inference from evolution of the B-band luminosity function which implied that massive red galaxies have doubled in mass from $z \sim 1.1$ to the present. As with total mass density, a discrepancy is to be expected due to not taking account of the evolution of stellar mass to light ratios and their dependence on metallicity and galaxy mass.

5.0.6. Limitations of the present study and plans for future work

Applying our new K-correction method to the WISE filters

The Wide-Field Infrared Survey (Wright et al. 2010) will provide all-sky coverage in four infrared wavebands. Data from this survey are likely to extensively used by the astronomical community in the same way that SDSS data have been in the optical. Publication of K-correction parameters for these wavebands, similar to those we calculated for the SDSS wavebands, would make a valuable extension to our work in Chapter 2.

The effect of environment on luminosity function evolution

The large sample size and large volume of our sample mean that it could readily be split into subsamples in regions of high and low galactic density. Doing this would enable evolution of the luminosity function to be measured in different environments, i.e. in the field as compared with in groups, clusters and filaments. This extension of the present work would be valuable in constraining models of galaxy evolution because they make quantitative predictions regarding galactic space densities in different environments.

Luminosity function evolution in other wavebands

The work in Chapters 3 and 4 measuring B and K-band luminosity function evolution could easily be extended to other wavebands. U and V-band absolute magnitudes have already been calculated so it would be particularly easy to produce luminosity functions for these wavebands. However, R and I-band luminosity function evolution also provide exceptionally useful extensions as luminosities in these wavebands are less affected by star formation and therefore more closely related to galaxy masses.

Improved photometric redshifts

Uncertainty in the template based photometric redshift values, particularly beyond $z = 1.0$, and particularly for blue galaxies, forms the principal methodological limitation of this study. The quality of these redshifts could be greatly improved by obtaining additional NEWFIRM $JHKs$ imaging in the Extended Groth Strip (EGS), an area of about one square degree within which thousands of spectra of fainter galaxies have been obtained. This field already has NDWFS $BwRI$ and IRAC 3.6, 4.5, 5.8 and 8.0 μm imaging and the addition of $JHKs$ imaging would provide an identical set of photometry to what we used in the Boötes field. Including the EGS alongside Boötes would therefore enable us to accurately correct our template based photometric redshifts beyond $z = 0.8$, and so derive more robust measurements of luminosity and mass evolution beyond $z = 1.0$.

Modelling of galaxy template evolution

The present work does not take account of evolution of our ∼125 galaxy templates, whereas galaxies and the stellar populations within them are known to evolve significantly with redshift, especially beyond $z \sim 1$. A substantial improvement should result if the existing galaxy templates, which are based on local galaxy SEDs, could be evolved backwards in time using realistic stellar population synthesis models or otherwise. This would no doubt involve

considerable research effort and might not be feasible at the present time, given existing uncertainties regarding stellar initial mass functions, star formation histories, and other components of SPS models. Future observational work using improved telescope technology combined with more refined simulations of galaxy formation and evolution will result in improved understanding of the factors involved in SPS models. This will then enable the template SEDs from Brown et al. (2013) to be evolved backwards in time, so providing more accurate evolving K-corrections, template based photometric redshifts and stellar mass to light ratios.

REFERENCES

Almeida, C., Baugh, C. M., Wake, D. A., Lacey, C. G., Benson, A. J., Bower, R. G., & Pimbblet, K. 2008, MNRAS, 386, 2145

Alpher, R. A., Bethe, H., & Gamow, G. 1948, Physical Review, 73, 803

Arnouts, S., et al. 2002, MNRAS, 329, 355

—. 2007, A&A, 476, 137

Ashby, M. L. N., et al. 2009, ArXiv e-prints: 0906.0024

Autry, R. G., et al. 2003, in Society of Photo-Optical Instrumentation Engineers (SPIE) Conference Series, Vol. 4841, Society of Photo-Optical Instrumentation Engineers (SPIE) Conference Series, ed. M. Iye & A. F. M. Moorwood, 525–539

Baade, D., et al. 1999, The Messenger, 95, 15

Baldry, I. K., et al. 2012, MNRAS, 421, 621

Baugh, C. M., Lacey, C. G., Frenk, C. S., Granato, G. L., Silva, L., Bressan, A., Benson, A. J., & Cole, S. 2005, MNRAS, 356, 1191

Bell, E. F., & Bower, R. G. 2000, MNRAS, 319, 235

Bell, E. F., & de Jong, R. S. 2001, ApJ, 550, 212

Bell, E. F., McIntosh, D. H., Katz, N., & Weinberg, M. D. 2003, ApJS, 149, 289

Bell, E. F., et al. 2004, ApJ, 608, 752

Benson, A. J., Bower, R. G., Frenk, C. S., Lacey, C. G., Baugh, C. M., & Cole, S. 2003, ApJ, 599, 38

Bertin, E., & Arnouts, S. 1996, A&AS, 117, 393

Binney, J., & Merrifield, M. 1998, Galactic Astronomy

Blanton, M. R. 2006, ApJ, 648, 268

Blanton, M. R., Lupton, R. H., Schlegel, D. J., Strauss, M. A., Brinkmann, J., Fukugita, M., & Loveday, J. 2005a, ApJ, 631, 208

Blanton, M. R., & Roweis, S. 2007, AJ, 133, 734

Blanton, M. R., et al. 2003a, AJ, 125, 2348

—. 2003b, ApJ, 592, 819

—. 2005b, AJ, 129, 2562

Bondi, H., & Gold, T. 1948, MNRAS, 108, 252

Bonne et al. in prep.

Borch, A., et al. 2006, A&A, 453, 869

Bower, R. G., Benson, A. J., Malbon, R., Helly, J. C., Frenk, C. S., Baugh, C. M., Cole, S., & Lacey, C. G. 2006, MNRAS, 370, 645

Brammer, G. B., van Dokkum, P. G., & Coppi, P. 2008, ApJ, 686, 1503

Brown, M. J. I., Dey, A., Jannuzi, B. T., Brand, K., Benson, A. J., Brodwin, M., Croton, D. J., & Eisenhardt, P. R. 2007, ApJ, 654, 858

Brown, M. J. I., et al. 2008, ApJ, 682, 937

—. 2013, ArXiv e-prints

Bruzual, G. 2007, ArXiv Astrophysics e-prints

Bruzual, G., & Charlot, S. 2003, MNRAS, 344, 1000

Bundy, K., et al. 2006, ApJ, 651, 120

Chabrier, G. 2003, PASP, 115, 763

Chary, R., & Elbaz, D. 2001, ApJ, 556, 562

Chilingarian, I. V., Melchior, A.-L., & Zolotukhin, I. Y. 2010, MNRAS, 405, 1409

Cirasuolo, M., McLure, R. J., Dunlop, J. S., Almaini, O., Foucaud, S., & Simpson, C. 2010, MNRAS, 401, 1166

Coil, A. L., et al. 2011, ApJ, 741, 8

Cole, S., Lacey, C. G., Baugh, C. M., & Frenk, C. S. 2000, MNRAS, 319, 168

Cole, S., et al. 2001, MNRAS, 326, 255

Coleman, G. D., Wu, C.-C., & Weedman, D. W. 1980, ApJS, 43, 393

Collister, A. A., & Lahav, O. 2004, PASP, 116, 345

Connolly, A. J., Szalay, A. S., Bershady, M. A., Kinney, A. L., & Calzetti, D. 1995, AJ, 110, 1071

Conselice, C. J., Yang, C., & Bluck, A. F. L. 2009, MNRAS, 394, 1956

Cool, R. J., et al. 2012, ApJ, 748, 10

—. 2013, ApJ, 767, 118

Copi, C. J., Schramm, D. N., & Turner, M. S. 1995, Science, 267, 192

Cowie, L. L., Songaila, A., Hu, E. M., & Cohen, J. G. 1996, AJ, 112, 839

Cowsik, R., & McClelland, J. 1972, Physical Review Letters, 29, 669

Croton, D. J., et al. 2006, MNRAS, 365, 11

da Cunha, E., Charlot, S., & Elbaz, D. 2008, MNRAS, 388, 1595

Davis, M., Efstathiou, G., Frenk, C. S., & White, S. D. M. 1985, ApJ, 292, 371

Davis, M., et al. 2003, in Society of Photo-Optical Instrumentation Engineers (SPIE) Conference Series, Vol. 4834, Society of Photo-Optical Instrumentation Engineers (SPIE) Conference Series, ed. P. Guhathakurta, 161–172

De Lucia, G., & Blaizot, J. 2007, MNRAS, 375, 2

De Lucia, G., Springel, V., White, S. D. M., Croton, D., & Kauffmann, G. 2006, MNRAS, 366, 499

de Vaucouleurs, G. 1948, Annales d'Astrophysique, 11, 247

de Vaucouleurs, G. 1974, in IAU Symposium, Vol. 58, The Formation and Dynamics of Galaxies, ed. J. R. Shakeshaft, 1–52

de Vaucouleurs, G., de Vaucouleurs, A., Corwin, Jr., H. G., Buta, R. J., Paturel, G., & Fouqué, P. 1991, Third Reference Catalogue of Bright Galaxies. Volume I: Explanations and references. Volume II: Data for galaxies between 0^h and 12^h. Volume III: Data for galaxies between 12^h and 24^h.

Devereux, N., Willner, S. P., Ashby, M. L. N., Willmer, C. N. A., & Hriljac, P. 2009, ApJ, 702, 955

Dicke, R. H., Peebles, P. J. E., Roll, P. G., & Wilkinson, D. T. 1965, ApJ, 142, 414

Driver, S. P., et al. 2009, Astronomy and Geophysics, 50, 050000

—. 2011, MNRAS, 413, 971

—. 2012, MNRAS, 427, 3244

Drory, N., Bender, R., Feulner, G., Hopp, U., Maraston, C., Snigula, J., & Hill, G. J. 2003, ApJ, 595, 698

Drory, N., Feulner, G., Bender, R., Botzler, C. S., Hopp, U., Maraston, C., Mendes de Oliveira, C., & Snigula, J. 2001, MNRAS, 325, 550

Efstathiou, G., Ellis, R. S., & Peterson, B. A. 1988, MNRAS, 232, 431

Eggen, O. J., Lynden-Bell, D., & Sandage, A. R. 1962, ApJ, 136, 748

Einasto, J., Kaasik, A., & Saar, E. 1974, Nature, 250, 309

Eisenhardt, P. R. M., et al. 2008, ApJ, 684, 905

Faber, S. M., et al. 2003, in Society of Photo-Optical Instrumentation Engineers (SPIE) Conference Series, Vol. 4841, Society of Photo-Optical Instrumentation Engineers (SPIE) Conference Series, ed. M. Iye & A. F. M. Moorwood, 1657–1669

Faber, S. M., et al. 2007, ApJ, 665, 265

Fazio, G. G., et al. 2004, ApJS, 154, 10

Fioc, M., & Rocca-Volmerange, B. 1997, A&A, 326, 950

Firth, A. E., Lahav, O., & Somerville, R. S. 2003, MNRAS, 339, 1195

Gabor, J. M., & Davé, R. 2012, MNRAS, 427, 1816

Gamow, G. 1946, Physical Review, 70, 572

Geller, M. J., Dell'Antonio, I. P., Kurtz, M. J., Ramella, M., Fabricant, D. G., Caldwell, N., Tyson, J. A., & Wittman, D. 2005, ApJ, 635, L125

Gershtein, S. S., & Zel'dovich, Y. B. 1966, Soviet Journal of Experimental and Theoretical Physics Letters, 4, 120

Giavalisco, M., et al. 2004, ApJ, 600, L93

Gonzalez et al. in prep.

Graham, A. W., Driver, S. P., Petrosian, V., Conselice, C. J., Bershady, M. A., Crawford, S. M., & Goto, T. 2005, AJ, 130, 1535

Guo, Q., & White, S. D. M. 2008, MNRAS, 384, 2

Guth, A. H. 1981, Phys. Rev. D, 23, 347

Hirschmann, M., Naab, T., Somerville, R. S., Burkert, A., & Oser, L. 2012, MNRAS, 419, 3200

Hogg, D. W., Baldry, I. K., Blanton, M. R., & Eisenstein, D. J. 2002, ArXiv Astrophysics e-prints

Hoyle, F. 1954, ApJS, 1, 121

Hubble, E. 1929, Proceedings of the National Academy of Science, 15, 168

Hubble, E., & Humason, M. L. 1931, ApJ, 74, 43

Hubble, E. P. 1926, ApJ, 64, 321

—. 1936, Realm of the Nebulae

Humason, M. L., Mayall, N. U., & Sandage, A. R. 1956, AJ, 61, 97

Ilbert, O., et al. 2005, A&A, 439, 863

—. 2006a, A&A, 457, 841

—. 2006b, A&A, 453, 809

—. 2010, ApJ, 709, 644

—. 2013, A&A, 556, A55

Jannuzi, B. T., & Dey, A. 1999, in ASP Conf. Ser. 191: Photometric Redshifts and the Detection of High Redshift Galaxies, ed. R. Weymann, L. Storrie-Lombardi, M. Sawicki, & R. Brunner, 111

Jarrett, T. H., Chester, T., Cutri, R., Schneider, S., Skrutskie, M., & Huchra, J. P. 2000, AJ, 119, 2498

Jenkins, A., Frenk, C. S., White, S. D. M., Colberg, J. M., Cole, S., Evrard, A. E., Couchman, H. M. P., & Yoshida, N. 2001, MNRAS, 321, 372

Jones, D. H., Peterson, B. A., Colless, M., & Saunders, W. 2006, MNRAS, 369, 25

Kauffmann, G., Colberg, J. M., Diaferio, A., & White, S. D. M. 1999, MNRAS, 303, 188

Kennicutt, Jr., R. C. 1983, ApJ, 272, 54

Kewley, L. J., Dopita, M. A., Sutherland, R. S., Heisler, C. A., & Trevena, J. 2001, ApJ, 556, 121

Kinney, A. L., Calzetti, D., Bohlin, R. C., McQuade, K., Storchi-Bergmann, T., & Schmitt, H. R. 1996, ApJ, 467, 38

Kochanek, C. S., et al. 2001, ApJ, 560, 566

—. 2012, ApJS, 200, 8

Koekemoer, A. M., et al. 2007, ApJS, 172, 196

Labbé, I., et al. 2003, AJ, 125, 1107

Lawrence, A., et al. 2007, MNRAS, 379, 1599

Le Fèvre, O., et al. 2003, in Society of Photo-Optical Instrumentation Engineers (SPIE) Conference Series, Vol. 4841, Instrument Design and Performance for Optical/Infrared Ground-based Telescopes, ed. M. Iye & A. F. M. Moorwood, 1670–1681

Le Fèvre, O., et al. 2004, A&A, 428, 1043

—. 2005, A&A, 439, 845

Lee, D. D., & Seung, H. S. 1999, Nature, 401, 788

Lilly, S. J., et al. 2007, ApJS, 172, 70

Lin, H., Yee, H. K. C., Carlberg, R. G., Morris, S. L., Sawicki, M., Patton, D. R., Wirth, G., & Shepherd, C. W. 1999, ApJ, 518, 533

Lonsdale, C. J., et al. 2003, PASP, 115, 897

Lotz, J. M., Jonsson, P., Cox, T. J., Croton, D., Primack, J. R., Somerville, R. S., & Stewart, K. 2011, ApJ, 742, 103

Loveday, J. 1997, ApJ, 489, 29

—. 2000, MNRAS, 312, 557

—. 2004, MNRAS, 347, 601

Loveday, J., Peterson, B. A., Efstathiou, G., & Maddox, S. J. 1992, ApJ, 390, 338

Loveday, J., et al. 2012, MNRAS, 420, 1239

Maddox, S. J., Efstathiou, G., Sutherland, W. J., & Loveday, J. 1990, MNRAS, 242, 43P

Madgwick, D. S., et al. 2002, MNRAS, 333, 133

Maraston, C. 2005, MNRAS, 362, 799

Marshall, H. L., Tananbaum, H., Avni, Y., & Zamorani, G. 1983, ApJ, 269, 35

Martin, D. C., et al. 2005, ApJ, 619, L1

Marzke, R. O., da Costa, L. N., Pellegrini, P. S., Willmer, C. N. A., & Geller, M. J. 1998, ApJ, 503, 617

McCracken, H. J., et al. 2012, A&A, 544, A156

Morrissey, P., et al. 2007, ApJS, 173, 682

Mortlock, A., Conselice, C. J., Bluck, A. F. L., Bauer, A. E., Grützbauch, R., Buitrago, F., & Ownsworth, J. 2011, MNRAS, 413, 2845

Mostek, N., Coil, A. L., Moustakas, J., Salim, S., & Weiner, B. J. 2012, ApJ, 746, 124

Moustakas, J., et al. 2013, ApJ, 767, 50

Murakami, H., et al. 2007, PASJ, 59, 369

Norberg, P., et al. 2002, MNRAS, 336, 907

Oke, J. B., & Sandage, A. 1968, ApJ, 154, 21

Opik, E. 1922, ApJ, 55, 406

Ostriker, J. P., Peebles, P. J. E., & Yahil, A. 1974, ApJ, 193, L1

Penzias, A. A., & Wilson, R. W. 1965, ApJ, 142, 419

Perlmutter, S., et al. 1999, ApJ, 517, 565

Polletta, M., et al. 2007, ApJ, 663, 81

Pozzetti, L., et al. 2003, A&A, 402, 837

Press, W. H., & Schechter, P. 1974, ApJ, 187, 425

Rieke, G. H., Alonso-Herrero, A., Weiner, B. J., Pérez-González, P. G., Blaylock, M., Donley, J. L., & Marcillac, D. 2009, ApJ, 692, 556

Riess, A. G., et al. 1998, AJ, 116, 1009

Roming, P. W. A., et al. 2005, Space Sci. Rev., 120, 95

Rubin, V. C., & Ford, Jr., W. K. 1970, ApJ, 159, 379

Rubin, V. C., Ford, W. K. J., & . Thonnard, N. 1980, ApJ, 238, 471

Rubin, V. C., Thonnard, N., & Ford, Jr., W. K. 1978, ApJ, 225, L107

Rudnick, G., et al. 2003, ApJ, 599, 847

Salpeter, E. E. 1955, ApJ, 121, 161

Schechter, P. 1976, ApJ, 203, 297

Schmidt, M. 1968, ApJ, 151, 393

Scoville, N., et al. 2007, ApJS, 172, 1

Skrutskie, M. F., et al. 2006, AJ, 131, 1163

Smith, R. E., & Markovic, K. 2011, Phys. Rev. D, 84, 063507

Spergel, D. N., et al. 2003, ApJS, 148, 175

—. 2007, ApJS, 170, 377

Springel, V., et al. 2005, Nature, 435, 629

Stern, D., et al. 2005, ApJ, 631, 163

Stoughton, C., et al. 2002, AJ, 123, 485

Taylor, E. N., et al. 2009, ApJS, 183, 295

—. 2011, MNRAS, 418, 1587

Tinsley, B. M. 1968, ApJ, 151, 547

Toomre, A., & Toomre, J. 1972, ApJ, 178, 623

Turner, M. S., & White, M. 1997, Phys. Rev. D, 56, 4439

van der Wel, A., Franx, M., van Dokkum, P. G., Rix, H.-W., Illingworth, G. D., & Rosati, P. 2005, ApJ, 631, 145

van Dokkum, P. G. 2005, AJ, 130, 2647

van Dokkum, P. G., et al. 2009, PASP, 121, 2

Westra, E., Geller, M. J., Kurtz, M. J., Fabricant, D. G., & Dell'Antonio, I. 2010, PASP, 122, 1258

Whitaker, K. E., et al. 2011, ApJ, 735, 86

White, S. D. M., & Frenk, C. S. 1991, ApJ, 379, 52

White, S. D. M., & Rees, M. J. 1978, MNRAS, 183, 341

Wilkins, S. M., Gonzalez-Perez, V., Baugh, C. M., Lacey, C. G., & Zuntz, J. 2013, MNRAS, 431, 430

Willmer, C. N. A., et al. 2006, ApJ, 647, 853

Wolf, C., Meisenheimer, K., Rix, H.-W., Borch, A., Dye, S., & Kleinheinrich, M. 2003, A&A, 401, 73

Wright, E. L., et al. 2010, AJ, 140, 1868

York, D. G., et al. 2000, AJ, 120, 1579

Zehavi, I., Patiri, S., & Zheng, Z. 2012, ApJ, 746, 145

Zibetti, S., Charlot, S., & Rix, H.-W. 2009, MNRAS, 400, 1181

Zwicky, F. 1933, Helvetica Physica Acta, 6, 110